主論文

CREATION OF NOVEL HELICENE-BASED NONPLANAR AROMATICS

ヘリセン構造を基盤とした新しい非平面芳香族分子の創製

BY TAKAO FUJIKAWA

藤川 鷹王

Department of Chemistry, Graduate School of Science
Nagoya University

2016

Preface

The studies presented in this thesis have been carried out under the direction of Professor Kenichiro Itami at Department of Chemistry, Graduate School of Science, Nagoya University from April 2012 to November 2016. The studies are concerned with CREATION OF NOVEL HELICENE-BASED NONPLANAR AROMATICS.

First and foremost, I would like to express the sincerest gratitude to my doctoral advisor, Professor Kenichiro Itami for arranging the opportunity for me to work together with him and enjoy the world of chemistry. Without his enthusiasm and hearty encouragement, I could not have traveled the obscure and artistic field of nonplanar aromatics.

I would like to express my heartfelt appreciation to Designated Associate Professor Yasutomo Segawa for his kind guidance during the amazing long-term journey. He gifted me a lot of valuable discussion with a constructive criticism, technical assistance to push my project forward, and scientific education to mold me into a scientist.

I would like to strongly acknowledge Associate Professor Junichiro Yamaguchi, Associate Professor Shinya Hagihara, Lecturer Hideto Ito, and Assistant Professor Kei Murakami for insightful comments and encouragements. Their aggressive posture on science has stimulated me unceasingly.

Special and deep thanks to Professor Lawrence T. Scott (Boston College, USA) for accepting me as a visiting student from July to September 2013. During the course of the synthetic study on circosesquifulvalene, his bottomless wisdom has always lighted up the right way to go.

I would like to deeply appreciate Professor Tsunehiko Higuchi (Nagoya City University) for hearty encouragement and guidance at the dawning of my research activities when I was an undergraduate student.

I must make a special mention of Associate Professor Atsushi Wakamiya and Dr. Hidetaka Nishimura (Kyoto University) for wonderful collaborations, discussion, and assistance on the fabrication of organic photovoltaic devices. I deeply appreciate Dr. Nobuhiko Mitoma for kindly teaching me the outline of organic field-effect transistor and its fabrication method. I also wish to thank Associate Professor Akinori Saeki (Osaka University) for measurements and discussion

on the time-resolved microwave conductivity. I am grateful to Professor Kendall N. Houk, Dr. Ilhan Yazus, and Ms. Janice B. Lin (University of California, Los Angeles, USA) for theoretical prediction of carrier transport abilities of my compounds. I heartily appreciate Dr. Dorin V. Preda (Boston College, USA), an alumnus of the LTS group, for his quondam studies on corannulene–helicenes leading to my synthetic study on circosesquifulvalene. I must thank Associate Professor Lingkui Meng (Huazhong University of Science and Technology, China) for giving me the opportunity to handle the missing triple helicene in my helicene chemistry.

Many thanks to Dr. Katsuaki Kawasumi, Mr. Kenta Kato, Mr. Yuuta Yano, and Mr. Kazuya Kawai for active collaborations and constant discussion. They have been traveling buddies on my sailing the undulating sea of carbons.

I thank Mr. Toshiaki Noda, Ms. Hideko Natsume, and Mr. Hisakazu Okamoto for their excellent work on scientific glassware. This thesis cannot exist without their glassware.

I express grate gratitude to Mr. Yuichi Amano, Mr. Koya Inagaki, Mr. Hiromu Hattori, Mr. Keisuke Suzuki, Mr. Hideyuki Sawada, Mr. Takeshi Tsusaka, Mr. Tatsuro Murakami, Mr. Yoshihisa Mimura, and Ms. Yuuka Morita. They have been precious friends giving me courage even separated across the sea.

I heartily thank to Dr. Masakazu Nambo, Dr. Eiji Yamaguchi, Dr. Venkataramana Gandikota, Dr. Jiao Jiao, Dr. Asraa Ziadi, Dr. Guillaume Povie, Dr. Kazuya Yamaguchi, Mr. Shin Miyamura, Mr. Takeshi Kaneda, Mr. Taito Hatakeyama, Ms. Hiromi Yamaguchi, Mr. Hiroyuki Kitano, Dr. Atsushi Kinoshita, Mr. Kaoru Arisue, Dr. Debashis Mandal, Dr. Kirika Ueda, Dr. Haruka Omachi, Dr. Atsushi Yamaguchi, Dr. Takehisa Maekawa, Dr. Kazuhiro Hata, Dr. Kazuma Amaike, Dr. Kyohei Ozaki, Mr. Kazuki Kimura, Dr. Katsuma Matsui, Dr. Kei Muto, Dr. Akiko Yagi, Mr. Hiroyuki Ishikawa, Mr. Yuuki Ishii, Mr. Takahiro N. Uehara, Mr. Tomonori Kajino, Ms. Keika Hattori, Ms. Yukari Mitamura, Mr. Tetsushi Yoshidomi, Mr. Hiroki Kondo, Mr. Kakishi Uno, Ms. Misaho Araki, Ms. Yuko Kamada, Ms. Natsumi Kubota, Mr. Yutaro Saito, Mr. Shin Suzuki, Mr. Ryosuke Takise, Mr. Masahiko Yoshimura, Mr. Tsuyoshi Oshima, Mr. Jun Orii, Ms. Mari Shibata, Ms. Kaho Maeda, Mr. Kiyotaka Mori, Mr. Shun Yamashita, Mr. Keishu Okada, Mr. Takahiro Kawakami, Ms. Chisa Kobayashi, Ms. Masako Fushimi, Mr. Keiichiro Murai, Ms. Manami Muraki, Mr. Shuya Yamada, Ms. Eri Ito, Mr. Kazushi Kumazawa, Mr. Yoshito Koga, Mr. Jumpei Suzuki, Ms. Wakana Hayashi, Mr. Wataru Matsuoka, Ms. Yip Shu Jan, Ms. Akari Saito, Mr. Yota Sakakibara, Mr. Michihisa Toya, Mr. Taito Hiraga, Ms. Ayana Mashimo, Ms.

Letitia Sarah, Dr. Anna Junker, Dr. Lilia Lohrey, Dr. Christoph Rosorius, Mr. Richard Maceiczyk, Dr. Friederike Sibbel, Dr. Nils Schröder, Mr. Dominik Johannes Bergmann, Dr. Eva Koch, Mr. Artur Kokornaczyk, Dr. Kiran Sagar Unikela, Dr. Chepiga Kathryn Megan, Mr. Michael Wade Wolfe McCreery, Ms. Huimin Dai, Mr. Mina Narouz, Mr. Shijian Jin, Mr. Chunxiao Li, Mr. Jake Schlessinger, Ms. Enikö Baligács, Ms. Sophie Cemaj, Ms. Quynh Do, Ms. Rika Kato, Ms. Yui Ueyama, Mr. Satoru Kawai, Ms. Akemi Saito, Ms. Nanako Kato and all alumni of Itami group.

I appreciate the Japan Society for the Promotion of Science (JSPS) for the research fellowship for young scientists (DC1). I also thank to Integrative Graduate Education and Research Program in Green Natural Scientists (IGER) for the financial support.

Last but not least, I would like express my deepest appreciation to my family, especially my parents, Mr. Kiyoyuki Fujikawa, Ms. Teruko Fujikawa, and Mr. Tatsuma Fujikawa for their constant assistance and encouragement.

Takao Fujikawa

Department of Chemistry
Graduate School of Science
Nagoya University
2016

Contents

General Introduction

Overview of the Chemistry of Nonplanar Aromatics

According to Hückel's rule,[1] aromaticity is defined as a property of planar and cyclic π-conjugated molecules with ($4n$ + 2) of electrons delocalizing roundly, where a significant thermal stabilization is gained compared with linear counterparts. After the launch of Hückel's rule in 1931, however, organic chemists have often expanded the rule of "planar", and a tremendous number of "nonplanar" aromatics have been synthesized.

To Make Nonplanar Aromatics

Tricks are required for arranging nonplanar aromatics. In this context, four approaches have been employed to achieve a deformation of π-system (Chart 1). The first approach is to place a nonhexagonal ring inside the carbon skeleton (type A).[2–4] Because π-surface becomes nonplanar to retain the typical C–C bond lengths and bond angles, some of polycyclic aromatics containing nonhexagonal rings exhibit curved structures. This approach can be divided into two subclasses whether the embedded ring is smaller (type A-1) or larger (type A-2) than hexagonal ring. The second approach is to replace a quaternary sp^2-carbon atom with a heteroatom (type B).[5] In this case, several characteristics of heteroatoms such as the presence of an unshared electron pair, the difference in bond length (C–C vs C–X bonds), and the state of hybridization intricately affect in each other, rendering the embedded heteroatom pyramidalized, and the π-system is finally deformed. The above-mentioned two approaches can be classified in an endoskeletal approach since p-orbital's connectivity inside the π-skeleton is directly altered. The third and fourth approaches are to introduce a tightly bridged transannular connection (type C)[6,7] or a steric hindrance from atom crowdedness (type D),[8,9] forcing the π-system to be out of plane. Type C approach can be divided into two subclasses whether the transannular connection is unconjugated (type C-1) or conjugated (type C-2). Type D approach also includes two subclasses whether the steric hindrance is derived from π-skeleton itself (type D-1) or substituents (type D-2). In contrast to the endoskeletal approaches, the last two approaches can be classified in an exoskeletal approach because the deformation of π-system is achieved without the change of p-orbital's connectivity. Based on these approaches, a wide variety of nonplanar aromatics have been synthesized nowadays.

Chart 1. A classificatory criterion of approaches for a deformation of π-system.

Endoskeletal approach		Exoskeletal approach	
Type A-1	Embedding a nonhexagonal ring (number of ring members < 6)	**Type C-1**	Adding a tightly bridged transannular unconjugated connections
Type A-2	Embedding a nonhexagonal ring (number of ring members > 6)	**Type C-2**	Adding a tightly bridged transannular conjugated connection
Type B	Embedding a heteroatom instead of a sp^2-carbon atom	**Type D-1**	Adding a steric hindrance derived from π-skeleton itself
		Type D-2	Adding a steric hindrance derived from substituents

Shape Generates Properties

In the chemistry of nonplanar aromatics, the most important aspect is that a variety of incidental effects unachievable by planar ones are acquired depending on the shape of π-system.

For example, fullerenes exhibit an excellent electron-accepting ability and unique chemical reactivity due to the spherical π-systems (Figure 1, left).[3] Their hollow-cavity have a fundamentally different topology from that of other aromatics, therefore enabling complete isolation of small atoms, molecules, and metal ions inside the carbon cage.[10]

Bringing down a small fragment from fullerenes, geodesic (bowl-shaped) polyarenes such as corannulene[4a] and sumanene[11] are generated (Figure 1, middle).[2b–d,12] In addition to the electron-accepting ability and chemical reactivity inherited from fullerenes, geodesic structures display facile bowl-to-bowl inversion dynamics and concave–convex π-interactions.[13] These properties derived from bowl-shaped molecular geometries are also observed in a series of phosphangulenes (Figure 1, right).[5]

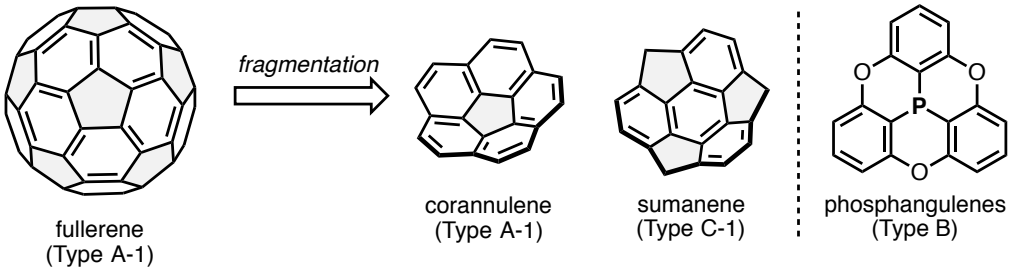

Figure 1. Nonplanar aromatics with positive Gaussian curvature.

The Gaussian curvature is one of the indices to describe the character of curved π-systems. Fullerenes and bowl-shaped π-systems stated above have positive curvature due to the presence of pentagonal and tetragonal rings instead of hexagonal rings or heteroatoms instead of carbon

atoms. To the contrary, the presence of larger ring structures inside the hexagonal lattice inherently expands the curved surface, resulting in saddle-shaped π-systems with negative curvature (Figure 2).[4c,d,g,h] Tub-to-tub inversion dynamics via a low-energy pseudorotation is one of the characters of little-explored saddle-shaped π-systems.[4h] Due to their unique molecular geometries, chemists have also envisaged the use of them as a fragment of unprecedented nanocarbons with negative curvature, as bowl-shaped molecules are regarded as a fragment of fullerenes and related nanocarbons with positive curvature.[2a]

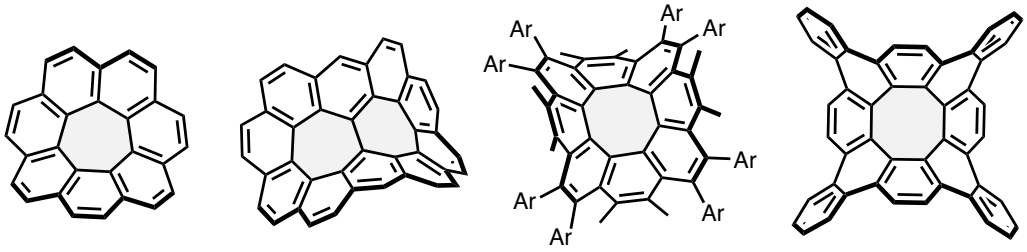

Figure 2. Nonplanar aromatics with negative Gaussian curvature.

Focusing on the π-systems with zero-curvature, belt-shaped π-systems termed "cyclophanes" have been well-studied (Figure 3).[6,7] A tight bridging by transannular connections forces bent aromatic structures, which make the π-systems more chemically labile and dramatically alter the electronic properties.[14,15] A high proximity of two aromatic rings located with a face-to-face fashion has been beneficial for examining through-space π-interactions.[16] The infinite radial π-conjugation of large cyclophanes such as cyclic paraphenyleneacetylenes and cycloparaphenylenes also gathered much attention in their encapsulation behavior[17] and electronic properties.[18]

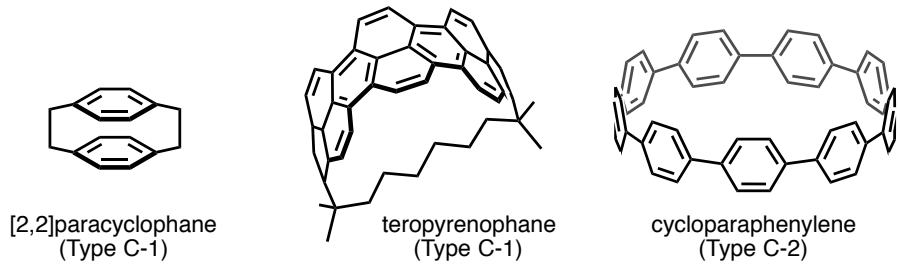

Figure 3. Nonplanar aromatics with zero Gaussian curvature.

Helical and twisted π-systems are discriminated from the other nonplanar aromatics due to the existence of intrinsic chirality (Figure 4).[8–9] Especially, chiroptical properties of these π-systems such as optical rotation, circular dichroism (CD), and circular polarization luminescence make them peculiar materials in the field of optoelectronics.[19] Their chiral π-systems have also been important motifs for a creation of asymmetric catalysis, molecular machine, and molecular recognition materials.

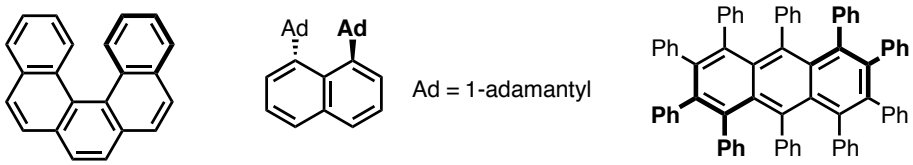

[5]helicene (Type D-1) | 1,8-bis(1-adamantyl)naphthalene (Type D-2) | decaphenylanthracene (Type D-2)

Figure 4. Helical and twisted π-systems exhibiting intrinsic chirality.

In This PhD Thesis

Prominent molecular geometries endow aromatics with exceptional electronic properties, unique molecular dynamics, and special usage depending on each molecular shape, and therefore, creating hitherto-unknown nonplanar aromatics has been a key issue for organic chemists to pioneer a new chemical space. That said, designing a conceptually new form of aromatics has ended up becoming a tough work in modern times. In this PhD thesis, the author tackled this problem by blending helical motifs of helicenes with other structural motifs. Helicenes are one of the most abundant molecules having nonplanar entities, hence whose structures are relatively accessible and easy to be customized compared with other nonplanar aromatics. By exploiting a flexibility in molecular design of helicenes, a variety of helicene-based nonplanar aromatics were developed herein in order to unearth new shape-dependent properties. Before stating the author's PhD works, the chemistry of helicenes is outlined in the next section.

The Chemistry of Helicenes

Helicenes are screw-shaped molecules defined as *ortho*-fused polycyclic aromatic compounds in which all rings are helically arranged. Among several classes of nonplanar aromatics, helicenes have the longest history over one hundred years. The first synthesis of helicenes was achieved by Meisenheimer and Witte in 1903 (Figure 5, left).[20] After several decades with little progress, the chemistry of helicenes truly sprouted in 1956 when Newman and Lednicer achieved the first synthesis and optical resolution of [6]helicene (Figure 5, right),[21] and since then, numerous helicene derivatives have been synthesized.

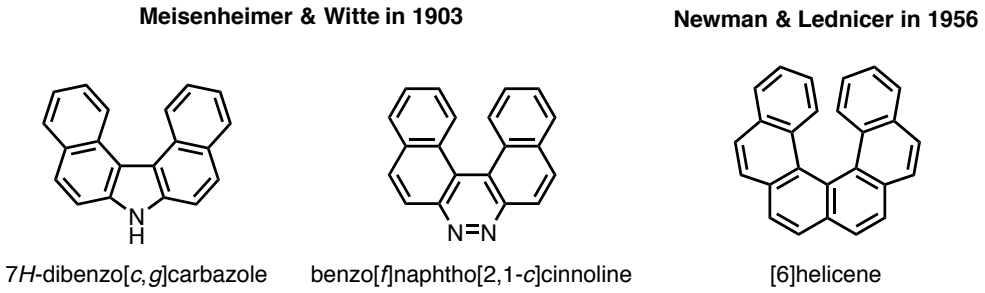

Figure 5. The dawning of helicenes.

In order to grasp the overview of π-skeletons of helicenes, a classificatory criterion shown in Chart 2 is employed herein. The number of *ortho*-fused rings (*n*) is the major classification of all helicenes. Next, each [*n*]helicene can be divided into two classes: carbohelicenes and heterohelicenes. A lateral π-extension to the simply helical basic skeleton enables further structural modifications. Finally, if the laterally-extended moieties have other helical motifs, such helicenes can be termed "multihelicenes". In this way, all helicenes can be positioned somewhere in the classification chart on the basis of the structural features.

Chart 2. A classificatory criterion of π-skeleton of helicenes.

	The number of *ortho*-fused rings (*n*)							
	4	5	6	7	8	9	10	•••
Carbo[*n*]helicenes	Simple helicenes							
	Laterally π-extended helicenes							
	Multihelicenes (if laterally extended moieties have other helical motifs)							
Hetero[*n*]helicenes	Laterally π-extended helicenes							
	Simple helicenes							

Helically Elongated Helicenes

Historically, elongation of helix has been of great interest for chemists in terms of not only understanding its effects on helical properties but also synthetic approaches constructing highly crowded structures. To date, simple carbo[*n*]helicenes with *n* = 4–14, 16 have been prepared (Figure 6).[22] A majority of them were synthesized by using oxidative photocyclization approach, in which stilbene-like substructures were converted into corresponding phenanthrene-like substructures (Figure 7). The first application of photocyclization approach to the synthesis of helicenes was performed by Martin in 1967.[22g] An improved procedure using propylene oxide was reported by Katz in 1991.[23] The single-step photochemical synthesis of [16]helicene, the longest of carbo[*n*]helicene, by Fujita in 2015 should be counted as one of the culminations in the synthetic chemistry of helicenes.[22a]

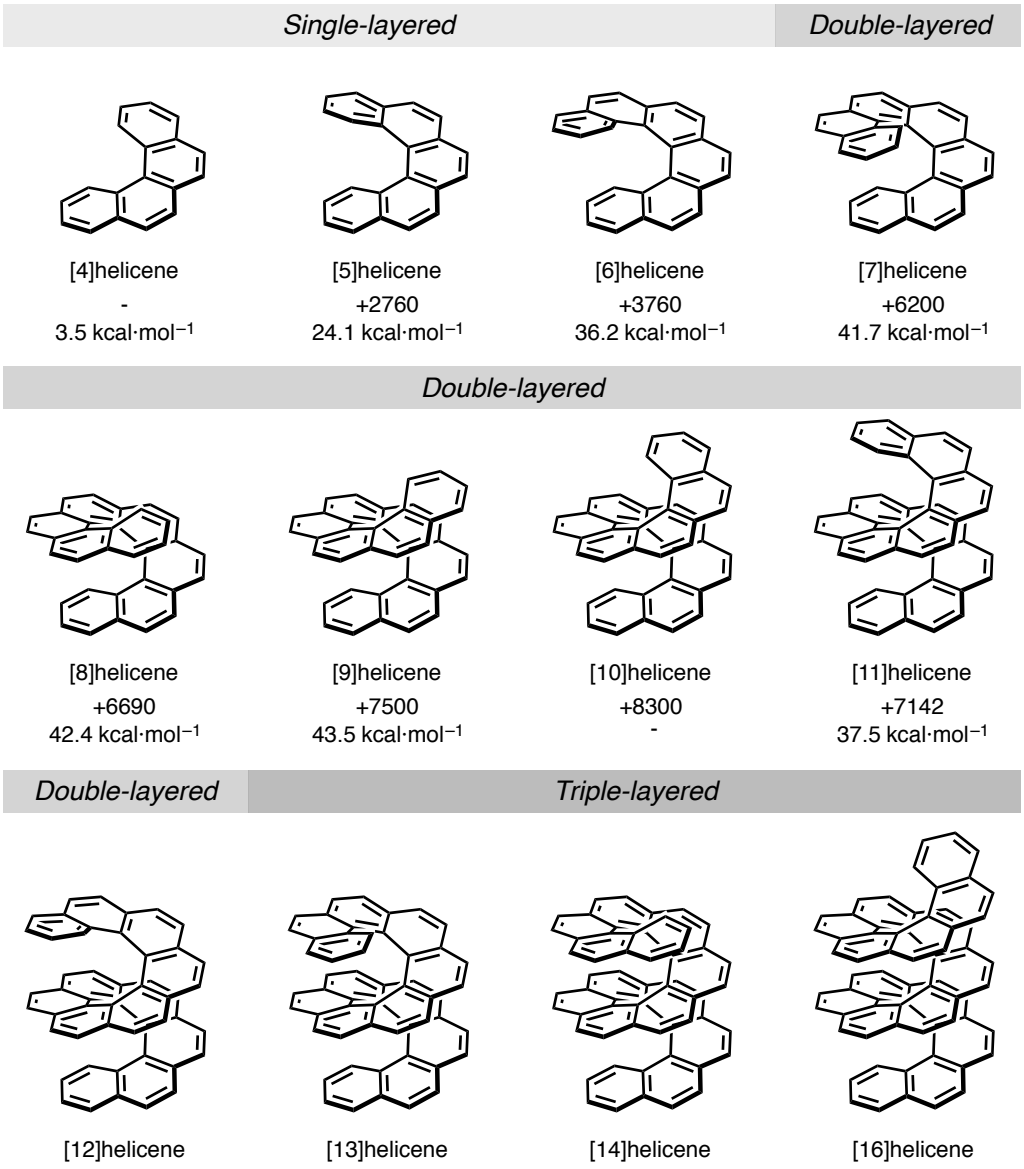

Figure 6. Carbo[*n*]helicenes with specific optical rotations and isomerization barriers.

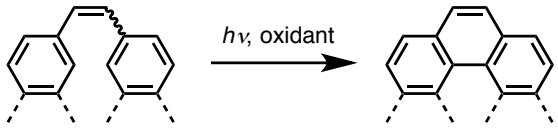

Figure 7. General scheme of oxidative photocyclization.

Focusing on the series of carbo[*n*]helicene comprising only benzene rings, systematic research on the relationship between helical elongation (the number of *n*) and helical properties has been performed on both sides of experiment and theory.[24,25] From the viewpoint of helical structure, steric congestion of helical termini occurs when $n \geq 4$. Double-layered structures are obtained when $n \geq 7$ and triple-layered ones are obtained when $n \geq 13$. A multi-layered structure of higher helicene is expected to provide larger effective conjugation length for helicenes ($n \approx 50$) than those for *ortho*- and *para*-phenylenes ($n \approx 10$), oligothiophenes ($n \approx 20$), and acenes ($n \approx 24$–25), probably due to the large intramolecular overlap.[24a,26] The transannular π–π interaction across the helical pitch also reduces the energy gap between the highest occupied molecular orbital (HOMO) and the lowest unoccupied molecular orbital (LUMO) compared with corresponding phenacenes.[24b] Electric transition dipole and magnetic transition dipole progressively line up in parallel with the increase of *n*, affording intensified Cotton effect.[24a] Enantiomerization of [*n*]helicenes proceeds via transition states with rebelled, face-to-face orientation of aromatic rings (Figure 8) except the case of [4]helicene whose enantiomerization proceeds with a planar geometry.[25] Therein, isomerization barrier of [*n*]helicenes increases in a range of $n = 4$–9 (3.5–43.5 kcal·mol^{-1}) despite that there is a slight difference between $n = 7$–9, and finally decreases when $n = 11$ (37.5 kcal·mol^{-1}). In this way, various physicochemical properties of helicenes strongly depend on the length of helices.

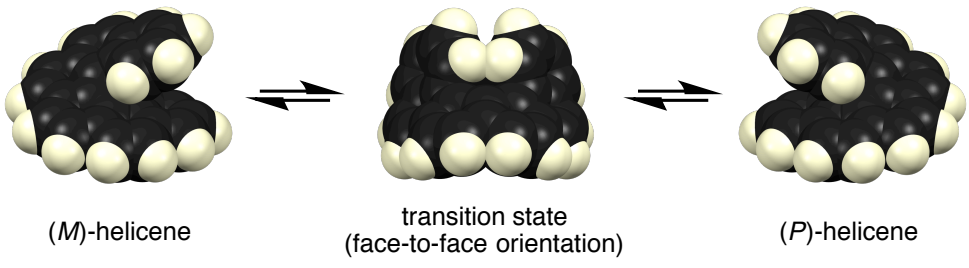

Figure 8. Isomerization dynamics of [6]helicene.

Carbohelicenes and Heterohelicenes

Carbohelicenes consist exclusively of carbon atoms and hydrogen atoms. In addition to alternant helicenes comprising only benzene rings, nonalternant helicenes containing nonhexagonal rings[27] and alkyl-chain bridged helicene homologs[28] are classified in this family (Figure 9).

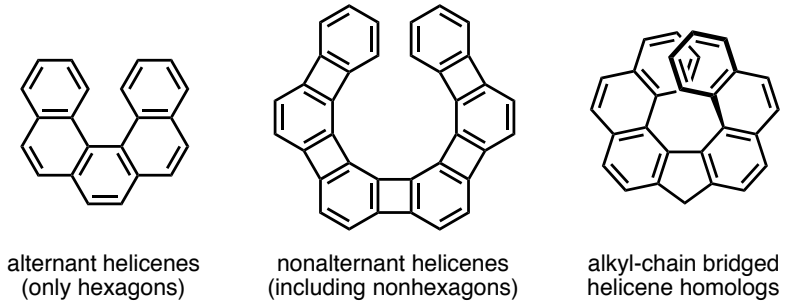

Figure 9. Examples of carbohelicenes.

Heterohelicenes are obtained by replacing the carbon atoms of such carbohelicenes with heteroatoms (Figure 10a).[29–32] Differential electronegativity, presence of unshared electron pairs, and unmatched atomic orbital sizes of replaced heteroatoms have a great effect on optoelectronic properties of helicenes. Also, replacement of benzene rings (hexagonal rings) to heteroles (pentagonal rings) significantly changes the molecular geometry and the degree of eclipse of terminal aromatic rings due to the difference of in-plane turn angles: benzene (60°) > phosphole oxide/sulfide (50°) > thiophene (45°) > pyrrole (35°) > furan (32°) (Figure 10b).

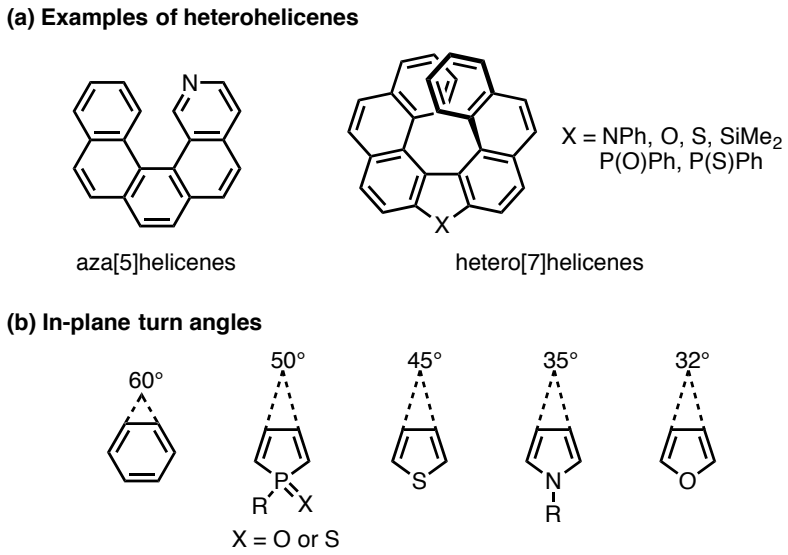

Figure 10. (a) Examples of heterohelicenes. (b) In-plane turn angles of benzene and heteroles.

One of the agenda is how the photophysical properties of helicenes are affected upon heteroatom introduction. Schmidt and Brédas collectively examined photophysical properties of monoaza[5]helicenes (Figure 10a, left) and revealed that the relative ratio of phosphorescence and fluorescence, which is connected with the degree of spin–orbit coupling, obviously depends on the position of the nitrogen atoms.[33] In general, helicenes are poorly emissive materials due to the fast intersystem crossing from the singlet excited state to the triplet state.[34] Sila[7]helicene reported by Nozaki (Figure 10a, right), however, exhibited excellent solid state luminescence with notably high quantum efficiency up to 17% and relatively high dissymmetry factor (*g*) of circular polarized luminescence, encouraging their use as chiroptical materials.[32h]

Energy levels and spatial distribution of frontier molecular orbitals of helicenes have also been tuned by heteroatom introduction (Figure 11). For example, theoretical studies by Kertesz predicted significantly narrower HOMO–LUMO energy gap for thiahelicenes than for carbohelicenes and C_2S helicenes (helical oligothiophenes), which were rationalized by the sulfur π-orbital couplings and the difference of effective conjugations.[24b,29,30] In the case of azaboradibenzo[6]helicene reported by Nakamura and Hatakeyama, unique inversion of carrier transport was observed between heterochiral and homochiral crystals.[32j] Rajca reported that both radical cation and neutral radical species of azathia[7]helicene display higher energy levels of HOMO than those of SOMO.[32a] Such energy level inversion phenomenon violates the Aufbau principle, providing interesting helical materials for spintronics.

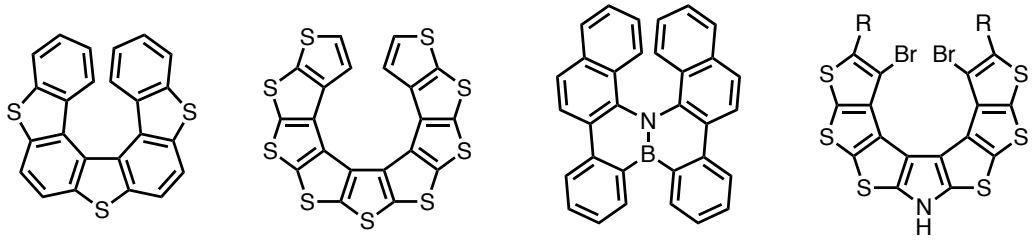

Figure 11. Examples of heterohelicenes whose electronic states are strongly perturbed by imbedded heteroatoms.

CH–π interactions dominate the molecular packing structure of helicenes due to the 3D π-systems, and π–π interactions are mostly excluded. Nozaki challenged to this problem by employing dipole–dipole interactions derived from a phosphole sulfide moiety imbedded in the helicene framework.[32i] Therein, homochiral one-dimensional columnar packing structure was

obtained for phospha[7]helicene (Figure 10a, right), which is a quite uncommon packing manner for helicenes.

Heterohelicenes are attractive nonplanar molecules in the field of asymmetric catalysis due to large and chiral entities with coordinating heteroatoms. The first asymmetric reaction employing chiral ligand based on helicenes was reported by Reetz in 1997, in which a chiral catalyst was prepared in situ by mixing PHelix and $Rh(cod)_2BF_4$, and hydrogenation of dimethyl itaconate was performed under mild conditions yielding dimethyl (*S*)-2-methylsuccinate with moderated enantiomer excess (Figure 12a).[35] Since then, several phosphane-substituted helicenes and azahelicenes have been developed and employed in asymmetric reactions (Figure 12b).[36]

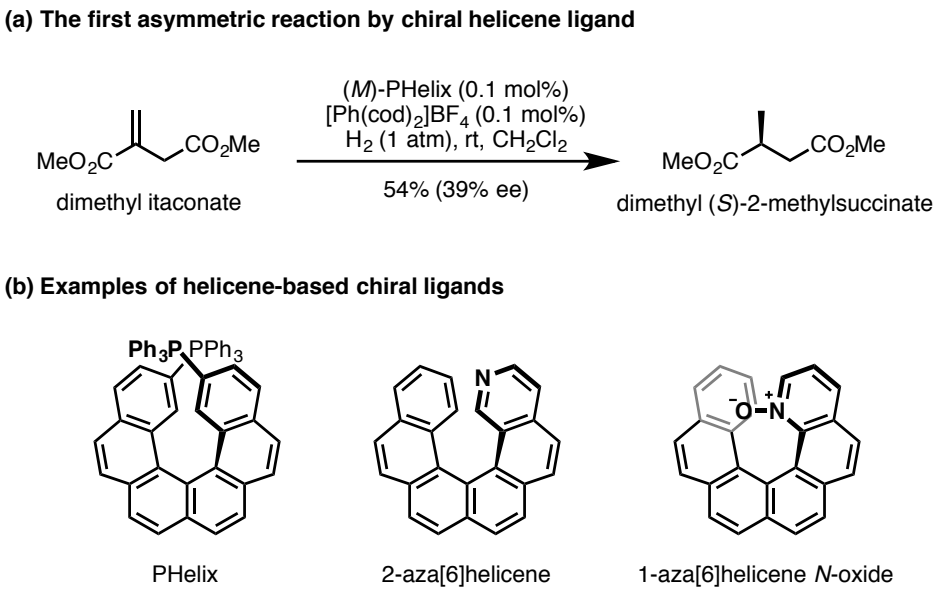

Figure 12. (a) The first asymmetric reaction using helicene-based chiral ligand reported by Reetz. (b) Examples of helicene-based chiral ligands.

Heteroatom introduction is a widespread strategy for fine tuning of π-systems. By employing this strategy, characteristic properties of helicenes such as chirality, nonplanarity, chiroptical properties, and nonlinear optical effects have been wonderfully tuned for various applications in materials science.

Laterally π-Extended Helicenes

The π-extension approach plays an important role to modulate the properties of polyaromatic compounds.[37] From this perspective, the helical elongation approach has been a leading theme in the helicene chemistry for a long time (Figure 13, left). In contrast, the lateral π-extension approach, in which π-systems of helicenes are extended in a direction vertical to the helical axis, has become frequent in recent years (Figure 13, right). There exist several merits in this approach when compared with simply *ortho*-fused helicenes. The presence of fused rings sometimes makes the construction of helix more efficient. Extended, helical π-surfaces facilitate chirality transfer in asymmetric reactions mediated by helicene-based catalysts.[36c–f] Changing the viewpoint, solubility problem commonly observed in extended π-systems can be alleviated by the incorporation of nonplanar helicene motifs.[38]

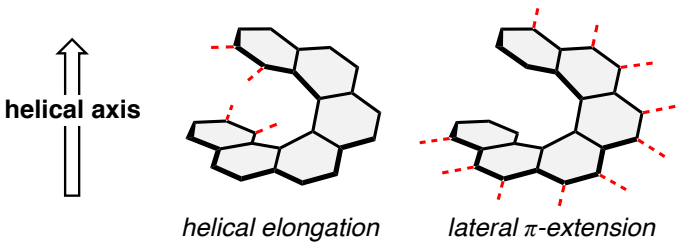

Figure 13. Two π-extension approaches in the helicene chemistry.

The simplest of laterally π-extended helicenes are *cata*-condensed benzohelicenes. From the late 1960's to 1970's, Laarhoven engaged in the synthesis of benzohelicenes, examined their physicochemical properties, and revealed that annulation of one or more benzene rings resulted in a conformational change of helix.[39a–c] Nowadays, a variety of benzohelicenes have been synthesized by using versatile methodologies such as oxidative photocyclization, transition metal catalyzed cycloaddition, and oxidative stitching reaction (Figure 14).[39d–h]

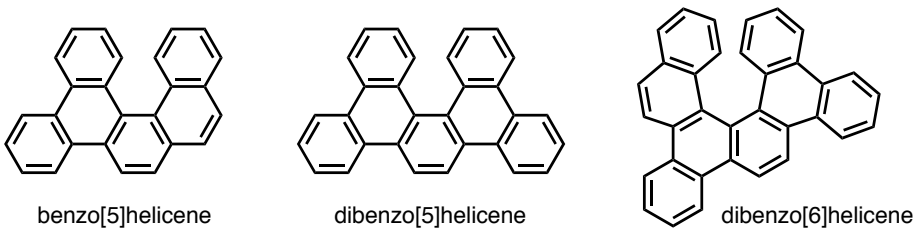

Figure 14. Examples of benzohelicenes.

As larger homologs, naphthohelicenes, laterally π-extended helicenes fused with naphthalene ring, are conventionally termed "pyrenohelicenes" (Figure 15). The first pyrenohelicenes were reported by Vingiello in 1965 although they did not recognize their molecules as helicenes.[40a] In 2010's, Yamato, Collins, Durola, and Stará reported pyrenohelicenes and examined their helical properties.[40b–i] Reduced HOMO–LUMO energy gap and excimer-like emission are representative properties of pyrenohelicenes, which were attributed to the laterally extended π-surfaces of pyrene moieties.

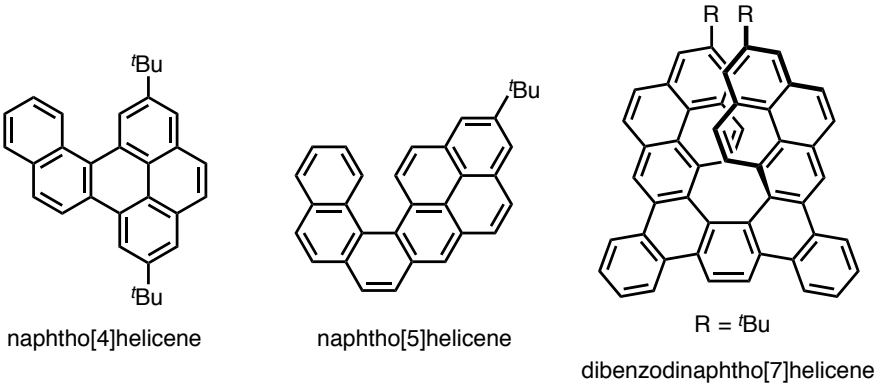

Figure 15. Examples of naphthohelicenes (pyrenohelicenes).

The proximity of helical termini of laterally π-extended helicenes was exploited excellently in the recent work by Nuckolls and Steigerwald (Figure 16).[41] They prepared perylene diimide helicenes (PDI-helicenes) having two PDI moieties fixed at the termini of helicenes, and clarified the through-space electronic delocalization between the two PDI moieties by monitoring the interplay of them during electrochemical reduction events.

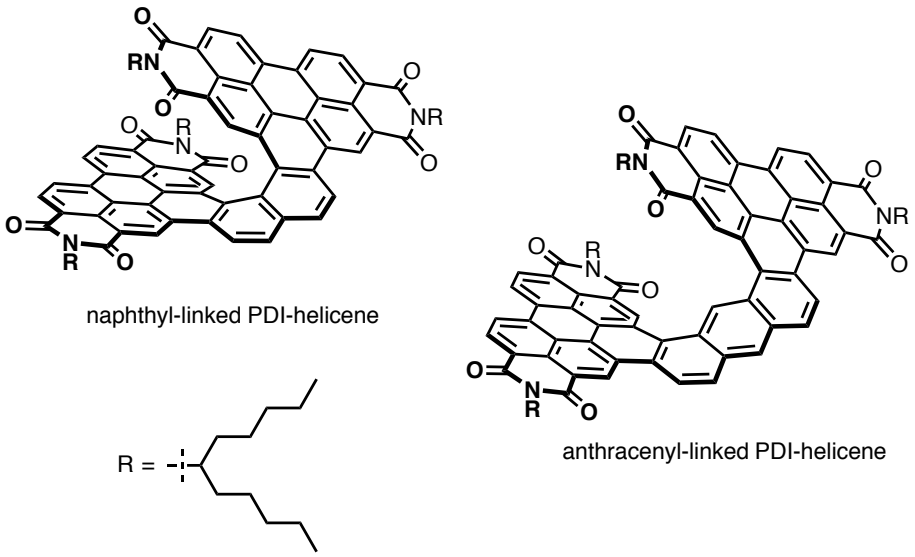

Figure 16. PDI-helicenes reported by Nuckolls.

Union of two or more distinctive nonplanar motifs is of interest to create conceptually new class of nonplanar π-systems. Pascal prepared hybrid molecules of helicenes and twisted acenes, which were termed "hairpin furans" (Figure 17, top).[42] Although both two nonplanar motifs of hairpin furans are chiral, the positional relation between the helical axis and the mean plane of constituent rings was different in each other. The former have helical axes vertical to rings and the latter have propagation axes parallel to rings. They proposed that the unusual topology of hairpin furans will lead to Moebius polycycles, one of imaginary nonplanar polyaromatics. Very recently, Stuparu reported the synthesis of corannulene–helicene hybrid molecules, where bowl-shaped motifs are merged with helicene motifs (Figure 17, bottom).[43]

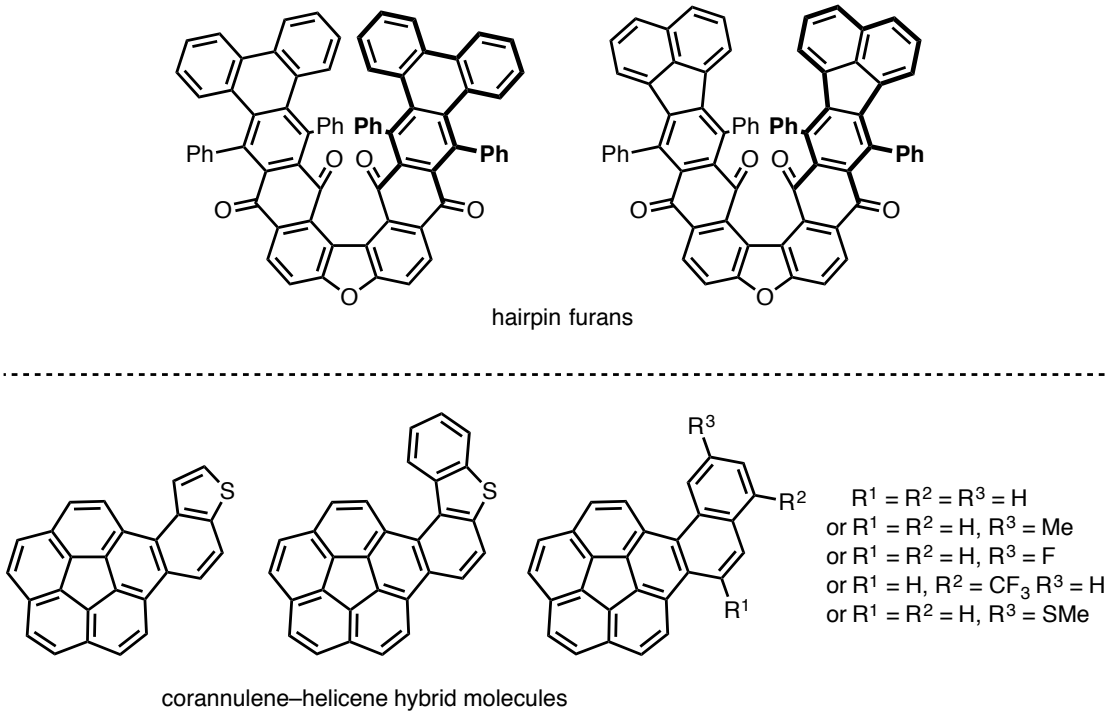

Figure 17. Laterally π-extended helicenes merged with other nonplanar motifs.

Multihelicenes

Among laterally π-extended helicenes, multihelicenes are classified in a distinctive category due to the simultaneity of two or more helical motifs in the same π-system. General characteristics of multihelicenes are, for instance, the presence of plural electronic states (diastereomers), complex interconversion pathways, a significant perturbation of optoelectronic properties, unique molecular packing modes, and generation of highly distorted, congested π-systems. Over the past few decades, a number of multihelicenes with various multiplicities, including double, triple, quadruple, sextuple, and octuple helicenes, have been synthesized.[44–48]

The dawning of multihelicenes was the synthesis of S-shaped double [6]helicene by Laarhoven in 1971 (Figure 18).[44a] They attempted oxidative photocyclization of 2,6-bis(3-phenanthrylethenyl)naphthalene and isolated two dehydrocyclization products with identical mass spectra. The presence of two [6]helicene moieties fused together provided three possible stereoisomers: one pair of enantiomers ((*P*,*P*)- and (*M*,*M*)-isomers) and one meso-isomer ((*P*,*M*)-isomer). The configurational difference of the two diastereomers was examined by probing the proton chemical shifts in proton nuclear magnetic resonance (^{1}H NMR) measurements. In this way, multihelicenes with sufficiently high isomerization barriers can provide two or more distinguishable molecular geometries with different properties.

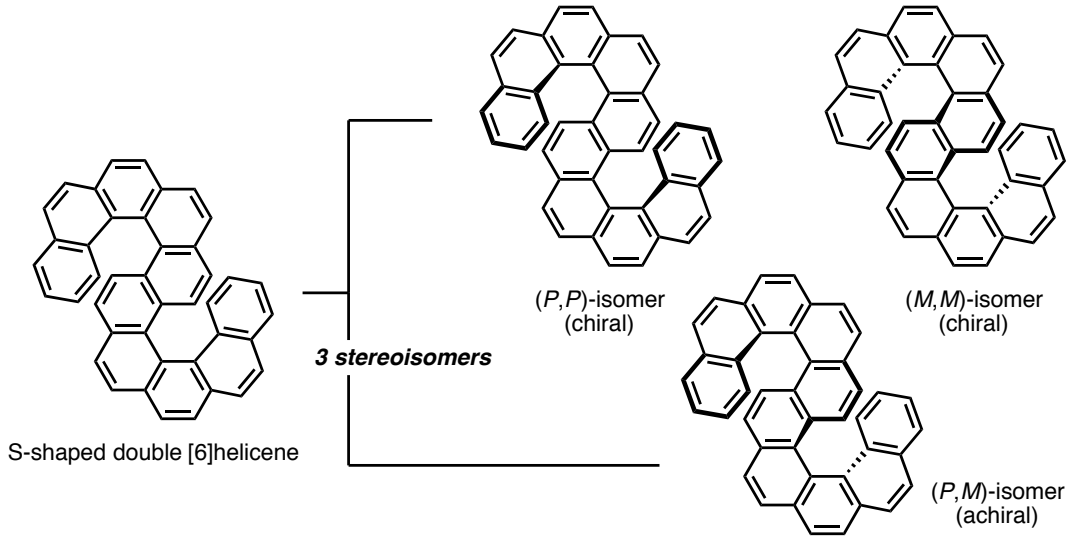

Figure 18. Three stereoisomers of S-shaped double [6]helicene reported by Laarhoven.

To compare optoelectronic properties of multihelicenes with corresponding single helicenes is an interesting issue to understand the essence of chiral π-systems. Thereby, S-shaped chiral molecular geometries of double helicenes have been reexamined in recent years because of enhanced chiroptical properties. Mori reported that the aforementioned S-shaped double car-

bo[6]helicene showed a larger Cotton effect in CD spectrum compared with pristine carbo[6]helicene.[49] The S-shaped double aza[6]helicenes reported by Tanaka also exhibited an amazing enhancement of dissymmetry (*g*) factor of circular polarized luminescence (Figure 19).[45g] These two studies well demonstrated the potential of accumulating helical motifs for chiroptical tuning of helicenes.

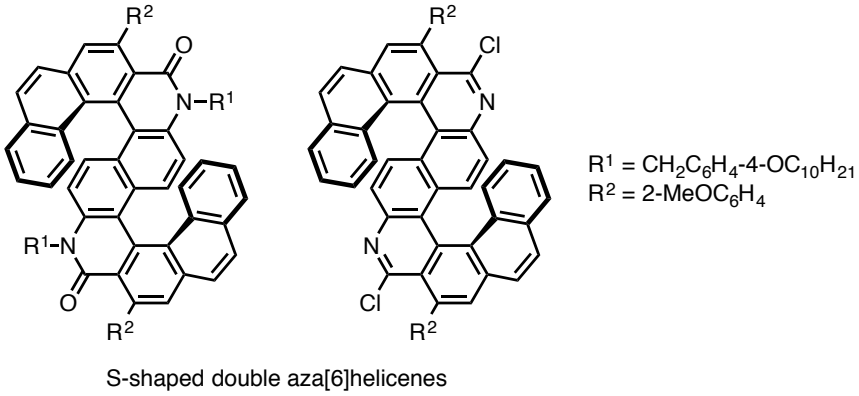

Figure 19. S-shaped double aza[6]helicenes reported by Tanaka.

Multihelical π-systems are also beneficial for crystal engineering unachievable for other planar or nonplanar π-systems. For example, some of double helicenes with extended π-systems are, in the twisted configurations, prone to provide contorted brickwork arrangements in crystalline state. Miao has exploited the unique assembling feature of such double helicenes and fabricated monolayer field-effect transistor using long-chain substituted double [5]helicenes (Figure 20, top), which functioned as p-type transistor with excellent hole mobility.[44e] As multihelicenes with higher multiplicity, PDI-based triple [5]helicenes reported by Wang *et al.* displayed unconventional three-dimensional π-π staking network by utilizing the nonplanar, triply helical structures (Figure 20, bottom).[46a] The triple helicenes was also applied to some organic electronics devices, and the thus-fabricated single-crystal transistors and solar cells worked excellently.

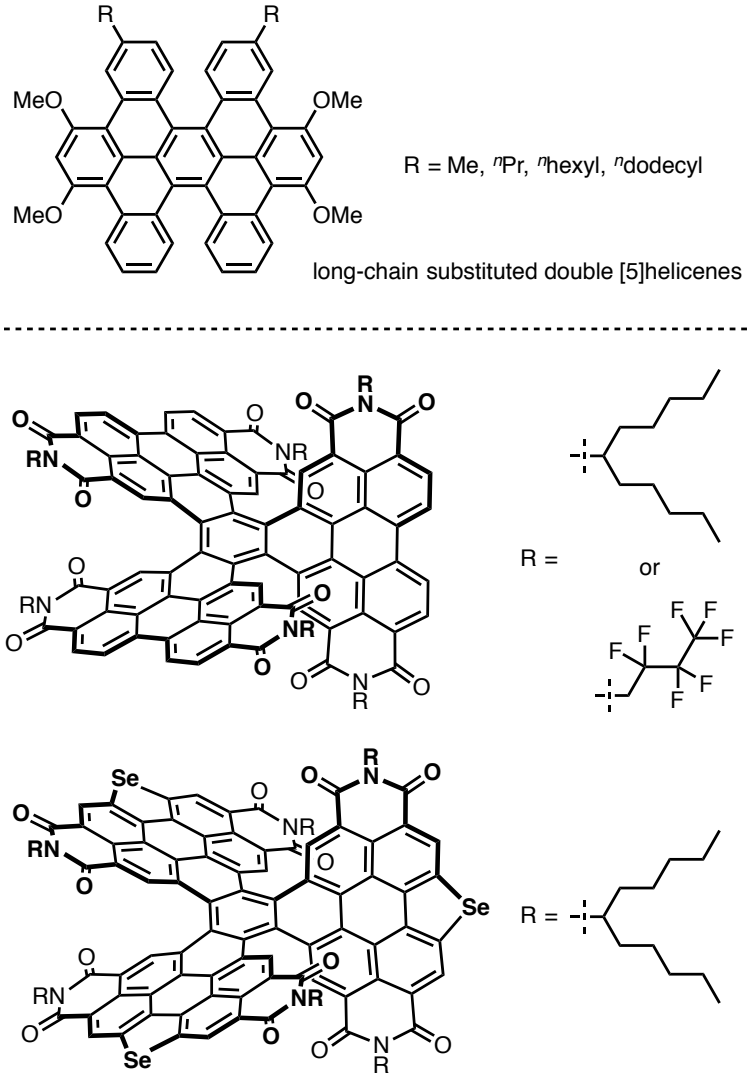

Figure 20. Multihelicenes exhibiting unconventional molecular packing.

Contorted polyaromatics reported by Nuckolls such as *cata*-condensed hexabenzocoronenes (sextuple helicenes), octabenzocircumbiphenyls (octuple helicenes), and PDI-oligomers (double, quadruple, and sextuple helicenes) are also attractive series of multihelicenes with great potentials in organic electronics (Figure 21).[48]

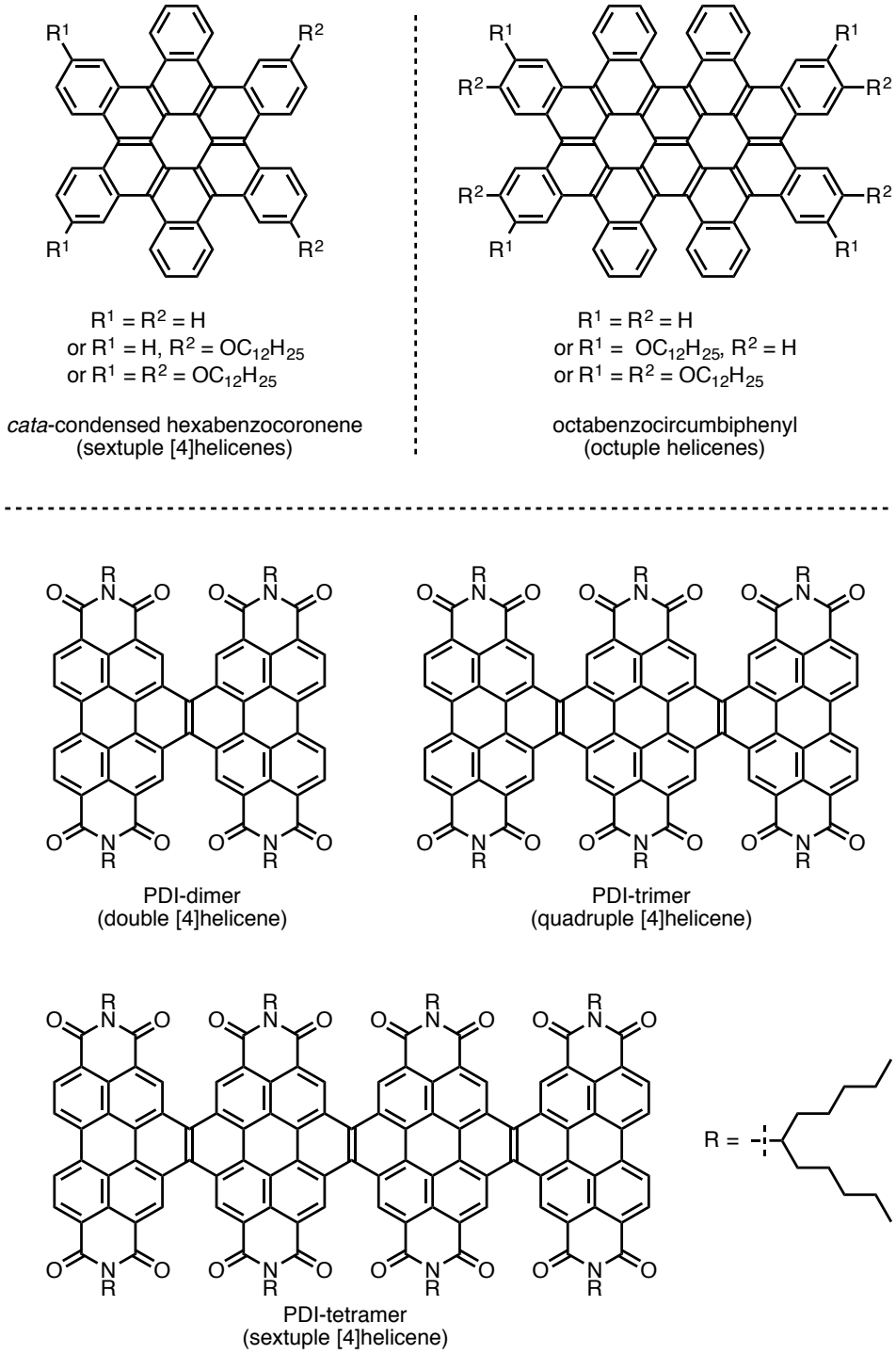

Figure 21. Contorted polyaromatics reported by Nuckolls.

The symmetry of higher multihelicenes sometimes forms chiral one-dimensional columnar stacking. Homochiral, quadruply helical metal phthalocyanines synthesized by Katz were found to form columnar aggregates, thereby providing very large second-order nonlinear optical responses in Langmuir–Blodgett films (Figure 22, top).[47] A triply helical oligothiophene reported by Aida (Figure 22, bottom) also displayed a helical columnar liquid crystal structure with efficient intracolumnar S–S interactions, which showed top-class carrier mobility with ambipolar character as liquid crystal semiconductor.[46c]

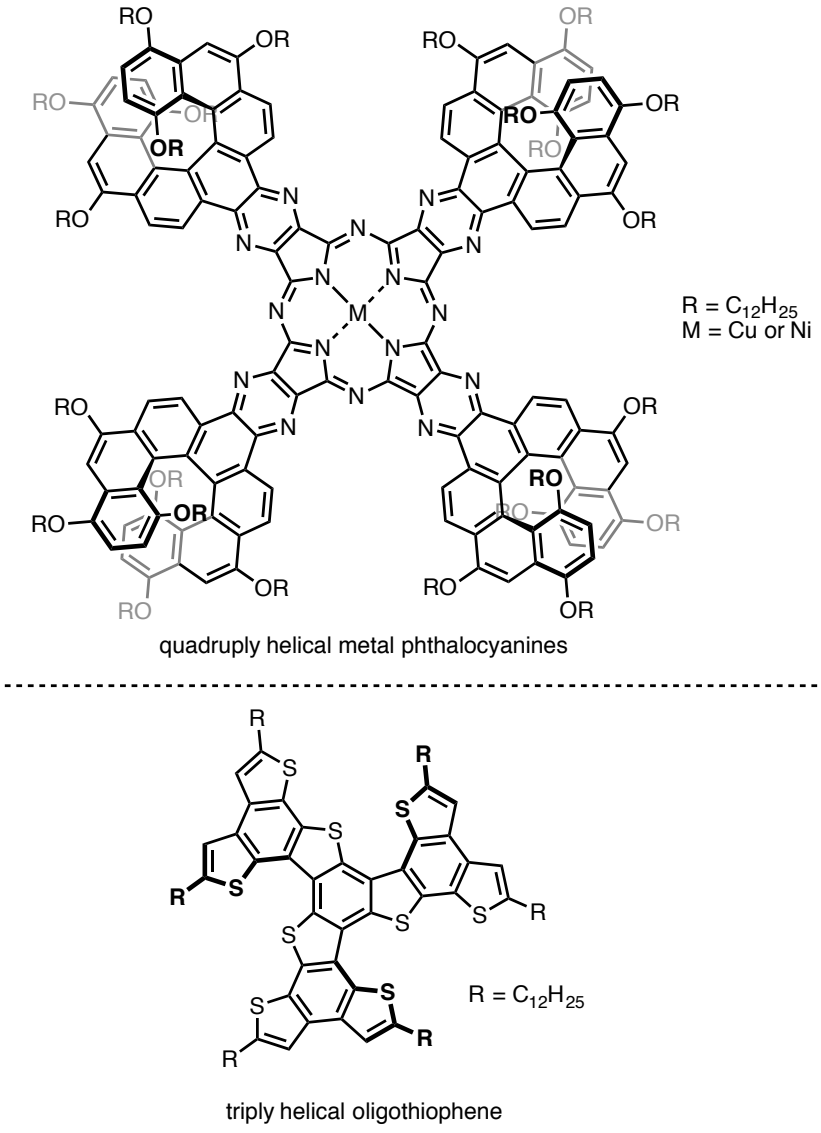

Figure 22. Multihelicenes exhibiting chiral one-dimensional columnar stacking.

Highly crowded structures of multihelicenes are suitable models to test the limit of the deformation of aromatics (Figure 23). For example, the synthesis of P-fused double [5]helicene reported by Hatakeyama and Nakamura demonstrated a new strategy for bending benzene rings.[45f] The central benzene ring of their double helicene displayed a highly distorted structure, whose bending angle of 23° was comparable to that of [1,1]paracyclophane (24.9°).

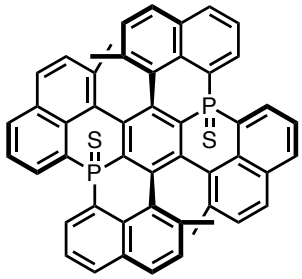

P-fused double [5]helicene

Figure 23. P-fused double [5]helicene reported by Hatakeyama and Nakamura.

Survey of This Thesis

The author's PhD research aimed the creation of novel forms of nonplanar aromatics and exploration of shape-dependent properties. To achieve this, the author focused on the potential of laterally π-extended helicenes, the synthetic concept of which is a merge of helical motifs with other structural motifs. As indicated now, the series of laterally π-extended helicenes have provided a massive synthetic opportunity for us to create a new form of nonplanar aromatics. In this PhD thesis, helical motifs of helicenes were exploited as a cornerstone of molecular design and merged with other structural motifs, *i.e.*, bowl-shaped motifs (Chapter 1), large planar motifs (Chapter 2–3), saddle-shaped motifs (Chapter 4), and extra helical motifs (Chapter 5), yielding a variety of laterally π-extended helicenes with novel molecular geometries and shape-dependent properties.

In Chapter 1, carbo- and thia[6]helicene moieties were merged with a corannulene moiety (bowl-shaped motif), generating corannulene–helicene hybrid molecules. The incorporation of helical motifs endowed a corannulene core with skeletal chirality and provided unforeseen molecular behavior. This represents the first example of simple chiral corannulene fused with just a single helical motif, and enantiomers of corannulene-based skeletally chiral molecules was successfully separated for the first time. Corannulene–helicene hybrid molecules were also exploited as synthetic intermediates of circosesquifulvalene, a polycyclic aromatic hydrocarbon embedded with one of each pentagonal and heptagonal ring. In order to construct the warped carbon lattice of circosesquifulvalene, oxidative stitching of [6]helicene moieties was attempted. Consequently, desired heptagonal ring closing of a [6]helicene moiety successfully proceeded in corannulene–thia[6]helicene hybrid molecule, yielding a small carbon flake with odd-membered ring defects.

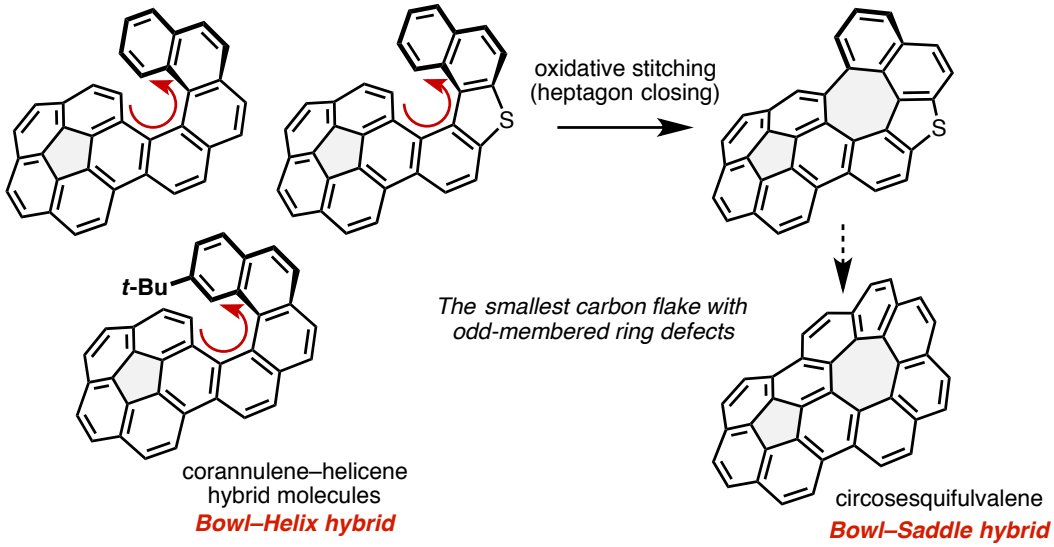

*Note that corannulene–helicene hybrid molecules have also been reported by Stuparu very recently (see Figure 17, bottom).

In Chapter 2, a [6]helicene moiety was merged with a tribenzo[*b,n,pqr*]perylene moiety (large planar motif), generating planar–helix hybrid molecules. Concise synthesis of these π-extended double carbo[6]helicenes was achieved by oxidative stitching of tetrakis(biphenylyl)naphthalene precursors. Therein, two relatively planar π-blades were concatenated, giving globally twisted nonplanar π-systems due to the steric repulsion of two [6]helicene moieties. A combination of planar and nonplanar π-systems of the thus-obtained double [6]helicenes provided unconventional contorted two- and three-dimensional lamellar packing structures. Electronic state variation resulting from the molecular geometry difference between two diastereomers was also examined by the photophysical measurements. Computational studies on the charge transfer characteristics were also performed.

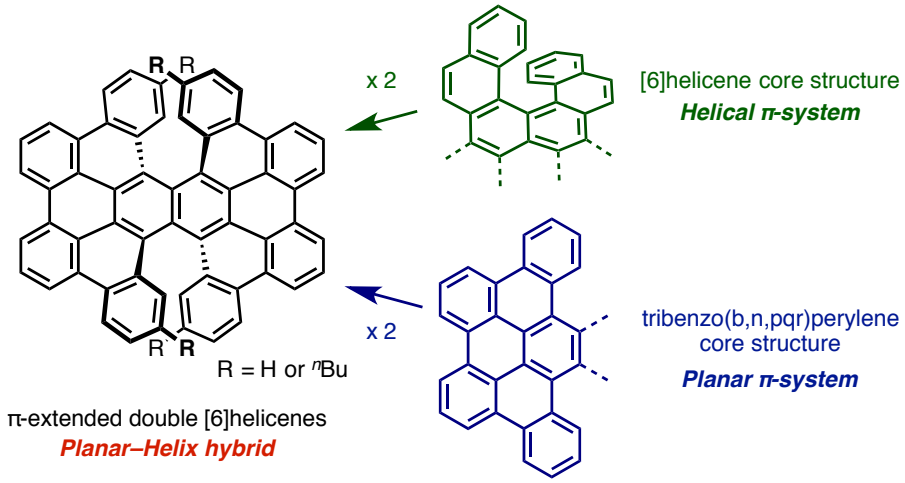

*Note that competitive studies on brickwork packing of double helicenes have been reported by Miao (see Figure 20 top).

As a continuous work in Chapter 2, Chapter 3 describes the synthesis and hole-transport ability of π-extended double dithia[6]helicene. The synthesis was accomplished by the oxidative stitching of tetrakis(thienylphenyl)naphthalene precursor using $MoCl_5$ as an oxidant. In addition to a three-dimensional π–π stacking, an isotropic electronic coupling in crystalline state was estimated for the obtained double dithia[6]helicene, which was a quite unconventional feature among π-conjugated materials. Time-resolved microwave conductivity (TRMC) measurements and single-crystal field-effect transistor fabrication revealed that the prepared double dithia[6]helicene functioned as p-type semiconductor with a moderate hole-mobility.

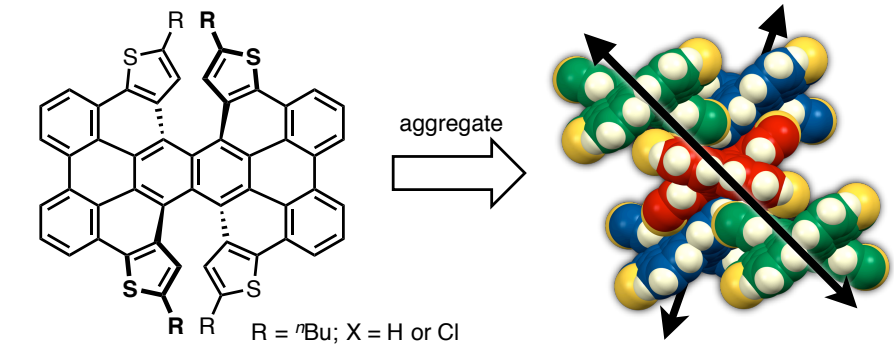

In Chapter 4, a dithia[6]helicene moiety was merged with a dithiahexa[7]circulene moiety (saddle-shaped motif), generating wide laterally π-extended dithia[6]helicenes. During the condition screening of $MoCl_5$-mediated synthesis of double dithia[6]helicene in Chapter 3, it was found that the presence of molecular oxygen push one additional C–C bond formation, generating π-extended single dithia[6]helicene with a heptagonal ring. This fully-fused helix was estimated to have an extraordinary high isomerization barrier, which enabled optical resolution and chiroptical measurements. Other photophysical and electrochemical measurements also revealed the electronic structures of huge helicenes.

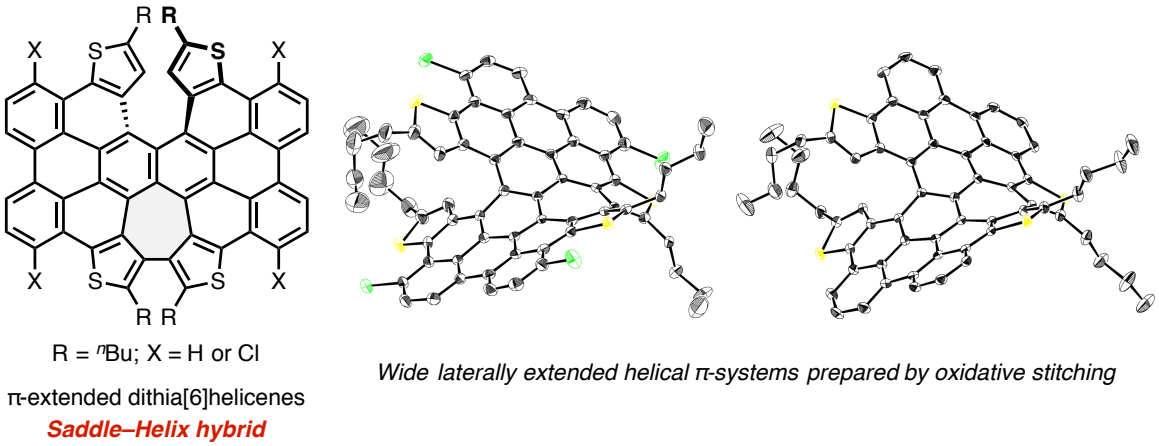

In Chapter 5, two each of dithia[6]helicene moiety and [5]helicene moiety was merged together around naphthalene core (helix accumulation), yielding highly crowded quadruple helicenes. From the precursor of π-extended dithia[6]helicenes in Chapter 3 and 4, a partial closing to quadruple helicene was accomplished by a treatment of lower proportion of $MoCl_5$ in the presence of molecular sieves. Two differently distorted structures of a propeller-shaped isomer and a saddle-shaped isomer were unambiguously determined by X-ray crystallography. In the

latter case, a proper accumulation of repulsions on the helical motifs twisted the central naphthalene core to the limit (69.5°), which is the highest degree of twisting deformation per benzene unit (35.3° at most). The fourfold helicity also provided nine stereoisomers in total including four pairs of enantiomers and one meso-isomer. Photophysical, electrochemical, and theoretical studies also disclosed a unique electronic state dependency on the molecular geometry. Complex interconversion pathways among nine stereoisomers were also disclosed by kinetic studies.

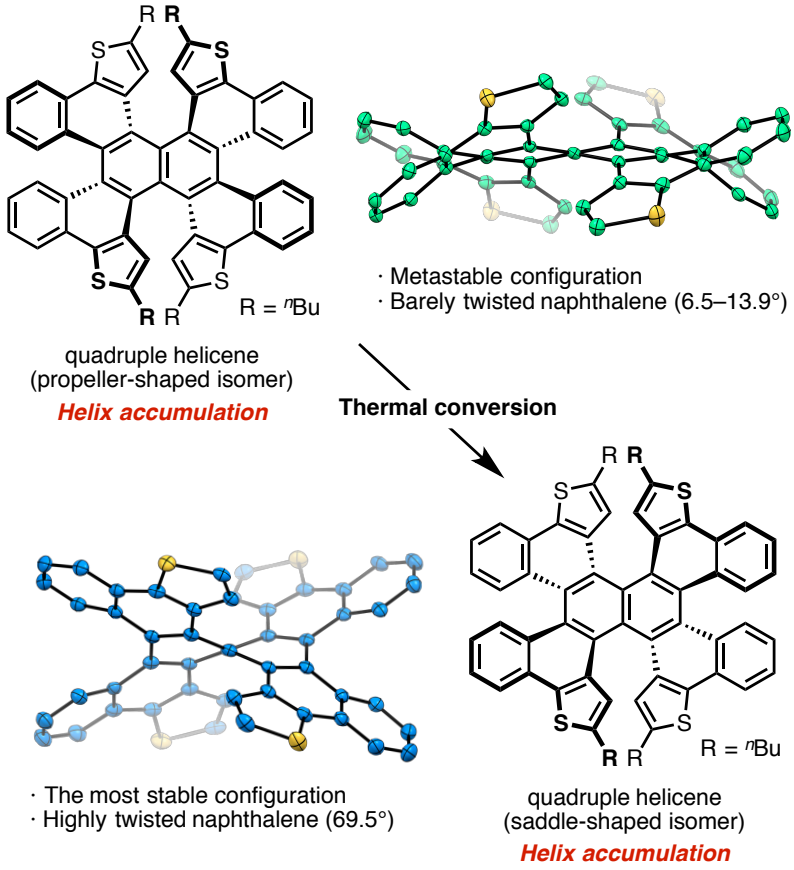

Reference

1. Hückel, E. *Z. Physik* **1931**, *70*, 204.
2. Reviews on nonhexagonal ring embedded π-systems: (a) Segawa, Y.; Ito, H.; Itami, K. *Nat. Rev. Mater.* **2016**, *1*, 15002. (b) Sygula, A. *Eur. J. Org. Chem.* **2011**, 1611. (c) Tsefrikas, V. M.; Scott, L. T. *Chem. Rev.* **2006**, *106*, 4868. (d) Wu, Y.-T.; Siegel, J. S. *Chem. Rev.* **2006**, *106*, 4843.
3. Fullerenes: (a) David, W. I. F.; Ibberson, R. M.; Matthewman, J. C.; Prassides, K.; Dennis, T. J. S.; Hare, J. P.; Kroto, H. W.; Taylor, R.; Walton, D. R. M. *Nature* **1991**, *353*, 147. (b) Hirsch, A.; Brettreich, M. *Fullerenes: Chemistry and Reactions*, Wiley-VCH, Weiheim, **2005**. (c) *Fullerenes: Chemistry, Physics, and Technology* (Eds.: Kadish, K. M.; Ruoff, R. S.), Wiley, New York, **2000**. (d) *Fullerenes: Principles and Applications* (Eds.: Lang, F.; Nierengarten, J.-F.), RSC, Cambridge, **2007**.
4. Circulenes: (a) Barth, W. E.; Lawton, R. G. *J. Am. Chem. Soc.* **1966**, *88*, 380. (b) Scott, L. T.; Hashemi, M. M.; Meyer, D. T.; Warren, H. B. *J. Am. Chem. Soc.* **1991**, *113*, 7082. (c) Yamamoto, K.; Harada, T.; Okamoto, Y.; Chikamatsu, H.; Nakazaki, M.; Kai, Y.; Nakao, T.; Tanaka, M.; Harada, S.; Kasai, N. *J. Am. Chem. Soc.* **1988**, *110*, 3578. (d) Yamamoto, K.; Saitho, Y.; Iwaki, D.; Ooka, T. *Angew. Chem., Int. Ed.* **1991**, *30*, 1173. (e) Bharat; Bhola, R.; Bally, T.; Valente, A.; Cyrański, M. K.; Dobrzycki, Ł.; Spain, S. M.; Rempała, P.; Chin, M. R.; King, B. T. *Angew. Chem., Int. Ed.* **2010**, *49*, 399. (f) Butterfield, A. M.; Gilomen, B.; Siegel, J. S. *Org. Process Res. Dev.* **2012**, *16*, 664. (g) Feng, C.-N.; Kuo, M.-Y.; Wu, Y.-T. *Angew. Chem., Int. Ed.* **2013**, *52*, 7791. (h) Sakamoto, Y.; Suzuki, T. *J. Am. Chem. Soc.* **2013**, *135*, 14074.
5. Heteroatom embedded π-systems: (a) Yamamura, M.; Hasegawa, T.; Nabeshima, T. *Org. Lett.* **2016**, *18*, 816. (b) Yamamura, M.; Nabeshima, T. *Bull. Chem. Soc. Jpn.* **2016**, *89*, 42. (c) Higashibayashi, S.; Pandit, P.; Haruki, R.; Adachi, S.; Kumai, R. *Angew. Chem., Int. Ed.* **2016**, *55*, 10830. (d) Yamamura, M.; Saito, T.; Nabeshima, T. *J. Am. Chem. Soc.* **2014**, *136*, 14299. (e) Krebs, F. C.; Larsen, P. S.; Larsen, J.; Jacobsen, C. S.; Boutton, C.; Thorup, N. *J. Am. Chem. Soc.* **1997**, *119*, 1208. (f) Madsen, G. K. H.; Krebs, F. C.; Lebech, B.; Larsen, F. K. *Chem. –Eur. J.* **2000**, *6*, 1797.
6. Reviews on cyclophanes: (a) Gleiter, R.; Hopf, H. *Modern Cyclophane Chemistry*; Wiley-VCH, Weinheim, 2004. (b) Kane, V. V.; De Wolf, W. H.; Bickelhaupt, F. *Tetrahedron* **1994**, *50*, 4575.
7. Cyclic π-conjugated molecules: (a) Segawa, Y.; Yagi, A.; Matsui, K.; Itami, K. *Angew. Chem., Int. Ed.* **2016**, *55*, 5136. (b) Omachi, H.; Segawa, Y.; Itami, K. *Acc. Chem. Res.*

2012, *45*, 1378. (c) Kawase, T.; Darabi, H. R.; Oda, M. *Angew. Chem., Int. Ed.* **1996**, *35*, 2664. (d) Kawase, T.; Ueda, N.; Tanaka, K.; Seirai, Y.; Oda, M. *Tetrahedron Lett.* **2001**, *42*, 5509.

8. Reviews on helicenes: (a) Gingras, M. *Chem. Soc. Rev.* **2013**, *42*, 968. (b) Gingras, M.; Félix, G.; Peresutti, R. *Chem. Soc. Rev.* **2013**, *42*, 1007. (c) Gingras, M. *Chem. Soc. Rev.* **2013**, *42*, 1051. (d) Shen, Y.; Chen, C.-F. *Chem. Rev.* **2012**, *112*, 1463.
9. Twisted acenes: (a) Yamamoto, K.; Oyamada, N.; Xia, S.; Kobayashi, Y.; Yamaguchi, M.; Maeda, H.; Nishihara, H.; Uchimaru, T.; Kwon, E. *J. Am. Chem. Soc.* **2013**, *135*, 16526. (b) Wang, K. K. *Top. Curr. Chem.* **2012**, *349*, 31. (c) Aikawa, H.; Takahira, Y.; Yamaguchi, M. *Chem. Commun.* **2011**, *47*, 1479. (d) Pascal, R. A., Jr. *Chem. Rev.* **2006**, *106*, 4809. (e) Lu, J.; Ho, D. M.; Vogelaar, N. J.; Kraml, C. M.; Pascal, R. A., Jr. *J. Am. Chem. Soc.* **2004**, *126*, 11168. (f) Schuster, I. I.; Craciun, L.; Ho, D. M.; Pascal, R. A., Jr. *Tetrahedron* **2002**, *58*, 8875. (g) Qiao, X.; Ho, D. M.; Pascal, R. A., Jr. *Angew. Chem., Int. Ed. Engl.* **1997**, *36*, 1531. (h) Qiao, X.; Padula, M. A.; Ho, D. M.; Vogelaar, N. J.; Schutt, C. E.; Pascal, R. A., Jr. *J. Am. Chem. Soc.* **1996**, *118*, 741. (i) Smyth, N.; Van Engen, D.; Pascal, R. A., Jr. *J. Org. Chem.* **1990**, *55*, 1937. (j) Pascal, R. A., Jr.; McMillan, W. D.; Van Engen, D.; Eason, R. G. *J. Am. Chem. Soc.* **1987**, *109*, 4660.
10. Encapsulation behavior of fullerenes: (a) Zhang, R.; Murata, M.; Aharen, T.; Wakamiya, A.; Shimoaka, T.; Hasegawa, T.; Murata, Y. *Nat. Chem.* **2016**, *8*, 435. (b) Lu, X.; Feng, L.; Akasaka, T.; Nagase, S. *Chem. Soc. Rev.* **2012**, *41*, 7723. (c) Kurotobi, K.; Murata, Y. *Science* **2011**, *333*, 613. (d) Morinaka, Y.; Tanabe, F.; Murata, M.; Murata, Y.; Komatsu, K. *Chem. Commun.* **2010**, *46*, 4532. (e) Murata, M.; Murata, Y.; Komatsu, K. *J. Am. Chem. Soc.* **2006**, *128*, 8024. (f) Komatsu, K.; Murata, M.; Murata, Y. *Science* **2005**, *307*, 238.
11. Sumanene: Sakurai, H.; Daiko, T.; Hirao, T. *Science* **2003**, *301*, 1878.
12. Reviews on buckybowls: (a) Schmidt, B. M.; Lentz, D. *Chem. Lett.* **2014**, *43*, 171. (b) Higashibayashi, S.; Sakurai, H. *Chem. Lett.* **2011**, *40*, 122. (c) Amaya, T.; Hirao, T. *Chem. Commun.* **2011**, *47*, 10524.
13. Properties of buckybowls: (a) Zabula, A. V.; Spisak, S. N.; Filatov, A. S.; Grigoryants, V. M.; Petrukhina, M. A. *Chem. –Eur. J.* **2012**, *18*, 6476. (b) Zabula, A. V.; Filatov, A. S.; Spisak, S. N.; Rogachev, A. Y.; Petrukhina, M. A. *Science* **2011**, *333*, 1008. (c) Sygula, A.; Saebø, S. *Int. J. Quantum Chem.* **2009**, *109*, 65. (d) Kawase, T.; Kurata, H. *Chem. Rev.* **2006**, *106*, 5250. (e) Kavitha, K.; Manoharan, M.; Venuvanalingam, P. *J. Org. Chem.* **2005**, *70*, 2528. (f) Seiders, T. J.; Baldridge, K. K.; Grube, G. H.; Siegel, J. S. *J. Am. Chem. Soc.* **2001**, *123*, 517. (g) Preda, D. V.; Scott, L. T. *Tetrahedron Lett.* **2000**, *41*, 9633. (h) Ayalon,

A.; Rabinovitz, M.; Cheng, P.-C.; Scott, L. T. *Angew. Chem., Int. Ed. Engl.* **1992**, *31*, 1636. (i) Scott, L. T.; Hashemi, M. M.; Bratcher, M. S. *J. Am. Chem. Soc.* **1992**, *114*, 1920.

14. Pyrenophanes: (a) Merner, B.; Unikela, K. S.; Dawe, L. N.; Thompson, D. W.; Bodwell, G. J. *Chem. Commun.* **2013**, *49*, 5930. (b) Merner, B. L.; Dawe, L. N.; Bodwell, G. J. *Angew. Chem., Int. Ed.* **2009**, *48*, 5487. (c) Bodwell, G. J.; Bridson, J. N.; Houghton, T. J.; Kennedy, J. W. J.; Mannion, M. R. *Angew. Chem., Int. Ed.* **1996**, *35*, 1320.
15. Electronic properties of cyclophanes: (a) Elango, M.; Parthasarathi, R.; Subramanian, V. Chattaraj, P. K. *Journal of Molecular Structure: THEOCHEM* **2007**, *820*, 1. (b) Tsuji, T.; Nishida, S. *J. Am. Chem. Soc.* **1988**, *110*, 2157. (c) Tobe, Y.; Ueda, K.; Kakiuchi, K.; Odaira, Y. *Tetrahedron* **1986**, *42*, 1851. (d) Jenneskens, L. W.; de Kanter, F. J. J.; Kraakman, P. A.; Turkenburg, L. A. M.; Koolhaas, W. E. de Wolf, W. H.; Bickelhaupt, F. *J. Am. Chem. Soc.* **1985**, *107*, 3716.
16. (a) Molina-Ontoria, A.; Wielopolski, M.; Gebhardt, J.; Gouloumis, A.; Clark, T.; Guldi, D. M.; Martín, N. *J. Am. Chem. Soc.* **2011**, *133*, 2370. (b) Elacqua, E.; MacGillivray, L. R. *Eur. J. Org. Chem.* **2010**, 6883. (c) Oldham, W. J., Jr.; Miao, Y.-J.; Lachicotte, R. J.; Bazan, G. C. *J. Am. Chem. Soc.* **1998**, *120*, 419. (d) Zyss, J.; Ledoux, I.; Volkov, S.; Chernyak, V.; Mukamel, S.; Bartholomew, G. P.; Bazan, G. C. *J. Am. Chem. Soc.* **2000**, *122*, 11956.
17. (a) Ueno, H.; Nishihara, T.; Segawa, Y.; Itami, K. *Angew. Chem., Int. Ed.* **2015**, *54*, 3707. (b) Nakanishi, Y.; Omachi, H.; Matsuura, S.; Miyata, Y.; Kitaura, R.; Segawa, Y.; Itami, K.; Shinohara, H. *Angew. Chem., Int. Ed.* **2014**, *53*, 3102. (c) Iwamoto, T.; Slanina, Z.; Mizorogi, N.; Guo, J.; Akasaka, T.; Nagase, S.; Takaya, H.; Yasuda, N.; Kato, T.; Yamago, S. *Chem. Eur. J.* **2014**, *20*, 14403. (d) Iwamoto, T.; Watanabe, Y.; Takaya, H.; Haino, T.; Yasuda, N.; Yamago, S. *Chem. Eur. J.* **2013**, *19*, 14068. (e) Xia, J.; Bacon, J. W.; Jasti, R. *Chem. Sci.* **2012**, *3*, 3018. (f) Iwamoto, T.; Watanabe, Y.; Sadahiro, T.; Haino, T.; Yamago, S. *Angew. Chem., Int. Ed.* **2011**, *50*, 8342. (g) Kawase, T.; Tanaka, K.; Seirai, Y.; Shiono, N.; Oda, M. *Angew. Chem., Int. Ed.* **2003**, *42*, 5597. (h) Kawase, T.; Nishiyama, Y,; Nakamura, T.; Ebi, T.; Matsumoto, K.; Kurata, H.; Oda, M. *Angew. Chem., Int. Ed.* **2007**, *46*, 1086. (i) Zhao, Y.; Truhlar, D. G. *J. Am. Chem. Soc.* **2007**, *129*, 8440.
18. (a) Kayahara, E.; Fukayama, K.; Nishinaga, T.; Yamago, S. *Chem. Asian J.* **2016**, *11*, 1793. (b) Golder, M. R.; Jasti, R. *Acc. Chem. Res.* **2015**, *48*, 557. (c) Darzi, E. R.; Jasti, R. *Chem. Soc. Rev.* **2015**, *44*, 6401. (d) Toriumi, N.; Muranaka, A.; Kayahara, E.; Yamago, S.; Uchiyama, M. *J. Am. Chem. Soc.* **2014**, *137*, 82. (e) Camacho, C.; Niehaus, T. A.; Itami, K.; Irle, S. *Chem. Sci.* **2013**, *4*, 187.
19. (a) Farshchi, R.; Ramsteiner, M.; Herfort, J.; Tahraoui, A.; Grahn, H. T. *Appl. Phys. Lett.* **2011**, *98*, 162508. (b) Wagenknecht, C.; Li, C.-M.; Reingruber, A.; Bao, X.-H.; Goebel, A.;

Chen, Y.-A.; Zhang, Q.; Chen, K.; Pan, J.-W. Nat. *Photonics* **2010**, *4*, 549. (c) Furumi, S.; Sakka, Y. *Adv. Mater.* **2006**, *18*, 775. (d) Verbiest, T.; Elshocht, S. V.; Kauranen, M.; Hellemans, L.; Snauwaert, J.; Nuckolls, C.; Katz, T. J.; Persoons, A. *Science* **1998**, *282*, 913.

20. Meisenheimer, J.; Witte, K. *Chem. Ber.* **1903**, *36*, 4153.
21. Newman, M. S.; Lednicer, D. *J. Am. Chem. Soc.* **1956**, *78*, 4765.
22. Synthesis of carbo[*n*]helicenes: (a) Mori, K.; Murase, T.; Fujita, M. *Angew. Chem., Int. Ed.* **2015**, *54*, 6847. (b) Sehnal, P.; Stará, I. G.; Šaman, D.; Tichý, M.; Míšek, J.; Cvačka, J.; Rulíšek, L.; Chocholoušová, J.; Vacek, J.; Goryl, G.; Szymonski, M.; Císařová, I.; Starý, I. *Proc. Natl. Acad. Sci. USA* **2009**, *106*, 13169. (c) Pathak, R.; Vandayar, K.; van Otterlo, W. A. L.; Michael, J. P.; Fernandes, M. A.; de Koning, C. B. *Org. Biomol. Chem.* **2004**, *2*, 3504. (d) Martin, R. H.; Baes, M. *Tetrahedron* **1975**, *31*, 2135. (e) Moradpour, A.; Kagan, H.; Baes, M.; Morren, G.; Martin, R. H. *Tetrahedron* **1975**, *31*, 2139. (f) Martin, R. H.; Morren, G.; Schurter, J. J. *Tetrahedron Lett.* **1969**, *10*, 3683. (g) Flammang-Barbieux, M.; Nasielski, J.; Martin, R. H. *Tetrahedron Lett.* **1967**, *8*, 743.
23. Liu, L.; Yang, B.; Katz, T. J.; Poindexter, M. K. *J. Org. Chem.* **1991**, *56*, 3769.
24. (a) Nakai, Y.; Mori, T.; Inoue, Y. *J. Phys. Chem. A* **2012**, *116*, 7372. (b) Tian, Y.-H.; Park, G.; Kertesz, M. *Chem. Mater.* **2008**, *20*, 3266. (c) Botek, E.; Champagne, B.; Turki, M.; André, J.-M. *J. Chem. Phys.* **2004**, *120*, 2042. (d) Schulman, J. M.; Disch, R. L. *J. Phys. Chem. A* **1999**, *103*, 6669. (e) Rulíšek, L.; Exner, O.; Cwiklik, L.; Jungwirth, P.; Starý, I.; Pospíšil, L.; Havlas, Z. *J. Phys. Chem. C* **2007**, *111*, 14948.
25. Isomerization barriers of carbo[*n*]helicenes: (a) Janke, R. H.; Haufe, G.; Würthwein, E.-U.; Borkent, J. H. *J. Am. Chem. Soc.* **1996**, *118*, 6031. (b) Grimme, S.; Peyerimhoff. *Chem. Phys.* **1996**, *204*, 411. (c) Martin, R. H.; Marchant, M. J. *Tetrahedron* **1973**, *30*, 347.
26. Effective conjugation length: (a) Martin, R. E.; Diederich, F. *Angew. Chem., Int. Ed.* **1999**, *38*, 1350. (b) Tönshoff, C.; Bettinger, H. F. *Angew. Chem., Int. Ed.* **2010**, *49*, 4125.
27. Nonalternant helicenes: (a) Han, S.; Anderson, D. R.; Bond, A. D.; Chu, H. V.; Disch, R. L.; Holmes, D.; Schulman, J. M.; Teat, S. J.; Vollhardt, K. P. C.; Whitener, G. D. *Angew. Chem., Int. Ed.* **2002**, *41*, 3227. (b) Han, S.; Bond, A. D.; Disch, R. L.; Holmes, D.; Schulman, J. M.; Teat, S. J.; Vollhardt, K. P. C.; Whitener, G. D. *Angew. Chem., Int. Ed.* **2002**, *41*, 3223.
28. Alkyl-chain bridged helicene homologs: (a) Oyama, H.; Akiyama, M.; Nakano, K.; Naito, M.; Nobusawa, K.; Nozaki, K. *Org. Lett.* **2016**, *18*, 3654. (b) Stará, I. G.; Starý, I.; Kollárovič, A.; Teplý, F.; Vyskočil, Š.; Šaman, D. *Tetrahedron Lett.* **1999**, *40*, 1993. (c) Gingras, M.; Dubois, F. *Tetrahedron Lett.* **1999**, *40*, 1309.

29. Thiahelicenes: (a) Waghray, D.; de Vet, C.; Karypidou, K.; Dehaen, W. *J. Org. Chem.* **2013**, *78*, 11147. (b) Pieters, G.; Gaucher, A.; Marque, S.; Maurel, F.; Lesot, P.; Prim, D. *J. Org. Chem.* **2010**, *75*, 2096. (c) Norsten, T. B.; Peters, A.; McDonald, R.; Wang, M.; Branda, N. R. *J. Am. Chem. Soc.* **2001**, *123*, 7447. (d) Caronna, T.; Sinisi, R.; Catellani, M.; Malpezzi, L.; Meille, S. V.; Mele, A. *Chem. Commun.* **2000**, 1139. (e) Dopper, J. H.; Oudman, D.; Wynberg, H. *J. Am. Chem. Soc.* **1973**, *95*, 3692. (f) Yamada, K.; Ogashiwa, S.; Tanaka, H.; Nakagawa, H.; Kawazura, H. *Chem. Lett.* **1981**, 343. (g) Wynberg, H.; Groen, M. B. *J. Am. Chem. Soc.* **1970**, *92*, 6664.

30. C_2S helicenes: (a) Miyasaka, M.; Pink, M.; Olankitwanit, A.; Rajca, S.; Rajca, A. *Org. Lett.* **2012**, *14*, 3076. (b) Miyasaka, M.; Rajca, A.; Pink, M.; Rajca, S. *J. Am. Chem. Soc.* **2005**, *127*, 13806. (c) Rajca, A.; Wang, H.; Pink, M.; Rajca, S. *Angew. Chem., Int. Ed.* **2000**, *39*, 4481.

31. Azahelicenes: (a) Chocholoušová, J. V.; Vacek, J.; Andronova, A.; Míšek, J.; Songis, O.; Šámal, M.; Stará, I. G.; Meyer, M.; Bourdillon, M.; Pospíšil, L.; Starý, I. *Chem. Eur. J.* **2014**, *20*, 877. (b) Chercheja, S.; Klívar, J.; Jančařík, A.; Rybáček, J.; Salzl, S.; Tarábek, J.; Pospíšil, L.; Chocholoušová, J. V.; Vacek, J.; Pohl, R.; Císařová, I.; Starý, I.; Stará, I. G. *Chem. Eur. J.* **2014**, *20*, 8477. (c) Goto, K.; Yamaguchi, R.; Hiroto, S.; Ueno, H.; Kawai, T.; Shinokubo, H. *Angew. Chem., Int. Ed.* **2012**, *51*, 10333. (d) Nakano, K.; Hidehira, Y.; Takahashi, K.; Hiyama, T.; Nozaki, K. *Angew. Chem., Int. Ed.* **2005**, *44*, 7136. (e) Bazzini, C.; Brovelli, S.; Caronna, T.; Gambarotti, C.; Giannone, M.; Macchi, P.; Meinard, F; Mele, A.; Panzeri, W.; Recupero, F.; Sironi, A.; Tubino, R. *Eur. J. Org. Chem.* **2005**, 1247.

32. Other heterohelicenes: (a) Wang, T.; Zhang, H.; Pink, M.; Olankitwanit, A.; Rajca, S.; Rajca, A. *J. Am. Chem. Soc.* **2016**, *138*, 7298. (b) Yamamoto, Y.; Sakai, H.; Yuasa, J.; Araki, Y.; Wada, T.; Sakanoue, T.; Takenobu, T.; Kawai, T.; Hasobe, T. *J. Phys. Chem. C* **2016**, *120*, 7421. (c) Schickedanz, K.; Trageser, T.; Bolte, M.; Lerner, H.-W.; Wagner, M. *Chem. Commun.* **2015**, *51*, 15808. (d) Murayama, K.; Oike, Y.; Furumi, S.; Takeuchi, M.; Noguchi, K.; Tanaka, K. *Eur. J. Org. Chem.* **2015**, 1409. (e) Sundar, M. S.; Bedekar, A. V. *Org. Lett.* **2015**, *17*, 5808. (f) Miyamoto, F.; Nakatsuka, S.; Yamada, K.; Nakayama, K.; Hatakeyama, T. *Org. Lett.* **2015**, *17*, 6158. (g) Gouin, J.; Bürgi, T.; Guénée, L.; Lacour, J. *Org. Lett.* **2014**, *16*, 3800. (h) Oyama, H.; Nakano, K.; Harada, T.; Kuroda, R.; Naito, M.; Nobusawa, K.; Nozaki, K. *Org. Lett.* **2013**, *15*, 2104. (i) Nakano, K.; Oyama, H.; Nishimura, Y.; Nakasako, S.; Nozaki, K. *Angew. Chem., Int. Ed.* **2012**, *51*, 695. (j) Hatakeyama, T.; Hashimoto, S.; Oba, T.; Nakamura, M. *J. Am. Chem. Soc.* **2012**, *134*, 19600. (k) Hatakeyama, T.; Hashimoto, S.; Nakamura, M. *Org. Lett.* **2011**, *13,* 2130. (l) Fukawa, N.; Osaka, T.; Noguchi, K.;

Tanaka, K. *Org. Lett.* **2010**, *12*, 1324. (m) Dreher, S. D.; Weix, D. J.; Katz, T. J. *J. Org. Chem.* **1999**, *64*, 3671.

33. Schmidt, K.; Brovelli, S.; Coropceanu, V.; Beljonne, D.; Cornil, J.; Bazzini, C.; Caronna, T.; Tubino, R.; Meinardi, F.; Shuai, Z.; Brédas, J.-L. *J. Phys. Chem. A.* **2007**, *111*, 10490.
34. Intersystem crossing of helicenes: (a) Sapir, M.; Vander Donckt, E. V. *Chem. Phys. Lett.* **1975**, *36*, 108. (b) Beljonne, D.; Shuai, Z.; Pourtois, G.; Brédas, J. L. *J. Phys. Chem. A* **2001**, *105*, 3899. (c) Nijegorodov, N. I.; Downey, W. S. *J. Phys. Chem.* **1994**, *98*, 5639. (d) see ref 33.
35. Reetz, M. T.; Beuttenmüller, E. W.; Goddard, R. *Tetrahedron Lett.* **1997**, *38*, 3211.
36. (a) Šámal, M.; Míšek, J.; Stará, I. G.; Starý, I. *Collect. Czech. Chem. Commun.* **2009**, *74*, 1151. (b) Ehala, S.; Míšek, J.; Stará, I. G.; Starý, I.; Kašička, V. *J. Sep. Sci.* **2008**, *31*, 2686. (c) Chen, J.; Captain, B.; Takenaka, N. *Org. Lett.* **2011**, *13*, 1654. (d) Takenaka, N.; Chen, J.; Captain, B.; Sarangthem, R. S.; Chandrakumar, A. *J. Am. Chem. Soc.* **2010**, *132*, 4536. (e) Chen, J.; Takenaka, N. *Chem. Eur. J.* **2009**, *15*, 7268. (f) Takenaka, N.; Sarangthem, R. S.; Captain, B. *Angew. Chem., Int. Ed.* **2008**, *47*, 9708. (g) For other helicene-based asymmetric catalyst, see the reference in ref 8d.
37. (a) Harvey, R. G. *Polycyclic Aromatic Hydrocarbons*; Wiley-VCH: New York, 1997. (b) Rieger, R.; Müllen, K. *J. Phys. Org. Chem.* **2010**, *23*, 315.
38. Bock, H.; Subervie, D.; Mathey, P.; Pradhan, A.; Sarkar, P.; Dechambenoit, P.; Hillard, E. A.; Durola, F. *Org. Lett.* **2014**, *16*, 1546.
39. Benzohelicenes: (a) Laarhoven, W. H.; Nivard, R. J. F. *Tetrahedron* **1976**, *32*, 2445. (b) Laarhoven, W. H.; Cuppen, Th. J. H. M.; Nivard, R. J. F. *Tetrahedron* **1970**, *26*, 4865. (c) Laarhoven, W. H.; Cuppen, Th. J. H. M.; Nivard, R. J. F. *Recl. Trav. Chim. Pays-Bas* **1968**, *87*, 687. (d) see ref 38. (e) Sawada, Y.; Furumi, S.; Takai, A.; Takeuchi, M.; Noguchi, K.; Tanaka, K. *J. Am. Chem. Soc.* **2012**, *134* 4080. (f) Jančařík, A.; Rybáček, J.; Cocq, K.; Chocholoušová, J. V.; Vacek, J.; Pohl, R.; Bednárová, L.; Fiedler, P.; Císařová, I.; Stará, I. G.; Starý, I. *Angew. Chem., Int. Ed.* **2013**, *52*, 9970. (g) Chercheja, S.; Klívar, J.; Jančařík, A.; Rybáček, J.; Salzl, S.; Tarábek, J.; Pospíšil, L.; Chocholoušová, J. V.; Vacek, J.; Pohl, R.; Císařová, I.; Starý, I.; Stará, I. G. *Chem. Eur. J.* **2014**, *20*, 8477. (h) Pradhan, A.; Dechambenoit, P.; Bock, H.; Durola, F. *Angew. Chem., Int. Ed.* **2011**, *50*, 12582.
40. Pyrenohelicenes: (a) Vingiello, F. A.; Henson, P. D. *J. Org. Chem.* **1965**, *30*, 2842. (b) see ref 38. (c) Paudel, A.; Hu, J.-Y.; Yamato, T. *J. Chem. Res.* **2008**, 457. (e) Buchta, M.; Rybáček, J.; Jančařík, A.; Kudale, A. A.; Buděšínský, M.; Chocholoušová, J. V.; Vacek, J.; Bednárová, L.; Císařová, I.; Bodwell, G. J.; Starý, I.; Stará, I. G. *Chem. Eur. J.* **2015**, *21*, 8910. (f) Bédard, A.-C.; Vlassova, A.; Hernandez-Perez, A. C.; Bessette, A.; Hanan, G. S.;

Heuft, M. A.; Collins, S. K. *Chem. Eur. J.* **2013**, *19*, 16295. (g) Hu, J.-Y.; Paudel, A.; Seto, N.; Feng, X.; Era, M.; Matsumoto, T.; Tanaka, J.; Elsegood, M. R. J.; Redshaw, C.; Yamato, T. *Org. Biomol. Chem.* **2013**, *11*, 2186. (h) Hu, J.-Y.; Feng, X.; Paudel, A.; Tomiyasu, H.; Rayhan, U.; Thuéry, P.; Elsegood, M. R. J.; Redshaw, C.; Yamato, T. *Eur. J. Org. Chem.* **2013**, 5829. (i) Hayward, R. J.; Hopkinson, A. C.; Leznoff, C. C. *Tetrahedron* **1972**, *28*, 439.

41. PDI-helicenes: Schuster, N. J.; Paley, D. W.; Jockusch, S.; Ng, F.; Steigerwald, M. L.; Nuckolls, C. *Angew. Chem., Int. Ed.* **2016**, *55*, 13519
42. Hairpin furans: (a) Geng, X.; Mague, J. T.; Donahue, J. P.; Pascal, R. A., Jr. *J. Org. Chem.* **2016**, *81*, 3838. (b) Geng, X.; Donahue, J. P.; Mague, J. T.; Pascal, R. A., Jr. *Angew. Chem., Int. Ed.* **2015**, *54*, 13957.
43. Corannulene–helicene hybrid molecules: Rajeshkumar, V.; Stuparu, M. C. *Chem. Commun.* **2016**, *52*, 9957.
44. Double carbohelicenes: (a) Laarhoven, W. H.; Cuppen, Th. J. H. M. *Tetrahedron Lett.* **1971**, 163. (b) Laarhoven, W. H.; Cuppen, Th. J. H. M.; Nivard, R. J. F. *Tetrahedron* **1974**, *30*, 3343. (c) Martin, R. H.; Eyndels, Ch.; Defay, N. *Tetrahedron* **1974**, *30*, 3339. (d) Kashihara, H.; Asada, T.; Kamikawa, K. *Chem. Eur. J.* **2015**, *21*, 6523. (e) Shan, L.; Liu, D.; Li, H.; Xu, X.; Shan, B.; Xu, J.-B.; Miao, Q. *Adv. Mater.* **2015**, *27*, 3418. (f) Luo, J.; Xu, X.; Mao, R.; Miao, Q. *J. Am. Chem. Soc.* **2012**, *134*, 13796. (g) Eversloh, C. L.; Liu, Z.; Müller, B.; Stangl, M.; Li, C.; Müllen, K. *Org. Lett.* **2011**, *13*, 5528. (h) Romero, C.; Peña, D.; Pérez, D.; Guitián, E. *J. Org. Chem.* **2008**, (i) Peña, D.; Cobas, A.; Pérez, D.; Guitián, E.; Castedo, L. *Org. Lett.* **2003**, *5*, 1863.
45. Double heterohelicenes: (a) Wang, X.-Y.; Wang, X.-C.; Narita, A.; Wagner, M.; Cao, X.-Y.; Feng, X.; Müllen, K. *J. Am. Chem. Soc.* **2016**, *138*, 12783. (b) Wang, X.-Y.; Narita, A.; Zhang, W.; Feng, X.; Müllen, K. *J. Am. Chem. Soc.* **2016**, *138*, 9021. (c) Katayama, T.; Nakatsuka, S.; Hirai, H.; Yasuda, N.; Kumar, J.; Kawai, T.; Hatakeyama, T. *J. Am. Chem. Soc.* **2016**, *138*, 5210. (d) Sakamaki, D.; Kumano, D.; Yashima, E.; Seki, S. *Chem. Commun.* **2015**, *51*, 17237. (e) Sakamaki, D.; Kumano, D.; Yashima, E.; Seki, S. *Angew. Chem., Int. Ed.* **2015**, *54*, 5404. (f) Hashimoto, S.; Nakatsuka, S.; Nakamura, M.; Hatakeyama, T. *Angew. Chem., Int. Ed.* **2014**. *53*, 14074. (g) Nakamura, K.; Furumi, S.; Takeuchi, M.; Shibuya, T.; Tanaka, K. *J. Am. Chem. Soc.* **2014**, *136*, 5555. (h) Wang, Z.; Shi, J.; Wang, J.; Li, C.; Tian, X.; Cheng, Y.; Wang, H. *Org. Lett.* **2010**, *12*, 456. (i) Liu, X.; Yu, P.; Xu, L.; Yang, J.; Shi, J.; Wang, Z.; Cheng, Y.; Wang, H. *J. Org. Chem.* **2013**, *78*, 6316. (j) Shiraishi, K.; Rajca, A.; Pink, M.; Rajca, S. *J. Am. Chem. Soc.* **2005**, *127*, 9312.

46. Triple helicenes: (a) Meng, D.; Fu, H.; Xiao, C.; Meng, X.; Winands, T.; Ma, W.; Wei, W.; Fan, B.; Huo, L.; Doltsinis, N. L.; Li, Y.; Sun, Y.; Wang, Z. *J. Am. Chem. Soc.* **2016**, *138*, 10184. (b) Geng, X.; Mague, J. T.; Pascal, R. A., Jr. *J. Org. Chem.* **2015**, *80*, 4824. (c) Xiao, Q.; Sakurai, T.; Fukino, T.; Akaike, K.; Honsho, Y.; Saeki, A.; Seki, S.; Kato, K.; Takata, M.; Aida, T. *J. Am. Chem. Soc.* **2013**, *135*, 18268. (d) Peña, D.; Pérez, D.; Guitián, E.; Castedo, L. *Org. Lett.* **1999**, *1*, 1555. (e) Hagen, S.; Scott, L. T. *J. Org. Chem.* **1996**, *61*, 7198. (d) Barnett, L.; Ho, D. M.; Baldridge, K. K.; Pascal, R. A., Jr. *J. Am. Chem. Soc.* **1999**, *121*, 727. (e) ref 39h.

47. Quadruple helicenes: (a) Fox, J. M.; Katz, T. J.; Elshocht, S. V.; Verbiest, T.; Kauranen, M.; Persoons, A.; Thongpanchang, T.; Krauss, T.; Brus, L. *J. Am. Chem. Soc.* **1999**, *121*, 3453. (b) Sooksimuang, T.; Mandal, B. K. *J. Org. Chem.* **2003**, *68*, 652. (c) Chen, L. X.; Shaw, G. B.; Tiede, D. M.; Zuo, X.; Zapol, P.; Redfern, P. C.; Curtiss, L. A.; Sooksimuang, T.; Mandal, B. K. *J. Phys. Chem. B* **2005**, *109*, 16598.

48. Contorted polyaromatics: (a) Ball, M.; Zhong, Y.; Wu, Y.; Schenck, C.; Ng, F.; Steigerwald, M.; Xiao, S.; Nuckolls, C. *Acc. Chem. Res.* **2015**, *48*, 267. (b) Zhong, Y.; Trinh, M. T.; Chen, R.; Purdum, G. E.; Khlyabich, P. P.; Sezen, M.; Oh, S.; Zhu, H.; Fowler, B.; Zhang, B.; Wang, W.; Nam, C.-Y.; Sfeir, M. Y.; Black, C. T.; Steigerwald, M. L.; Loo, Y.-L.; Ng, F.; Zhu, X.-Y; Nuckolls, C. *Nat. Commun.* **2015**, *6*, 8242. (c) Zhong, Y.; Kumar, B.; Oh, S.; Trinh, M. T.; Wu, Y.; Elbert, K.; Li, P.; Zhu, X.; Xiao, S.; Ng, F.; Steigerwald, M. L.; Nuckolls, C. *J. Am. Chem. Soc.* **2014**, *136*, 8122. (d) Xiao, S.; Kang, S. J.; Wu, Y.; Ahn, S.; Kim, J. B.; Loo, Y.-L.; Siegrist, T.; Steigerwald, M. L.; Li, H.; Nuckolls, C. *Chem. Sci.* **2013**, *4*, 2018. (e) Xiao, S.; Myers, M.; Miao, Q.; Sanaur, S.; Pang, K.; Steigerwald, M. L.; Nuckolls, C. *Angew. Chem., Int. Ed.* **2005**, *44*, 7390.

49. Ikenosako, M.; Nakai, Y.; Mori, T.; Fukuhara, G.; Inoue, Y. 93th Annual Meeting of The Chemical Society of Japan 2013, 3A2−15.

Chapter 1

Synthetic Study on Circosesquifulvalene from Corannulene–Helicene Hybrid Molecules

ABSTRACT: Circosesquifulvalene is a small polycyclic aromatic hydrocarbon embedded with one of each pentagonal and heptagonal ring. The odd-membered-ring defects warp the carbon lattice both positively and negatively, making this carbon flake a promising material as a prototype and a fragment of unprecedented nanocarbons. Chapter 1 describes the synthetic study on circosesquifulvalene via the oxidative stitching of corannulene–[6]helicenes, bowl–helix hybrid molecules. Whereas cyclodehydrogenation of [6]helicene substructure can construct [7]circulene substructure in principle, there exist only a few example of heptagonal ring formation. Herein, substrate screening and DFT studies for the cyclization of heptagonal rings were performed, achieving a potential precursor for circosesquifulvalene with pentagonal and heptagonal rings. In addition to the synthetic study, the corannulene–helicenes prepared in this chapter provided fundamental insights into a little-explored combination of geodesic curvature and a helical motif.

Introduction

Corannulene, the smallest geodesic (bowl-shaped) polyarene, consisting of five radially fused benzene rings, occupies a venerated position among nonplanar π-systems.[1,2] Notable properties of this simple trigonal carbon framework include a high electron-accepting ability, facile bowl-to-bowl inversion dynamics, and unique chemical reactivity.[3] Furthermore, corannulene has been regarded as a fragment of nanocarbon due to its unique pentagon-embedded carbon lattice. As a landmark work, for example, Scott *et al.* reported the synthesis of short and structurally pure carbon nanotube end-cap from corannulene (Figure 1, left).[4] In this way, a number of related works have been reported in the field of geodesic polyarenes, envisioning a creation of building blocks of fullerenes and carbon nanotube end-caps.[2e,f]

In 2013, Itami and Scott *et al.* reported a distinguishing work on the synthesis of molecular nanocarbon from corannulene: the synthesis of warped nanographene (WNG) (Figure 1, right).[5] Unlike the corannulene-based geodesic polyarenes reported in the precedent works, WNG displays a grossly warped double-concave structure by embedding five heptagonal rings around the corannulene center. This multiple odd-membered-ring defects dramatically alter structural and physical properties of a graphene sheet; unique racemization pathway, high solubility to common organic solvents, and widened HOMO–LUMO energy gap compared with similar sized planar PAHs. Being able to provide a carbon lattice with positive and negative curvatures, WNG is also important as a molecule pioneering a new nanocarbon chemistry which is not pertinent to the existing nanocarbons such as fullerene, nanotube, and graphene.

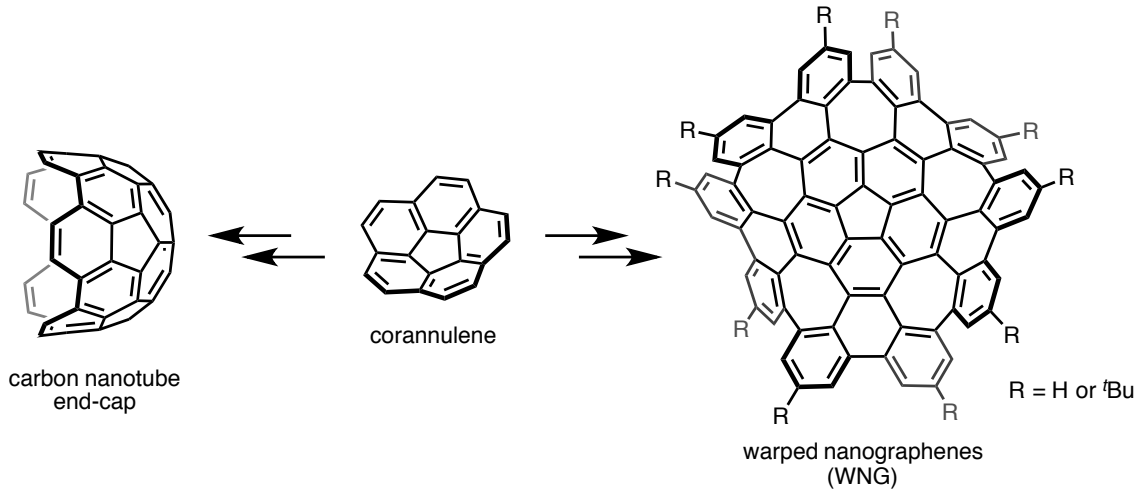

Figure 1. Examples of nanocarbon molecules synthesized from corannulene.

One of the curiosities in the synthesis of WNG is why the five heptagonal rings are formed by the Scholl reaction. While the Scholl reaction is an excellent oxidative stitching reaction to form multiple hexagonal rings in one-shot, there exist only a few example of heptagonal ring formation.[6] On this point, Itami *et al.* confirmed that the intermediates in the Scholl reaction to WNG are prone to form heptagonal rings before all hexagonal rings are formed (Scheme 1).[7] Therefore, it is speculated that the driving force of the heptagonal ring formation is the presence of pentagonal ring fused with [6]helicene substructures. On this assumption, synthetic study on circosesquifulvalene from corannulene–helicene hybrid molecules was conducted as described in this chapter.

Scheme 1. Synthesis of WNG, and assumed key intermediate possessing a [6]helicene structure fused with a pentagonal ring.

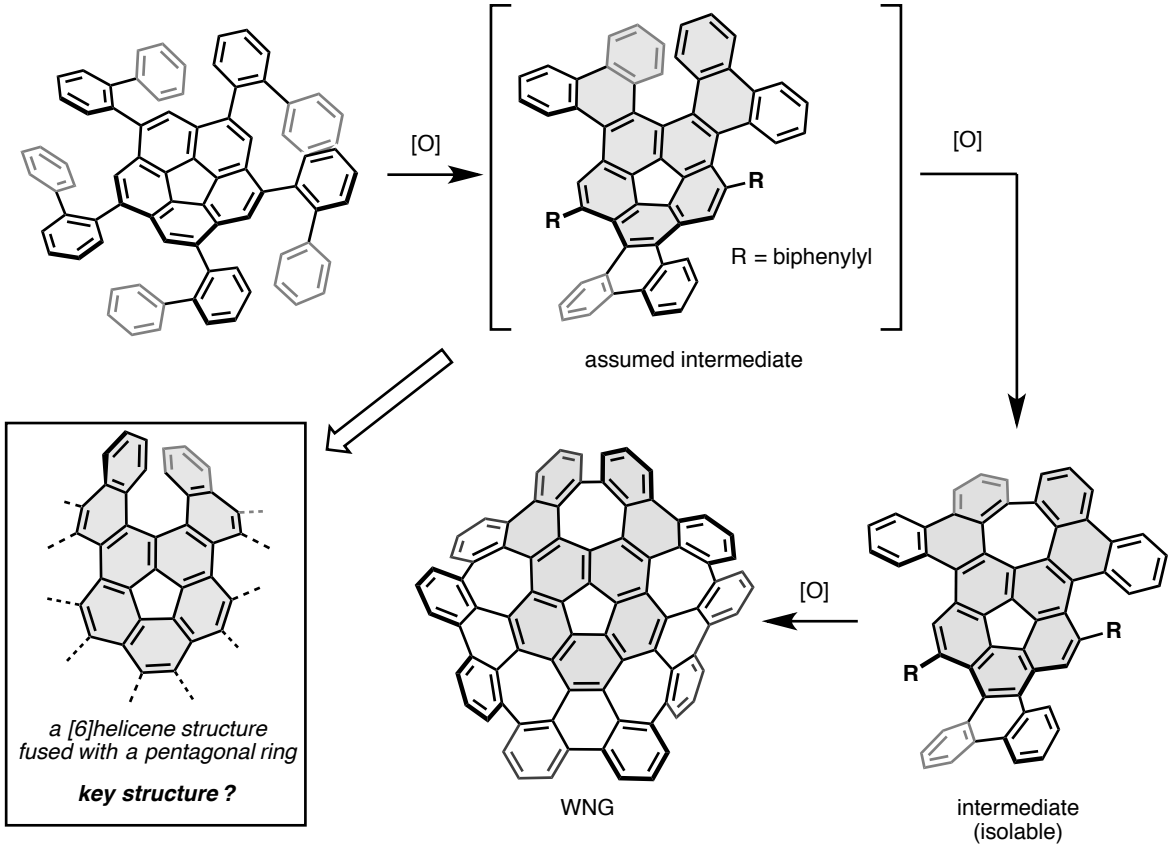

Circulene is a class of polycyclic aromatic hydrocarbons, which is characterized by fusion of benzene rings in a macrocyclic rearrangement.[8] Among the [*n*,*m*]circulenes (Figure 2), [5,5]circulene and [6,6]circulene (circobiphenyl) have been synthesized until now.[9] Circosesquifulvalene is the nonbenzenoid isomer of [6,6]circulene consisting of nine fused benzene rings surrounding sesquifulvalene.[10] Therein, the pentagonal and heptagonal rings are perfectly

embedded inside the carbon lattice, affording a small analogous structure of WNG. This one-to-one combination of the defects is expected not only to express fascinating characters such as a polarized electronic structure, redox feasibility, and unique molecular dynamics but also to be employed as a building block of unprecedented nanocarbons. For the synthesis of circosesquifulvalene, corannulene–helicene hybrid molecules were synthesized from corannulene, and the heptagonal ring closing of [6]helicene substructures was tried by the Scholl reaction.

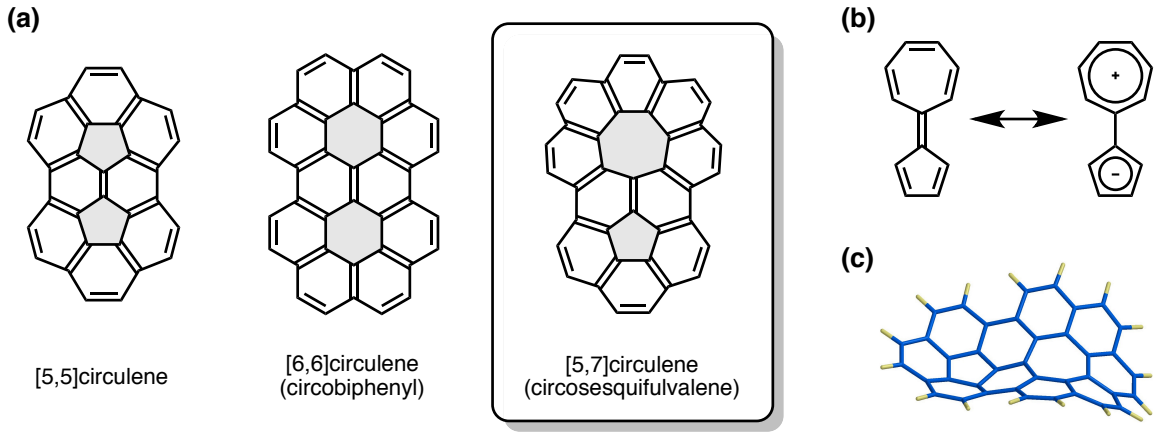

Figure 2. (a) [*n*,*m*]Circulenes. (b) The polarized resonance structure of sesquifulvalene. (c) The chair-shaped structure of circosesquifulvalene.

In addition to the synthetic study on circosesquifulvalene, fundamental properties of corannulene–helicene hybrid molecules is also described in the latter half of this chapter. Although many π-extended corannulenes have been synthesized,[2e,f] skeletally chiral corannulene derivatives have been little-studied. The corannulene cyclotrimer reported by Sygula (Figure 3a, left) is one of the rare examples, with three [5]helicene fjord regions and three distinct corannulene moieties, each of which has a different bowl-to-bowl inversion barrier.[11] WNG also exhibits chirality due to the presence of five helical hexa[7]circulene moieties, demonstrating wave-like dynamics in solution (Figure 3a, right). As in these molecules, the incorporation of a helical motif endows a corannulene core with skeletal chirality and provides unforeseen molecular behavior. Surprisingly, however, no simple chiral corannulene fused with just a single helical motif has ever been reported. The corannulene–helicenes synthesized in this work (Figure 3b) provides fundamental insights into a little-explored combination of geodesic curvature and a helical motif.

(a) corannulene-based skeletally chiral π-systems

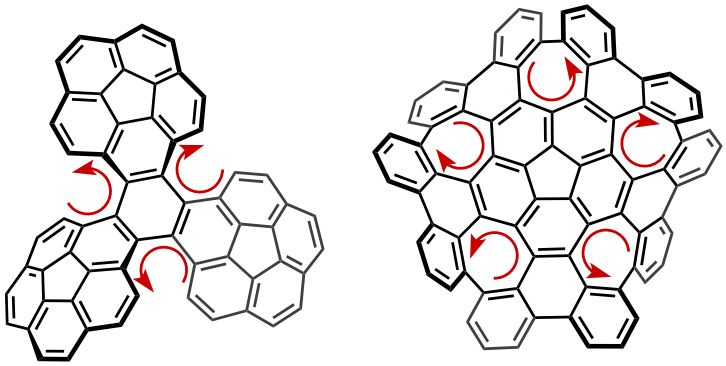

(b) corannulene-helicenes (this work)

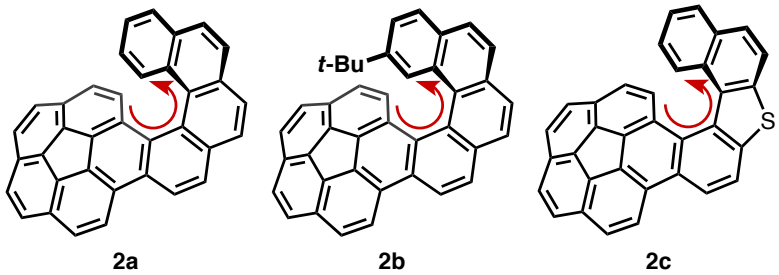

Figure 3. Corannulene-based skeletally chiral π-systems.

Result and Discussion

Retrosynthesis of Circosesquifulvalene

For the synthesis of circosesquifulvalene, two key reactions, *i.e.*, Diels–Alder reaction and the Scholl reaction, are employed (Scheme 2). Circosesquifulvalene would be generated by two-carbon unit installation to bay-region of heptagon-embedded PAH **1** via Diels–Alder reaction.[12] Compound **1** is expected to be prepared by cyclodehydrogenation of corannulene–[6]helicene (**2a**) to connect two helical termini of [6]helicene substructure based on the aforementioned assumption, although **2a** is not fully identical to the assumed key structure shown in Scheme 1. Construction of [6]helicene substructure of **2a** could be achieved via photocyclization of diarylethene **3a**.[13] The Wittig reaction of formylcorannulene **4** and phosphonium salt **5a**, both of which are known compounds, would afford **3a**.

Scheme 2. Retrosynthesis of circosesquifulvalene.

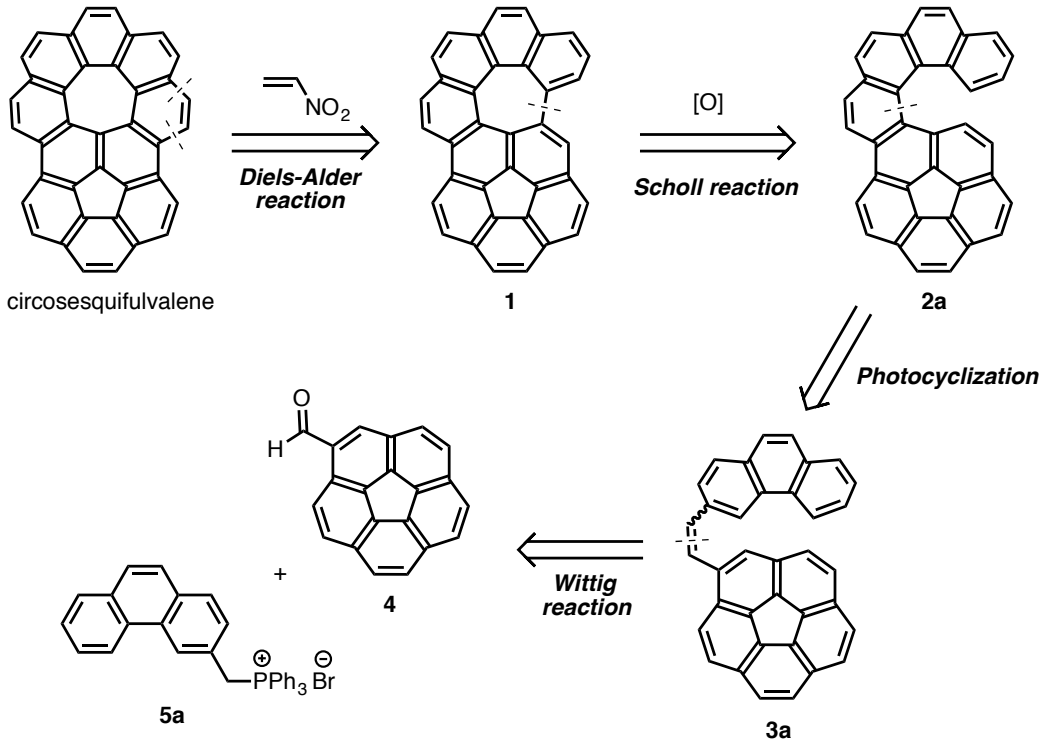

Synthetic Study on Circosesquifulvalene from Corannulene–[6]Helicene

Corannulene–[6]helicene **2a** and its *t*-butyl group substituted analog **2b** were synthesized as shown in Scheme 3. Wittig reactions of **4** with ylides derived from phosphonium salts **5a** and **5b** afforded the corresponding diarylethenes **3a** and **3b**. Subsequent photocyclization successfully furnished **2a** and **2b**. In the photocyclization, structural isomers **6a** and **6b** actually constituted the dominant products (**2b**/**6b** = **2c**/**6c** = 2:3). The greater steric congestion during [6]helicene formation probably accounts for the observed partitioning.

Scheme 3. Synthesis of corannulene–[6]helicenes (**2a** and **2b**).

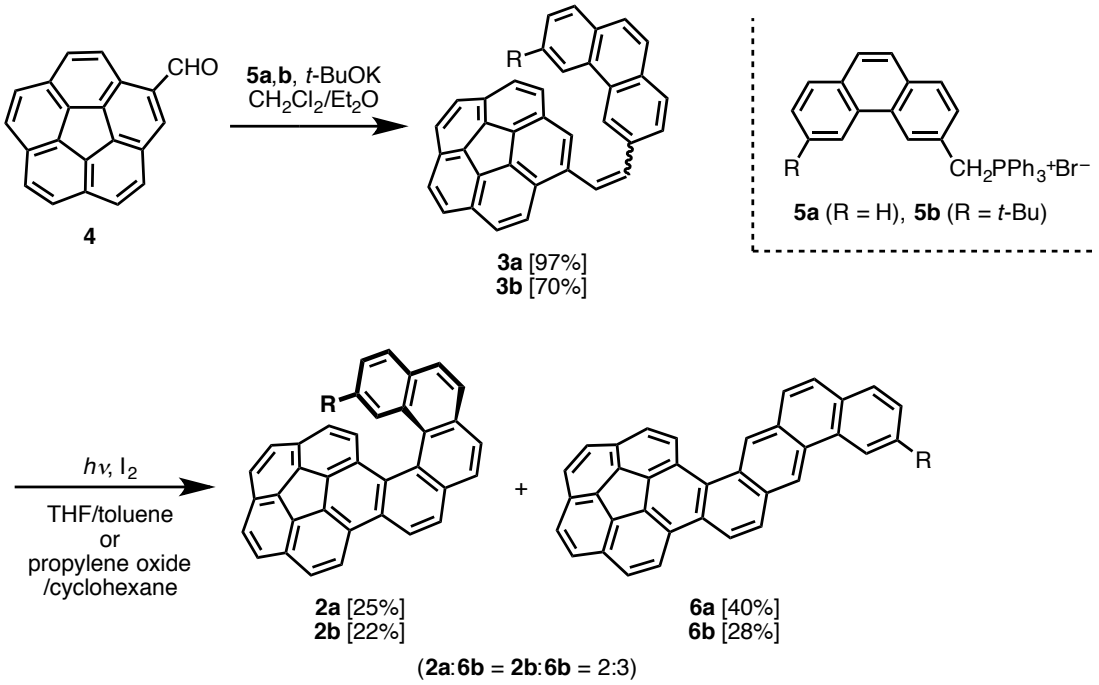

With the key intermediate **2a** in hand, condition screening of the Scholl reaction was conducted (Table 1). At the beginning, oxidative cyclodehydrogenation condition was examined. The Scholl reaction conditions using 2,3-dichloro-5,6-dicyano-1,4-benzoquinone (DDQ) and Brønsted acids such as trifluoromethanesulfonic acid (TfOH) and methanesulfonic acid gave no significant products and seemed to cause polymerization (entries 1, 2, and 4). Conversely, the reactions using Lewis acids were not strong enough to promote reactions and starting material was almost intact in crude ^{1}H NMR (entries 3–6). Reductive cyclodehydrogenation with excess amount of alkali metal was also unsuccessful (entries 7 and 8). In reference to the method using oxygen as oxidant in the synthesis of quaterrylene (Scheme 4),[14] dichloromethane solution of **2a** was treated with TfOH at –20 °C affording a single product (entry 12). Although this product has not been fully identified yet, the obtained product seemed not to be

the desired cyclized product **1** because aliphatic proton peaks were observed in ^{1}H NMR spectra. Particularly, the existence of methyl group suggested that undesired skeletal transformation happened under the strong acidic conditions.

Table 1. Condition screening of intramolecular cyclodehydrogenation of **1**.

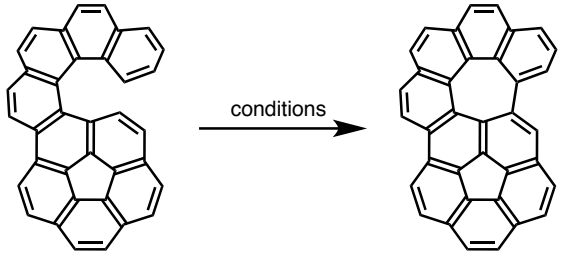

2a **1**

entry	condition	conc.	temp.	time	result
1	DDQ (1 equiv), CH_2Cl_2/TfOH (19:1)	10 mM	0 ˚C	40 min	polymerized
2	DDQ (0.5 equiv), CH_2Cl_2/TfOH (199/1)	1 mM	0 ˚C	10 min	polymerized
3	DDQ (1 equiv), $Sc(OTf)_3$ (1 equiv), 1,2-DCE	10 mM	80 ˚C	6 h	SM was intact by ^{1}H-NMR
4	DDQ (1 equiv), $Sc(OTf)_3$ (1 equiv), CH_2Cl_2 -> CH_2Cl_2/$MeSO_3H$ (99:1)	10 mM	0 ˚C	20 min -> 1h	Sm was no change on TLC -> polymerized
5	$FeCl_3$ (3 equiv), CH_2Cl_2/$MeNO_2$ (9:1)	10 mM	rt	1 h	SM was intact by ^{1}H-NMR
6	$FeCl_3$ (3 equiv), $AlCl_3$ (5 equiv) CH_2Cl_2/$MeNO_2$ (9:1)	10 mM	rt	1 h	SM was intact by ^{1}H-NMR
7	Li (excess), THF	5 mM	60 ˚C	17 h	SM was intact by ^{1}H-NMR
8	Na (excess), THF	5 mM	70 ˚C	28 h	decomposed
9	CH_2Cl_2/$MeSO_3H$ (19:1)	2.5 mM	rt	-	No reaction
10	CH_2Cl_2/TfOH (49:1)	1 mM	0 ˚C	3 min	unknown prduct was obtained
11	CH_2Cl_2/TfOH (49:1)	1 mM	-78 ˚C	30 min	SM remained
12	CH_2Cl_2/TfOH (49:1)	1 mM	-20 ˚C	7 min	unknown prduct was obtained

Scheme 4. Synthesis of quaterrylene using oxygen as an oxidant.

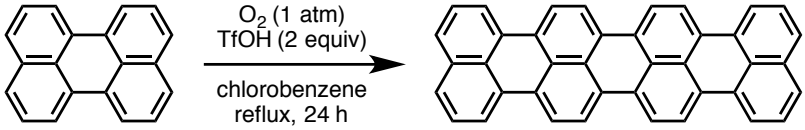

perylene [80%] quaterrylene

Synthetic Study on Circosesquifulvalene from Corannulene–Thia[6]helicene

While there is still room to examine the cyclization conditions of **2a** toward the heptagonal ring embedded compound **1**, it was found that conventional cyclodehydrogenation conditions are not effective. In order to understand this result, optimized structures of potential substrates for heptagonal ring closing were calculated by density functional theory (DFT) method at the B3LYP/6-31G(d) level of theory (Figure 4).

Focusing on the carbon-carbon distance between the two helical termini of [6]helicene substructures (*d*), it was found that a shorter *d* value tend to result in the successful heptagonal ring closing. For example, the *d* value of the plausible intermediate in the synthesis of WNG (**7**) was calculated to be 3.185 Å, which was comparable to that of [6]helicene (3.188 Å). In contrast, the corannulene–[6]helicene **2a** shows much larger *d* value of 3.294 Å, which probably makes it difficult to trigger the C–C bond formation of the two terminal carbon atoms. In 1975, Wynberg *et al.* reported that the Scholl reaction of pristine [6]helicene using $AlCl_3$/NaCl gave no well-defined products.[15] Although several modified reaction conditions reported after their work[16] were also attempted in this work, oxidative cyclization of [6]helicene turned out to be unsuccessful. However, Wynberg also reported that heptagonal ring closing occurred in thia[6]helicenes **8**–**10** by using the same condition as the trial in [6]helicene. The *d* values of these thia[6]helicenes were found to be very shorter (**8**: 3.009 Å; **9**: 3.073 Å; **10**: 3.093 Å) than that of [6]helicene, presumably enabling heptagonal ring closing. Hence, corannulene–thia[6]helicene **2c** was designed as a new synthetic precursor for circosesquifulvalene. The calculated *d* value of **2c** (3.077 Å) was much shorter than that of the initial substrate **2a** (3.294 Å) due to the presence of thiophene ring. This thiophene moiety would be convertible to benzene ring by two-carbon unit installation via the Diels–Alder reaction.[17] Gratifyingly, undesirable structural isomers like **6a** and **6b** in the photocyclization step can be excluded in this case.

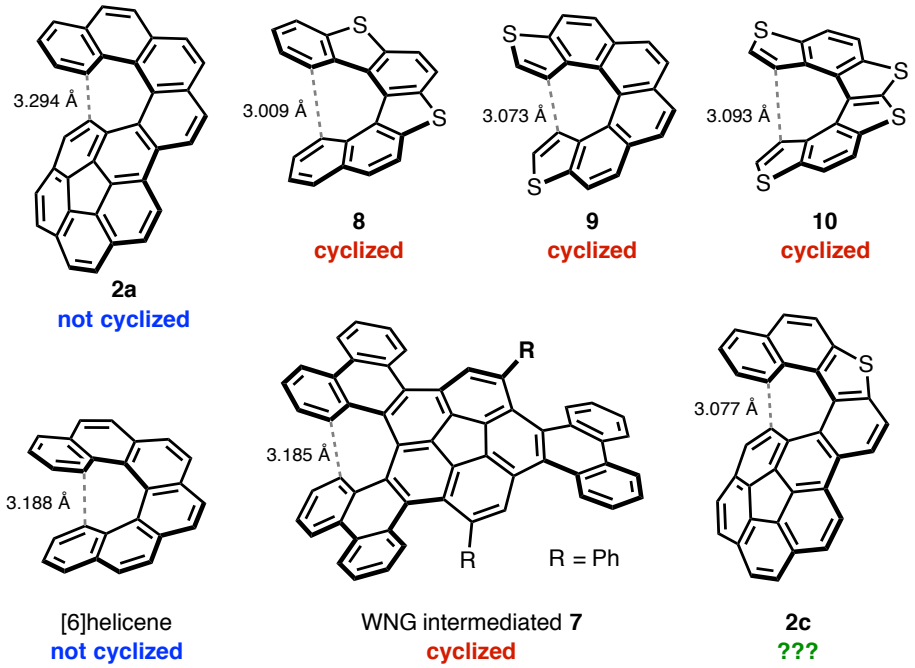

Figure 4. Potential substrates for heptagonal ring closing and the *d* values calculated at the B3LYP/6-31G(d) level of theory. To simplify the calculation, biphenyl groups of WNG intermediate **7** were replaced by phenyl groups.

As with the synthesis of **2a** and **2b**, **2c** was prepared from **4** and phosphonium salt of 2-methylnaphthothiophene (**5c**) (Scheme 5). The Wittig reaction of **4** with ylides derived from **5c** afforded the diarylethene **3c**. Subsequent photocyclization successfully furnished **2c** in moderate yield. Next, the Scholl reaction using DDQ and TfOH in dichloromethane solution successfully afforded the heptagonal ring embedded compound **11**. Even though **11** constituted the dominant product in the crude mixture after the Scholl reaction, poor solubility originated from the high planarity hampered its purification. Hence, sulfur atom oxidation was performed by treating *m*-chloroperoxybenzoic acid (mCPBA) in highly diluted dichloromethane solution, to afford sulfone **12** in 67% yield in 2 steps.

Scheme 5. Synthetic study on circosesquifulvalene via corannulene–thia[6]helicene (**2c**).

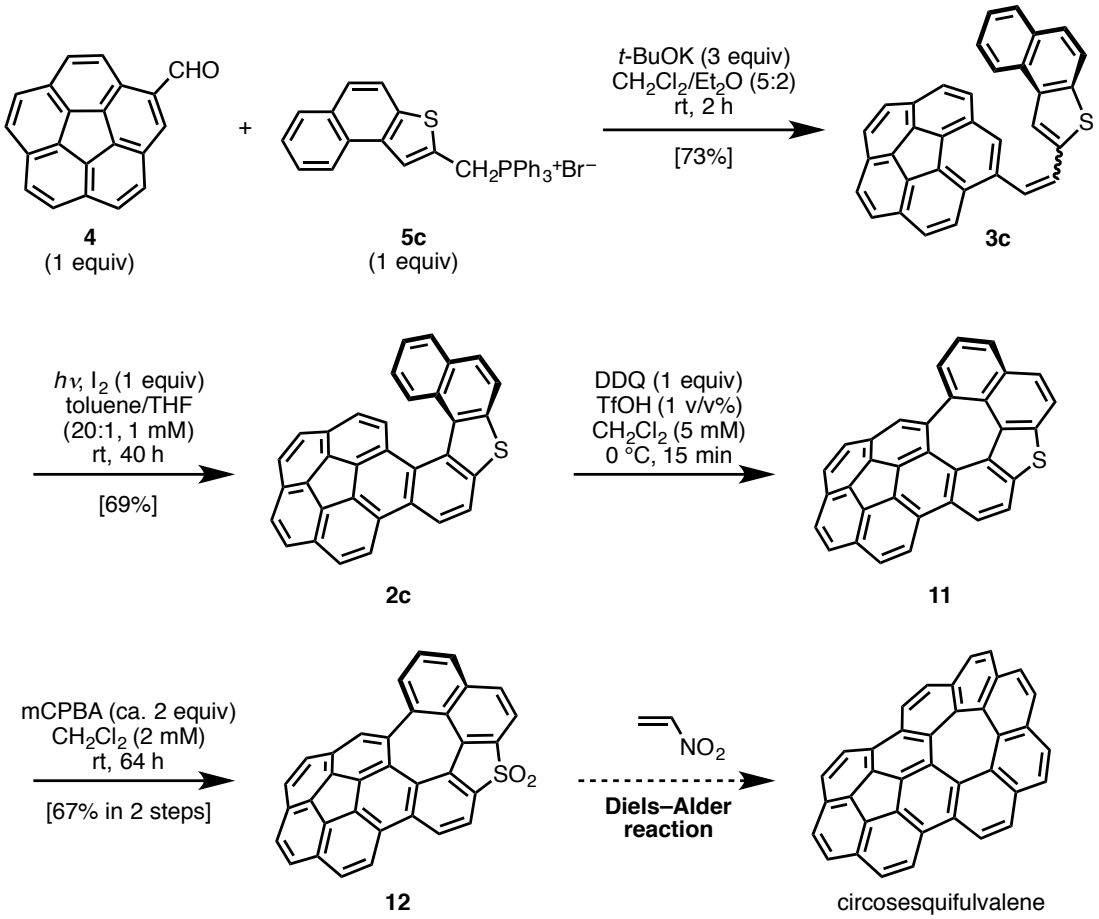

The molecular structures of **2a**, **2c**, and **12** were revealed by single-crystal X-ray diffraction analysis (Figure 5). As expected from the DFT study, the *d* values of two crystallographically independent molecules of **2c** (3.011(5) Å and 3.111(5) Å) were found to be much shorter than those of **2a** (3.176(3) Å and 3.223(3) Å). On the other hand, the dihedral angle of the bay-region of **12** was determined to be 27.7(3)° in the crystal, which is, unfortunately, a little bit large value as a diene to proceed with the Diels–Alder reaction.

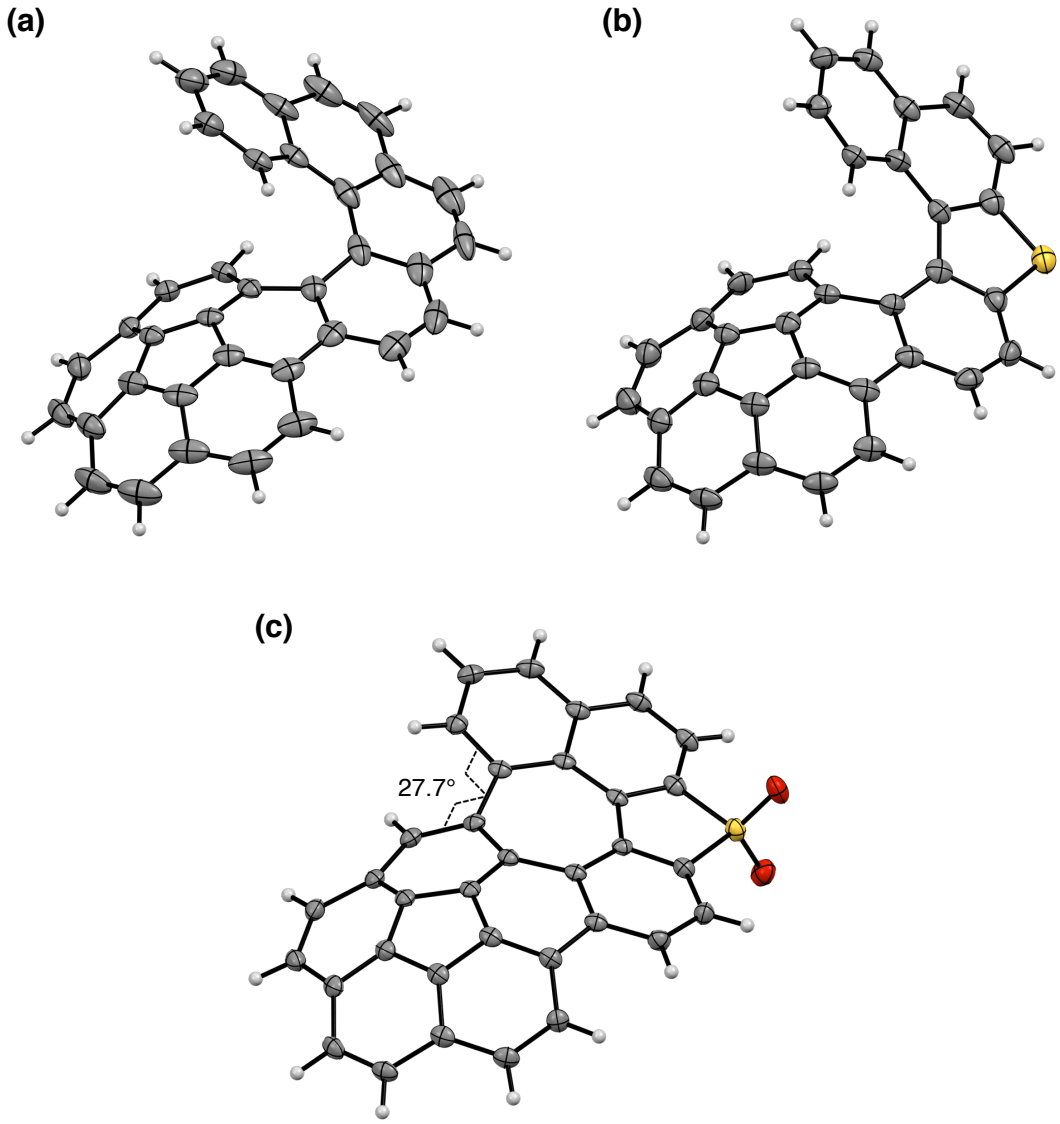

Figure 5. ORTEP drawings of (a) *P*-**2a**, (b) *P*-**2c**, and (c) **12** shown with 50% probabilities. One of two crystallographically independent molecules are shown for **2a** and **2c**.

In this work, the Diels–Alder reaction of **12** for double two-carbon installation has not been attempted, but the Scholl reaction condition for heptagonal ring closing was discovered. The following efforts for the synthesis of circosesquifulvalene will be performed in the near future.

Hereafter, structural features and fundamental properties of corannulene–[6]helicene **2a** and **2b** are described as representatives of chiral π-systems comprising both bowl and helical motifs.

Structural Analysis of Corannulene–[6]Helicene (2a)

An important aspect of the structures of corannulene-helicenes is the existence of two diastereomeric forms. The terminal ring of the helicene can face either the convex or the concave surface of the bowl. Helix inversion results in *P*- and *M*-helicenes, producing four stereoisomers in total (*convex-P*, *concave-P*, *convex-M*, and *concave-M*).

X-ray crystallographic analysis of a racemic single crystal of **2a** confirmed the distortion caused by the combination of the bowl and the helix, with the molecule adopting a *convex* form (Figure 5a). Structural parameters of the two crystallographically independent molecules of *convex*-**2a** in the crystal and the two parent molecules, corannulene and [6]helicene, are listed in Table 2. While corannulene has a C_{5v} symmetrical structure, the X-ray crystal structure of *convex*-**2a** shows significant bond length changes. For example, the rim bond *a*, which is annulated with the helical motif, is greatly lengthened to 1.439(3)/1.437(3) Å compared to 1.383 Å for that of corannulene. The flank bonds *b*,*d* and the hub bond *c* were also lengthened slightly. The sum of the four dihedral angles calculated from the four inner carbon atoms of the [6]helicene moiety of *convex*-**2a** (96.8°/93.8°) was larger than that of [6]helicene (86.8°). Focusing on the four dihedral angles independently, the angles near the termini of the helix (*d*,*g*) are increased and the angles in the middle of helix (*e*,*f*) are decreased, respectively, relative to those in [6]helicene.

Table 2. Structural parameters of the X-ray crystal structures of corannulene,[18] [6]helicene,[19] and **2a**. Bond lengths *a*–*d* for the X-ray structure of corannulene are averaged values. Dihedral angles were calculated by using four consecutive inner carbon atoms inside the helix.

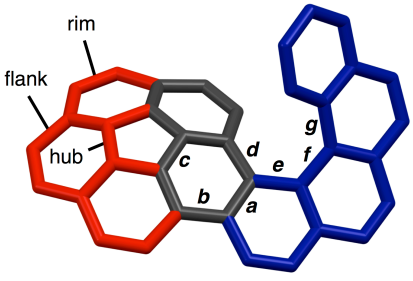

corannulene: black & red
[6]helicene: black & blue
corannulene-[6]helicene (**2a**): all

	corannulene	[6]helicene	**2a**
bond *a* (Å)	1.383	–	1.439(3)/1.437(3)
bond *b* (Å)	1.446	–	1.460(3)/1.462(3)
bond *c* (Å)	1.415	–	1.429(3)/1.430(3)
bond *d* (Å)	1.446	–	1.473(3)/1.477(3)
dihedral *d*	–	15.2°	27.4(3)°/26.4(3)°
dihedral *e*	–	30.3°	25.9(3)°/24.2(3)°
dihedral *f*	–	30.0°	24.8(3)°/25.3(3)°
dihedral *g*	–	11.3°	18.7(3)°/17.9(3)°

The frozen structure of **2a** in the crystal is fixed to a convex conformation, but it is expected to be flexible in solution. Hence, to estimate the dynamic behavior of corannulene-helicene hybrid system, DFT calculations at the B3LYP/6-31G(d) level of theory were performed on both the *convex* and *concave* forms, and the transition states for the bowl and helix inversions. A substantial disparity between the thermodynamic stabilities of the *convex* and the *concave* conformations was found; *convex*-**2a** is more stable than *concave*-**2a** by 6.3 kcal·mol^{-1}. This result clearly derives from the difference in steric congestion between the two forms. For example, the *d* value in the optimized structure of *convex*-**2a** is significantly shortened in *concave*-**2a** (3.294 Å *vs* 3.061 Å). A barrier for bowl-to-bowl inversion from the *convex* to the *concave* conformation was also estimated to be 10.1 kcal·mol^{-1}. This value is slightly lower than that for pristine corannulene (~11.5 kcal·mol^{-1}),[3d,e] reflecting the steric influence of the helical motif on the corannulene motif during the inversion. The calculations indicate that the *convex* form is the greatly favored conformation and that fast interconversion between the two diastereomeric forms should occur in solution. These conclusions are consistent with the ^{1}H NMR spectra, which exhibit signals for just 18 hydrogen atoms for **2a** and 17 hydrogen atoms for **2b**.

As with the slightly lowered bowl-to-bowl inversion barrier, the calculated helix inversion barrier of **2a** (34.6 kcal·mol^{-1}) predicts easier racemization processes relative to that of pristine [6]helicene (36.2 kcal·mol^{-1}).[20] A conventional transition state with face-to-face oriented terminal rings of the helicene moiety was found. The curved structure of the corannulene moiety, which resembles the deformations seen in the transition state, helps to lower the energetic cost for the helix inversions in **2a**.

Enantiomerizations of corannulene–[6]helicene require both of the two inversion motions discussed above. Namely, when starting from the thermodynamically most stable *convex* form, either one of the inversions of the two flexible motifs, bowl or helix, takes place first to generate a corresponding *concave* form. Then, subsequent inversion of the other motif completes the enantiomerization (Figure 6).

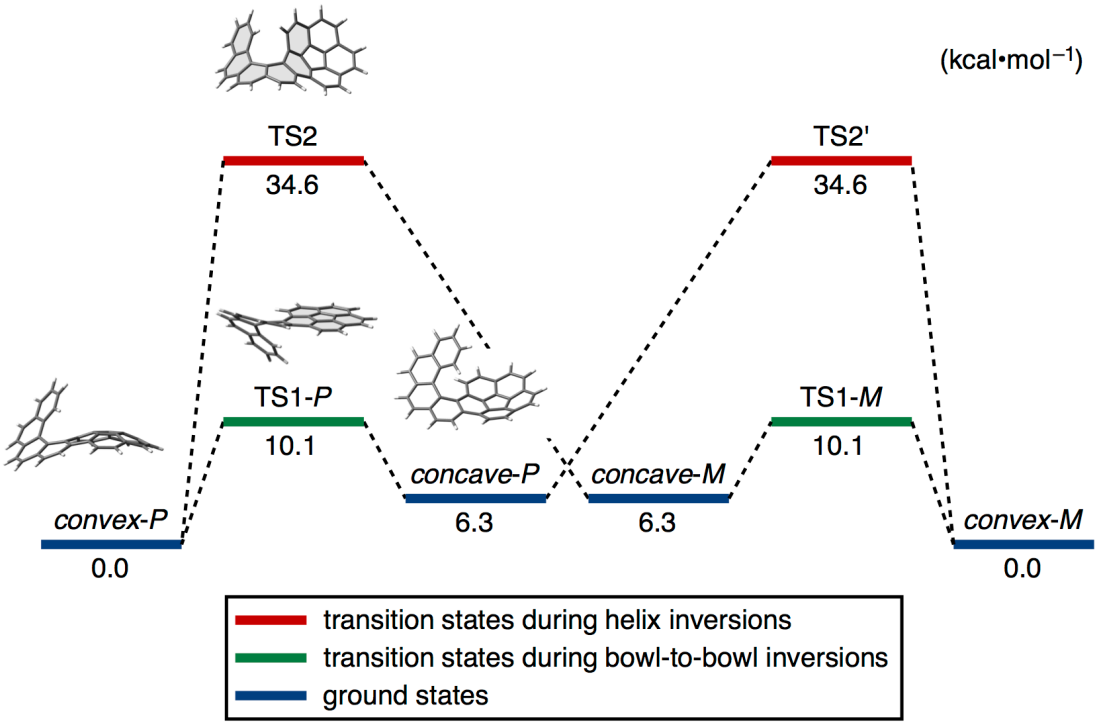

Figure 6. The interconversion pathways of **2a** as a representative of corannulene-helicenes. Relative Gibbs free energies (ΔG) were calculated at the B3LYP/6-31G(d) level.

Fortunately, optical resolution of *convex*-**2a** was achieved by means of high-performance liquid chromatography (HPLC) equipped with a COSMOSIL Cholester column (Figure 7a,b). Probably, this is the first example of a successful separation of enantiomers of a corannulene-based skeletally chiral molecule.[21] With the enantioenriched sample in hand, a kinetic study on the thermal racemization process of *convex*-**2a** in 1,2,4-trichlorobenzene solution was performed by monitoring the decreasing enantiomeric excess (*ee*) by HPLC (Figure 7c–e). The activation parameters of the helix inversion were experimentally determined to be $\Delta H^{\ddagger}$ of 31.5 kcal·mol^{-1} and $\Delta S^{\ddagger}$ of −6.9 cal·mol^{-1}·K^{-1}, which gives $\Delta G^{\ddagger}$ of 33.5 kcal·mol^{-1} at 25 °C This value is smaller than that for helix inversion of [6]helicene and agrees well with the calculations.

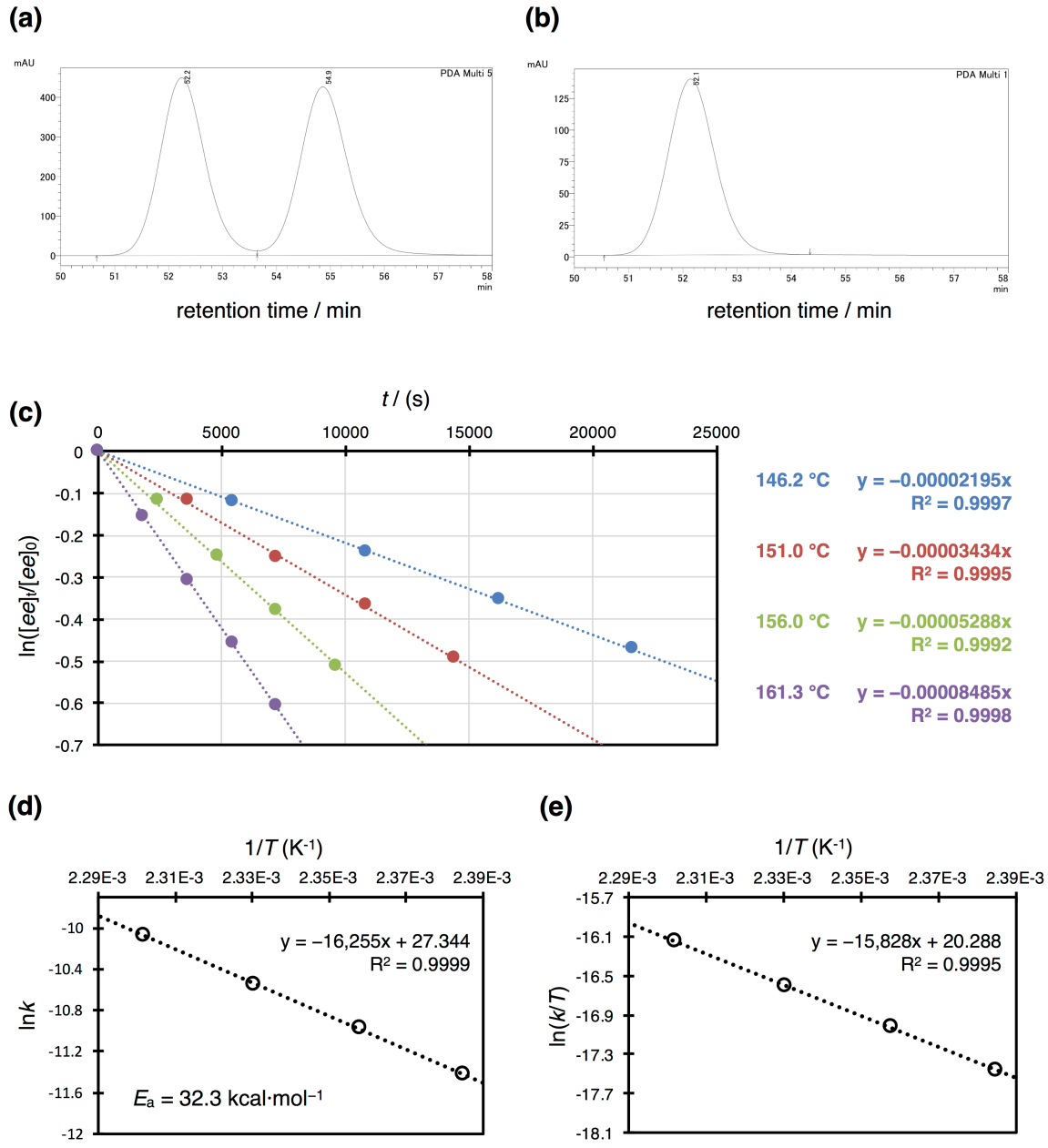

Figure 7. HPLC analysis of (a) the racemic mixture of **2a** and (b) the separated *P*-**2a** (eluted by chloroform/methanol = 2:8). (c) Plots of the decreasing *ee* of *M*-**2a** upon heating at several temperatures in 1,2,4-trichlorobenzene. (d) Arrhenius plot and (e) Eyring plot of the thermal racemization of *M*-**2a**.

Electronic Structure of Corannulene–[6]Helicene (2a)

The UV–Vis absorption spectrum of **2a** in $CHCl_3$ solution shows maxima at 418 nm (ε = 1.6×10^3), 315 nm (ε = 4.8×10^4), 289 nm (ε = 4.1×10^4), and 263 nm (ε = 6.0×10^4), with a shoulder-like absorption around 343 nm (Figure 8a). The fluorescence maxima appear at 425 nm and 447 nm (Φ_F = 0.06) (Figure 8b). The CD spectrum of the fast-eluting peak (> 99% *ee*) in the HPLC separation exhibits a positive Cotton effect in the region 300–430 nm ($\Delta\varepsilon^{343\ nm}$ = +168 $M^{-1}\cdot cm^{-1}$), and negative ones below 300 nm ($\Delta\varepsilon^{265\ nm}$ = −231 $M^{-1}\cdot cm^{-1}$). From the CD spectrum simulated by time-dependent DFT (TD DFT) calculation, this fast-moving enantiomer was assigned as *convex-P*-**2a** (Figure 9). The overall CD spectrum is similar, but red-shifted with smaller ellipticity, relative to that of *P*-[6]helicene ($\Delta\varepsilon^{324\ nm}$ = +259 $M^{-1}\cdot cm^{-1}$ and $\Delta\varepsilon^{246\ nm}$ = −272 $M^{-1}\cdot cm^{-1}$).[22] The specific rotation of *convex-P*-**2a** was also determined to be $[\alpha]^{21}_D$ +4037 (*c* = 0.0108, $CHCl_3$), which is larger than $[\alpha]^{25}_D$ +3707 (*c* = 0.082, $CHCl_3$) of *P*-[6]helicene. In contrast to the cases of the hitherto reported π-extended helicenes, corannulene annulation confers an additional optical rotatory power on the helicene core.[23]

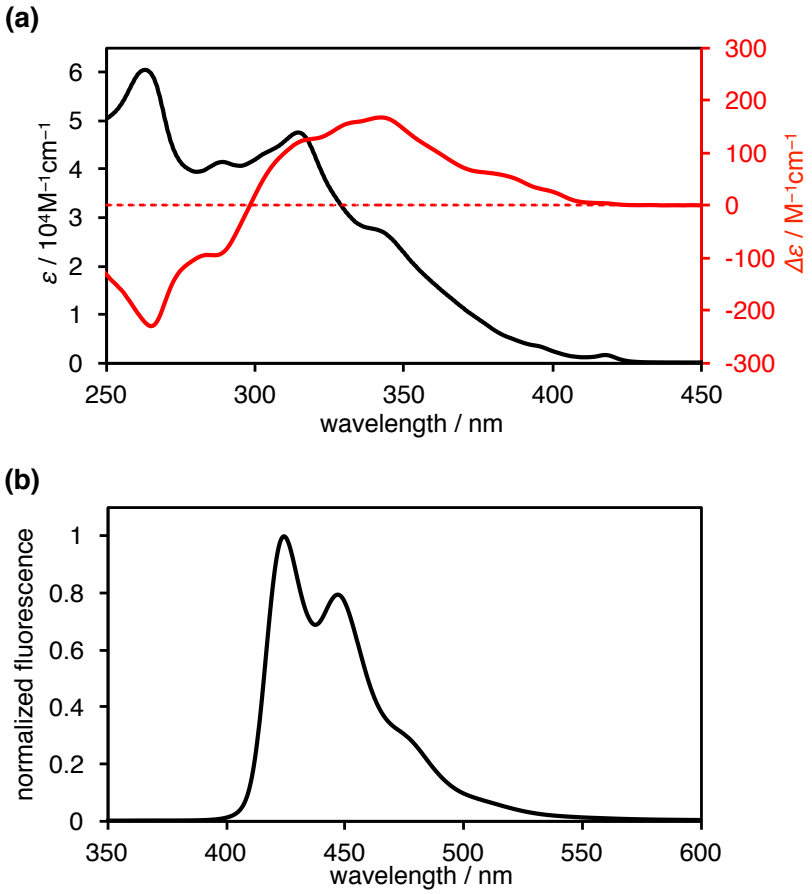

Figure 8. (a) UV–Vis absorption (black line) and CD spectra (red line) of **2a** (the fast-eluting enantiomer in the HPLC separation was used for the CD spectra measurement).

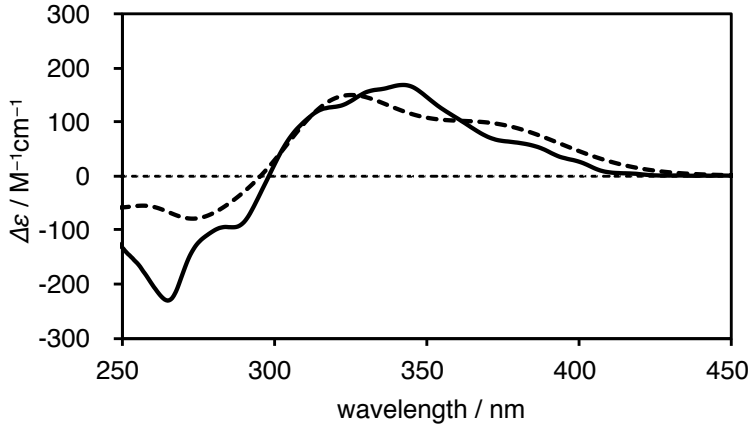

Figure 9. CD spectra of *P*-**2a**. Experimental spectrum is solid line, and simulated spectrum (B3LYP/6-31G(d) level) are broken lines.

Cyclic voltammetry of **2a** was performed to investigate the electrochemical behavior of corannulene-helicene hybrid π-systems (Figure 10). As with the case of corannulene,[24] **2a** showed an irreversible one-step oxidation wave with the peak potential E_p of 1.14 V (vs FcH/FcH^+) in acetonitrile. On the other hand, the good electron-accepting ability of corannulene was maintained,[3g] and two reversible reduction waves were observed in THF with half-wave potentials $E_{1/2}$ of −2.35 V and −2.65 V (vs FcH/FcH^+).

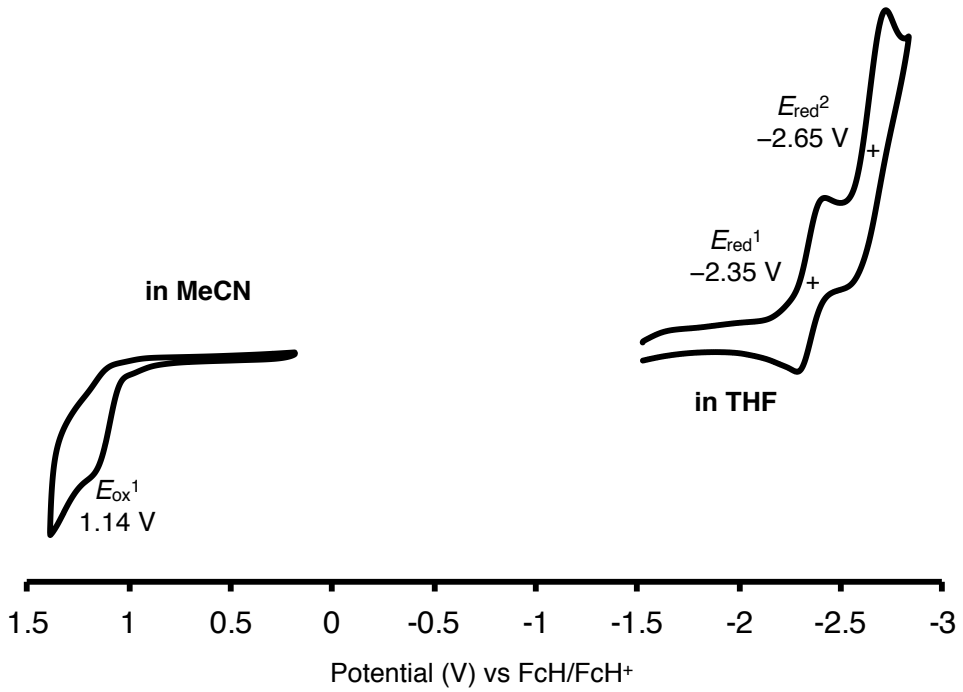

Figure 10. Cyclic voltammetry of **2a** in acetonitrile (for oxidation, 0.02 $V \cdot s^{-1}$) and THF (for reduction, 0.1 $V \cdot s^{-1}$) containing 100 mM of $TBAPF_6$. FcH = ferrocene.

Magnetic Properties of *t*-Butyl Corannulene–[6]Helicene (2b)

Magnetic shielding effects by the ring currents in corannulenes have previously been reported to move chemical shifts upfield by 2 to 5 ppm.[25] All of these effects, however, were measured over the *concave* surfaces of corannulenes. The uniquely fixed aromatic ring over the corannulene moiety of **2b**, on the other hand, is suited for probing ring current effects over the *convex* surface of a geodesic π-system. The ^{1}H NMR signal of the *t*-butyl group of **2b**, whose *convex* form is also predicted to be favored over the *concave* form by 7.2 kcal·mol^{-1}, is shifted up-field by *ca*. 0.65 ppm when compared to the signal of the *t*-butyl group in **6b** (0.94 *vs* 1.59 ppm). Consequently, the *t*-butyl group probe in **2b** provides the first experimental evidence that magnetic shielding over the *convex* surface of corannulene does exist, and also that the shielding is not as great as that over the *concave* surface.

The NMR spectral calculations predict a chemical shift of 0.87 ppm for the *t*-butyl group in *convex*-**2b** and −0.06 ppm for that of *concave*-**2b**, as averaged values of the chemical shifts of nine hydrogen atoms in the optimized structures (Figure 11). The sizable difference in the predicted chemical shifts for the two forms presumably reflects the divergence of the shielding effect on the *convex* face and the convergence of the shielding effect on the *concave* face. The good agreement between the experimentally observed chemical shift of the *t*-butyl group in **2b** and that calculated for *convex*-**2b** adds further support to the conclusion that the *convex* form predominates not only in the solid state but also in solution.

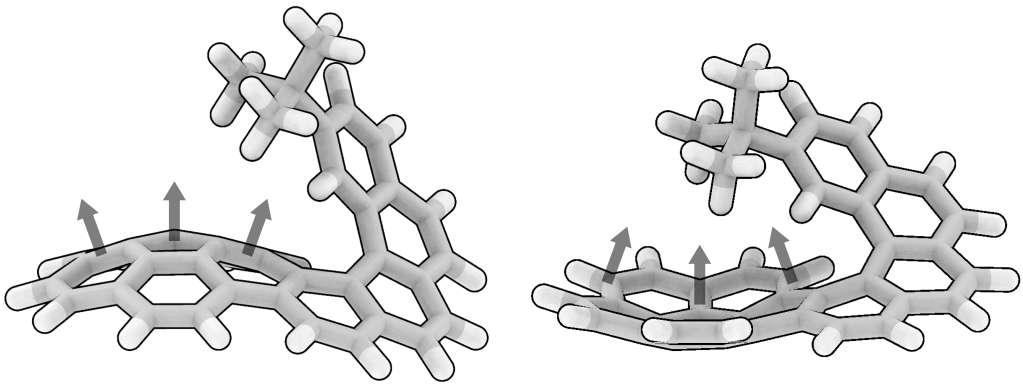

Figure 11. The divergent and convergent shielding effects from the geodesic polycyclic π-systems. ^{1}H NMR chemical shifts were calculated at the B3LYP/6-311+G(2d,p)// B3LYP/6-31G(d) level with $SiMe_4$ (0.0 ppm) as a reference.

Conclusion

In the former half of this chapter, synthetic study on circosesquifulvalene was conducted employing corannulene–[6]helicenes as key intermediates. Judging from the experimental facts and DFT studies, it was found to be effective to introduce a thiophene ring forcing proximity of the two terminal carbon atoms inside [6]helicene substructure, in order to achieve heptagonal ring closing by the oxidative stitching reaction. Indeed, cyclization of corannulene–thia[6]helicene (**2c**) successfully afforded the heptagonal ring embedded polycyclic π-system, which is a potential synthetic intermediate for circosesquifulvalene. As just described, heptagonal ring construction from [6]helicene derivatives would be quite beneficial for pioneering the undeveloped field of bowl–saddle hybrid molecules and related nanocarbons.

In the latter half of this chapter, the corannulene–[6]helicenes provided fundamental insights into a little-explored combination of geodesic curvature and a helical motif. On these characteristic π-systems, the theoretical and experimental studies revealed that the two merged nonplanar motifs, bowl and helix, mutually affect each other's inversion motions, lowering both energetic costs. Optical resolution of the corannulene-based skeletally chiral π-systems was accomplished for the first time, and the influence of bowl annulation on the chiroptical properties of [6]helicene was determined. Additionally, it proved possible to probe the magnetic environment above the convex surface of the corannulene core using the ^{1}H NMR signal of a *t*-butyl group attached to the helicene moiety. *t*-Butyl corannulene–[6]helicene (**2b**) is one of the first molecules designed to probe the magnetic environment above the convex surface of corannulene. Following the lead of this NMR study, further investigations with other strategically placed groups in helicene moieties could lead to even more interesting results. Similarly, because corannulene can be an aromatic ligand for alkali and transition metals,[3a–c,26] and helicenes are also able to coordinate with metals in a tweezer fashion,[27] properly designed corannulene–helicenes could serve as a new type of molecular tweezers with geodesic curvature by utilizing their intramolecularly proximal π-systems.

Experimental Section

General

Unless otherwise noted, all materials including dry solvents were obtained from commercial suppliers and used without further purification. 1-(*tert*-Butyl)-4-(4-methylstyryl)benzene (**13**),[28] formyl corannulene (**4**),[29] (phenanthren-3-ylmethyl)triphenylphosphonium bromide (**5a**),[30] and (naphtha[2,1-*b*]thien-2-ylmethyl)triphenylphosphonium bromide (**5c**),[31] were prepared according to the procedures reported in the literature. Unless otherwise noted, all reactions were performed with dry solvents under an atmosphere of nitrogen in dried glassware with standard vacuum-line techniques. All work-up and purification procedures were carried out with reagent-grade solvents in air.

Analytical thin-layer chromatography (TLC) was performed using E. Merck silica gel 60 F_{254} precoated plates (0.25 mm). The developed chromatogram was analyzed by UV lamp (254 nm and 365 nm). High-resolution mass spectra (HRMS) were obtained from a JEOL JMS-S3000 SpiralTOF (MALDI-TOF MS). Melting points were measured on a MPA100 Optimelt automated melting point system. Chiral HPLC analysis was conducted on a Shimadzu Prominence 2000 instrument equipped with COSMOSIL Cholester column (10 mm x 250 mm and 4.6 mm x 250 mm). NMR spectra were recorded on a JEOL JNM-ECA-600 (^{1}H 600 MHz, ^{13}C 150 MHz) spectrometer or a JEOL ECA 600II spectrometer with Ultra COOL^{TM} probe (^{1}H 600 MHz, ^{13}C 150 MHz). Chemical shifts for ^{1}H NMR are expressed in parts per million (ppm) relative to $CHCl_3$ (δ 7.26 ppm). Chemical shifts for ^{13}C NMR are expressed in ppm relative to $CDCl_3$ (δ 77.16 ppm) or $C_2D_2Cl_4$ (δ 73.78 ppm). Data are reported as follows: chemical shift, multiplicity (s = singlet, d = doublet, t = triplet, m = multiplet, br = broad signal), coupling constant (Hz), and integration.

Synthesis of 3-(*tert*-butyl)-6-methylphenanthrene (13)

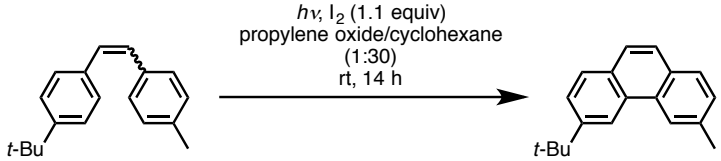

14 **13**

A mixture of *E*- and *Z*-isomers of 1-(*tert*-butyl)-4-(4-methylstyryl)benzene (**14**) (400 mg, 1.60 mmol), iodine (440 mg, 1.73 mmol), and propylene oxide (20 mL) in 600 mL of cyclohexane was irradiated for 14 hours using an Hanovia UV lamp. The solvent was evaporated under reduced pressure; the crude product was chromatographed on a short silica gel column using petroleum ether as eluent to afford 390 mg of **13** as a viscous oil that crystallizes slowly

into a white solid (98% yield).

^{1}H NMR (400 MHz, $CDCl_3$) δ 8.65 (s, 1H), 8.48 (s, 1H), 7.78 (d, J = 8.4 Hz, 1H), 7.74 (d, J = 8.0 Hz, 1H), 7.64 (dd, J = 8.4, 2.4 Hz, 1H), 7.62 (s, 2H), 7.38 (d, J = 8.0 Hz, 1H), 2.62 (s, 3H), 1.49 (s, 9H); ^{13}C NMR (100 MHz, $CDCl_3$) δ 149.1, 136.0, 130.6, 130.23, 130.20, 129.7, 128.5, 128.3, 128.2, 126.2, 125.6, 124.8, 122.2, 118.3, 35.5, 31.9, 22.5; HRMS (FAB) *m/z* calcd for $C_{19}H_{20}$ $[M]^+$: 248.1565, found: 248.1561; mp: 50–51 ºC.

Synthesis of 5b

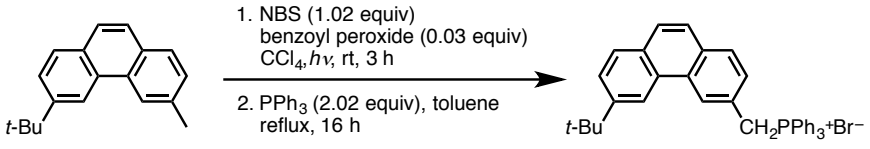

13 **5b**

A mixture of **13** (300 mg, 1.21 mmol), *N*-bromosuccinimide (NBS) (230 mg, 1.24 mmol), and benzoyl peroxide (10 mg, 0.040 mmol) in 70 mL of carbon tetrachloride was irradiated with a visible light lamp under reflux for 3 hours. The mixture was filtered, and the solvent was evaporated under reduced pressure. Toluene (100 mL) and triphenylphosphine (640 mg, 2.44 mmol) were added, and the resulting mixture was heated under reflux for 16 hours. The flask contents were cooled down, phosphonium salt **5b** was isolated by vacuum filtration, further washed with toluene (3×20 mL) to remove excess triphenylphosphine and dried under vacuum on the filter (425 mg, 60% yield for two steps).

^{1}H NMR (400 MHz, $CDCl_3$) δ 8.25 (bs, 1H), 8.10 (s, 1H), 7.80–7.68 (m, 10H), 7.66–7.55 (m, 9H), 7.52 (d, J = 8.8 Hz, 1H), 7.42 (d, J = 8.4 Hz, 1H), 5.64 (d, $^2J_{H–P}$ = 13.6 Hz, 2H), 1.41 (s, 9H); ^{13}C NMR (100 MHz, $CDCl_3$) δ 149.7, 138.5, 135.0 (d, $J_{C–P}$ = 3.0 Hz), 134.6 (d, $J_{C–P}$ = 9.8 Hz), 131.8 (d, $J_{C–P}$ = 3.0 Hz), 130.2 (d, $J_{C–P}$ = 12.1 Hz), 130.1, 129.8 (d, $J_{C–P}$ = 3.8 Hz), 129.4, 129.3, 128.3, 127.4, 125.8, 125.6 (d, $J_{C–P}$ = 5.0 Hz), 125.3, 125.1 (d, $J_{C–P}$ = 6.0 Hz), 118.0 (d, $J_{C–P}$ = 85.0 Hz), 35.3, 31.7, 31.4 (d, $J_{C–P}$ = 34.9 Hz) (20 out of 21 signals expected); HRMS (FAB) *m/z* calcd for $C_{37}H_{34}P$ $[M−Br]^+$: 509.2398, found: 509.2398; mp: 280 ºC (decomposed).

Synthesis of 3a

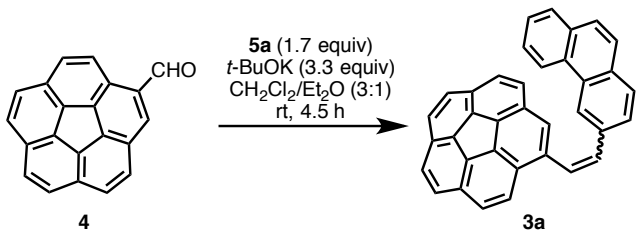

4 **3a**

To a solution of formylcorannulene (**4**) (167 mg, 0.600 mmol) and phosphonium salt **5a**

(533 mg, 1.00 mmol) in 30 mL of methylene chloride were added 10 mL of ether and potassium *t*-butoxide (224 mg, 2.00 mmol). The mixture was stirred at room temperature for 4.5 hours. To the reaction mixture was added 10 mL of methanol and then the resulting mixture was passed through a pad of silica gel using methylene chloride as an eluent. The solvent was removed under reduced pressure. To remove 3-methylphenanthrene, the crude product was washed with *n*-hexane by sonication, and the yellow precipitate was collected. The filtrate was evaporated and the residue was chromatographed on a silica gel column using *n*-hexane/methylene chloride = 9:1 to 7:3. The obtained yellow solid was combined with the yellow precipitate to afford 264 mg of **3a** as a mixture of *E*- and *Z*-isomers (97%, ratio *E*/*Z* = 1:1). For characterization purposes, a small amount was separated by silica gel column chromatography using *n*-hexane/methylene chloride = 9:1 as eluent to afford enriched samples of the *E*- and *Z*-isomers of **3a**.

E-**3a**: ^{1}H NMR (600 MHz, $CDCl_3$) δ 8.87 (s, 1H), 8.81 (d, *J* = 7.9 Hz, 1H), 8.27 (d, *J* = 8.8 Hz, 1H), 8.03 (d, *J* = 0.7 Hz, 1H), 8.00 (dd, *J* = 8.3, 1.4 Hz, 1H), 7.97–7.90 (m, 4H), 7.85–7.75 (m, 9H), 7.71 (td, *J* = 7.1, 1.4 Hz, 1H), 7.64 (td, *J* = 6.9, 1.0 Hz, 1H); ^{13}C NMR (150 MHz, $CDCl_3$) δ 137.8 (4º), 136.5 (4º), 136.3 (4º), 135.9 (4º), 135.8 (4º), 135.7 (4º), 135.6 (4º), 133.5 (CH), 132.6 (4º), 132.1 (4º), 131.2 (4º), 131.1 (4º), 130.97 (4º), 130.96 (4º), 130.8 (4º), 130.5 (4º), 129.3 (CH), 128.9 (CH), 127.7 (CH), 127.6 (CH), 127.5 (CH), 127.35 (CH), 127.32 (CH), 127.22 (CH), 127.21 (CH), 127.16 (CH), 127.1 (CH), 126.95 (CH), 126.86 (CH), 126.8 (CH), 126.0 (CH), 124.7 (CH), 124.4 (CH), 122.9 (CH), 122.1 (CH) (35 out of 36 signals expected); HRMS (DART) *m/z* calcd for $C_{36}H_{21}$ $[M+1]^+$: 453.1643, found: 453.1663; mp: 220 ºC (decomposed).

Z-**3a**: ^{1}H NMR (600 MHz, $CDCl_3$) δ 8.73 (s, 1H), 8.16 (d, *J* = 8.3 Hz, 1H), 7.82–7.75 (m, 7H), 7.73–7.61 (m, 7H), 7.49 (td, *J* = 7.2, 1.2 Hz, 1H), 7.35 (td, *J* = 7.2, 1.2 Hz, 1H), 7.18 (d, *J* = 12.4 Hz, 1H), 7.16 (d, *J* = 12.2 Hz, 1H); ^{13}C NMR (150 MHz, $CDCl_3$) δ 137.1 (4º), 136.3 (4º), 136.0 (4º), 135.9 (4º), 135.6 (4º), 135.3 (4º), 133.1 (CH), 132.2 (4º), 131.4 (4º), 131.2 (4º), 131.0 (4º), 130.8 (4º), 130.34 (4º), 130.32 (4º), 129.7 (4º), 128.6 (CH), 128.4 (CH), 128.15 (CH), 128.10 (CH), 127.4 (CH), 127.32 (CH), 127.26 (CH), 127.22 (CH), 127.20 (CH), 127.19 (CH), 127.16 (CH), 127.1 (CH), 126.69 (CH), 126.67 (CH), 126.64 (CH), 126.3 (CH), 124.0 (CH), 122.5 (CH) (33 out of 36 signals expected); HRMS (DART) *m/z* calcd for $C_{36}H_{20}$ $[M]^+$: 452.1565, found: 452.1577; mp: 185 ºC (decomposed).

Synthesis of 3b

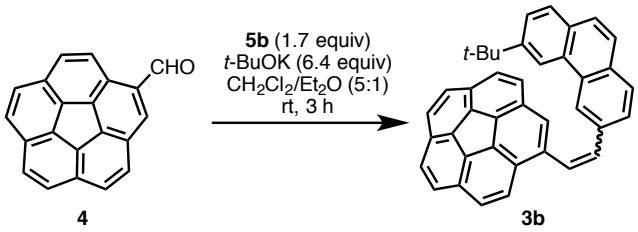

To a solution of formylcorannulene (**4**) (40 mg, 0.14 mmol) and phosphonium salt **5b** (140 mg, 0.237 mmol) in 25 mL of methylene chloride were added 5 mL of ether and potassium *t*-butoxide (100 mg, 0.891 mmol). The mixture was stirred at room temperature for 3 hours. The flask contents were poured into water, extracted with methylene chloride, dried over anhydrous magnesium sulfate, and the solvent was removed under reduced pressure. The crude product was chromatographed on a short silica gel column using petroleum ether as an eluent to afford a mixture that was analyzed by ^{1}H NMR spectroscopy, which revealed the presence of *E*- and *Z*-isomers of **3b** (ratio *E*/*Z* = 1:1) and of 3-*t*-butyl-6-metylphenanthrene as byproduct (estimated yield for **3b**: 50 mg, 70%). For yield purposes, this mixture was carried through to the next step without further purification. For characterization purposes, a small amount was separated by preparative thin-layer chromatography (on silica gel using petroleum ether/methylene chloride = 4:1 as eluent) to afford enriched samples of the *E*- and *Z*-isomers of **3b**.

HRMS (FAB) *m/z* calcd for $C_{40}H_{28}$ $[M]^+$: 508.2191, found: 508.2190.

E-**3b**: ^{1}H NMR (400 MHz, $CDCl_3$) δ 8.82 (s, 1H), 8.77 (d, *J* = 2.0 Hz, 1H), 8.27 (d, *J* = 8.8 Hz, 1H), 8.05 (s, 1H), 8.01 (dd, *J* = 8.0, 1.2 Hz, 1H), 7.96–7.80 (m, 9H), 7.75–7.62 (m, 5H), 1.55 (s, 9H); mp: 157–160 ºC (80–90% purity).

Z-**3b**: ^{1}H NMR (400 MHz, $CDCl_3$) δ 8.98 (s, 1H), 8.32 (d, *J* = 1.2 Hz, 1H), 7.82 (d, *J* = 1.6 Hz, 1H), 7.79–7.56 (m, 14H), 7.19 (d, *J* = 12.8 Hz, 1H), 7.12 (dd, *J* = 12.8, 1.2 Hz, 1H), 1.23 (s, 9H); mp: 142–145 ºC (60–70% purity).

Synthesis of 3c

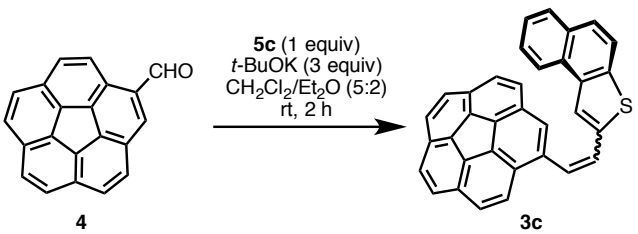

To a solution of formylcorannulene (**4**) (835 mg, 3.00 mmol) and phosphonium salt **5c** (1.62 g, 3.00 mmol) in 100 mL of methylene chloride were added 40 mL of ether and potassi-

um *t*-butoxide (1.01 g, 9.00 mmol). The mixture was stirred at room temperature for 2 hours. The reaction mixture was added 30 mL of methanol and then passed through a pad of silica gel using *n*-hexane/$CHCl_3$ (1:1) as an eluent. The solvent was removed under reduced pressure and the residue was chromatographed on a silica gel column using *n*-hexane/$CHCl_3$ = 9:1 to 4:1 to afford 264 mg of **3c** as a mixture of *E*- and *Z*-isomers (73%, ratio *E*:*Z* = 1:1). For characterization purposes, a small amount was separated by recycling preparative HPLC equipped with COSMOSIL Cholester column (20 mm x 250 mm) using chloroform/2-propanol (7:3) as eluent to afford enriched samples of the *E*- and *Z*-isomers of **3c**.

E-**3c** (the slow-eluting isomer): ^{1}H NMR (600 MHz, $CDCl_3$) δ 8.34 (d, *J* = 8.1 Hz, 1H), 8.21 (d, *J* = 8.9 Hz, 1H), 8.06 (s, 1H), 7.97 (s, 1H), 7.95 (d, *J* = 8.1 Hz, 1H), 7.90 (d, *J* = 8.8 Hz, 1H), 7.87–7.80 (m, 8H), 7.76 (d, *J* = 8.8 Hz, 1H), 7.69 (d, *J* = 15.8 Hz, 1H), 7.64 (td, *J* = 7.5, 1.1 Hz, 1H), 7.55 (td, *J* = 7.4, 1.0 Hz, 1H); ^{13}C NMR (150 MHz, $CDCl_3$) δ 143.0 (4º), 137.0 (4º), 136.9 (4º), 136.6 (4º), 136.5 (4º), 136.2 (4º), 135.9 (4º), 135.7 (4º), 135.6 (4º), 131.3 (4º), 131.2 (4º), 131.00 (4º), 130.99 (4º), 129.3 (4º), 129.0 (4º), 128.8 (CH), 128.2 (CH), 127.8 (CH), 127.6 (CH), 127.5 (CH), 127.3 (CH), 127.23 (CH), 127.18 (CH), 127.1 (CH), 126.8 (CH), 126.5 (CH), 125.9 (CH), 125.7 (CH), 125.6 (CH), 124.8 (CH), 123.7 (CH), 122.1 (CH), 120.7 (CH) (33 out of 34 signals expected).

Z-**3c** (the fast-eluting isomer): ^{1}H NMR (600 MHz, $CDCl_3$) δ 8.20 (d, *J* = 8.1 Hz, 1H), 8.04 (s, 1H), 7.96 (d, *J* = 0.9 Hz, 1H), 7.89 (d, *J* = 8.8 Hz, 1H), 7.86 (d, *J* = 8.1 Hz, 1H), 7.83–7.81 (m, 4H), 7.80–7.77 (m, 2H), 7.75 (d, *J* = 8.9 Hz, 1H), 7.62 (d, *J* = 8.9 Hz, 1H), 7.58–7.53 (m, 2H), 7.48 (td, *J* = 7.6, 0.7 Hz, 1H), 7.27 (d, *J* = 11.5 Hz, 1H), 7.06 (d, *J* = 11.7 Hz, 1H);
^{13}C NMR (150 MHz, $CDCl_3$) δ 139.9 (4º), 138.1 (4º), 136.3 (4º), 136.1 (4º), 136.0 (4º), 135.94 (4º), 135. 88 (4º), 135.1 (4º), 131.2 (4º), 131.12 (4º), 131.10 (4º), 131.07 (4º), 130.9 (4º), 130.2 (4º), 129.1 (4º), 128.7 (CH), 127.9 (CH), 127.5 (CH), 127.41 (CH), 127.36 (CH), 127.32 (CH), 127.26 (CH), 127.24 (CH), 127.16 (CH), 126.63 (CH), 126.60 (CH), 125.8 (CH), 125.7 (CH), 125.4 (CH), 124.6 (CH), 123.6 (CH), 120.6 (CH) (32 out of 34 signals expected).

Synthesis of 2a and 6a

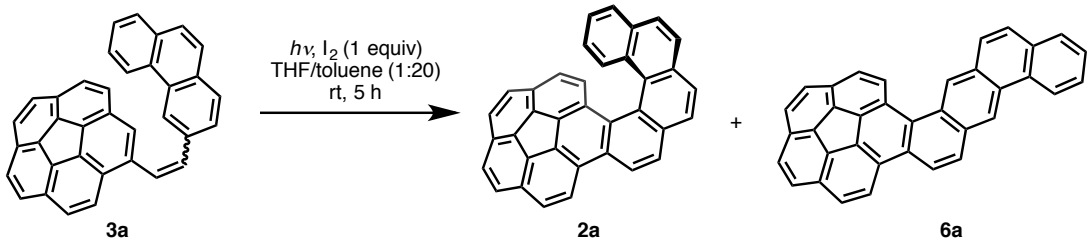

A mixture of *E*- and *Z*-isomers of compound **3a** (510 mg, 1.13 mmol), iodine (287 mg, 1.13 mmol), and THF (30 mL) in 600 mL of toluene was irradiated for 5 hours using an UV Ha-

novia lamp. The reaction mixture was evaporated under reduced pressure. The crude product was washed with methylene chloride and toluene several times. The poorly soluble yellow precipitate was collected to afford **6a** (206 mg, 40%). The filtrate was evaporated and the residue was chromatographed on a silica gel column using *n*-hexane/methylene chloride = 9:1 to afford 127 mg of **2a** as a white solid (25%).

2a: ^{1}H NMR (600 MHz, $CDCl_3$) δ 8.82 (d, *J* = 8.4 Hz, 1H), 8.78 (d, *J* = 8.6 Hz, 1H), 8.47 (d, *J* = 8.8 Hz, 1H), 8.17 (d, *J* = 8.4 Hz, 1H), 8.08 (d, *J* = 8.4 Hz, 1H), 8.01–7.98 (m, 5H), 7.83 (d, *J* = 8.7 Hz, 1H), 7.76 (d, *J* = 8.7 Hz, 1H), 7.69 (d, *J* = 8.6 Hz, 1H), 7.55 (d, *J* = 8.7 Hz, 1H), 7.42 (td, *J* = 6.8, 1.2 Hz, 1H), 7.15 (td, *J* = 6.7, 1.3 Hz, 1H), 7.03 (d, *J* = 8.9 Hz, 1H), 6.87 (d, *J* = 8.9 Hz, 1H); ^{13}C NMR (150 MHz, $CDCl_3$) δ 138.0 (4º), 136.5 (4º), 135.8 (4º), 135.7 (4º), 133.6 (4º), 133.1 (4º), 132.6 (4º), 131.94 (4º), 131.92 (4º), 131.6 (4º), 131.4 (4º), 131.0 (4º), 130.9 (4º), 130.8 (4º), 130.4 (CH), 130.2 (4º), 128.8 (4º), 128.5 (CH), 128.3 (4º), 128.0 (CH), 127.9 (CH), 127.8 (CH), 127.7 (CH), 127.3 (CH), 127.2 (CH), 127.1 (CH), 127.0 (CH), 126.8 (CH), 126.11 (CH), 126.07 (CH), 126.0 (CH), 125.4 (CH), 125.3 (CH), 123.5 (CH) (34 out of 36 signals expected); HRMS (MALDI TOF-MS) *m/z* calcd for $C_{36}H_{18}$ $[M]^+$: 450.1409, found: 450.1426; mp: 250 ºC (decomposed).

6a: ^{1}H NMR (600 MHz, $CDCl_3$) δ 10.03 (s, 1H), 9.37 (s, 1H), 8.94 (d, *J* = 8.1 Hz, 1H), 8.89 (d, *J* = 8.8 Hz, 1H), 8.76 (d, *J* = 8.9 Hz, 1H), 8.46 (d, *J* = 8.9 Hz, 1H), 8.38 (d, *J* = 8.8 Hz, 1H), 8.14 (d, *J* = 8.9 Hz, 1H), 8.05 (d, *J* = 8.6 Hz, 1H), 8.01 (d, *J* = 8.7 Hz, 1H), 7.96 (d, *J* = 7.5 Hz, 1H), 7.93 (d, *J* = 8.6 Hz, 1H), 7.89 (s, 2H), 7.87 (d, *J* = 8.7 Hz, 1H), 7.83 (d, *J* = 8.9 Hz, 1H), 7.76 (td, *J* = 7.52, 1.3 Hz, 1H), 7.69 (td, *J* = 7.4, 1.0 Hz, 1H); ^{13}C NMR (150 MHz, $C_2D_2Cl_4$) δ 137.4 (4º), 135.3 (4º), 135.1 (4º), 135.0 (4º), 134.6 (4º), 132.0 (4º), 131.5 (4º), 131.02 (4º), 130.95 (4º), 130.7 (4º), 130.6 (4º), 130.5 (4º), 130.1 (4º), 130.0 (4º), 128.84 (4º), 128.81 (4º), 128.7 (CH), 128.6 (CH), 128.5 (4º), 128.4 (CH), 128.3 (CH), 127.91 (CH), 127.86 (CH), 127.62 (CH), 127.59 (CH), 127.42 (CH), 127.40 (CH), 127.3 (CH), 127.1 (CH), 127.04 (CH), 126.9 (CH), 124.6 (CH), 123.04 (CH), 122.7 (CH), 122.3 (CH) (35 signals out of 36 expected); HRMS (MALDI TOF-MS) *m/z* calcd for $C_{36}H_{18}$ $[M]^+$: 450.1409, found: 450.1411; mp: >300 ºC.

Synthesis of 2b and 6b

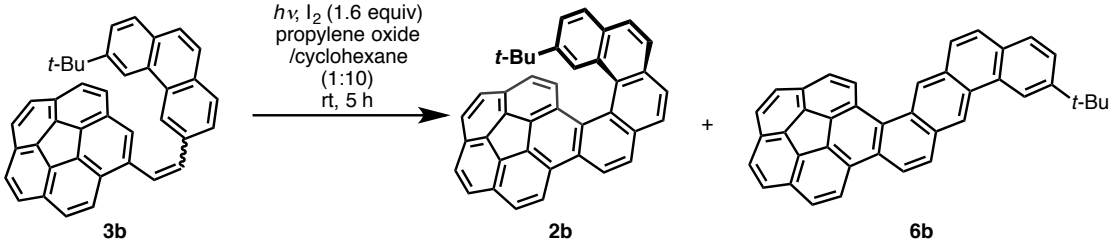

A crude mixture containing *E*- and *Z*-isomers of **3c** (*ca*. 50 mg, *ca*. 0.01 mmol) was dissolved in 5 mL of benzene and was added to a solution of iodine (40 mg, 0.16 mmol) in 100 mL of cyclohexane and 10 mL of propylene oxide. The resulting solution was irradiated for 5 hours using a Hanovia UV lamp. Removal of the solvent under reduced pressure afforded a solid that was analyzed by ^{1}H NMR spectroscopy to reveal the presence of **5b** and **6b** in the approximate ratio of **2b**/**6b** = 2:3. Preparative thin-layer chromatography on silica gel using petroleum ether/methylene chloride = 4:1 as eluent afforded relatively pure samples of **2b** (11 mg, 22% yield) and **6b** (14 mg, 28% yield).

2b: ^{1}H NMR (400 MHz, $CDCl_3$) δ 8.82 (d, *J* = 8.4 Hz, 1H), 8.79 (d, *J* = 0.8 Hz, 1H), 8.47 (d, *J* = 8.8 Hz, 1H), 8.17 (d, *J* = 8.4 Hz, 1H), 8.04 (d, *J* = 8.4 Hz, 1H), 7.99 (d, *J* = 8.8 Hz, 1H), 7.98 (s, 2H), 7.96 (d, *J* = 8.8 Hz, 1H), 7.94 (dd, *J* = 8.4, 0.8 Hz, 1H), 7.83 (d, *J* = 8.8 Hz, 1H), 7.75 (d, *J* = 8.8 Hz, 1H), 7.68 (d, *J* = 8.8 Hz, 1H), 7.54 (d, *J* = 8.8 Hz, 1H), 7.50 (dd, *J* = 8.4, 2.0 Hz, 1H), 7.01 (d, *J* = 8.8 Hz, 1H), 6.87 (d, *J* = 8.8 Hz, 1H), 0.94 (s, 9H); ^{13}C NMR (100 MHz, $CDCl_3$) δ 147.9, 138.0, 136.3, 135.9, 135.8, 135.3, 133.8, 133.0, 132.0, 131.8, 131.5, 131.0, 130.8, 130.7, 130.48, 130.45, 130.2, 129.6, 128.9, 128.3, 128.0, 127.88, 127.86, 127.59, 127.56, 127.3, 127.04, 126.96, 126.8, 126.1, 125.86, 125.84, 125.40, 125.35, 124.7, 123.3, 35.0, 31.2; HRMS (FAB) *m/z* calcd for $C_{40}H_{26}$ $[M]^+$: 506.2034, found: 506.2033; mp: 189–190 ºC.

6b: ^{1}H NMR (400 MHz, $CDCl_3$) δ 10.00 (s, 1H), 9.37 (s, 1H), 8.93 (bs, 1H), 8.89 (d, *J* = 8.8 Hz, 1H), 8.74 (d, *J* = 8.8 Hz, 1H), 8.45 (d, *J* = 8.8 Hz, 1H), 8.40 (d, *J* = 8.4 Hz, 1H), 8.08 (d, *J* = 8.8 Hz, 1H), 8.04 (d, *J* = 8.8 Hz, 1H), 7.99 (d, *J* = 8.8 Hz, 1H), 7.92 (d, *J* = 8.4 Hz, 1H), 7.90 (d, *J* = 8.4 Hz, 1H), 7.88 (s, 2H), 7.86 (d, *J* = 8.4 Hz, 1H), 7.80 (d, *J* = 8.8 Hz, 1H), 7.78 (dd, *J* = 8.4, 2.0 Hz, 1H), 1.59 (s, 9H); ^{13}C NMR (100 MHz, $CDCl_3$) δ 150.0, 135.36, 135.34, 131.6, 131.4, 131.2, 130.9, 130.78, 130.75, 130.2, 130.1, 130.0, 129.8, 129.3, 129.2, 128.9, 128.8, 128.5, 128.3, 128.2, 127.95, 127.92, 127.4, 127.3, 127.1, 126.99, 126.98, 125.6, 124.7, 124.1, 123.0, 122.7, 122.1, 119,1. 35,7, 32.0 (38 signals out of 40 expected); HRMS (FAB) *m/z* calcd for $C_{40}H_{26}$ $[M]^+$: 506.2034, found: 506.2033; mp: 156–158 ºC.

Synthesis of 2c

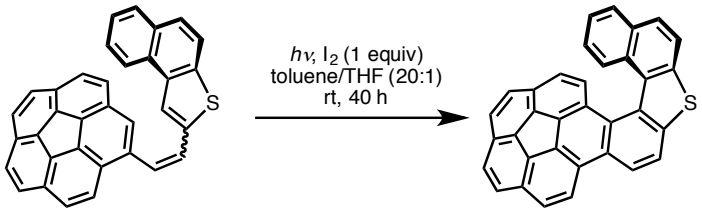

3c **2c**

A mixture containing *E*- and *Z*-isomers of **3c** (229 mg, 0.500 mmol) was added to a solu-

tion of iodine (127 mg, 0.500 mmol) in 500 mL of toluene and 25 mL of THF. The resulting solution was irradiated for 40 hours using a 100-W high-pressure Hg lamp. The reaction mixture was reduced under reduced pressure and added $CHCl_3$. The organic layer was washed with aqueous solution of NaOH (2N) and $Na_2S_2O_3$ (saturated), then evaporated *in vacuo*. The residue was chromatographed on a silica gel column using *n*-hexane/methylene chloride (19:1 to 4:1) to afford 157 mg of **2c** as a yellow solid (69%).

2c: ^{1}H NMR (600 MHz, $CDCl_3$) δ 8.87 (d, *J* = 8.1 Hz, 1H), 8.77 (d, *J* = 8.4 Hz, 1H), 8.46 (d, *J* = 8.8 Hz, 1H), 8.23 (d, *J* = 8.4 Hz, 1H), 8.10 (dd, *J* = 8.3, 0.7 Hz, 1H), 8.08–8.05 (m, 2H), 8.02 (d, *J* = 8.8 Hz, 1H), 7.87 (d, *J* = 8.6 Hz, 1H), 7.80 (d, *J* = 8.6 Hz, 1H), 7.78 (d, *J* = 8.6 Hz, 1H), 7.67 (d, *J* = 8.6 Hz, 1H), 7.56 (td, *J* = 7.5, 1.0 Hz, 1H), 7.45 (d, *J* = 8.8 Hz, 1H), 7.37 (td, *J* = 7.6, 1.4 Hz, 1H), 7.28 (d, *J* = 8.8 Hz, 1H); ^{13}C NMR (150 MHz, $CDCl_3$) δ 140.3 (4º), 139.3 (4º), 138.0 (4º), 136.0 (4º), 135.7 (4º), 135.6 (4º), 133.9 (4º), 133.0 (4º), 131.82 (4º), 131.78 (4º), 131.23 (4º), 131.18 (4º), 131.1 (4º), 130.8 (4º), 130.27 (4º), 130.26 (4º), 130.0 (4º), 129.0 (4º), 128.80 (CH), 128.75 (CH), 128.7 (CH), 128.3 (CH), 128.2 (CH), 127.3 (CH), 127.2 (CH), 127.1 (CH), 127.0 (CH), 125.45 (CH), 125.42 (CH), 125.3 (CH), 125.2 (CH), 123.1 (CH), 121.6 (CH), 121.0 (CH).

Synthesis of 12

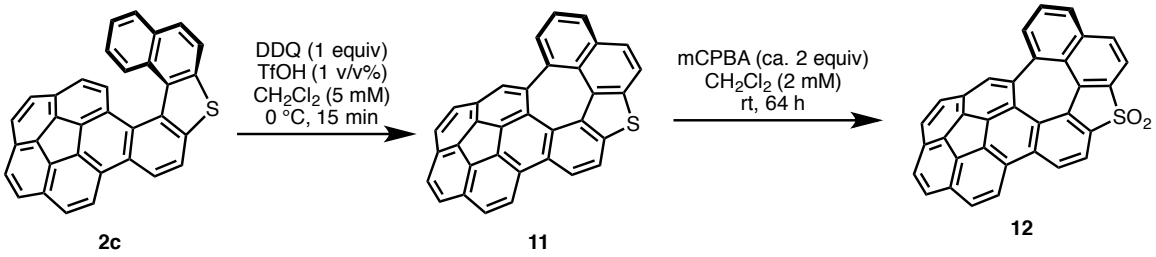

To a solution of **2c** (18.3 mg, 0.0401 mmol) and DDQ (9.1 mg, 0.040 mmol) in dry CH_2Cl_2 (8 mL) was added trifluoromethanesulfonic acid (80 μL) at 0 ºC. After stirring for 15 min, the reaction mixture was neutralized with triethylamine (500 μL) in $CHCl_3$ (2.5 mL), and then diluted by $CHCl_3$ (20 mL). The organic layer was passed through a pad of silica-gel using *n*-hexane/$CHCl_3$ (1:1) as an eluent to afford crude **11** as a yellow solid. Compound **11** was used in next step without further purification.

To a solution of crude **11** in $CHCl_3$ (20 mL) was added *m*-chloroperoxybenzoic acid with 25% water (18.7 mg, 0.0813 mmol). The reaction mixture was stirred for 64 h at room temperature, and then passed through a pad of silica-gel using $CHCl_3$ as an eluent. The filtrate was evaporated *in vacuo*. The residue was purified by silica-gel chromatographed on a silica gel column using *n*-hexane/ethyl acetate (4:1 to 3:2) to afford **12** as a yellow solid (13.0 mg, 69%

in 2 steps).

12: ^{1}H NMR (600 MHz, $CDCl_3$) δ 8.83 (d, *J* = 8.4 Hz, 1H), 8.23–8.21 (m, 2H), 8.12 (d, *J* = 8.1 Hz, 1H), 8.08–8.06 (m, 2H), 7.99 (d, *J* = 8.8 Hz, 1H), 7.96 (dd, *J* = 7.2, 0.7 Hz, 1H), 7.93 (d, *J* = 8.3 Hz, 1H), 7.87 (d, *J* = 8.8 Hz, 1H), 7.85–7.82 (m, 3H), 7.75 (t, *J* = 7.7 Hz, 1H).

Enantiomer Separation by HPLC

HPLC analysis was conducted on a Shimadzu Prominence 2000 instrument equipped with COSMOSIL Cholester column (two different size column (10 mm × 250 mm and 4.6 mm × 250 mm) were connected). Eluted products were analyzed at 310 nm. Flow rate was 2.0 mL/min and temperature was 25 ˚C. Eluted by chloroform/methanol (2:8).

Kinetic Study

Kinetics of the racemization process of **2a** was studied by monitoring the decreasing *ee* of *M*-**2a** in 1,2,4-trichlorobenzene at 146.2, 151.0, 156.0, and 161.3 °C. All reactions were conducted in test tube upon the heating by oil bath under nitrogen. Reactions were stopped by cooling the test tube in ice bath at each time and *ee* was determined by HPLC analysis.

Photophysical Study

UV–Vis absorption spectra were recorded on a Shimadzu UV-3510 spectrometer with a resolution of 0.5 nm. Emission spectra were measured with an FP-6600 Hitachi spectrometer with a resolution of 0.2 nm upon excitation at 315 nm. CD spectra were measured with a JASCO FT/IR6100. Dilute solutions in degassed spectral grade chloroform in a 1 cm square quartz cell were used for measurements. Absolute fluorescence quantum yield of **2a** was determined with a Shimadzu RF-6000 with calibrated integrating sphere system (207-21460-41) upon excitation at 315 nm.

X-ray Crystallography

Single crystals of **2a** and **2c** suitable for X-ray crystal structure analysis were obtained by recrystallization of a racemic mixture from chloroform/*n*-hexane in vapor diffusion method. Single crystals of **12** suitable for X-ray crystal structure analysis were obtained by recrystallization of a racemic mixture from chloroform/Et_2O in vapor diffusion method. Details of the crystal data and a summary of the intensity data collection parameters are listed in Table 3. A suitable crystal was mounted with mineral oil on a glass fiber and transferred to the goniometer of a Rigaku PILATUS diffractometer. Graphite-monochromated Mo Kα radiation (λ = 0.71075 Å) was used. The structures were solved by direct methods with (SIR-97)[32] and re-

fined by full-matrix least-squares techniques against F^2 (SHELXL-97).[33] The intensities were corrected for Lorentz and polarization effects. The non-hydrogen atoms were refined anisotropically. Hydrogen atoms were placed using AFIX instructions.

Table 3. Crystallographic data and structure refinement details for **2a**, **2c**, and **12**.

	2a	**2c**	**12**
formula	$C_{36}H_{18}$	$C_{34}H_{16}S$	$C_{34}H_{14}O_2S$
fw	450.50	456.53	486.51
T (K)	123(2)	123(2)	123(2)
λ (Å)	0.71075	0.71075	0.71075
cryst syst	Monoclinic	Monoclinic	Monoclinic
space group	*Cc*	*Cc*	$P2_1/n$
a (Å)	28.619(3)	26.2368(7)	14.135(3)
b (Å)	13.5049(14)	13.1269(4)	7.3236(10)
c (Å)	11.3279(11)	12.5790(3)	20.769(4)
α	90°	90°	90°
β	101.050(2)°	103.824(3)°	107.039(3)°
γ	90°	90°	90°
V (Å^3)	4297.0(8)	4206.8(2)	2055.6(7)
Z	8	8	4
D_{calc} (g / cm^3)	1.393	1.442	1.572
μ (mm^{-1})	0.079	0.177	0.560
F(000)	1872	1888	0.194
cryst size (mm)	0.25 × 0.10 × 0.10	0.10 × 0.10 × 0.02	0.25 × 0.05 × 0.02
θ range	3.02–25.00°	2.278–24.999°	3.015 –24.999°
reflns collected	15464	16590	14483
indep reflns/R_{int}	6579/0.0289	6608/0.0532	3563/0.0517
params	649	631	743
GOF on F^2	1.047	1.067	1.028
R_1, wR_2 [$I>2\sigma(I)$]	0.0330, 0.0811	0.0426, 0.0969	0.0373, 0.0853
R_1, wR_2 (all data)	0.0406, 0.0893	0.0648, 0.1270	0.0591, 0.0940

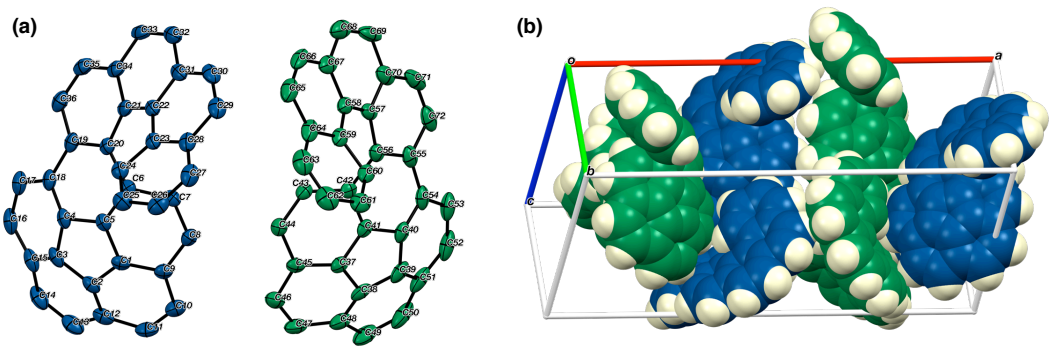

Figure 12. (a) ORTEP drawing and (b) packing structure of **2a**. Two crystallographically independent molecules are colored in blue and green, respectively.

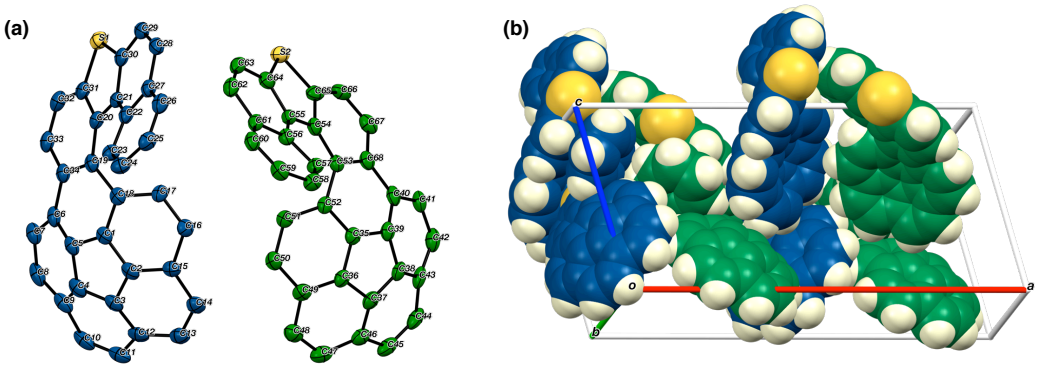

Figure 13. (a) ORTEP drawing and (b) packing structure of **2c**. Two crystallographically independent molecules are colored in blue and green, respectively.

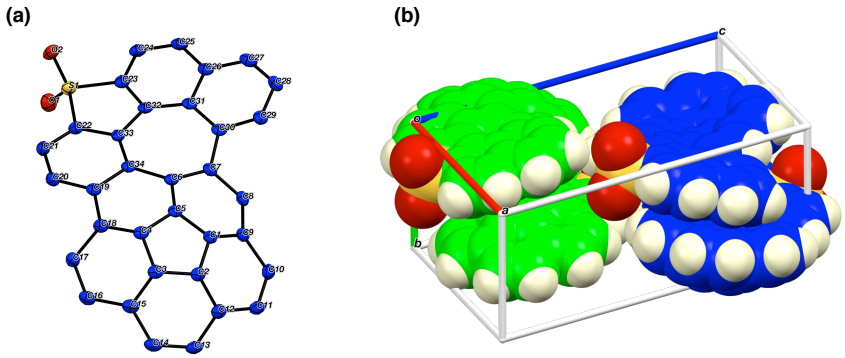

Figure 14. (a) ORTEP drawing and (b) packing structure of **12**. A pair of enantiomers appears in the crystal due to the helicity around heptagonal ring; *P*-**12** and *M*-**12** were colored in green and blue, respectively.

Computational Study

The Gaussian 09 program[34] running on a SGI Altix4700 system was used for optimization (B3LYP/6-31G(d)).[35] All structures were optimized without any symmetry assumptions. Zero-point energy, enthalpy, and Gibbs free energy at 298.15 K and 1 atm were estimated from the gas-phase studies unless otherwise noted. Harmonic vibration frequency calculations at the same level were performed to verify all stationary points as local minima (with no imaginary frequency) or transition states (with one imaginary frequency). All NMR study was performed at B3LYP/6-311+G(2d,p) level. Tetramethylsilane ($SiMe_4$) was used as reference (δ 0.00 ppm) for the estimation of ^1H NMR chemical shifts. Visualization of the results was performed by use of GaussView 5.0 software.

Table 4. Uncorrected and thermal-corrected (298 K) energies of stationary points (Hartree).[a]

structure	*E*	*E* + *ZPE*	*H*	*G*
convex-**2a**	-1382.70924974	-1382.289858	-1382.266590	-1382.339318
concave-**2a**	-1382.69889563	-1382.279691	-1382.256388	-1382.329238
TS1 (**2a**)	-1382.69385719	-1382.274727	-1382.252127	-1382.323298
TS2 (**2a**)	-1382.65508792	-1382.236328	-1382.213880	-1382.284217
convex-**2b**	-1539.96500364	-1539.432887	-1539.403883	-1539.489308
concave-**2b**	-1539.95468870	-1539.422388	-1539.393496	-1539.477842
convex-**2c**	-1703.48190518	-1703.095446	-1703.072458	-1703.144791
[6]helicene	-1000.44294361	-1000.107877	-1000.089572	-1000.152127
7	-2612.99454886	-2612.179155	-2612.132186	-2612.257003
8	-1641.98678973	-1641.717683	-1641.699969	-1641.761624
9	-1641.96934408	-1641.701052	-1641.683407	-1641.744832
10	-2283.49839078	-2283.296094	-2283.278932	-2283.339917

a) *E*: electronic energy; *ZPE*: zero-point energy; *H* (= $E + ZPE + E_{vib} + E_{rot} + E_{trans} + RT$): sum of electronic and thermal enthalpies; *G* (= $H - TS$): sum of electronic and thermal free energies.

Reference

1. (a) Barth, W. E.; Lawton, R. G. *J. Am. Chem. Soc.* **1966**, *88*, 380. (b) Lawton, R. G.; Barth, W. E. *J. Am. Chem. Soc.* **1971**, *93*, 1730. (c) Scott, L. T.; Hashemi, M. M.; Meyer, D. T.; Warren, H. B. *J. Am. Chem. Soc.* **1991**, *113,* 7082. (d) Borchardt, A.; Fuchicello, A.; Kilway, K. V.; Baldridge, K. K.; Siegel, J. S. *J. Am. Chem. Soc.* **1992**, *114*, 1921. (e) Scott, L. T.; Cheng, P.-C.; Hashemi, M. M.; Bratcher, M. S.; Meyer, D. T.; Warren, H. B. *J. Am. Chem. Soc.* **1997**, *119*, 10963. (f) Butterfield, A. M.; Gilomen, B.; Siegel, J. S. *Org. Process Res. Dev.* **2012**, *16*, 664.
2. Reviews on nonplanar π-systems: (a) Rieger, R.; Müllen, K. *J. Phys. Org. Chem.* **2010**, *23*, 315. (b) Dodziuk, H. *Strained Hydrocarbons: Beyond the van't Hoff and Le Bel Hypothesis*; Wiley-VCH: Weinheim, 2009. (c) Harvey, R. G. *Polycyclic Aromatic Hydrocarbons*; Wiley-VCH: New York, 1997. (d) Pascal, R. A., Jr. *Chem. Rev.* **2006**, *106*, 4809. (e) Tsefrikas, V. M.; Scott, L. T. *Chem. Rev.* **2006***, 106,* 4868. (f) Wu, Y.-T.; Siegel, J. S. *Chem. Rev.* **2006**, *106*, 4843.
3. (a) Zabula, A. V.; Filatov, A. S.; Spisak, S. N.; Rogachev, A. Y.; Petrukhina, M. A. *Science* **2011**, *333*, 1008. (b) Zabula, A. V.; Spisak, S. N.; Filatov, A. S.; Grigoryants, V. M.; Petrukhina, M. A. *Chem. Eur. J.* **2012**, *18*, 6476. (c) Ayalon, A.; Rabinovitz, M.; Cheng, P.-C.; Scott, L. T. *Angew. Chem., Int, Ed. Engl.* **1992**, *31*, 1636. (d) Seiders, T. J.; Baldridge, K. K.; Grube, G. H.; Siegel, J. S. *J. Am. Chem. Soc.* **2001**, *123*, 517. (e) Scott, L. T.; Hashemi, M. M.; Bratcher, M. S. *J. Am. Chem. Soc.* **1992**, *114*, 1920. (f) Kavitha, K.; Manoharan, M.; Venuvanalingam, P. *J. Org. Chem.* **2005**, *70*, 2528. (g) Preda, D. V.; Scott, L. T. *Tetrahedron Lett.* **2000**, *41*, 9633. (g) Bruno, C.; Benassi, R.; Passalacqua, A.; Paolucci, F.; Fontanesi, C.; Marcaccio, M.; Jackson, E. A.; Scott, L. T. *J. Phys. Chem. B* **2009**, *113*, 1954.
4. Scott, L. T.; Jackson, E. A.; Zhang, Q.; Steinberg, B. D.; Bancu, M.; Li, B. *J. Am. Chem. Soc.* **2012**, *134*, 107.
5. Kawasumi, K.; Zhang, Q.; Segawa, Y.; Scott, L. T.; Itami, K. *Nat. Chem.* **2013**, *5*, 739.
6. Examples of heptagonal ring formation by the Scholl reaction.
7. Kato, K.; Segawa, Y.; Scott, L. T.; Itami, K. *Chem. Asian J.* **2015**, *10*, 1635.
8. Circulenes: (a) Barth, W. E.; Lawton, R. G. *J. Am. Chem. Soc.* **1965**, *88*, 380. (b) Scott, L. T.; Hashemi, M. M.; Meyer, D. T.; Warren, H. B. *J. Am. Chem. Soc.* **1991**, *113*, 7082. (c) Yamamoto, K.; Harada, T.; Okamoto, Y.; Chikamatsu, H.; Nakazaki, M.; Kai, Y.; Nakao, T.; Tanaka, M.; Harada, S.; Kasai, N. *J. Am. Chem. Soc.* **1988**, *110*, 3578. (d) Yamamoto, K.; Saitho, Y.; Iwaki, D.; Ooka, T. *Angew. Chem., Int. Ed.* **1991**, *30*, 1173. (e) Butterfield, A. M.; Gilomen, B.; Siegel, J. S. *Org. Process Res. Dev.* **2012**, *16*, 664. (f) Feng, C.-N.; Kuo, M.-Y.; Wu, Y.-T. *Angew. Chem., Int. Ed.* **2013**, *52*, 7791. (g) Sakamoto, Y.; Suzuki, T. *J. Am. Chem. Soc.* **2013**, *135*, 14074.

9. Rabideau, P. W.; (a) Abdourazak, A. H.; Folsom, H. E.; Marcinow, Z.; Sygula, A.; Sygula, R. *J. Am. Chem. Soc.* **1994**, *116*, 7891. (b) Clar, E.; Mackay, C. C. *Tetrahedron* **1972**, *28*, 6041.
10. Prinzbach, H.; Seip, D.; Knathe, L.; Faisst, W. *Liebigs Ann. Chem.* **1966**, *698*, 34.
11. Yanney, M.; Fronczek, F. R.; Henry, W. P.; Beard, D. J.; Sygula, A. *Eur. J. Org. Chem.* **2011**, 6636.
12. (a) Fort, E. H.; Scott, L. T. *Angew. Chem., Int. Ed.* **2010**, *49*, 6626. (b) Fort, E. H.; Scott, L. T. *J. Mater. Chem.* **2011**, *21*, 1373. (c) Fort, E. H.; Donovan, P. M.; Scott, L. T. *J. Am. Chem. Soc.* **2009**, *131*, 16006.
13. (a) Flammang-Barbieux, M.; Nasielski, J.; Martin, R. H. *Tetrahedron Lett.* **1967**, *743*. (b) Laarhoven, W. H.; Cuppen, Th. J. H. M.; Nivard, R. J. F. *Tetrahedron* **1970**, *26*, 4865. (c) Liu, L.; Yang, B.; Katz, T. J.; Poindexter, M. K. *J. Org. Chem.* **1991**, *56*, 3769.
14. Thamatam, R.; Skraba, S. L.; Johnson, R. P. *Chem. Commun.* **2013**, *49*, 9122.
15. Dopper, J. H.; Wynberg, H. *J. Org. Chem.* **1975**, *40*, 3398.
16. (a) King, B. T.; Kroulík, J.; Robertson, C. R.; Rempala, P.; Hilton, C. L.; Korinek, J. D.; Gortari, L. M. *J. Org. Chem.* **2007**, *72*, 2279. (b) Zhai, L.; Shukla, R.; Rathore, R. *Org. Lett.* **2009**, *11*, 3474. (c) Rempala, P.; Kroulík, J.; King, B. T.; *J. Org. Chem.* **2006**, *71*, 5067.
17. Thiemann, T.; Fujii, H.; Ohira, D.; Arima, K.; Li, Y.; Mataka, S. *New J. Chem.* **2003**, *27*, 1377.
18. Petrukhina, M. A.; Andreini, K. W.; Mack, J.; Scott, L. T. *J. Org. Chem.* **2005**, *70*, 5713.
19. De Rango, C.; Tsoucaris, G.; Delerq, J. P.; Germain, G.; Putzeys, J. P. *Cryst. Struct. Commun.* **1973**, *2*, 189.
20. Martin, R. H.; Marchant, M. J. *Tetrahedron* **1974**, *30*, 347.
21. For examples of corannulene derivatives with chiral substituents, see: (a) Kang, J.; Miyajima, D.; Itoh, Y.; Mori, T.; Tanaka, H.; Yamauchi, M.; Inoue, Y.; Harada, S.; Aida, T. *J. Am. Chem. Soc.* **2014**, *136*, 10640. (b) Bandera, D.; Baldridge, K. K.; Linden, A.; Dorta, R.; Siegel, J. S. *Angew. Chem., Int. Ed.* **2011**, *50*, 865.
22. Nakai, Y.; Mori, T.; Inoue, Y. *J. Phys. Chem. A* **2012**, *116*, 7372.
23. (a) Buchta, M.; Rybáček, J.; Jančařík, A.; Kudale, A. A.; Buděšínský, M.; Chocholoušová, J. V.; Vacek, J.; Bednárová, L.; Císařová, I.; Bodwell, G. J.; Starý, I.; Stará, I. G. *Chem. Eur. J.* **2015**, *21*, 8910. (b) Jančařík, A.; Rybáček, J.; Cocq, K.; Chocholoušová, J. V.; Vacek, J.; Pohl, R.; Bednárová, L.; Fiedler, P.; Císařová, I.; Stará, I. G.; Starý, I. *Angew. Chem., Int. Ed.* **2013**, *52*, 9970.
24. Janata, J.; Gendell, J.; Ling, C.-Y.; Barth, W. Backes, L.; Mark, H. B., Jr.; Lawton, R. G. *J. Am. Chem. Soc.* **1967**, *89*, 3056.
25. (a) Yanney, M.; Fronczek, F. R.; Sygula, A. *Org. Lett.* **2012**, *14*, 4942. (b) Sygula, A.; Fronczek, F. R.; Sygula, R.; Rabideau, P. W.; Olmstead, M. M. *J. Am. Chem. Soc.* **2007**, *129*, 3842. (c) Seiders, T. J.; Baldridge, K. K.; Siegel, J. S. *Tetrahedron* **2001**, *57*, 3737. (d) Seiders, T. J.; Baldridge, K. K.; Siegel, J. S. *J. Am. Chem. Soc.* **1996**, *118*, 2754.

26. Petrukhina, M. A.; Scott, L. T. *Dalton Trans.* **2005**, 2969.
27. Saleh, N.; Shen, C.; Crassous, J. *Chem. Sci.* **2014**, *5*, 3680.
28. Younes, S.; Tchani, G.; Baziard-Mouysset, G.; Stigliani, J. L.; Payard, M.; Bonnafous, R.; Tisne-Versailles, J. *Eur. J. Med. Chem.* **1994**, *29*, 87.
29. Rajeshkumar, V.; Lee, Y. T.; Stuparu, M. C. *Eur. J. Org. Chem.* **2016**, 36.
30. Akiyama, S.; Nakasuji, K.; Nakagawa, M. *Bull. Chem. Soc. Jpn.* **1971**, *44*, 2231.
31. Dopper, J. H.; Oudman, D.; Wynberg, H. *J. Am. Chem. Soc.* **1973**, *95*, 3692.
32. Altomare, A.; Burla, M. C.; Camalli, M.; Cascarano, G. L.; Giacovazzo, C.; Guagliardi, A.; Moliterni, A. G. G.; Polidori, G.; Spagna, R. *J. Appl. Crystallogr.* **1999**, *32*, 115.
33. Sheldrick, G. M. University of Göttingen: Göttingen, Germany, 1997.
34. Frisch, M. J.; Trucks, G. W.; Schlegel, H. B.; Scuseria, G. E.; Robb, M. A.; Cheeseman, J. R.; Scalmani, G.; Barone, V.; Mennucci, B.; Petersson, G. A.; Nakatsuji, H.; Caricato, M.; Li, X.; Hratchian, H. P.; Izmaylov, A. F.; Bloino, J.; Zheng, G.; Sonnenberg, J. L.; Hada, M.; Ehara, M.; Toyota, K.; Fukuda, R.; Hasegawa, J.; Ishida, M.; Nakajima, T.; Honda, Y.; Kitao, O.; Nakai, H.; Vreven, T.; Montgomery, Jr., J. A.; Peralta, J. E.; Ogliaro, F.; Bearpark, M.; Heyd, J. J.; Brothers, E.; Kudin, K. N.; Staroverov, V. N.; Keith, T.; Kobayashi, R.; Normand, J.; Raghavachari, K.; Rendell, A.; Burant, J. C.; Iyengar, S. S.; Tomasi, J.; Cossi, M.; Rega, N.; Millam, J. M.; Klene, M.; Knox, J. E.; Cross, J. B.; Bakken, V.; Adamo, C.; Jaramillo, J.; Gomperts, R.; Stratmann, R. E.; Yazyev, O.; Austin, A. J.; Cammi, R.; Pomelli, C.; Ochterski, J. W.; Martin, R. L.; Morokuma, K.; Zakrzewski, V. G.; Voth, G. A.; Salvador, P.; Dannenberg, J. J.; Dapprich, S.; Daniels, A. D.; Farkas, O.; Foresman, J. B.; Ortiz, J. V.; Cioslowski, J.; Fox, D. J. Gaussian 09, Revision D.01, Gaussian, Inc., Wallingford CT, 2013.
35. (a) Becke, A. D. *J. Chem. Phys.* **1993**, *98*, 5648. (b) Lee, C.; Yang, W.; Parr, R. G. *Phys. Rev. B* **1988**, *37*, 785.

Chapter 2

Synthesis of π-Extended Double [6]Helicenes: A Combination of Planar and Nonplanar π-Systems

ABSTRACT: π-Extended double [6]helicenes (**DH1** and **DH2**) reported in this chapter provides a new prospect for the solid-state molecular packing of polyaromatic compounds. Due to the two relatively planar π-blades, *i.e.*, tribenzo[*b,n,pqr*]perylene substructures, concatenated in a twisting fashion (a planar–helix hybrid structure), *twisted*-isomer of **DH1** displayed a contorted three-dimensional lamellar packing structure in the crystal, giving a large intermolecular overlap of π-surface albeit its globally nonplanar π-system. The twin of [6]helicene substructures of **DH1** also afforded a *meso*-isomer with a chair-like structure. The three stereoisomers were separated by chiral HPLC and characterized by CD spectroscopy as well as by TD DFT studies. Electronic state variation resulting from the molecular geometry difference between the two diastereomers (*twisted*-**DH1** and *meso*-**DH1**) was examined by the UV–Vis absorption and fluorescence spectra. In addition, **DH2**, a *n*-butyl group substituted analog of **DH1**, was also prepared, which displayed a contorted two-dimensional lamellar packing structure in the crystal. Finally, computational study on the charge transfer characteristics of **DH1** and **DH2** revealed that the dimensionality of charge transport network impacts the hole mobility in disordered morphology.

Introduction

Controlling the molecular packing of aromatic compounds in crystalline state is an essential issue for functional materials.[1] From this perspective, planar and nonplanar polyaromatic compounds mutually show contrasting properties (Figure 1). Planar aromatics such as acenes, phenacenes, and rylenes tend to exhibit strong π–π stacking since the planar π-surfaces overlap with each other.[2] However, the molecular packing of polycyclic aromatic hydrocarbons (PAHs) is difficult to control precisely and is limited to either the herringbone (CH–π dominant) or lamellar (π–π dominant) structures. Nonplanar aromatics such as [*n*]circulenes ($n \neq 6$)[3] and helicenes[4] possess curved and twisted π-surfaces. While nonplanar molecules show a variety of fascinating molecular packing with respect to planar ones, the curved π-electron system often disturbs π–π stacking, which is indispensable for self-assembling or semiconducting materials utilizing the intermolecular electronic interaction.[5] To achieve the π–π overlap, [*n*]circulenes ($n \neq 6$) are required to stack in a one-dimensional manner to fit their curvature completely. As for conventional helicenes, only partial π–π stacking is usually observed. Hence, it is important to uncover unconventional molecular packing that maintain π–π stacking in order to discover the unexplored functionalities of nonplanar aromatic systems in crystalline state.

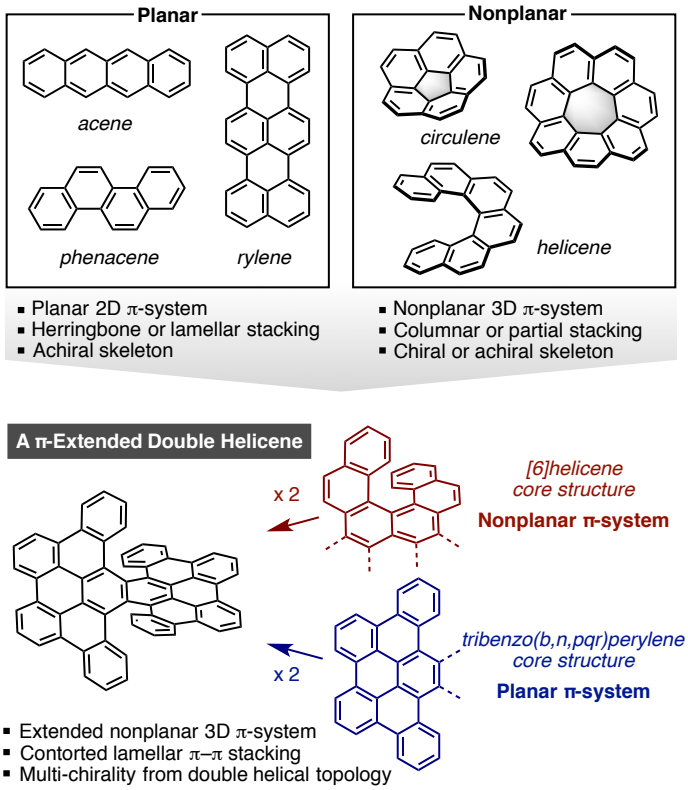

Figure 1. Features of planar and nonplanar π-systems, and π-extended double [6]helicenes.

This chapter describes the synthesis, crystal structures, and properties of π-extended double [6]helicenes (**DH1** and **DH2**) bearing concatenated two planar tribenzo[*b,n,pqr*]perylene substructures with fully-conjugated double [6]helicene substructures, a combination of planar and nonplanar π-systems. Despite the nonplanar π-systems of **DHs** as entire structures, their relatively planar π-blades realized large π–π overlap among neighboring molecules in the crystal. Studying the chemistry of **DHs** is considered to be a good starting point to explore a new area that merges the aspects of planar and nonplanar aromatics. As one of such example, theoretical prediction of hole transport properties of **DH1** and **DH2** was performed by using a method rooted in Marcus theory and kinetic Monte Carlo simulations (Figure 2). Therein, a direct link between the morphology, transport connectivity, and hole mobilities was established.

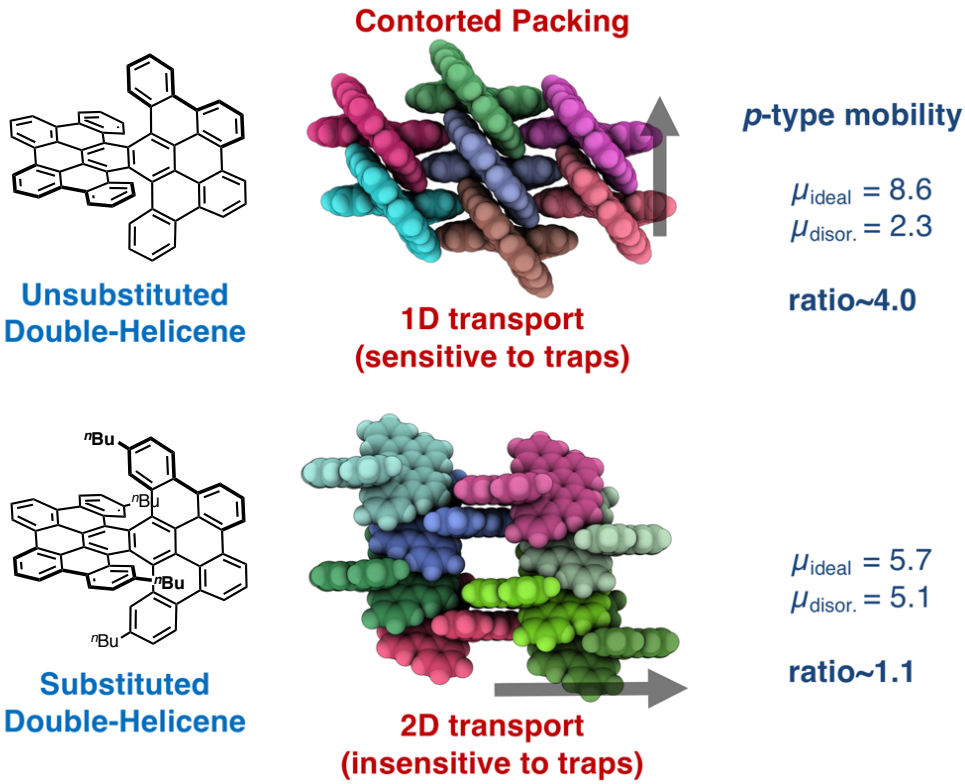

Figure 2. Impact of transport network on charge transport properties.

Result and Discussion

Synthesis of π-Extended Double [6]Helicenes

Two synthetic routes for **DH1** were developed; a step-economical C–H activation route[6] and a Suzuki–Miyaura coupling route (Scheme 1). At the beginning, Pd(II)/*o*-chloranil catalytic method[7] was applied to allow the rapid installation of biphenyl units onto naphthalene by C–H arylation. Naphthalene was treated with tris(*o*-biphenylyl)boroxine in the presence of $Pd(OAc)_2$ and *o*-chloranil to afford a complex mixture containing regioisomers of fourfold biphenylated naphthalene **1**. The formation of **1** was confirmed by mass spectroscopy. Although the exact structures and isomer ratio of **1** could not be determined, treatment of the mixture with DDQ in 1,2-dichloroethane/TfOH successfully promoted the Scholl reaction to afford **DH1**.[8,9] Unfortunately, the yield was too low to be practical (1% yield in two steps from naphthalene).

Thus, to obtain sufficient amounts of **DH1**, synthetic approach was switched to a classical Suzuki–Miyaura coupling route. Commercially available 2,7-dihydroxynaphthalene was converted to 3,6-dibromonaphthalene-2,7-diyl bis(trifluoromethanesulfonate) (**2**) by using the reported bromination-triflation procedure (56% yield in three steps).[10] Next, a fourfold Suzuki–Miyaura coupling reaction of **2** with *o*-biphenylylboronic acid in the presence of $Pd_2(dba)_3$, 2-dicyclohexylphosphino-2',6'-dimethoxybiphenyl (SPhos), and Cs_2CO_3 provided 2,3,6,7-tetrabiphenylylnaphthalene (**3**) in 84% yield. The final Scholl reaction of **3** with DDQ (7 equiv) in 1,2-dichloroethane/TfOH at 0 °C afforded **DH1** as a red solid in 64% yield.[8,9] Unlike the Scholl reaction for the synthesis of WNG,[11] a seven-membered ring was not formed in this reaction. **DH1** is expected to exist as three isomers: the twisted (*P*,*P*)- and (*M*,*M*)-enantiomers and the (*P*,*M*)-isomer as the meso form. ^{1}H NMR spectra of the isomeric mixture of **DH1** indicated the existence of two different species, which was assigned as *twisted*-**DH1** and *meso*-**DH1** (in a 43:57 ratio).

Scheme 1. Synthesis of **DH1**.

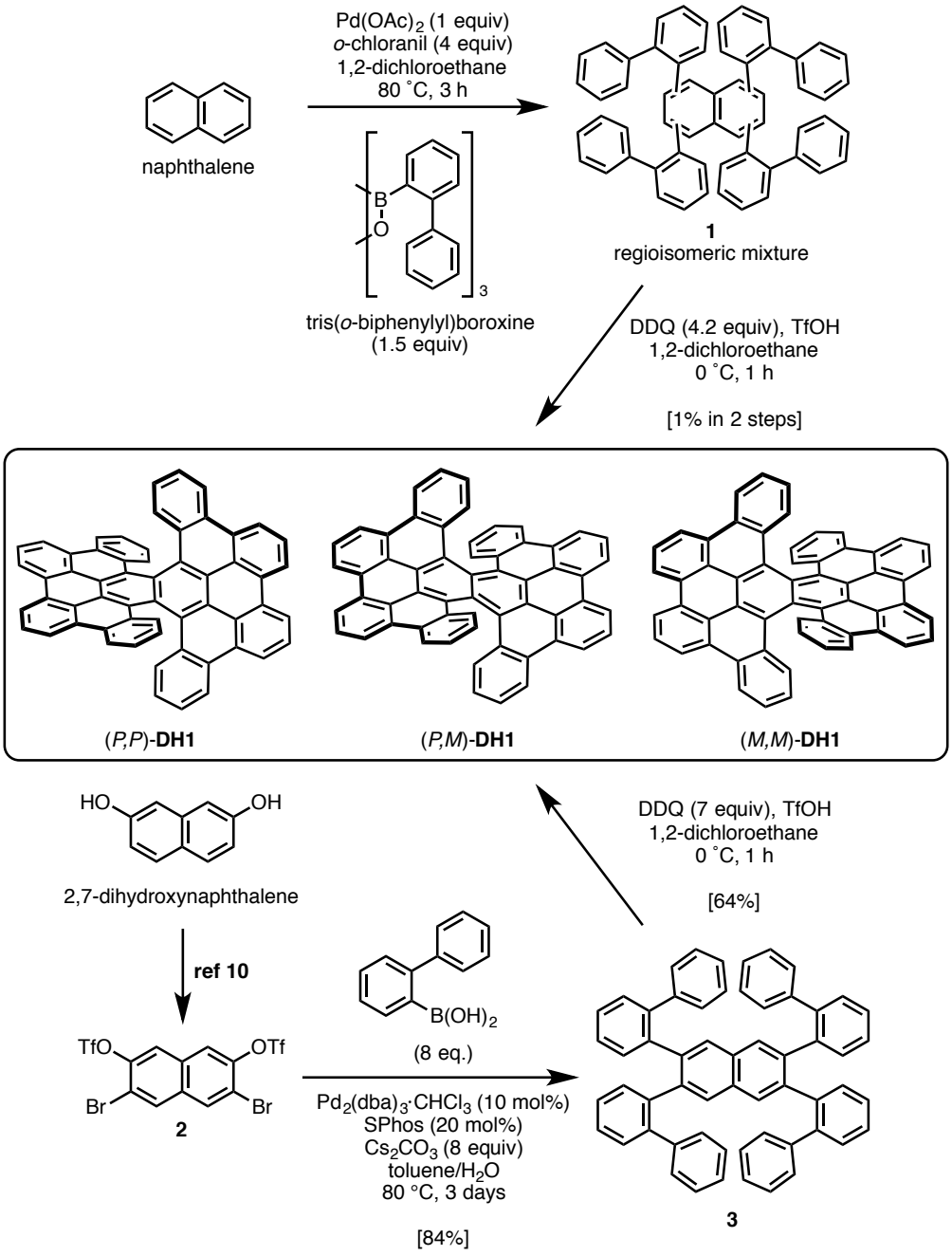

Contrary to the trend that nonplanar π-systems showed high solubility to organic solvents, **DH1** exhibited a poor solubility which is detrimental to evaluation of properties. Hence, a *n*-butyl-substituted derivative **DH2** was also synthesized in a similar procedure with that of **DH1** (Scheme 2). 2,3,6,7-Tetrakis(4'-butyl-[1,1'-biphenyl]-2-yl)naphthalene (**5**), an analogous compound of **3**, was prepared by a fourfold Suzuki–Miyaura coupling reaction of (4'-butyl-[1,1'-biphenyl]-2-yl)boronic acid (**4**) with **2** in 88% yield. The subsequent oxidative stitching in the presence of $MoCl_5$ afforded the twisted isomer of **DH2**, *i.e.*, (*P,P*)-**DH2** and (*M,M*)-**DH2**, in 13% yield. In contrast to the synthesis of **DH1**, the *meso*-isomer of **DH2**, *i.e.*, (*P,M*)-**DH2**, was not detected. It was suspected that the formation of the *meso*-isomer is unfavorable under the applied oxidative reaction conditions, and that the *twisted*-isomer was therefore obtained exclusively.

Scheme 2. Synthesis of **DH2**.

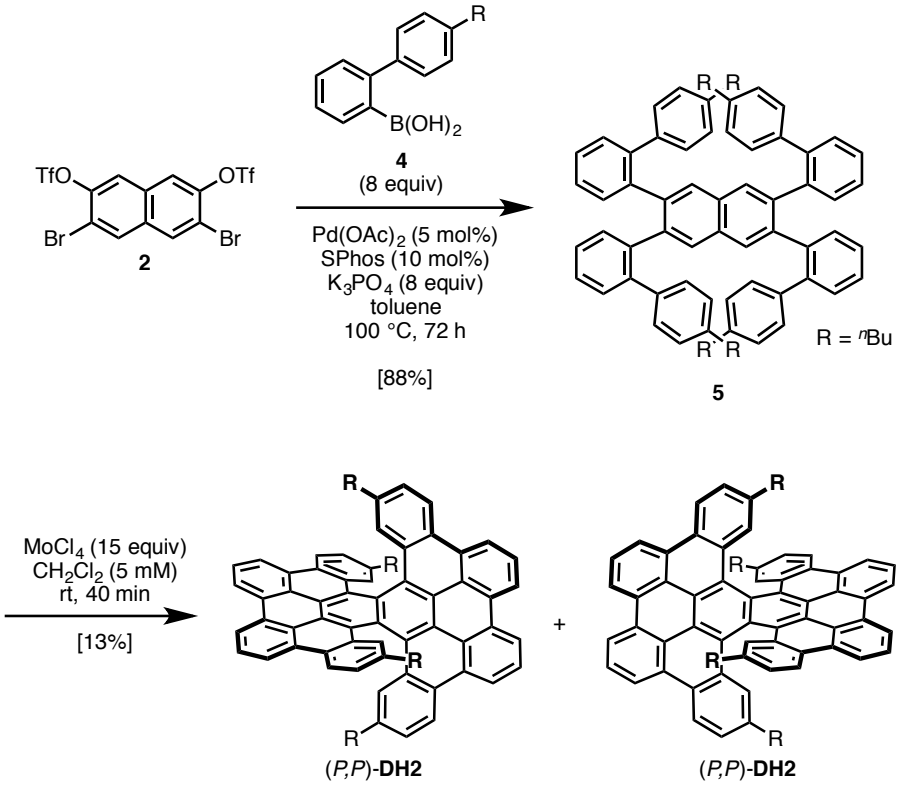

Structures and Molecular Packings of DHs

The two-blade propeller structure of *twisted*-**DH1** and *twisted*-**DH2** were unambiguously confirmed by X-ray crystallography using racemic single crystals (Figures 3a,e). A single crystal of **DH1** was recrystallized from a CS_2 solution of an isomeric mixture via slow addition of *n*-hexane vapor at room temperature. A single crystal of **DH2** was recrystallized from a chloroform solution of the *twisted*-isomer via slow addition of *n*-pentane vapor at room temperature. The X-ray crystal structure of **DHs** confirms an extended doubly-twisted π-system.

The twisting distortion of **DH1** and **DH2** in the crystal was determined using the dihedral angles of the mean planes of the two π-blades (**1**: 47.2°; **2**: 52.0°). Theoretically, on the B3LYP/6-31G(d) level of theory, twisting distortion of 46.6° was estimated for the optimized structures of **DH1** and the methyl analog of **DH2**. Considering that the theoretical predictions suggest that a substitution with alkyl groups should hardly affect the molecular geometry, the larger distortion of **DH2** compared to **DH1** in the crystals was tentatively assigned to the difference in the molecular packing structures and the associated intermolecular interactions. These profound distortions of the π-system gave rise to unique multi-dimensional stacking structures, where **DH1** and **DH2** aggregate in distinguishable molecular packings in each other.

In the crystal of **DH1**, the (*P*,*P*)- and (*M,M*)-isomers tightly arrange themselves in an offset stacking array so that no solvent molecule was present inside the crystal (Figures 3b–d). Although planar π-conjugated molecules tend to adopt herringbone or lamellar packing structures,[2] it is difficult to categorize the crystal packing of *twisted*-**DH1** in these typical patterns, as **DH1** displays a contorted three-dimensional lamellar packing structure.[1b,1e] Homochiral molecular layers of each enantiomer lying on the *ac* plane (Figure 3c) alternately laminate along the *b*-axis (Figures 3b,d), in which unilateral blades in a homochiral layer fill the gaps of the adjacent enantio-homochiral layer. Inside the homochiral layer, slipped π–π stacking is observed along the *c*-axis. In addition, heterochiral stacking exhibits π–π stacking over different homochiral layers. Consequently, in contrast to one- or two-dimensional stacking of planar π-system, the crystal of *twisted*-**DH1** has three-dimensional electronic interactions exhibiting the unconventional molecular packing by exploiting the virtues of "planarity" and "nonplanarity".

Unlike **DH1**, a two-dimensional stacking was observed in the crystals of **DH2**, whereby molecules of *n*-pentane were inserted within the stacks (Figures 3f,g). Two types of π–π stackings can be distinguished: one forms a slipped one-dimensional heterochiral stacking along the *a*-axis, while the other connects the adjoining aforementioned slipped π–π stacking in the direction of the *b*-axis. Consequently, a two-dimensional stacking layer spreads over the *ab*-plane, and the *n*-butyl groups fill the gap between neighboring layers, thus preventing electronic in-

teractions along the *c*-axis.

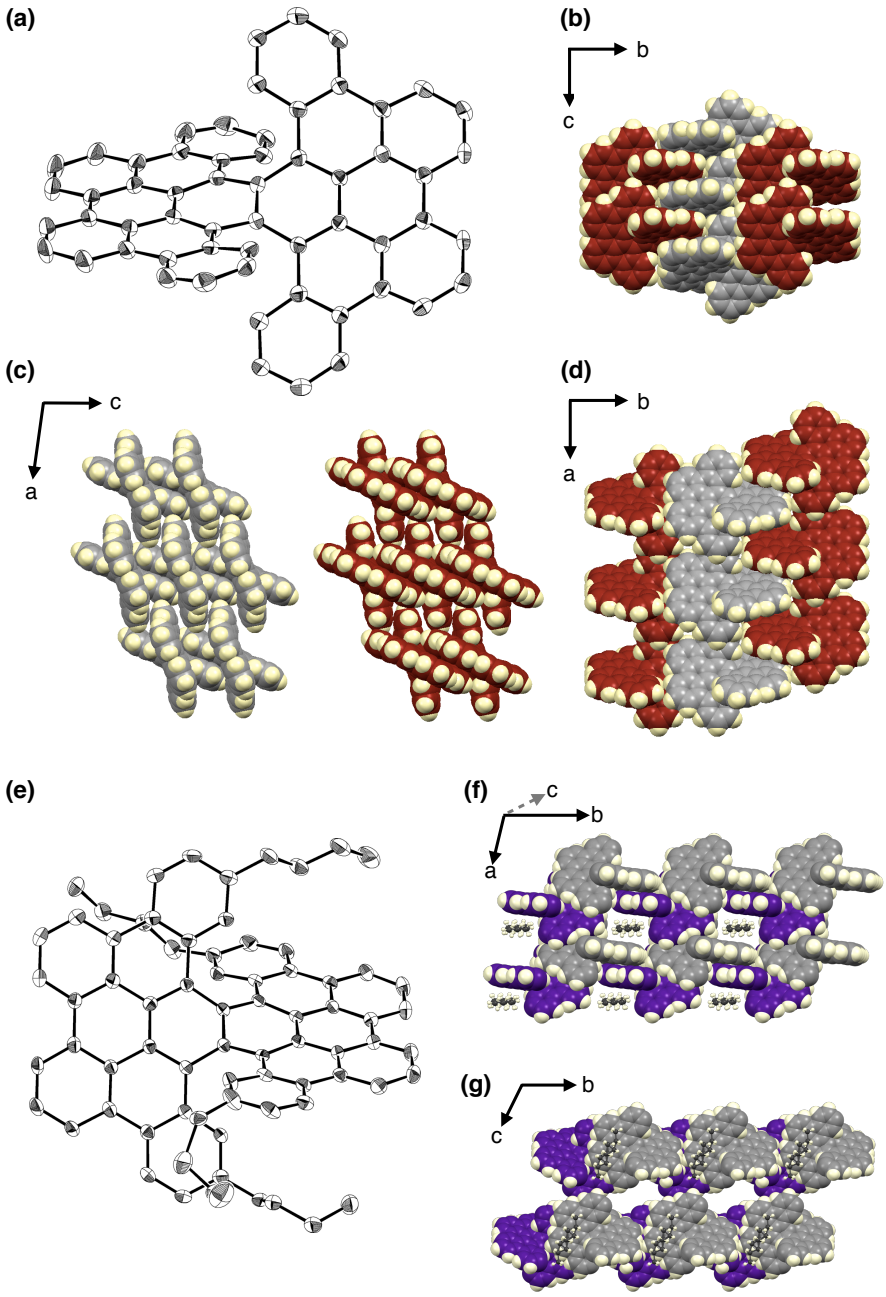

Figure 3. ORTEP drawing of (a) (*P*,*P*)-**DH1** and (b) (*M*,*M*)-**DH2** with 50% probability (hydrogen atoms are omitted for clarity; the minor part of the disordered moieties and *n*-pentane molecule are also omitted for **2**). Packing structures of (b)–(d) **DH1** and (f), (g) **DH2** (π-skeletons and *n*-pentane molecules are depicted as a space-filling model and a ball-and-stick model, respectively; *n*-butyl groups of **DH2** are omitted for clarity; (*P*,*P*)-isomers of **DH1** and **DH2** are colored in red and purple, respectively, and (*M*,*M*)-isomers of **DH1** and **DH2** are colored in gray).

Isomerization, Separation, and CD Spectra of the Isomers of DH1

To uncover the thermodynamic stability and dynamic behavior of the *twisted*- and *meso*-isomers, DFT calculations of the interconversion process of **DH1** was performed at the B3LYP/6-31G(d) level (Figure 4a). From these calculations, it was estimated that *twisted*-**DH1** is thermodynamically more stable than *meso*-**DH1** by 0.9 kcal·mol^{-1}. The *twisted*-to-*meso* interconversion process was found to proceed through a transition state with face-to-face oriented terminal aromatic rings of [6]helicene substructure.[12] The calculated isomerization barrier (43.5 kcal·mol^{-1}) was considerably higher than that of [6]helicene (37.3 kcal·mol^{-1}, Figure 4b), and comparable with that of [7]helicene (41.7 kcal·mol^{-1}).[13] As described in some literatures,[14] isomerization barriers of double helicenes are known to be higher than those of single helicene substructures.

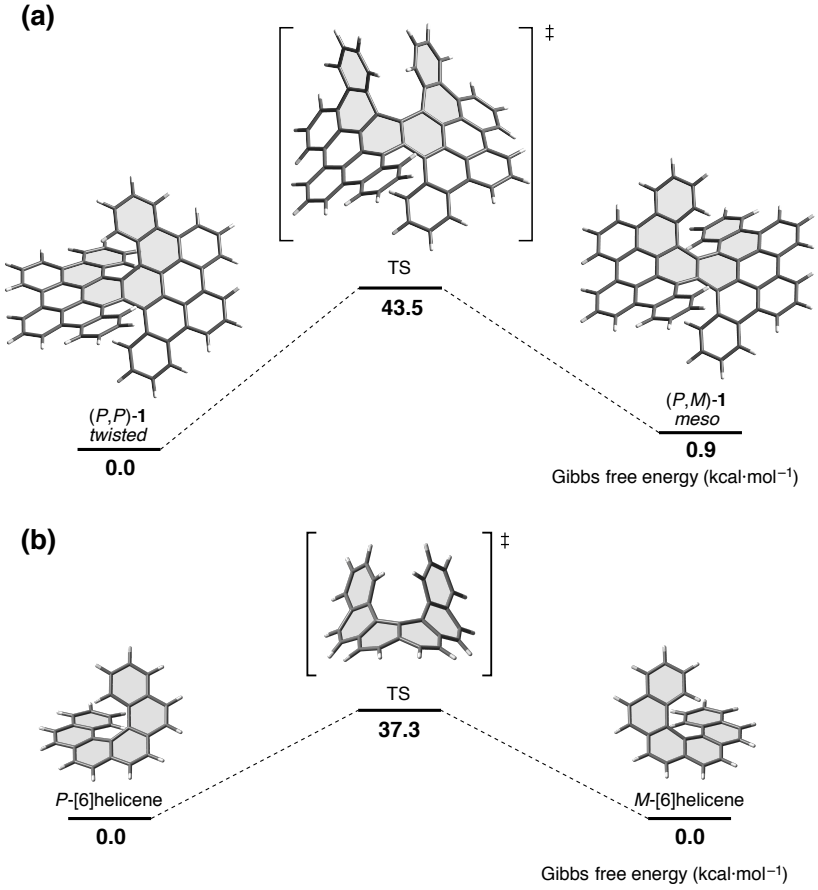

Figure 4. The isomerization (a) between (*P*,*P*)-**DH1** and (*P*,*M*)-**DH1**, and (b) between *P*-isomer and *M*-isomer of [6]helicene.

The very high isomerization barriers between the isomers prompted us to separate these isomers. After extensive investigation, it was found that the three isomers could be separated by a chiral HPLC (column, CHIRALPAK IF; eluent, *n*-hexane/chloroform = 3:7) (Figure 5a).

While the poor solubility of a mixture of **DH1** to general organic solvents (*e.g.*, chloroform, 0.15 g/L; carbon disulfide, 0.60 g/L; *n*-hexane, insoluble) hampered separation of quantitative amount of each isomer upon HPLC separation, enantiopure *twisted*-**DH1** showed increased solubility to organic solvents compared with the racemic sample. Note that enantiopure *twisted*-**DH1** is soluble to *n*-hexane even though there is no applicable value on solubility. Judging from the good agreement of the CD spectra with the simulated ones by TD DFT calculations (B3LYP/6-31G(d)), the three peaks in the chiral HPLC were suggested to be (*P*,*P*)-**DH1** (1st peak), (*M*,*M*)-**DH1** (2nd peak), and (*P*,*M*)-**DH1** (3rd peak) (Figure 5b). Unlike the large optical rotation of (*P*)-[6]helicene ($[\alpha]^{25}_{D}$ = +3707°),[15] tentatively assigned (*P*,*P*)-**DH1** showed much smaller and opposite optical rotation ($[\alpha]^{20}_{D}$ = −81°, *c* 0.0036, chloroform). Comparison of CD spectra of (*P*)-[6]helicene[16] and (*P*,*P*)-**DH1** also suggested no clear correlation of π-conjugated double [6]helicene substructure of **DH1** and pristine [6]helicene on chiroptical properties.

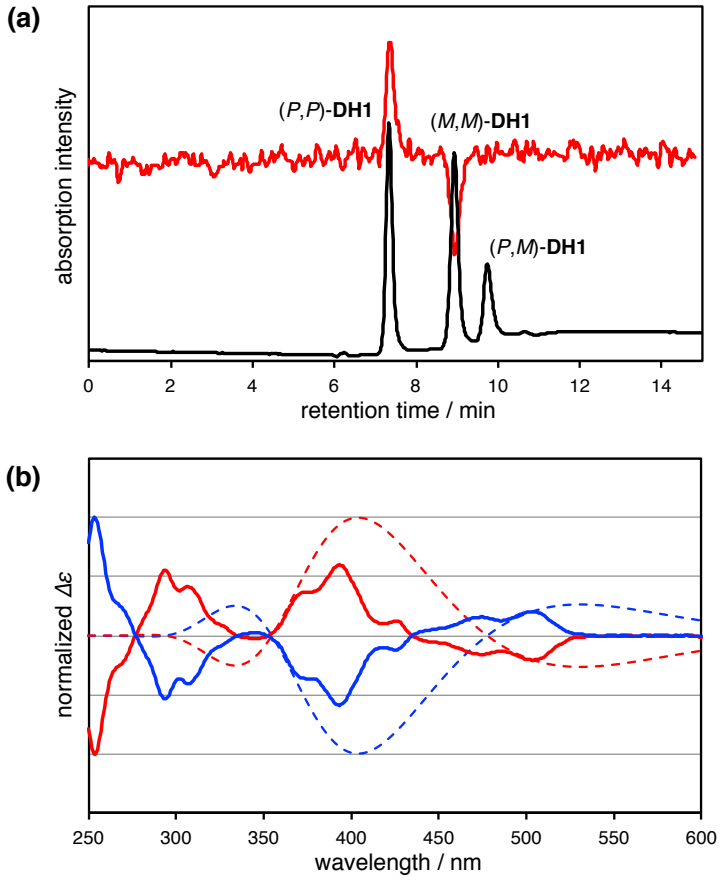

Figure 5. (a) Chiral HPLC of **DH1** eluted by *n*-hexane/chloroform (3:7) using CHIRALPAK IF (black line: absorption intensity at 400 nm; red line: optical rotation). (b) CD spectra of the first peak (red solid line) and the second peak (blue solid line), and simulated ones of (*P*,*P*)-**DH1** (red dashed line) and (*M*,*M*)-**DH1** (blue dashed line) at the B3LYP/6-31G(d) level of theory.

The diphenyl ether solution of *meso*-isomer enriched **DH1** was heated at various temperatures and analyzed periodically by HPLC. As expected from the DFT calculation, the *twisted-meso* interconversion (isomerization) does not occur below 200 °C. At higher temperatures over 230 °C (Figure 6), absorption intensities of *twisted*-**DH1** (the two faster peaks) gradually increased and that of *meso*-**DH1** (the third peak) decreased inversely. Unfortunately, experimental value of the isomerization barrier could not be determined due to the low quality of data and competitive decomposition reaction.

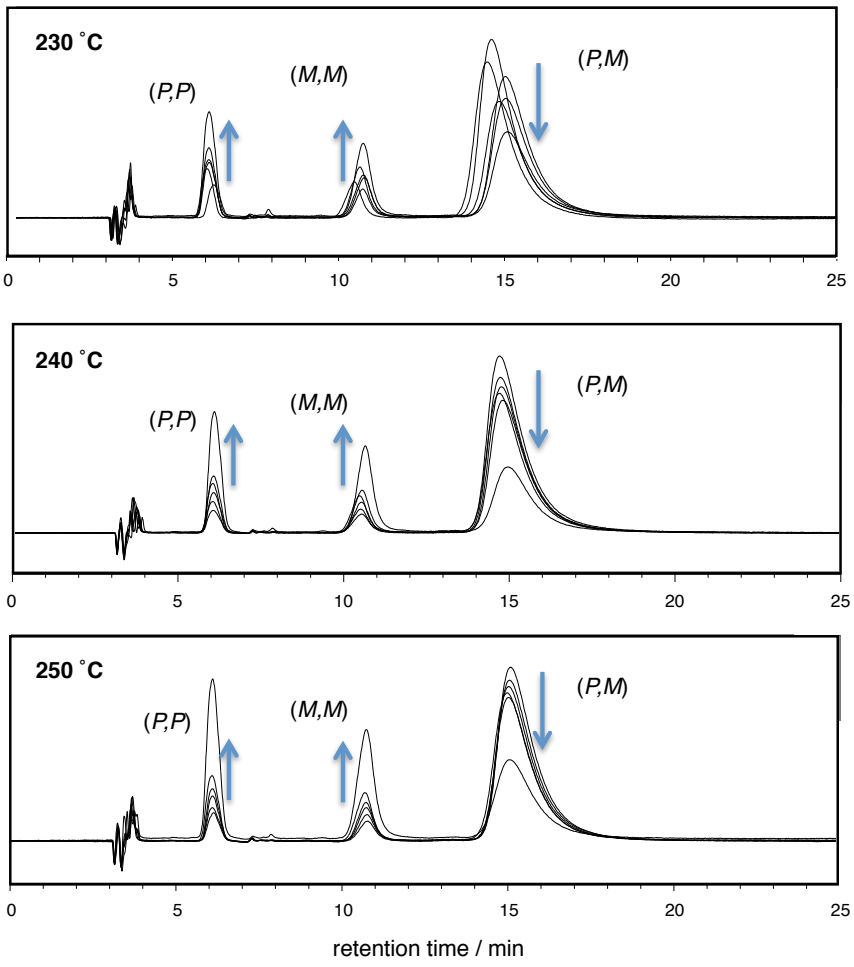

Figure 6. Examination of thermal isomerization of **DH1** at elevated temperature. Allows indicate the change of absorption intensities of each peak upon heating time (230 °C: 0, 2, 4, 6, 8, 10 h; 240 °C: 0, 40, 80, 120, 160, 200 min; 250 °C: 0, 20, 40, 60, 80, 100 min).

Electronic Structures of DHs

The photophysical properties of *twisted*-**DH1**, *meso*-**DH1**, and *twisted*-**DH2** were measured in chloroform to elucidate the effect of the molecular geometry difference and *n*-butyl group substitution on the electronic state of **DHs** (Figure 7). Finger-shaped absorption spectra with clear vibronic structures as observed in typical PAHs were obtained in each case. *Twisted*-**DH1** has longer maxima at 506, 476 and 450 nm, and the sharpest maximum at 401 nm. Meanwhile, *meso*-**DH1** shows similar but blue-shifted absorption spectrum with the longer maxima at 491, 460 and 434 nm, and the sharpest maximum at 382 nm. A blue shift was also observed in the fluorescence spectrum of *meso*-**DH1** (λ_{em} = 498 nm) compared to that of *twisted*-**DH1** (λ_{em} = 528 nm). Intriguingly, *meso*-**DH1** fluoresces much more efficiently than *twisted*-**DH1** (*twisted*-**DH1**: Φ_F = 0.052; *meso*-**DH1**: Φ_F = 0.42). Fluorescence lifetimes (τ_s) of *twisted*-**DH1** and *meso*-**DH1** were 1.6 ns and 6.5 ns, respectively. According to the equations, $\Phi_F = k_r \times \tau_s$ and $k_r + k_{nr} = \tau_s^{-1}$, the radiative ($k_r$) and nonradiative ($k_{nr}$) decay rate constants from the singlet excited state were determined (*twisted*-**DH1**: $k_r = 3.3 \times 10^7$ s^{-1}, $k_{nr} = 5.9 \times 10^8$ s^{-1}; *meso*-**DH1**: $k_r = 6.5 \times 10^7$ s^{-1}, $k_{nr} = 8.9 \times 10^7$ s^{-1}). Judging from this result, the difference of fluorescence quantum yields between two diastereomers was mainly attributed to the rigidness of π-skeleton, which affects the rate of nonradiative decay. Namely, the molecular geometry of *meso*-isomer maybe more rigid than that of *twisted*-isomer, suppressing a thermal deactivation from the excited state. Conversely, the unclear vibronic structure in fluorescence spectra and the superior absorption coefficient of 0–1 transition (475 nm) than that of 0–0 transition (506 nm) of *twisted*-**DH1** inferred its structural flexibility. The smaller Stokes shifts of *meso*-**DH1** (5 nm, 206 cm^{-1}) than that of *twisted*-**DH1** (19 nm, 716 cm^{-1}) also supports the rigidness of former isomer.

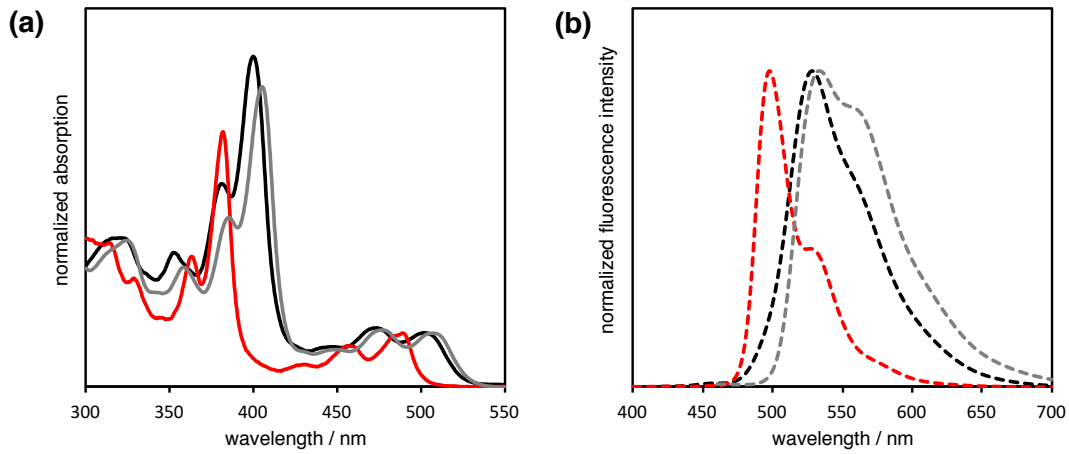

Figure 7. (a) UV–Vis absorption spectra and (b) fluorescence spectra of *twisted*-**DH1** (black lines), *meso*-**DH1** (gray lines), and *twisted*-**DH2** (red lines) in chloroform solution.

The UV–Vis absorption spectrum of *twisted*-**DH2** is almost identical to that of *twisted*-**DH1**, exhibiting longer maxima at 507, 477 and 450 nm, and the sharpest maximum at 405 nm. On the other hand, the fluorescence spectrum of *twisted*-**DH2** shows clearer shoulder emission at around 560 nm with maximum at 534 nm. There is no significant difference in fluorescence quantum yield between *twisted*-**DH1** (Φ_F = 0.052) and *twisted*-**DH2** (Φ_F = 0.059).

In order to understand the nature of absorption, a TD DFT study of *twisted*- and *meso*-**DH1** was performed at the B3LYP/6-31G(d) level. The energy diagrams of the dominant excitations are depicted in Figure 8. In the case of *twisted*-**DH1**, it was estimated that longer-wavelength maxima at around 500 nm are characterized by a large contribution of HOMO→LUMO and a small contribution of HOMO−1→LUMO+1 transition (S_1, 517 nm, f_{calc} = 0.1475), and the sharpest maximum (401 nm) is characterized by almost equal contributions of HOMO−1→LUMO and HOMO→LUMO+1 transitions (S_4, 401 nm, f_{calc} = 0.8786). On the other hand, the longer-wavelength maxima at around 490 nm in the absorption of *meso*-**DH1** are characterized by a large contribution of HOMO→LUMO and a small contribution of HOMO−2→LUMO+2 transition (S_1, 503 nm, f_{calc} = 0.1704). The sharpest maximum (382 nm) is characterized by almost equal contributions of HOMO−2→LUMO and HOMO→LUMO+2 transitions (S_6, 384 nm, f_{calc} = 0.9034). The origin of the spectral shift was estimated by the calculated spatial distribution and the molecular energy, which suggested that *twisted*-**DH1** has low-lying LUMO and LUMO+1 orbitals and a high-lying HOMO−1 compared with the corresponding molecular orbitals of *meso*-**DH1** (LUMO, LUMO+1 and HOMO−1 of *twisted*-**DH1** correspond to LUMO, LUMO+2 and HOMO−2 of *meso*-**DH1**, respectively).

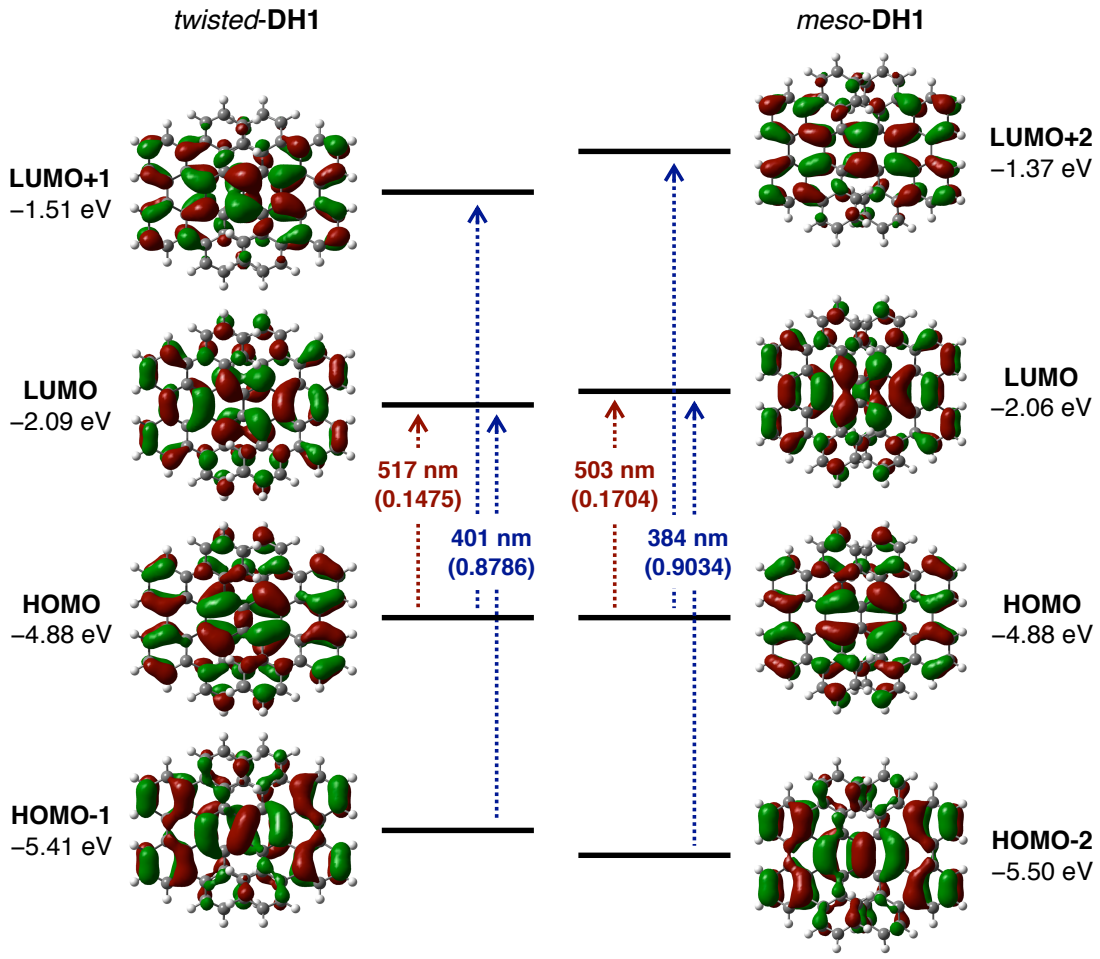

Figure 8. Energy diagrams of *twisted*-**DH1** and *meso*-**DH1** calculated at the B3LYP/6-31G(d) level of theory. Excitation energies were computed by TD DFT at the same level. Values in parentheses represent the oscillator strengths (*f*).

Theoretical Prediction of Hole-Transport Properties of DHs

π-Conjugated molecules displaying unique molecular packings have been of interest in the field of organic semiconductor. From this perspective, **DH1** and **DH2** would be a good model for investigating the impact of morphology on the charge-transport properties as they have similar electronic structures in each other and display different molecular packings in the crystal (Figure 3). Herein, kinds of parameters related to the charge-transport were calculated for perfect order and disordered **DHs** crystal systems by employing a method rooted in Marcus theory and kinetic Monte Carlo simulations.

Molecular dynamics simulations of positional disorder of crystalline state

At the beginning, room temperature molecular dynamics (MD) simulations were performed to predict structural order in **DH1** and **DH2** in the solid state. In order to quantify the effect of temperature on the structures, the root-mean-square deviation (RMSD) of the change in the center of masses of each molecule against experimental structures were calculated from a single MD snapshot. The RMSD of **DH1** was found to be 0.73 Å, while that of **DH2** was 1.28 Å. To account for the influence of *n*-butyl side-chains, RMSD of **DH2** with the exclusion of alkyl side-chains was also calculated and a value of 0.88 Å was obtained, which is still higher than but closer to that of **DH1**. The average RMSD over individual molecules is ~0.2Å for both **DH1** and **DH2**, indicating that the RMSD deviation is largely due to relative orientations of the molecules and highlighting the significance of the unique packing arrangements of the two **DHs**.

In order to quantify the positional disorder between neighboring molecules, the paracrystallinity parameter *g* along the strong π–π stacking directions, defined as $g = s/\langle d \rangle$, were calculated, where *d* is the distance between neighboring molecules exhibiting strong π–π stacking (the stacking along the *c*-axis for **DH1** and along the *a*-axis for **DH2**), *s* is the standard deviation of an ensemble of *d* distances and <…> represents an ensemble average.[17] Studies have shown that *g*~0-1% corresponds to a nearly perfect order and g~1-10% corresponds to crystalline order.[17a] Paracrystallinity parameters for **DH1** and **DH2** are calculated to be 1.7% and 2.2%, respectively, suggesting that **DH2** is structurally more disordered, which is consistent with the RMSD analysis.

Charge-transport parameters

In order to probe the differences in charge transport, a number of parameters including reorganization energy, electronic-coupling, and energetic disorder of **DH1** and **DH2** were calculated. Pentacene and rubrene were employed as benchmark systems to compare

charge-transport parameters with those of **DHs**. The reorganization energy λ is an intrinsic property of the system that quantifies energetic changes due to structural variations between ground and excited state structures. Gas phase optimizations of **DH1** and **DH2** were performed to calculate λ according to the four-point rule. Reorganization energies are very similar for **DH1** and **DH2** (λ = 117 and 122 meV, respectively), indicating that the addition of side-chains have negligible influence on λ due to the inherently similar core structures. The reorganization energies of the **DHs** are comparable to those of pentacene and rubrene (λ = ~100 and 160 meV, respectively), both of which have shown highly efficient charge transport in thin film transistors.

Next, the variations in site-energy difference distributions in the equilibrated morphologies from MD was investigated, which are often used to predict energetic disorder.[18] The width of the site-energy difference distributions is similar for **DH1** and **DH2**; however, the standard deviation, i.e., energetic disorder σ, of **DH1** (50 meV) is higher than of **DH2** (44 meV) (Figure 9). These values are systematically lower than the typical σ values calculated for rubrene and pentacene using the same methodology. For example, energetic disorder of pentacene and rubrene are predicted to be 68 and 53 meV, respectively.[19] Energetically, **DH1** and **DH2** are both ordered, which is favorable for efficient charge-transport.

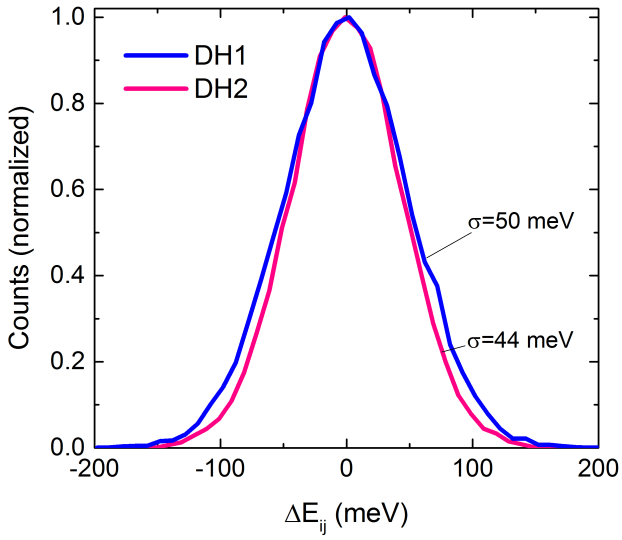

Figure 9. Site-energy difference distribution of **DH1** and **DH2**. Standard deviations, i.e., energetic disorders (σ) are indicated.

The electronic coupling values between center-of-masses in perfect crystal **DH1** and **DH2** were calculated using ZINDO (Figure 10). Electronic coupling (*J*) values in the strong π-π stacking direction are high for both **DH1** and **DH2** (58 meV and 73 meV, respectively). The

ZINDO-calculated *J* values in the π–π stacking direction of pentacene and rubrene are ~60 and 80 meV, respectively.[20] Similar to the λ values, *J* values of both **DH1** and **DH2** are comparable to high mobility pentacene and rubrene and indicative of high charge-transport performance. Electronic coupling determines charge-transport propensity. Thus, the transport pathway of **DH1** is predominantly one-dimensional while the transport pathway of **DH2** is alternating.

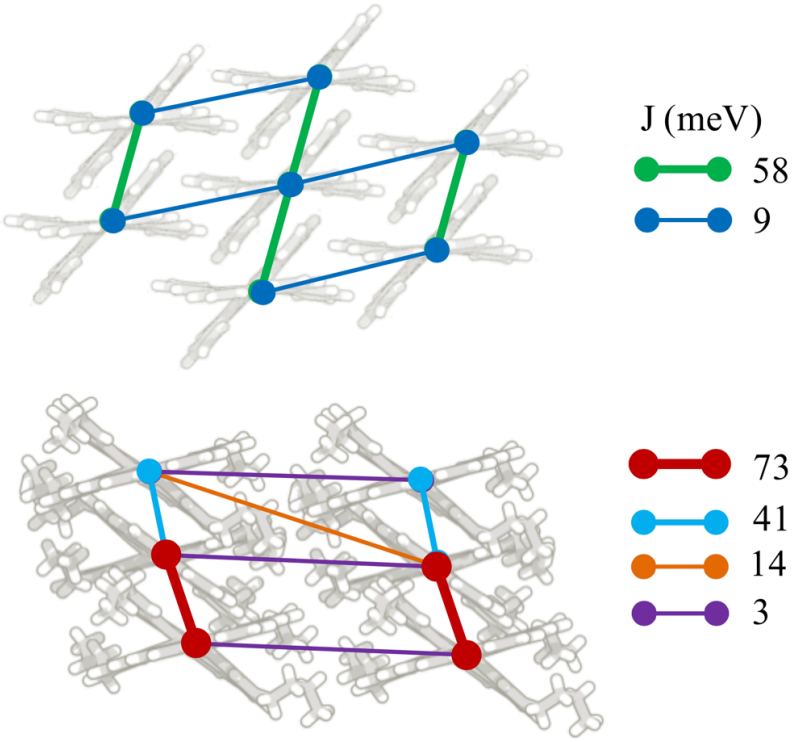

Figure 10. Perfect crystal packing motifs and transport pathways of **DH1** (top) and **DH2** (bottom).

Mobility calculations

Finally, using the calculated charge transport parameters, hole mobilities of **DH1** and **DH2** were predicted based on the perfect order crystal system obtained from XRD analysis and disordered crystal systems obtained from MD simulations. The summary of prominent charge-transport parameters along with the hole mobilities of **DH1** and **DH2** are given in Table 1. The results are compared with those of high mobility pentacene and rubrene, where the parameters were calculated using the same method. First, hole mobilities from the unit-cells were calculated, where hypothetically perfect order was considered ($g = 0$, $\sigma = 0$). As discussed earlier, reorganization energies of **DH1** and **DH2** are similar and the electronic coupling of **DH1** is weaker than **DH2**. However, the predicted hole mobility of **DH1** (8.6 cm^2/Vs) is higher than that of **DH2** (5.7 cm^2/Vs), which is surprising since the charge-transfer rate is proportional to

J^2. Charge-transfer rates are consistent with the resulting hole mobilities for all but **DH2**, which is likely due to its transport connectivity. In **DH1**, pentacene, and rubrene, charge transfer is confined to a single direction, while the transfer travels in two directions for **DH2** (Figure 10). In a defect-free ideal crystal, an alternating pattern in charge transport results in a decrease in the charge-carrier's net velocity, which is related to the lower hole mobility. If a charge-carrier is formed in a hopping site where transfer to the surrounding sites is unfavorable, the probability for the carrier to oscillate in the site and remain stagnant, causing an overall decrease in hole mobility.

Table 1. Summary of charge-transport parameters for **DH1**, **DH2,** pentacene, and rubrene. Reorganization energy (λ), electronic coupling (J), and energetic disorder (σ) are in units of meV. Marcus charge-transfer rate (k), paracrystallinity parameter (g), and hole mobility (μ) are in units of $psec^{-1}$, %, and cm^2/Vs, respectively.

		perfect crystal				Crystalline			
		λ	$J_{\pi-\pi}$	$k_{\pi-\pi}$	μ	g	$\langle J_{\pi-\pi}\rangle$	σ	μ
DH1		117	58	53	8.6	1.7	49	50	2.3
DH2	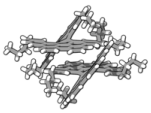	122	73	78	5.7	2.2	72	44	5.1
pentacene		95	61	81	15.6	2.5	32	68	0.7
rubrene		160	81	58	11.6	1.5	75	53	1.9

However, the situation is dramatically different for the case of crystalline morphologies. Starting supercells were equilibrated in MD simulations, generating slight positional disorder. Due to positional and energetic disorder, hole mobilities of **DH1** and **DH2** decreased (2.3 cm^2/Vs and 5.1 cm^2/Vs, respectively). Therein, while the hole mobility of **DH1** decreased roughly by a factor of four relative to its perfect order hole mobility, that of **DH2** was only slightly affected by positional and energetic disorder. Moreover, although the perfect order hole mobility of **DH2** was the lowest among the molecules in Table 1, crystalline hole mobility was the highest, which is close to its single crystal value.

In order to understand disproportionate changes in the predicted crystalline hole mobilities

of **DH1** and **DH2** due to the inclusion of disorder, connectivity graphs showing the transport networks in a single MD snapshot were plotted (Figure 11). The center-of-masses of **DH1** and **DH2** are represented by green and blue spheres, respectively, and electronic couplings between these sites (where $J > 20$ meV) are represented by the red lines. For **DH1**, connectivity is mostly in the *y*-*z* plane (with some in the *x*-*y* direction) and thus transport network is mainly one-dimensional. Even though there is a strong charge transport path along one direction in **DH1** ($\langle J \rangle = 46 \pm 13$ meV), the system is sensitive to charge-trapping due to positional disorder. On the other hand, the transport of **DH2** is largely two-dimensional. Although the diverse connectivity in a perfect order crystal is unfavorable for charge-transport as discussed earlier, it is beneficial in its crystalline morphology, as a charge-carrier can easily bypass a trap-state by following other favorable paths. This finding is in line with the previous studies on conjugated organic polymers. Noriega *et al.* showed that the requirement for high mobility in conjugated polymers was the presence of interconnected aggregates rather than an increase in crystallinity.[17c] Molecular dynamics simulations by Jackson *et al.* also indicated that conformationally-disordered polymers can result in efficient devices due to the ability of the polymers to form local molecular ordering, which is of higher importance than long-range crystallinity.[21] Similarly, although crystalline **DH2** shows high positional disorder, its ability to form interconnected hopping sites allow for high mobility. Molecules having a diverse transport paths like **DH2** are promising crystalline organic materials and potentially may have one of the highest hole mobilities as an organic semiconductor that can readily be implemented in both single crystal and thin film technology.

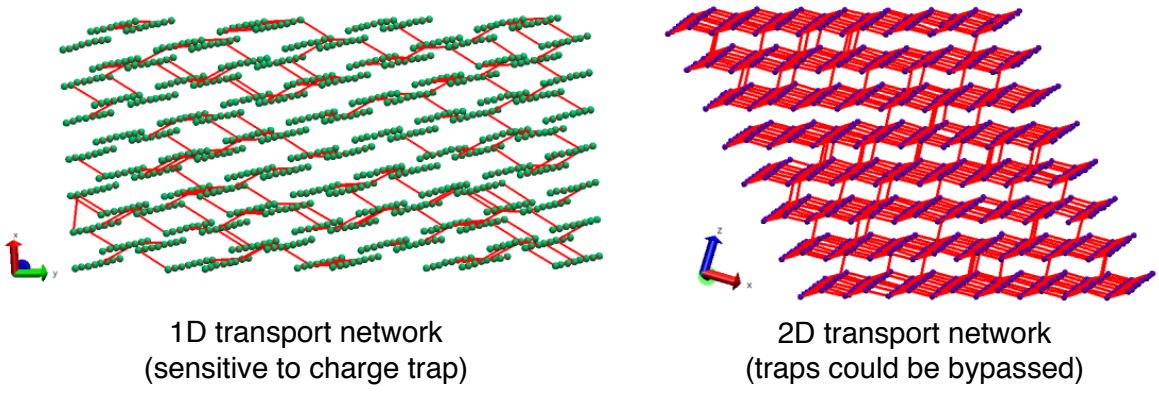

Figure 11. Connectivity graphs presenting the transport networks of crystalline **DH1** (left) and **DH2** (right). Green and blue spheres indicate the center-of-masses of **DH1** and **DH2**, respectively, and, connection colored in red represent electronic coupling between neighboring pairs. Only electronic coupling values of $J > 20$ meV are included in connectivity graphs.

Conclusion

In this chapter, the short-step synthesis of new π-extended double [6]helicenes (**DH1** and **DH2**) was described. The three isomers resulting from the two [6]helicene moieties of **DH1** were successfully separated by chiral HPLC and their fundamental properties originated from the different molecular geometries were investigated experimentally and computationally. The highly distorted π-conjugated systems of racemic *twisted*-**DH1** and *twisted*-**DH2** were unambiguously confirmed by X-ray crystallography, whereby the contorted three-dimensional lamellar packing structure was obtained for **DH1**, and the two-dimensional one for **DH2**. Such molecular packings exhibiting large overlap of π-surface between adjoining molecules are rarely observed in nonplanar polyaromatic compounds. To explore the nature of contorted lamellar packing of **DHs**, theoretical prediction of charge transport properties was performed for perfect order and disordered crystal systems by employing a method rooted in Marcus theory and kinetic Monte Carlo simulations. Therein, it was found that, in disordered crystalline morphologies, having diverse pathways is beneficial for charge transport due to the increased probability of a charge carrier being able to bypass charge traps.

Experimental Section

General

Unless otherwise noted, all materials including dry solvents were obtained from commercial suppliers and used without further purification. *o*-Chloranil was purchased from TCI and recrystallized in benzene before use. Tris(*o*-biphenylyl)boroxine,[22] 3,6-dibromonaphthalene-2,7-diyl bis(trifluoromethanesulfonate) (**2**),[10] and 2-bromo-4'-butyl-1,1'-biphenyl (**6**)[23] were prepared according to the procedures reported in the literature. Unless otherwise noted, all reactions were performed with dry solvents under an atmosphere of nitrogen in dried glassware with standard vacuum-line techniques. All work-up and purification procedures were carried out with reagent-grade solvents in air.

Analytical thin-layer chromatography (TLC) was performed using E. Merck silica gel 60 F_{254} precoated plates (0.25 mm). The developed chromatogram was analyzed by UV lamp (254 nm and 365 nm). High-resolution mass spectra (HRMS) were obtained from a Thermo Fisher Scientific Exactive. Melting points were measured on a MPA100 Optimelt automated melting point system. Chiral HPLC analysis was conducted on a Shimadzu Prominence 2000 instrument equipped with DAICEL CHIRALPAK IF (4.6 mm x 250 mm). Optical rotation during chiral HPLC analysis was measured using an IBZ MESSTECHNIK CHIRALYSER. NMR spectra were recorded on a JEOL ECA 600II spectrometer with Ultra COOLTM probe (^{1}H 600 MHz, ^{13}C 150 MHz). Chemical shifts for ^{1}H NMR are expressed in parts per million (ppm) relative to $CDHCl_2$ (δ 5.32 ppm) or C_2DHCl_4 (δ 6.00 ppm). Chemical shifts for ^{13}C NMR are expressed in ppm relative to CD_2Cl_2 (δ 54.0 ppm) or $C_2D_2Cl_4$ (δ 73.78 ppm). Data are reported as follows: chemical shift, multiplicity (s = singlet, d = doublet, t = triplet, m = multiplet, br = broad signal), coupling constant (Hz), and integration.

Synthesis of DH1 through C–H Activation Route

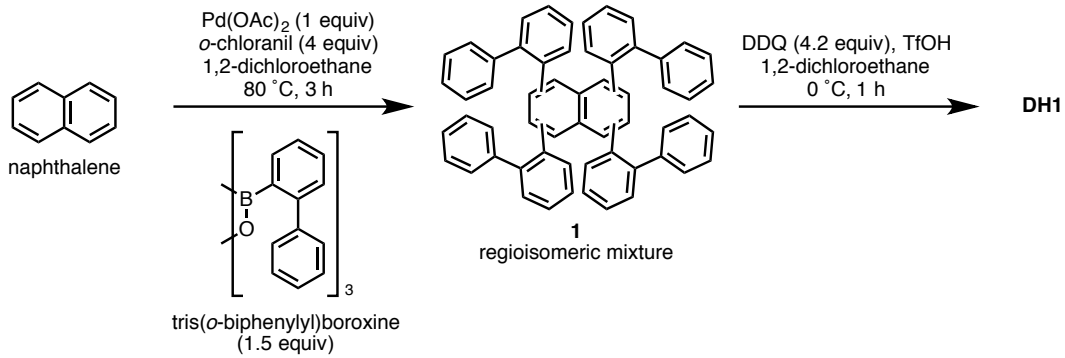

A mixture of naphthalene (12.8 mg, 100 μmol), *o*-biphenylylboroxine (81.0 mg, 150 μmol), $Pd(OAc)_2$ (22.7 mg, 100 μmol) and *o*-chloranil (98.4 mg, 400 μmol) in 1,2-dichloroethane (2

mL) was stirred for 3 h at 80 °C. After cooling, the reaction mixture was passed through a pad of silica gel (eluted by ethyl acetate) and the filtrate was concentrated *in vacuo*. The residue was roughly purified by preparative thin layer chromatography (eluted by *n*-hexane/ethyl acetate = 2:1) and gel permeation chromatography to afford regioisomeric mixture of **1**. To a solution of regioisomeric mixture of **1** (9.9 mg, *ca.*14 μmol) and DDQ (11.1 mg, 48.8 μmol) in 1,2-dichloroethane (2 mL) was added TfOH (20 μL) at 0 °C and the reaction mixture was stirred for 30 min. The acidic solution mixture was neutralized with triethylamine and passed through a pad of silica gel (eluted by chloroform). The filtrate was evaporated and the residue was washed with MeOH to afford **1** (2.0 mg, 1% in two steps) as an orange solid.

twisted-**DH1**: ^{1}H NMR (600 MHz, CD_2Cl_2) δ 9.16 (d, *J* = 7.7 Hz, 4H), 9.08 (d, *J* = 7.9 Hz, 4H), 8.76 (d, *J* = 8.1 Hz, 4H), 8.23 (t, *J* = 7.8 Hz, 4H), 8.00 (dd, *J* = 8.5, 1.0 Hz, 4H), 7.41 (ddd, *J* = 8.1, 6.8, 1.3 Hz, 4H), 6.87 (ddd, *J* = 8.3, 6.9, 1.4 Hz, 4H); ^{13}C NMR (150 MHz, CD_2Cl_2) δ 131.4 (CH), 130.8 (4º), 130.4 (4º), 130.2 (4º), 127.7 (CH), 127.1 (CH), 126.8 (CH), 126.0 (4º), 125.6 (4º), 123.9 (CH), 123.2 (4º), 123.0 (CH), 122.7 (CH), 121.9 (4º); HRMS (APCI) *m/z* calcd for $C_{58}H_{29}$ $[M+1]^+$: 725.2251, found: 725.2264; mp: >300 ºC (recrystallized from CS_2/*n*-hexane).

meso-**DH1**: ^{1}H NMR (600 MHz, CD_2Cl_2) δ 9.17 (d, *J* = 7.6 Hz, 4H), 9.05 (d, *J* = 7.9 Hz, 4H), 8.69 (d, *J* = 7.9 Hz, 4H), 8.25 (t, *J* = 7.7 Hz, 4H), 7.52 (dd, *J* = 8.0, 0.9 Hz, 4H) 7.38 (ddd, *J* = 8.0, 6.8, 1.3 Hz, 4H), 6.82 (ddd, *J* = 8.0, 6.9, 1.0 Hz, 4H); HRMS (APCI) *m/z* calcd for $C_{58}H_{29}$ $[M+1]^+$: 725.2232, found: 725.2264; mp: not applied.

Synthesis of 3

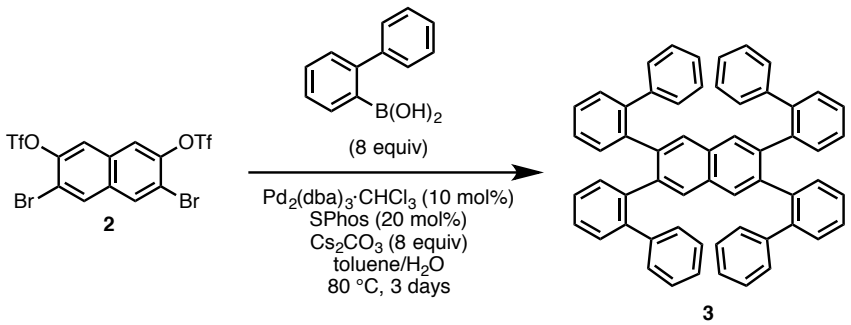

To a solution of **2** (1.01 g, 1.74 mmol), *o*-biphenylylboronic acid (2.74 g, 13.8 mmol), $Pd_2(dba)_3 \cdot CHCl_3$ (183 mg, 177 μmol, 10 mol%), and SPhos (145 mg, 353 μmol, 20 mol%) in toluene (15 mL) were added a solution of Cs_2CO_3 (4.50 g, 13.8 mmol) in H_2O (5 mL), and the mixture was stirred at 80 °C for 3 days under nitrogen. After cooling the mixture to room temperature, the reaction mixture was extracted with $CHCl_3$. The combined organic layer was washed with brine, dried over Na_2SO_4, and the solution was evaporated *in vacuo*. The crude

material was purified by silica-gel column chromatography (eluent: hexane/CH_2Cl_2 = 90:10 to 60:40) followed by recrystallization from toluene to afford **3** (1.08 g, 84%) as a white crystal. ^{1}H NMR (600 MHz, $C_2D_2Cl_4$, 140 ºC) δ 7.57 (s, 4H), 7.27 (t, *J* = 7.5 Hz, 4H), 7.20–7.16 (m, 8H), 7.09 (t, *J* = 7.7 Hz, 8H), 7.05 (t, *J* = 7.5 Hz, 4H), 6.76 (d, *J* = 7.7 Hz, 4H), 6.55 (br d, 4H); ^{13}C NMR (150 MHz, $C_2D_2Cl_4$, 140 ºC) δ 141.4 (4º), 140.6 (4º), 139.31 (4º), 139.28 (4º), 131.7 (CH), 131.3 (4º), 130.1 (CH), 129.5 (CH), 129.3 (CH), 127.2 (CH), 126.6 (CH), 126.4 (CH), 125.8 (CH); HRMS (APCI) *m/z* calcd for $C_{58}H_{41}$ $[M+1]^+$: 737.3220, found: 737.3203; mp: >300 ºC (recrystallized from toluene).

Synthesis of DH1 through Suzuki–Miyaura Coupling Route

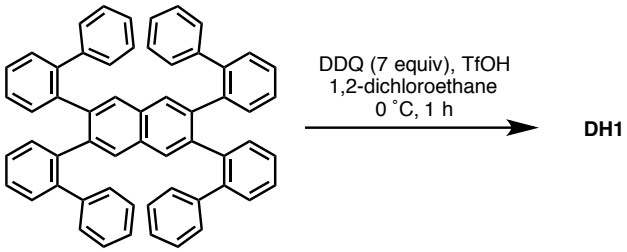

To a solution of **3** (73.4 mg, 100 μmol) in dry CH_2Cl_2 (20 mL) was added DDQ (157 mg, 692 μmol) at 0 ºC. After stirring for 5 min, trifluoromethanesulfonic acid (0.2 mL) was added to the solution. The solution was stirred for 1 h at 0 °C. The reaction mixture was neutralized with triethylamine, and then suspended overnight. The precipitate was collected, and the filtrate was diluted with acetone. The supernatant was removed and the residue was washed with MeOH. All precipitate obtained was combined and dried *in vacuo* to afford isomer mixture of **DH1** (45.9 mg, 64%) as an orange solid. The ratio of *twisted*-**DH1**/*meso*-**DH1** was 43:57 determined by ^{1}H NMR.

Synthesis of 5

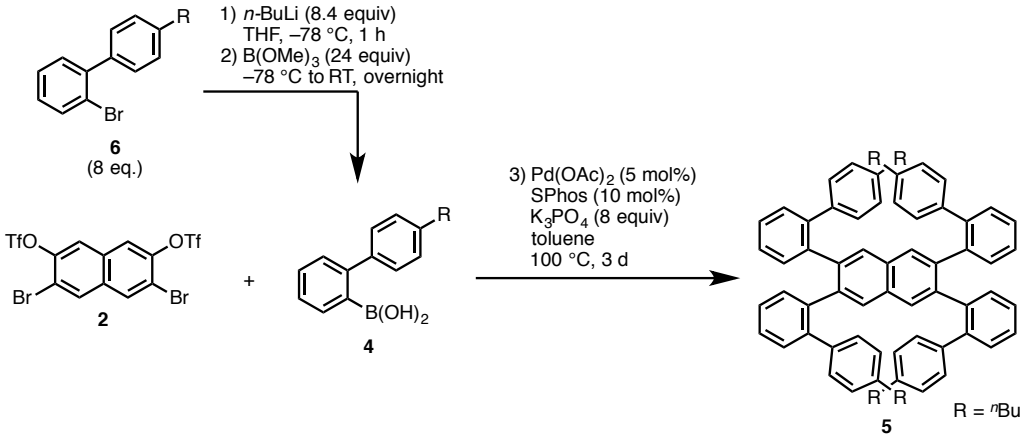

To a solution of 2-bromo-4'-butyl-1,1'-biphenyl (**6**) (11.6 g, 40.0 mmol) in THF was added a pentane solution of *n*-butyllithium (1.6 M, 26.3 mL, 42.0 mmol) at –78 °C dropwise over 10 min, and the mixture was stirred for 1 h under nitrogen. Trimethoxyborane (13.4 mL, 120 mmol) was added, and then the reaction mixture was allowed to warm to room temperature. After stirring the mixture overnight, the reaction was quenched by the addition of 2N HCl aqueous solution. The organic layer was extracted with Et_2O, washed with brine, dried over Na_2SO_4, and then evaporated *in vacuo* to afford a crude mixture of (4'-butyl-[1,1'-biphenyl]-2-yl)boronic acid (**4**) as a white solid. Compound **4** was used in next step without further purification.

A mixture of **2** (2.91 g, 5.00 mmol), **4**, $Pd(OAc)_2$ (56.1 mg, 0.250 mmol, 5 mol%), SPhos (205 mg, 0.500 mmol, 10 mol%), and K_3PO_4 (8.49 g, 40.0 mmol) in toluene (20 mL) was stirred at 100 °C for 3 days under nitrogen. After cooling to room temperature, the reaction was passed through a pad of silica-gel and eluted with dichloromethane, and then the volatile was evaporated *in vacuo*. Recrystallization from dichloromethane/*n*-hexane bilayer system afforded **5** (4.24 g, 88%) as a white solid.

^{1}H NMR (600 MHz, $C_2D_2Cl_4$, 130 °C) δ 7.56 (s, 4H), 7.24 (t, *J* = 7.5 Hz, 4H), 7.17 (d, *J* = 7.6 Hz, 4H), 6.99 (t, *J* = 7.2 Hz, 4H), 6.90 (d, *J* = 7.8 Hz, 8H), 6.65 (d, *J* = 7.0 Hz, 8H), 6.50 (broad s, 4H), 2.62 (t, *J* = 7.5 Hz, 8H), 1.71–1.63 (m, 8H), 1.49–1.38 (m, 8H), 1.00 (t, *J* = 7.2 Hz, 12H); ^{13}C NMR (150 MHz, $C_2D_2Cl_4$, 130 °C) δ 140.5 (4º), 140.4 (4º), 139.4 (4º), 139.3 (4º), 138.7 (4º), 131.7 (CH), 131.4 (4º), 130.1 (CH), 129.3 (CH), 129.2 (CH), 127.2 (CH), 126.5 (CH), 126.1 (CH), 35.0 (CH_2), 33.1 (CH_2), 22.0 (CH_2), 13.4 (CH_3); HRMS (MALDI TOF-MS) *m/z* calcd for $C_{74}H_{72}Na$ $[M+Na]^+$: 983.5532, found: 983.5526; mp: 219–220 ºC (re-crystallized from dichloromethane/*n*-hexane).

Synthesis of DH2

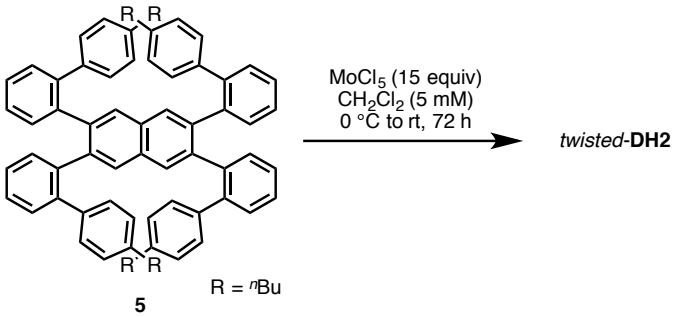

5

To a solution of **5** (19.2 mg, 0.020 mmol) in dichloromethane (4 mL) was added $MoCl_5$ (82.0 mg, 0.300 mmol) at 0 °C, and then the reaction mixture was stirred at room temperature for 3 days under nitrogen. The reaction was quenched by the addition of MeOH/$CHCl_3$ (1:1, 5

mL) solution and the resultant solution was directly passed through a pad of silica-gel with *n*-hexane/dichloromethane solution (9:1) eluent. The filtrate was evaporated *in vacuo*. The crude residue was purified by preparative thin-layer chromatography (eluent: *n*-hexane/$CHCl_3$ = 17:3) to afford **DH2** (2.4 mg, 13%) as a red solid.

^{1}H NMR (600 MHz, $CDCl_3$) δ 9.08 (d, *J* = 7.7 Hz, 4H), 8.96 (d, *J* = 7.7 Hz, 4H), 8.58 (d, *J* = 8.4 Hz, 4H), 8.15 (t, *J* = 7.8 Hz, 4H), 7.84 (d, *J* = 1.4 Hz, 4H), 7.18 (dd, *J* = 8.1, 1.6 Hz, 4H), 2.17–2.11 (m, 4H), 2.02–1.97 (m, 4H), 1.04–0.85 (m, 16H), 0.72 (t, *J* = 7.0 Hz, 12H); ^{13}C NMR (150 MHz, $CDCl_3$) δ 141.3 (4º), 131.3 (4º), 131.1 (4º), 130.2 (4º), 129.7 (CH), 128.0 (4º), 127.7 (CH), 127.0 (CH), 125.6 (4º), 125.2 (4º), 123.2 (CH), 123.0 (4º), 121.9 (CH), 121.8 (CH), 121.5 (4º), 35.6 (CH_2), 33.3 (CH_2), 22.3 (CH_2), 14.1 (CH_3); HRMS (MALDI TOF-MS) *m/z* calcd for $C_{74}H_{60}$ $[M]^+$: 948.4695, found: 948.4685; mp: >300 ºC (recrystallized from chloroform/*n*-pentane).

Diastereomer Separation of DH1 by Chiral HPLC

HPLC analysis was conducted on a Shimadzu Prominence 2000 instrument equipped with DAICEL CHIRALPAK IF (4.6 mm x 250 mm). Isomers of **DH1** were analyzed at 400 nm (black line) and simultaneously optical rotation was measured using an IBZ MESSTECHNIK CHIRALYSER at 426 nm (red line). Flow rate was 0.5 mL/min and temperature was 25 °C.

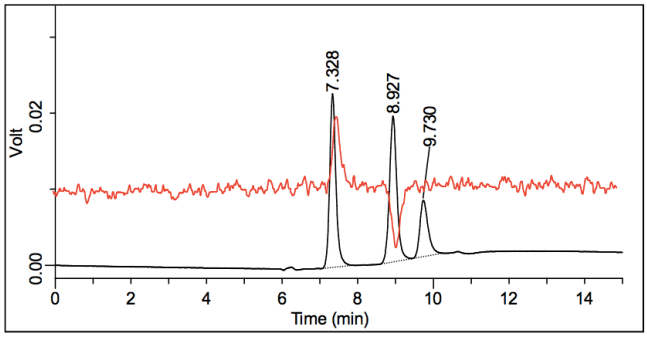

#	Time	Area	Area%	Height	Height%
1	7.328	264283	41.53	22834	46.23
2	8.927	259524	40.78	19162	38.80
3	9.730	112571	17.69	7391	14.97
		636378	100.00	49387	100.00

Figure 12. Chiral HPLC analysis of the mixture of **DH1** eluted by *n*-hexane/chloroform (3:7).

X-ray Crystallography

Recrystallization of isomer mixture of **DH1** from CS_2/*n*-hexane in vapor diffusion method yielded red crystals of *twisted*-**DH1** suitable for X-ray crystal structure analysis. Recrystallization of a racemic mixture of **DH2** from $CHCl_3$/*n*-pentane in vapor diffusion method yielded red crystals suitable for X-ray crystal structure analysis. Details of the crystal data and a summary of the intensity data collection parameters for $C_{58}H_{28}$ are listed in Table 2. A suitable crystal was mounted with mineral oil on a glass fiber and transferred to the goniometer of a Rigaku Saturn CCD diffractometer and a Rigaku PILATUS diffractometer. Graphite-monochromated Mo Kα radiation (λ = 0.71075 Å) was used. The structures were solved by direct methods with (SIR-97)[24] and refined by full-matrix least-squares techniques against F^2 (SHELXL-97).[25] The intensities were corrected for Lorentz and polarization effects. The non-hydrogen atoms were refined anisotropically. Hydrogen atoms were placed using AFIX instructions.

Table 2. Crystallographic data and structure refinement details for **DH1** and **DH2**

	twisted-**DH1**	*twisted*-**DH2**
formula	$C_{58}H_{28}$	$C_{76.5}H_{64}$
fw	724.80	983.27
T (K)	103(2)	123(2)
λ (Å)	0.71075	0.71075
cryst syst	Monoclinic	Triclinic
space group	*C*2/*c*	*P*-1
a (Å)	11.056(8)	11.0983(7)
b (Å)	39.67(3)	16.4648(10)
c (Å)	7.531(5)	16.7317(8)
α	90°	63.011(5)°
β	97.688(9)°	72.188(7)°
γ	90°	78.909(7)°
V (Å^3)	3273(4)	2588.7(3)
Z	4	2
D_{calc} (g / cm^3)	1.471	1.261
μ (mm^{-1})	0.084	0.071
F(000)	1504	1046
cryst size (mm)	0.10 × 0.10 × 0.02	0.20 × 0.10 × 0.10
θ range	3.08–25.00°	3.011–24.999°
reflns collected	14225	19357
indep reflns/R_{int}	2877/0.0649	8814/0.0414
params	262	788
GOF on F^2	1.098	1.187
R_1, wR_2 [I>2σ(I)]	0.0736, 0.1642	0.0713, 0.1617
R_1, wR_2 (all data)	0.1128, 0.1861	0.1027, 0.1990

Photophysical Study

The CD spectra were measured with a JASCO FT/IR6100. UV–Vis absorption spectra were recorded on a Shimadzu UV-3510 spectrometer with a resolution of 0.5 nm. Emission spectra were measured with an FP-6600 Hitachi spectrometer with a resolution of 0.2 nm. Dilute solutions in degassed spectral grade chloroform in a 1 cm square quartz cell were used for measurements. Absolute fluorescence quantum yields were determined with a Hamamatsu C9920-02 calibrated integrating sphere system upon excitation at 506 nm for *twisted*-**DH1**, at 491 nm for *meso*-**DH1**, and at 390 nm for *twisted*-**DH2**. Fluorescence lifetimes were measured with a Hamamatsu Picosecond Fluorescence Measurement System C11200 equipped with a picosecond light pulser PLP-10 (excitation wavelength 464 nm with a repetition rate of 10 Hz).

Computational Study on the Structures of DHs

The Gaussian 09 program[26] running on a SGI Altix4700 system was used for optimization (B3LYP/6-31G(d)).[27] All structures were optimized without any symmetry assumptions. Zero-point energy, enthalpy, and Gibbs free energy at 298.15 K and 1 atm were estimated from the gas-phase studies unless otherwise noted. Harmonic vibration frequency calculations at the same level were performed to verify all stationary points as local minima (with no imaginary frequency) or transition states (with one imaginary frequency). Visualization of the results was performed by use of POV-Ray for Windows v3.5 software.

Table 3. Uncorrected and thermal-corrected (298 K) energies of stationary points (Hartree).[a]

structure	*E*	*E* + *ZPE*	*H*	*G*
twisted-**DH1**	-2227.21163352	-2226.544092	-2226.506226	-2226.609860
meso-**DH1**	-2227.21016441	-2226.543166	-2226.505356	-2226.608383
twisted-**DH2**	-2384.48556171	-2383.708006	-2383.662450	-2383.784239
TS (**DH1**)	-2227.14355298	-2226.477334	-2226.440469	-2226.540461
[6]helicene	-1000.44294361	-1000.107877	-1000.089572	-1000.152127
TS ([6]helicene]	-1000.38370844	-1000.049734	-1000.032154	-1000.092676

a) *E*: electronic energy; *ZPE*: zero-point energy; *H* (= $E + ZPE + E_{vib} + E_{rot} + E_{trans} + RT$): sum of electronic and thermal enthalpies; *G* (= $H - TS$): sum of electronic and thermal free energies.

Table 4. TD DFT vertical one-electron excitation (6 states) calculated for the optimized structures of *twisted*-**DH1** (top) and *meso*-**DH1** (bottom).

excited state	energy	wavelength	oscillator strenghs (*f*)	description
1	2.3997 eV	516.67 nm	0.1475	HOMO -> LUMO (0.69402) HOMO-1 -> LUMO+1 (0.11980)
2	2.6235 eV	472.59 nm	0.0001	HOMO-1 -> LUMO (-0.47707) HOMO -> LUMO+1 (0.51416)
3	2.8822 eV	430.17 nm	0.0204	HOMO-2 -> LUMO (0.66451) HOMO -> LUMO+2 (-0.21753)
4	3.0909 eV	401.12 nm	0.8786	HOMO-1 -> LUMO (0.50779) HOMO -> LUMO+1 (0.46810)
5	3.1247 eV	396.79 nm	0.0743	HOMO-2 -> LUMO (0.21670) HOMO -> LUMO+2 (0.66150)
6	3.1608 eV	392.26 nm	0.0006	HOMO-3 -> LUMO (0.47191) HOMO -> LUMO+3 (0.51525)

excited state	energy	wavelength	oscillator strenghs (*f*)	description
1	2.4637 eV	503.25 nm	0.1704	HOMO -> LUMO (0.69482) HOMO-2 -> LUMO+2 (-0.10906)
2	2.7750 eV	446.79 nm	0.0032	HOMO-2 -> LUMO (0.52447) HOMO -> LUMO+2 (0.46460)
3	2.8803 eV	430.46 nm	0.0000	HOMO-1 -> LUMO (0.63275) HOMO -> LUMO+1 (0.29586)
4	3.0658 eV	404.41 nm	0.0000	HOMO-1 -> LUMO (-0.29606) HOMO -> LUMO+1 (0.63364)
5	3.1734 eV	390.69 nm	0.0006	HOMO-3 -> LUMO (-0.45541) HOMO -> LUMO+3 (0.52945)
6	3.2279 eV	384.11 nm	0.9034	HOMO-2 -> LUMO (-0.45743) HOMO -> LUMO+2 (0.51696)

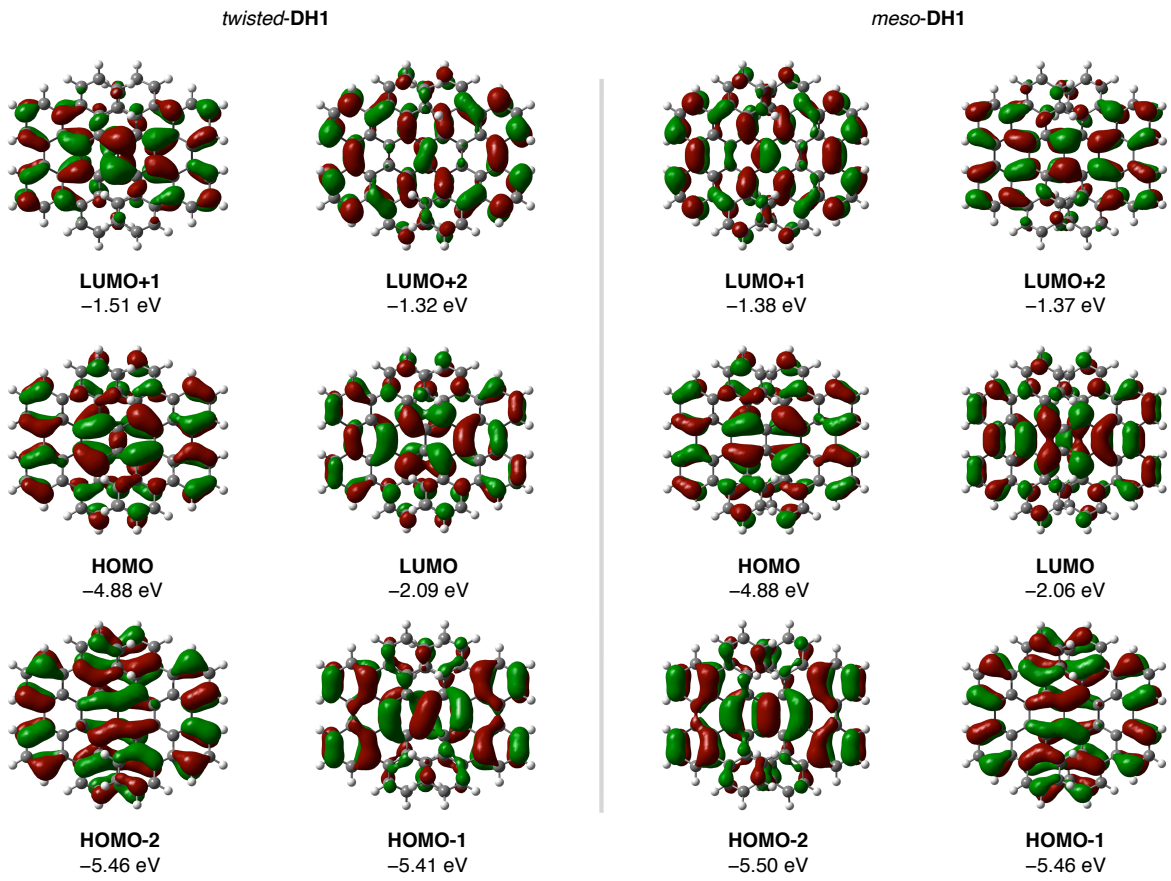

Figure 13. The molecular structure, the spatial distribution, and the energy of representative molecular orbitals of *twisted*-**DH1** (left) and *meso*-**DH1** (right).

Computational Study on the Molecular Dynamics and Charge Transport Properties

Experimental crystal structures obtained from XRD measurements were used as starting structures of **DH1** and **DH2**. To predict molecular ordering and charge-transport, we considered two morphological phases: (1) with perfect positional order (crystal phase) and (2) with positional disorder, incorporating thermal effects to XRD data (crystalline phase). Atomistic molecular dynamics (MD) simulations were used to predict mesoscale ordering in the crystalline phase. Initial supercells containing 896 and 1024 molecules were constructed for **DH1** and **DH2**, respectively, with periodic boundary conditions (PBC). MD simulations in an NPT ensemble were performed at 300K using the GPU version of Amber12.[28] GAFF force fields are used for molecular mechanics parameters.[29] Partial charges of ground-states were generated from B3LYP/6-311G(d,p)-optimized geometries via the Merz-Singh-Kollman scheme[30] using HF/6-31G(d), as implemented in Gaussian09.[31] Each supercell (**DH1** and **DH2**) was first heated from 0K to 300 K for 2 ns and then NPT equilibrated for another 2 ns at 300 K, restraining

the heavy atom positions.[32] Final 20 ns production run was performed at 300 K and time-averaged pressure at 1 atm. Snapshots of the MD simulations were taken at various timepoints in order to obtain atomistic morphologies for subsequent charge transport calculations.

With the MD-equilibrated morphologies in hand, charge-carrier dynamics simulations to calculate charge transfer rates were performed by using Marcus theory. Marcus theory relies on two assumptions: (1) charges are localized on each site (or molecule, in the case of organic semiconductors)[33] and (2) a non-adiabatic charge transfer reaction occurs through a hopping-type mechanism. The high-temperature limit of the Marcus charge-transfer rate is defined as:[34]

$$k_{ij} = \frac{J_{ij}^2}{} \sqrt{\frac{\pi}{\lambda k_b T}} \exp\left[-\frac{(\Delta E_{ij} - \lambda)}{4\lambda k_b T} \right] \quad (1)$$

where T is temperature, J is electronic coupling, λ is reorganization energy and ΔE_{ij} is free-energy (or site-energy) difference. Electronic coupling elements, J_{ij}, of the charge-transfer were calculated for defined molecular pairs using the semi-empirical method ZINDO.[35] Pairs are defined as molecules with centroid distances below 0.8 nm, each of which are added to a neighbor list, a compilation of all possible adjacent hopping sites. Reorganization energy λ of each molecule was calculated by the four-point rule using DFT with B3LYP/6-311G(d,p). Site energies were calculated self-consistently using Thole Model, which includes contributions from electrostatic interactions due to polarization and from an external electric field.[18a] In accordance with the method previously described for MD simulations, partial charges of neutral and charged states were generated via Merz-Singh-Kollman scheme,[30] using HF/6-31G(d) method based on B3LYP/6-311G(d,p)-optimized geometries. Isotropic atomic polarizabilities of the neutral and charged states were re-parameterized for each species to calibrate against molecular polarizabilities obtained using B3LYP/6-311G(d,p). Energetic disorders (σ) were extracted using the Gaussian Disorder Model (GDM), where the histogram of site energy differences (ΔE_{ij}) were fitted to the following Gaussian function:

$$f(\xi) = \frac{1}{\sigma\sqrt{2\pi}} \exp\left[-\frac{\xi^2}{2\sigma^2} \right] \quad (2)$$

Kinetic Monte Carlo (kMC) methods were used to predict charge transport of a charge carrier in an applied external electric field, as implemented in VOTCA, and hole mobilities were obtained using velocity-averaging.[36]

Reference

1. Selected examples controlling molecular packing for functional materials: (a) Verbiest, T.; Elshocht, S. V.; Kauranen, M.; Hellemans, L.; Snauwaert, J.; Nuckolls, C.; Katz, T. J.; Persoons, A. *Science* **1998**, *282*, 913. (b) Tanaka, H.; Okano, Y.; Kobayashi, H.; Suzuki, W.; Kobayashi, A. *Science* **2001**, *291*, 285. (c) Kaiser, T. E.; Wang, H.; Stepanenko, V.; Würthner, F. *Angew. Chem., Int. Ed.* **2007**, *46*, 5541. (d) Amaya, T.; Seki, S.; Moriuchi, T.; Nakamoto, K.; Nakata, T.; Sakane, H.; Saeki, A.; Tagawa, S.; Hirao, T. *J. Am. Chem. Soc.* **2009**, *131*, 408. (e) Gsänger, M.; Oh, J. H.; Könemann, M.; Höffken, H. W.; Krause, A.-M.; Bao, Z.; Würthner, F. *Angew. Chem., Int. Ed.* **2010**, *49*, 740. (f) Würthner, F.; Kaiser, T. E.; Saha-Möller, C. R. *Angew. Chem., Int. Ed.* **2011**, *50*, 3376. (g) Hatakeyama, T.; Hashimoto, S.; Oba, T.; Nakamura, M. *J. Am. Chem. Soc.* **2012**, *134*, 19600. (h) Pola, S.; Kuo, C.-H.; Peng, W.-T.; Islam, M. M.; Chao, I.; Tao, Y.-T. *Chem. Mater.* **2012**, *24*, 2566.
2. Molecular packing of planar aromatic systems: (a) Anthony, J. E. *Chem. Rev.* **2006**, *106*, 5028. (b) Wang, C.; Dong, H.; Li, H.; Zhao, H.; Meng, Q.; Hu, W. *Cryst. Growth Des.* **2010**, *10*, 4155. (c) Zhang, L.; Cao, Y.; Colella, N. S.; Liang, Y.; Brédas, J.-L.; Houk, K. N.; Briseno, A. L. *Acc. Chem. Res.* **2015**, *48*, 500.
3. Circulenes: (a) Barth, W. E.; Lawton, R. G. *J. Am. Chem. Soc.* **1965**, *88*, 380. (b) Scott, L. T.; Hashemi, M. M.; Meyer, D. T.; Warren, H. B. *J. Am. Chem. Soc.* **1991**, *113*, 7082. (c) Yamamoto, K.; Harada, T.; Okamoto, Y.; Chikamatsu, H.; Nakazaki, M.; Kai, Y.; Nakao, T.; Tanaka, M.; Harada, S.; Kasai, N. *J. Am. Chem. Soc.* **1988**, *110*, 3578. (d) Yamamoto, K.; Saitho, Y.; Iwaki, D.; Ooka, T. *Angew. Chem., Int. Ed.* **1991**, *30*, 1173. (e) Butterfield, A. M.; Gilomen, B.; Siegel, J. S. *Org. Process Res. Dev.* **2012**, *16*, 664. (f) Feng, C.-N.; Kuo, M.-Y.; Wu, Y.-T. *Angew. Chem., Int. Ed.* **2013**, *52*, 7791. (g) Sakamoto, Y.; Suzuki, T. *J. Am. Chem. Soc.* **2013**, *135*, 14074.
4. Reviews on helicenes: (a) Shen, Y.; Chen, C.-F. *Chem. Rev.* **2012**, *112*, 1463. (b) Gingras, M. *Chem. Soc. Rev.* **2013**, *42*, 968. (c) Gingras, M.; Félix, G.; Peresutti, R. *Chem. Soc. Rev.* **2013**, *42*, 1007. (d) Gingras, M. *Chem. Soc. Rev.* **2013**, *42*, 1051.
5. Functional molecules utilizing π–π stacking force: (a) Brédas, J.-L.; Beljonne, D.; Coropceanu, V.; Cornil, J. *Chem. Rev.* **2004**, *104*, 4971. (b) Chen, Z.; Lohr, A.; Saha-Möller, C. R.; Würthner, F. *Chem. Soc. Rev.* **2009**, *38*, 564. (c) Niimi, K.; Shinamura, S.; Osaka, I.; Miyazaki, E.; Takimiya, K. *J. Am. Chem. Soc.* **2011**, *133*, 8732. (d) Saeki, A.; Koizumi, Y.; Aida, T.; Seki, S. *Acc. Chem. Res.* **2012**, *45*, 1193. (e) Foster, R. *Organic Charge-Transfer Complexes*; Academic Press, New York, 1969.
6. Reviews on C–H activation: (a) Yamaguchi, J.; Yamaguchi A. D.; Itami, K. *Angew. Chem., Int. Ed.* **2012**, *51*, 8960. (b) Chen, X.; Engle, K. M.; Wang, D.-H.; Yu, J.-Q. *Angew. Chem., Int. Ed.* **2009**, *48*, 5094. (c) Ackermann, L.; Vicente, R.; Kapdi, A. R. *Angew. Chem., Int. Ed.* **2009**, *48*, 9792. (d)

Wencel-Delord, J.; Glorius, F. *Nat. Chem.* **2013**, *5*, 369. (e) Segawa, Y.; Maekawa, T.; Itami, K. *Angew. Chem., Int. Ed.* **2015**, *54*, 66.

7. Mochida, K.; Kawasumi, K.; Segawa, Y.; Itami, K. *J. Am. Chem. Soc.* **2011**, *133*, 10716.
8. Review on Scholl reaction: Grzybowski, M.; Skonieczny, K.; Butenschön, H.; Gryko, D. T. *Angew. Chem., Int. Ed.* **2013**, *52*, 9900.
9. Scholl reaction in helicene chemistry: (a) Pradhan, A.; Dechambenoit, P.; Bock, H.; Durola, F. *Angew. Chem., Int. Ed.* **2011**, *50*, 12582. (b) Navale, T. S.; Thakur, K.; Rathore, R. *Org. Lett.* **2011**, *13*, 1634. (c) Danz, M.; Tonner, R.; Hilt, G. *Chem. Commun.* **2012**, *48*, 377. (d) Pradhan, A.; Dechambenoit, P.; Bock, H.; Durola, F. *J. Org. Chem.* **2013**, *78*, 2266.
10. (a) Cooke, R. G.; Johnson, B. L.; Owen, W. R. *Aust. J. Chem.* **1960**, *13*, 256. (b) Shinamura, S.; Osaka, I.; Miyazaki, E.; Nakao, A.; Yamagishi, M.; Takeya, J.; Takimiya, K. *J. Am. Chem. Soc.* **2011**, *133*, 5024.
11. Kawasumi, K.; Zhang, Q.; Segawa, Y.; Scott, L. T.; Itami, K. *Nat. Chem.* **2013**, *5*, 739.
12. (a) Grimme, S.; Peyerimhoff, S. D. *Chem. Phys.* **1996**, *204*, 411. (b) Janke, R. H.; Haufe, G.; Würthwein, E.-U.; Borkent, J. H. *J. Am. Chem. Soc.* **1996**, *118*, 6031.
13. Martin, R. H.; Marchant, M. J. *Tetrahedron* **1974**, *30*, 347.
14. (a) Eversloh, C. L.; Liu, Z.; Müller, B.; Stangl, M.; Li, C.; Müllen, K. *Org. Lett.* **2011**, *13*, 5528. (b) Luo, J.; Xu, X.; Mao, R.; Miao, Q. *J. Am. Chem. Soc.* **2012**, *134*, 13796. (c) Kashihara, H.; Asada, T.; Kamikawa, K. *Chem. Eur. J.* **2015**, *21*, 6523. (d) Xiao, S.; Kang, S. J.; Wu, Y.; Ahn, S.; Kim, J. B.; Loo, Y.-L.; Siegrist, T.; Steigerwald, M. L.; Li, H.; Nuckolls, C. *Chem. Sci.* **2013**, *4*, 2018. (d) Shiraishi, K.; Rajca, A.; Pink, M.; Rajca, S. *J. Am. Chem. Soc.* **2005,** *127,* 9312. (e) Sakamaki, D.; Kumano, D.; Yashima, E.; Seki, S. *Angew. Chem., Int. Ed.* **2015**, *54*, 5404. (f) Liu, X.; Yu, P.; Xu, L.; Yang, J.; Shi, J.; Wang, Z.; Cheng, Y.; Wang, H. *J. Org. Chem.* **2013**, *78*, 6316.
15. Newman, M. S.; Lednicer, D. *J. Am. Chem. Soc.* **1956**, *78*, 4765.
16. Nakai, Y.; Mori, T.; Inoue, Y. *J. Phys. Chem. A* **2012**, *116*, 7372.
17. (a) Hindeleh, A.; Hosemann, R. *J. Phys. C* **1988**, *21*, 4155. (b) Rivnay, J.; Noriega, R.; Kline, R. J.; Salleo, A.; Toney, M. F. *Phys. Rev. B* **2011**, *84*, 045203. (c) Noiega, R.; Rivnay, J.; Vandewal, K.; Koch, F. P.; Stingelin, N.; Smith, P.; Toney, M. F.; Salleo, A. *Nat. Mater.* **2013**, *12*, 1038.
18. (a) Ruehle, V.; Lukyanov, A.; May, F.; Schrader, M.; Vehoff, T.; Kirkpatrick, J.; Baumeier, B.; Andrienko, D. *J. Chem. Theory Comput.* **2011**, *7*, 3335. (b) Kwiatkowski, J. J.; Nelson, J.; Li, H.; Bredas, J. L.; Wenzel, W.; Lennartz, C. Simulating charge transport in tris(8-hydroxyquinoline)aluminium (Alq3). *Phys. Chem. Chem. Phys.* **2008**, *10*, 1852. (c) Martinelli, N. G.; Savini, M.; Muccioli, L.; Olivier, Y.; Castet, F.; Zannoni, C.; Beljonne, D.; Cornil, J. *Adv. Func. Mater.* **2009**, *19*, 3254. (d) Tummala, N. R.; Zheng, Z.; Aziz, S. G.; Coropceanu, V.; Brédas,

J. L. *J. Phys. Chem. Lett.* **2015**, *6*, 3657. (e) Steiner, F.; Foster, S.; Losquin, A.; Labram, J.; Anthopoulos, T. D.; Frost, J. M.; Nelson, J. *Mater. Horiz.* **2015**, *2*, 113.

19. Marcus, R. A. *Rev. Mod. Phys.* **1993**, *65*, 599.
20. Yavuz, I.; Martin, B. N.; Park, J.; Houk, K. N. *J. Am. Chem. Soc.* **2015**, *137*, 2856, and references therein.
21. Jackson, N. E.; Kohlstedt, K. L.; Savoie, B. M.; de la Cruz, M. O.; Schatz, G. C.; Chen, L. X.; Ratner, M. A. *J. Am. Chem. Soc.* **2015**, *137*, 6254.
22. Chen, F.-X.; Kina, A.; Hayashi T. *Org. Lett.* **2006**, *8*, 341.
23. Suzuki, N.; Fujita, T.; Ichikawa, J. *Org. Lett.* **2015**, *17*, 4984.
24. Altomare, A.; Burla, M. C.; Camalli, M.; Cascarano, G. L.; Giacovazzo, C.; Guagliardi, A.; Moliterni, A. G. G.; Polidori, G.; Spagna, R. *J. Appl. Crystallogr.* **1999**, *32*, 115.
25. Sheldrick, G. M. University of Göttingen: Göttingen, Germany, 1997.
26. Frisch, M. J.; Trucks, G. W.; Schlegel, H. B.; Scuseria, G. E.; Robb, M. A.; Cheeseman, J. R.; Scalmani, G.; Barone, V.; Mennucci, B.; Petersson, G. A.; Nakatsuji, H.; Caricato, M.; Li, X.; Hratchian, H. P.; Izmaylov, A. F.; Bloino, J.; Zheng, G.; Sonnenberg, J. L.; Hada, M.; Ehara, M.; Toyota, K.; Fukuda, R.; Hasegawa, J.; Ishida, M.; Nakajima, T.; Honda, Y.; Kitao, O.; Nakai, H.; Vreven, T.; Montgomery, Jr., J. A.; Peralta, J. E.; Ogliaro, F.; Bearpark, M.; Heyd, J. J.; Brothers, E.; Kudin, K. N.; Staroverov, V. N.; Keith, T.; Kobayashi, R.; Normand, J.; Raghavachari, K.; Rendell, A.; Burant, J. C.; Iyengar, S. S.; Tomasi, J.; Cossi, M.; Rega, N.; Millam, J. M.; Klene, M.; Knox, J. E.; Cross, J. B.; Bakken, V.; Adamo, C.; Jaramillo, J.; Gomperts, R.; Stratmann, R. E.; Yazyev, O.; Austin, A. J.; Cammi, R.; Pomelli, C.; Ochterski, J. W.; Martin, R. L.; Morokuma, K.; Zakrzewski, V. G.; Voth, G. A.; Salvador, P.; Dannenberg, J. J.; Dapprich, S.; Daniels, A. D.; Farkas, O.; Foresman, J. B.; Ortiz, J. V.; Cioslowski, J.; Fox, D. J. Gaussian 09, Revision D.01, Gaussian, Inc., Wallingford CT, **2013**.
27. (a) Becke, A. D. *J. Chem. Phys.* **1993**, *98*, 5648. (b) Lee, C.; Yang, W.; Parr, R. G. *Phys. Rev. B* **1988**, *37*, 785.
28. (a) Case, D. A. *et al.* AMBER 12; University of California: San Francisco, CA, **2012**. (b) Salomon-Ferrer, R.; Götz, A. W.; Poole, D.; le Grand, S.; Walker, R. C. *J. Chem. Theory. Comput.* **2013**, *9*, 3878.
29. (a) Bayly, C. I.; Cieplak, P.; Cornell, W.; Kollman, P. A. *J. Phys. Chem.* **1993**, *97*, 10269. (b) Wang, J.; Wolf, R. M.; Caldwell, J. W.; Kollman, P. A.; Case, D. A. *J. Comput. Chem.* **2004**, *25*, 1157.
30. (a) Singh, U. C.; Kollman, P. A. An approach to computing electrostatic charges for molecules. *J. Comput. Chem.* **1984**, *5*, 129. (b) Besler, B. H.; Merz, K. M.; Kollman, P. A. *J. Comput. Chem.* **1990**, *11*, 431.

31. Frisch, M. J.; Trucks, G. W.; Schlegel, H. B.; Scuseria, G. E.; Robb, M. A.; Cheeseman, J. R.; Scalmani, G.; Barone, V.; Mennucci, B.; Petersson, G. A.; Nakatsuji, H.; Caricato, M.; Li, X.; Hratchian, H. P.; Izmaylov, A. F.; Bloino, J.; Zheng, G.; Sonnenberg, J. L.; Hada, M.; Ehara, M.; Toyota, K.; Fukuda, R.; Hasegawa, J.; Ishida, M.; Nakajima, T.; Honda, Y.; Kitao, O.; Nakai, H.; Vreven, T.; Montgomery, J. A., Jr.; Peralta, J. E.; Ogliaro, F.; Bearpark, M.; Heyd, J. J.; Brothers, E.; Kudin, K. N.; Staroverov, V. N.; Kobayashi, R.; Normand, J.; Raghavachari, K.; Rendell, A.; Burant, J. C.; Iyengar, S. S.; Tomasi, J.; Cossi, M.; Rega, N.; Millam, M. J.; Klene, M.; Knox, J. E.; Cross, J. B.; Bakken, V.; Adamo, C.; Jaramillo, J.; Gomperts, R.; Stratmann, R. E.; Yazyev, O.; Austin, A. J.; Cammi, R.; Pomelli, C.; Ochterski, J. W.; Martin, R. L.; Morokuma, K.; Zakrzewski, V. G.; Voth, G. A.; Salvador, P.; Dannenberg, J. J.; Dapprich, S.; Daniels, A. D.; Farkas, Ö.; Foresman, J. B.; Ortiz, J. V.; Cioslowski, J.; Fox, D. J. Gaussian 09, Revision D.01; Gaussian Inc: Wallingford, CT, **2009**.
32. Allen, M. P.; Tildesley, D. J. *Computer Simulation of Liquids*; Oxford University Press: Oxford, U.K., **1989**.
33. (a) Stafström, S. *Chem. Soc. Rev.* **2010**, *39*, 2484. (b) Troisi, A. *Chem. Soc. Rev.* **2011**, *40*, 2347.
34. (a) Marcus, R. A. *J. Chem. Phys.* **1956**, *24*, 966. (b) Marcus, R. A. *Rev. Mod. Phys.* **1993**, *65*, 599.
35. (a) Kirkpatrick, J. *Int. J. Quantum Chem.* **2008**, *108*, 51. (b) Brédas, J.-L.; Calbert, J. P.; da Silva Filho, D. A.; Cornil, J. *Proc. Natl. Acad. Sci. USA* **2002**, *99*, 5804.
36. (a) Ruehle, V.; Lukyanov, A.; May, F.; Schrader, M.; Vehoff, T.; Kirkpatrick, J.; Baumeier, B.; Andrienko, D. *J. Chem. Theory Comput.* **2011**, *7*, 3335. (b) Coropceanu, V.; Cornil, J.; da Silva Filho, D. A.; Olivier, Y.; Silbey, R.; Brédas, J.-L. *Chem. Rev.* **2007**, *107*, 926. (c) Bässler, H. *Phys. Status Solidi* (*B*), **1993**, *175*, 15.

Chapter 3

Synthesis of π-Extended Double Dithia[6]helicene Exhibiting Three-Dimensional Stacking Lattice

ABSTRACT: Among tremendous number of π-conjugated molecules reported so far, there exist a few examples exhibiting three-dimensional π–π stacking like the π-extended double [6]helicene (**DH1**) described in Chapter 2. A new π-extended double dithia[6]helicene (**DH3**) synthesized in this chapter not only provided such stacking mode but also resulted in an isotropic electronic coupling. Photophysical measurements and cyclic voltammetry unraveled the difference of electronic structures between the double carbo[6]helicenes (**DH1** and **DH2**) and its thiophene-containing analog (**DH3**). TRMC measurements indicated that **DH3** exhibits the highest transient conductivities among them. Finally, an organic field-effect transistor fabricated using **DH3** was also found to function as a p-type transistor.

Introduction

Precise control of the molecular packing of π-conjugated molecules is a critical issue to uncover the attractive functions, which are essential for the application to organic electronics and photonics. Unlike inorganic materials, however, general organic π-conjugated molecules are predestined to adopt lower dimensional, that is, one- or two-dimensional electronic structures in the crystalline state. This sharp contrast is derived from the nature of π-system confining π-electrons in the two-dimensional planar p-orbitals' conjugation. Consequently, to gain a continuous intermolecular electronic interaction, π-conjugated molecules are required to be aligned in a face-to-face manner to overlay the π-surfaces (π–π stacking). This constraint fatally lowers the dimensionality of bulk electronic structures. Although amorphous states of relatively flexible π-conjugated molecules can serve three-dimensional electronic interactions, there occurs a lack of periodicity. Hence, a full picture of precisely-defined three-dimensional electronic interactions achieved by organic molecules is still in the dark.

Over the past few decades, chemists have made enormous efforts to achieve control over the molecular packing of π-conjugated molecules in order to exploit the outstanding electronic and/or optical properties of these compounds.[1] A central theme of these efforts is the introduction of substituents such as long alkyl chains,[2] bulky substituents,[3] and noncovalent bonding entities[4] onto the periphery of the planar π-systems (Figure 1). Even though this strategy has been quite effective for the design of one- and two-dimensional stacking modes, it is unfortunately unsuitable for the design of three-dimensional stacking modes.

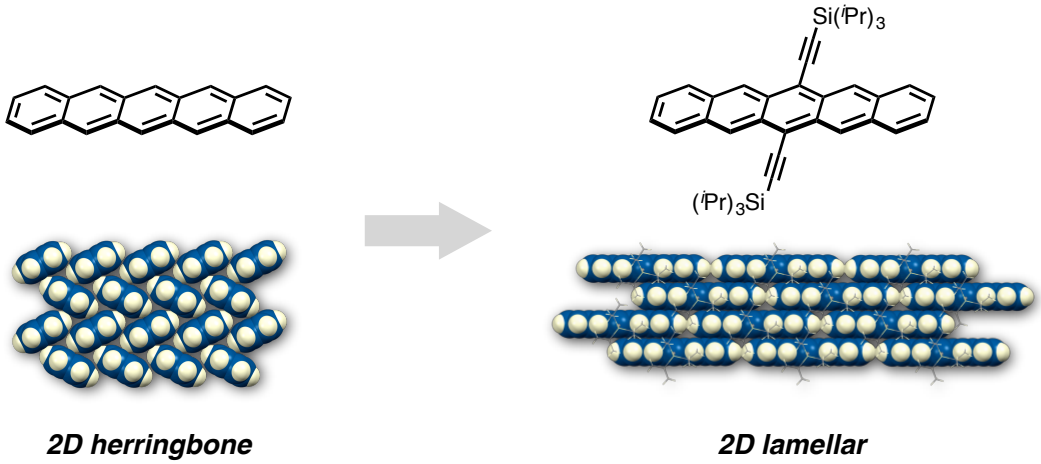

Figure 1. Chemical structures and packing structures of pristine pentacene (left) and substituted pentacene (right) as a representative example of the efforts for controlling the molecular packing of the planar π-conjugated molecules.

Another principal theme is based on employing intrinsically curved π-systems, as a disruption of the planarity of the π-system can diversify the way of molecular filling (Figure 2).[1b,c,e,f,i] In this respect, the most prominent example is fullerenes, whose spherical π-systems can provide omnidirectional π–π interactions, which renders these compounds essential isotropic materials in the context of organic electronics.[5] Apart from fullerenes, multihelicenes have emerged in recent years as another fascinating class of nonplanar π-systems.[6,7] In some cases, their *propeller*-shaped π-systems, comprising several π-blades, can facilitate unconventional multi-dimensional π–π stacking.[7a,b,f] One such example is π-extended double [6]helicene **DH1**, a planar–helix hybrid molecule, described in Chapter 2.[7e] As a consequence of the two relatively planar π-blades connected in a twisting fashion, a contorted three-dimensional lamellar packing was observed for **DH1** in the crystalline state. However, it was predicted that **DH1** showed one-dimensional hole transport path due to the anisotropic electronic couplings.

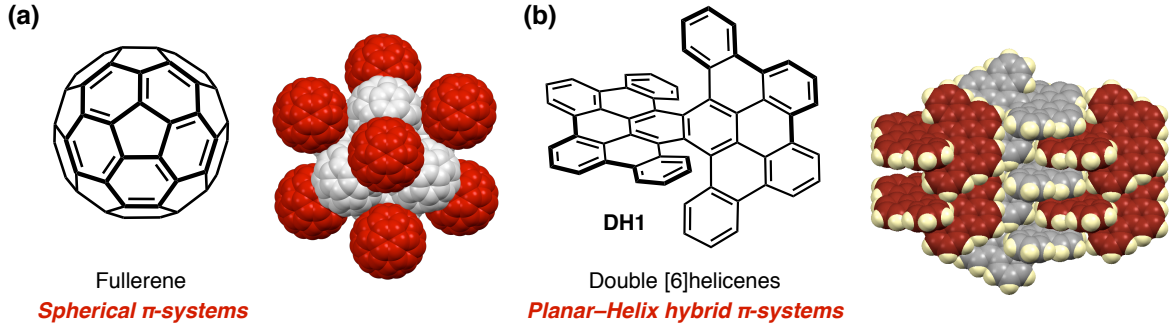

Figure 2. Intrinsically curved π-systems with interesting molecular packing. (a) Fullerene and its omnidirectional π–π stacking (spherical π-systems). (b) π-Extended double [6]helicene (**DH1**) and its three-dimensional π–π stacking (planar–helix hybrid π-systems).

In this chapter, the synthesis of a new π-extended double dithia[6]helicene (**DH3**) is described (Figure 3). With a view toward applications in semiconducting materials, **DH3** was designed in order to show improved solubility and proper frontier molecular orbitals (FMOs) with the support of theoretical calculations. A modular synthesis of the thus-designed **DH3** was accomplished by the Scholl reaction of a naphthalene derivative, which is similar to the precursor of **DH1** and **DH2** described in Chapter 2, and its fundamental electronic properties were examined. As expected from the molecular packing of **DH1**, a fascinating three-dimensional stacking structure was observed for **DH3**. Furthermore, predicted hole transfer integrals in the crystal suggested that **DH3** can be a unique isotropic hole transfer material. When **DH3** was incorporated in an organic field-effect transistor, its unique three-dimensional π–π stacking lattice resulted in a p-type semiconducting ability with a moderate hole mobility.

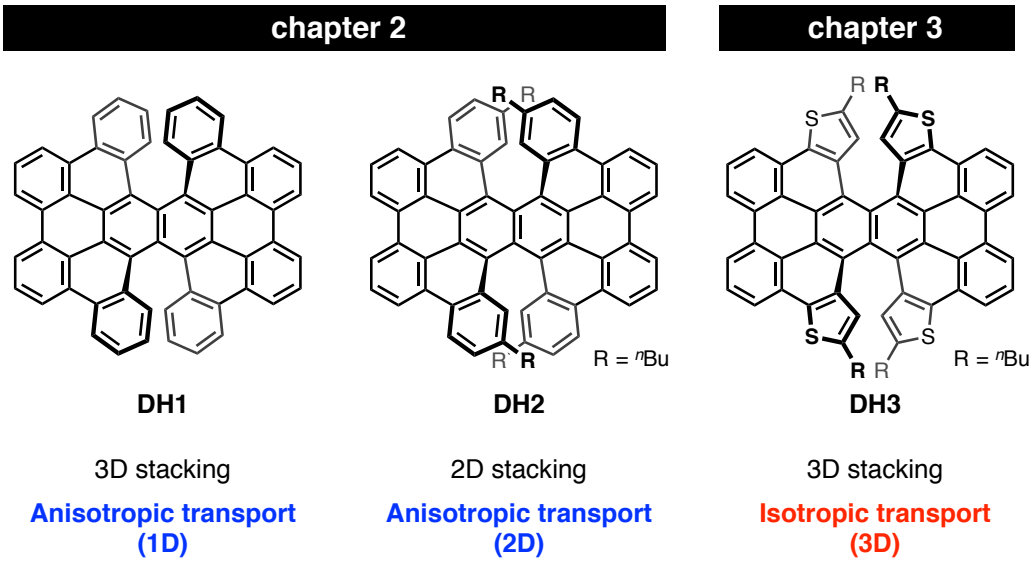

Figure 3. π-Extended double helicenes.

Result and Discussion

Molecular Design for Hole Transport Material

While the theoretical calculation in Chapter 2 predicted excellent hole transport ability of **DH1** and **DH2**, there are, unfortunately, several problems for their application as semiconducting materials.

The parent π-extended double [6]helicene **DH1** consists exclusively of hydrogen and sp^2-hybridized carbon atoms. Therein, two relatively planar tribenzo[*b,n,pqr*]perylene moieties (π-blades) are concatenated to afford the characteristic two-blade propeller structure. The thus formed fully-conjugated [6]helicene substructures afford enantiomers of *twisted*-isomer, *i.e.*, (*P,P*)-**DH1** and (*M,M*)-**DH1**. In the crystalline state, these enantiomers arrange in offset three-dimensional stacks. While this unique racemic crystal structure is fascinating in the application of **DH1** as a semiconducting material, its prohibitively low solubility in common organic solvents has so far hampered device fabrication. Although the alkyl-substituted analog **DH2** shows much higher solubility and an interesting contorted two-dimensional lamellar stacking, *n*-pentane molecules inserted inside π–π stacking may disturb the charge transport.

Another shortcoming of **DH1** and **DH2** is the pronounced naphthalene-like distribution of FMOs at the center of the molecule due to the heavily twisted π-conjugation (Figure 4). The molecular orbitals of **DHs** in the crystalline state overlap intermolecularly via the periphery of the π-system. Therefore, in order to gain larger transfer integrals, the molecular design should afford molecules that contain FMOs with a large distribution on the periphery of the two π-blades.

To satisfy the aforementioned requirements, the π-extended double dithia[6]helicene **DH3**, which exhibits dithia[6]helicene instead of the [6]helicene substructures, was designed. As with the case of **DH2**, *n*-butyl groups were introduced to improve the solubility. In addition, the FMOs of **DH3** displayed an enhanced distribution on the periphery of π-system. This is presumably due to the lower aromaticity of the thiophene rings relative to that of benzene, resulting in a perylene-like distribution of the FMOs on the two π-blades. Especially for **DH3**, an improved charge transport ability was anticipated, considering that a number of thiophene-containing π-conjugated molecules are excellent hole-transporting materials.[8]

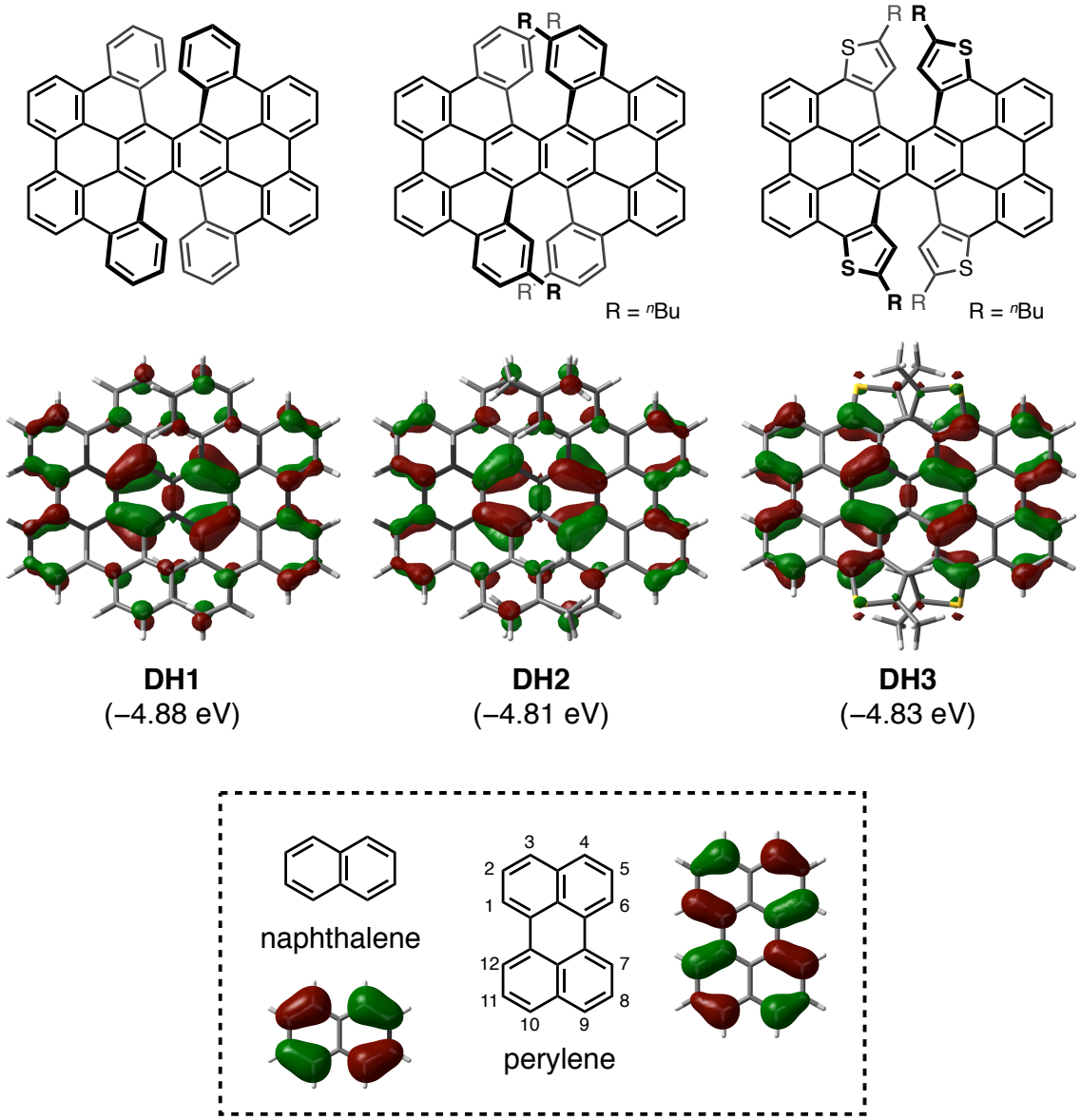

Figure 4. Chemical structures of **DHs**, naphthalene, and perylene, and their estimated distributions (isovalue = 0.03) and energy levels of HOMOs; for the calculations of **DH2** and **DH3**, their methyl analogs were employed (B3LYP/6-31G(d)).

Synthesis and Configurations

In reference to the synthesis of **DH1** and **DH2**, **DH3** was synthesized by the Scholl reaction of the naphthalene derivative with four biaryl units. The nucleophilic substitution of α-lithiated *n*-butylthiophene to 1,2-dibromobenzene (**1**) afforded 2-(2-bromophenyl)-5-butylthiophene (**2**) in 97% yield.[9] Successive lithiation of **2** and treatment with trimethyl borate produced boronic acid **3**, which was used in the following step without purification. Next, the fourfold Suzuki–Miyaura coupling reaction of **3** with 3,6-dibromonaphthalene-2,7-diyl bis(trifluoromethanesulfonate) (**4**) using $Pd_2(dba)_3$, 2-dicyclohexylphosphino-2',6'-dimethoxybiphenyl (SPhos), and Cs_2CO_3 provided **5** in 72% yield. With **5** in hand, oxidative stitching to **DH3** was attempted. During that screening, it was found that using slight excess of $MoCl_5$ (20 equiv) generated tetrachlorinated **DH3-Cl$_4$** in 26% yield. Since treatment of with lower proportions of the oxidant (12–16 equiv) did not afford well-defined products, it is likely that chlorination immediately after cyclization probably served to cap the reactive sites of intermediate **DH3**, *i.e.*, the most nucleophilic positions corresponding to those of perylene (3, 4, 9, and 10), thus suppressing unfavorable side reactions such as polymerization and decompositions.[10] This assumption is consistent with the enhanced perylene-like distribution of the HOMO of **DH3**. Thus, chlorination, which is often avoided during oxidative stitching in general, plays an important role in the synthesis of **DH3-Cl$_4$**. A subsequent palladium-catalyzed dechlorination of **DH3-Cl$_4$** furnished the target double helicene **DH3** quantitatvely.[11] A single-crystal X-ray diffraction analysis of **DH3** (*vide infra*) revealed that the configuration of the obtained double helicene is commensurate with the *twisted*-isomers (*P,P*)-**DH3** and (*M,M*)-**DH3**. Similar to the synthesis of **DH2**, the *meso*-isomers (*P,M*)-**DH3** or (*P,M*)-**DH3-Cl$_4$** were not detected.

Scheme 1. Synthesis of **DH3**.

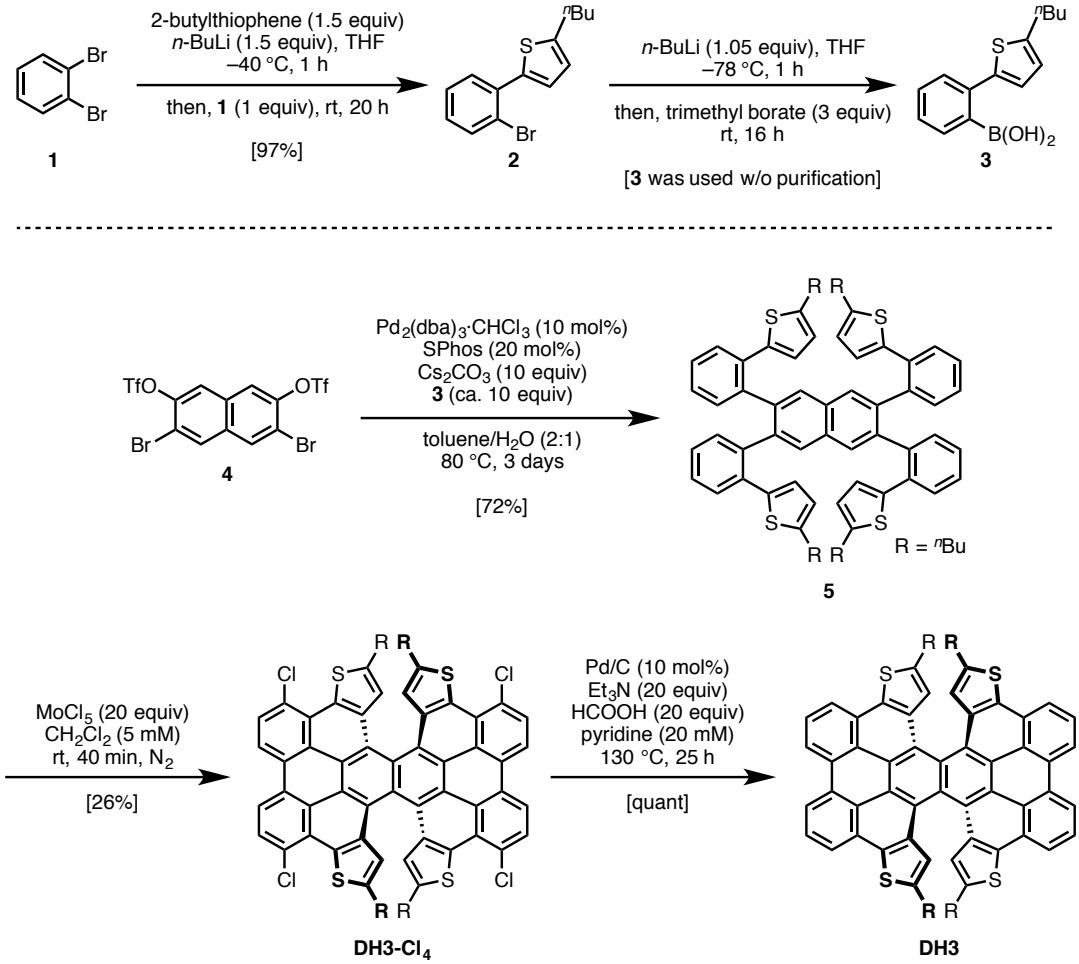

To elucidate the thermodynamic stability and the dynamic behavior of the diastereomers of **DH3**, DFT calculations were carried out at the B3LYP/6-31G(d) level for the *twisted*-isomers, the *meso*-isomers, and the interjacent transition states. In Chapter 2, it has already been predicted that *twisted*-**DH1** should be thermodynamically more stable than *meso*-**DH1** (0.9 kcal·mol^{-1}) and that the activation barrier for the *twisted*-to-*meso* interconversion should amount to 43.5 kcal·mol^{-1} (Figure 4a in Chapter 2). It should also be noted that in case of double dithia[6]helicene **DH3**, the *meso*-**DH3** is substantially destabilized (7.2 kcal·mol^{-1}) relative to the *twisted*-**DH3** (Figure 5). The absence of *meso*-**DH3-Cl$_4$** after the Scholl reaction could thus potentially be attributed to the inaccessibility of *meso*-**DH3** during the oxidative cyclization, which may be explained by its highly strained structure. A significant destabilization was also observed for the transition state of the *twisted*-to-*meso* interconversion of **DH3**, for which an activation barrier of 50.8 kcal·mol^{-1} was estimated. This higher barrier compared with carbo[6]helicene analogs was attributed to the difference of the direction of the internal C–H bonds within the helixes. On account of the smaller interior bond angles of the thiophene rings, the congestion between the two C–H bonds within the helix should prevent the two helical termini to get into close spatial proximity during the transition state. Indeed, a closer proximity of the hydrogen atoms within the helix was observed in the optimized transition state of **DH3** (1.81 Å) relative to that of **DH1** (1.88 Å), inferring a larger steric demand. In Chapter 2, it has already been confirmed that the isomerization of *meso*-**DH1** to *twisted*-**DH1** requires high temperature (> 230 °C). Therefore, although the optical separation of **DH3** was unsuccessful, its interconversion should need severely elevated temperatures and should thus be difficult to observe.

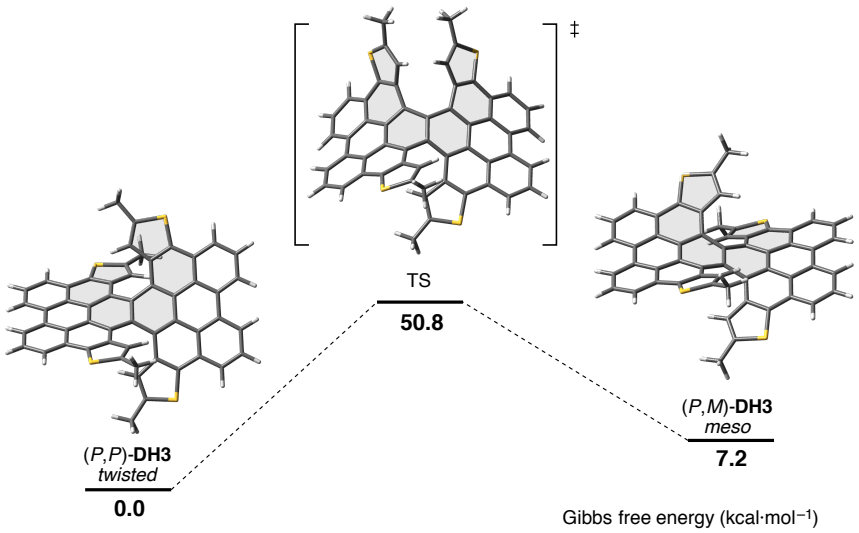

Figure 5. The isomerization between (*P*,*P*)-**DH3** and (*P*,*M*)-**DH3**. For the calculations at the B3LYP/6-31G(d) level of theory, the *n*-butyl groups are replaced with methyl groups.

Electronic Properties

In order to investigate the electronic influence of thiophene ring, the photophysical properties of **DH3** was compared with those of **DH2** (Figure 6). Dithia[6]helicene analog **DH3** afforded a similar absorption spectrum with **DH2**, with a hyperchromic effect and a clearer vibronic structure. Absorption maxima for **DH3** were observed at 509, 477, 445, and 405 nm (most intense peak). A clear vibronic structure was also observed for the fluorescence spectrum of **DH3**, which exhibited maxima at 524 and 558 nm. These maxima are comparable, yet slightly blue-shifted relative to those of **DH2** (534 nm and a shoulder emission at ~560 nm). Notably, the fluorescence quantum yield of **DH3** (Φ_F = 0.20) was much higher than those of carbohelicene congeners (Φ_F = 0.052 for *twisted*-**DH1**; 0.059 for *twisted*-**DH2**), which suggests a distinctive influence of the helical substructures on the entire π-systems. Bathochromic shift was observed in the spectra of **DH3-Cl$_4$** when compared with those of **DH3**. A slight increase of the fluorescence quantum yield was observed upon chlorination (Φ_F = 0.29 for **DH3-Cl$_4$**).

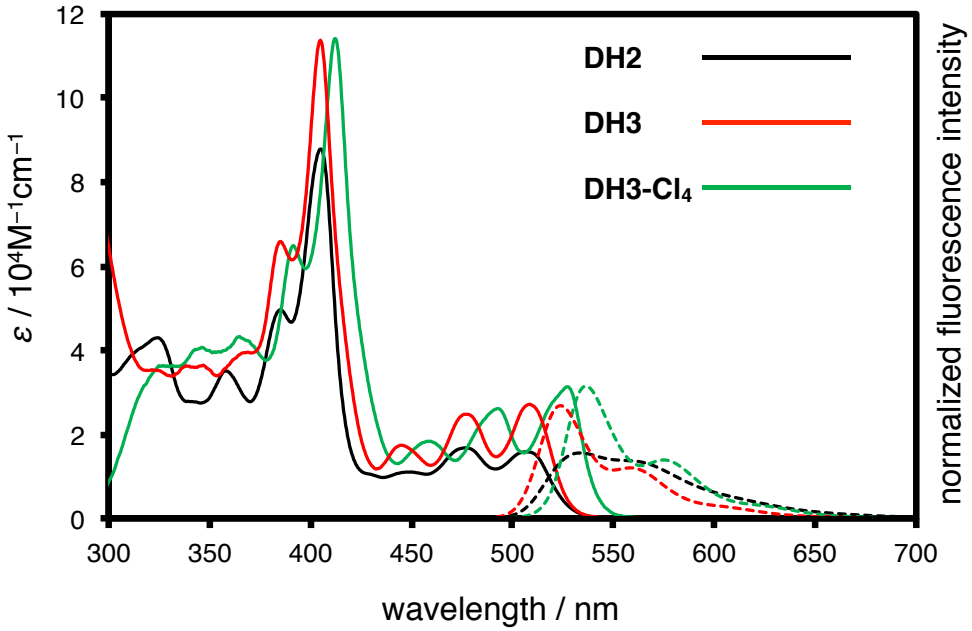

Figure 6. UV–Vis absorption spectra (solid lines) and fluorescence spectra (broken lines) of **DH2** and **DH3** in chloroform solution.

The improved solubility in organic solvents enables us to investigate the electrochemical behavior of π-extended double helicenes by cyclic voltammetry technique (vs FcH/FcH^+) (Figure 7). Double dithia[6]helicenes exhibited highly reversible two-step oxidation wave with the half-wave potentials $E_{1/2}$ of 0.50 V and 0.83 V for **DH3-Cl$_4$**, and 0.43 V and 0.80 V for **DH3**, respectively, indicating good electrochemical stability of oxidized species. When comparing the cyclic voltammogram of **DH3** with that of **DH2** ($E_{1/2}$ of 0.45 V and 0.92 V), a negligible difference regarding the first oxidation potential was observed as indicated by the DFT-derived HOMO energy levels. In contrast, a moderate cathodic shift of the second oxidation potential (0.12 V) was observed for **DH3**, which may be rationalized in terms of a stabilization of the cation by the sulfur atoms.

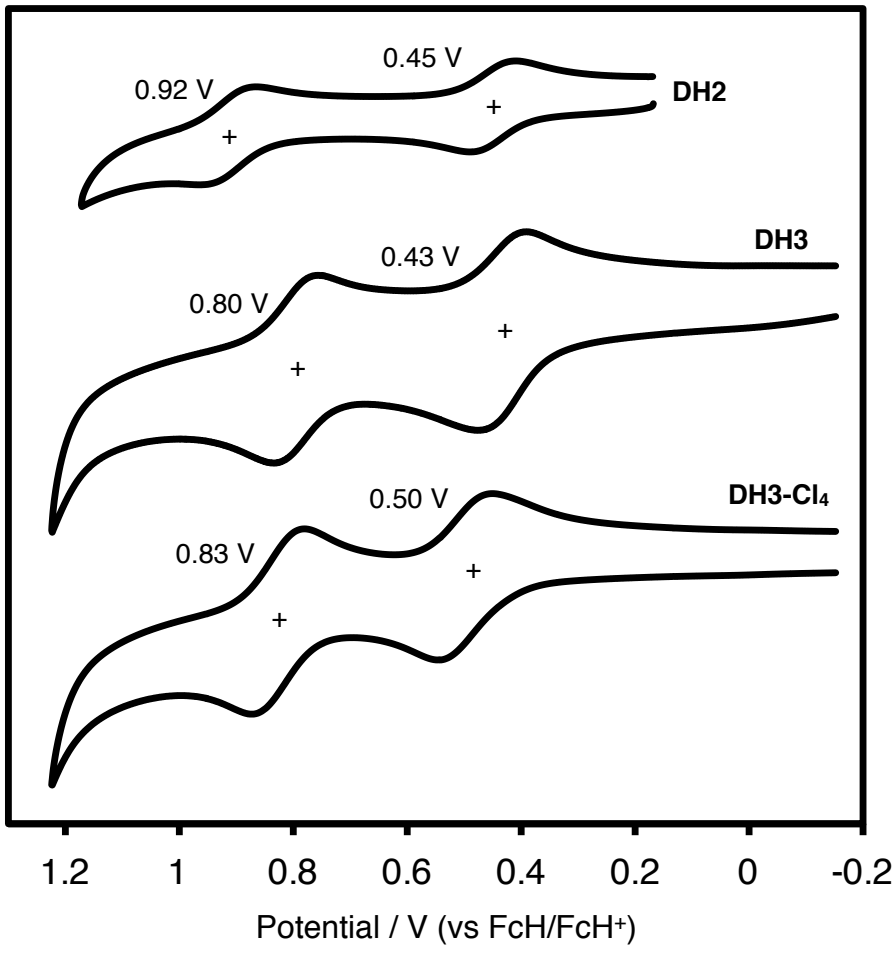

Figure 7. Cyclic voltammograms of π-extended double helicenes in dichloromethane solution containing 100 mM of $TBAPF_6$ at scan rate of 0.1 $V \cdot s^{-1}$. FcH = ferrocene.

Crystal Structures

The crystal structure of **DH3** was revealed by single-crystal X-ray diffraction analysis (Figure 8). The dihedral angle of the two blades of **DH3** reached to 52.1°. As expected initially, this profound distortion of π-system realized a unique three-dimensional π–π stacking lattice. One of the two π-blades per molecule (red molecule) participates in a slipped one-dimensional heterochiral stacking ($d_{\pi-\pi}$ = 3.43 Å) illustrated by the stacking along the blue–red–blue molecules, while the other π-blade participates in a slipped one-dimensional heterochiral stacking ($d_{\pi-\pi}$ = 3.51 Å) in a different direction, illustrated by the stacking along the green–red–green molecules. Therefore, these alternately arranged two types of stackings are electronically connected to each other, providing an unprecedented three-dimensional lattice of π–π stacking.

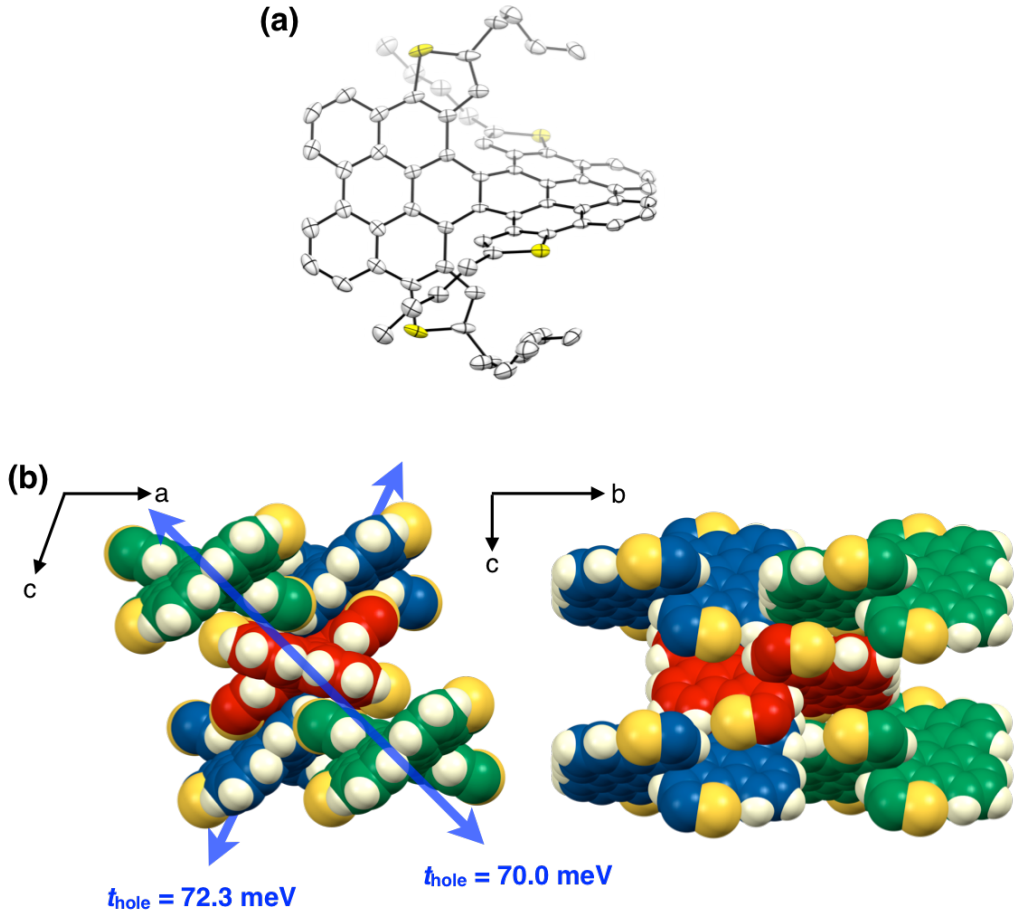

Figure 8. (a) ORTEP drawings of (*M*,*M*)-**DH3** with 50% probability (the hydrogen atoms and the minor part of the disordered moieties are omitted for clarity). (b) Packing structure of **DH3** (*n*-butyl groups are omitted for clarity; homochiral molecules on the same *ac*-plane are colored in blue, red, and green).

Conductive Behavior

The excellent reversibility of the electrochemical oxidation and the unique molecular packing in the π-extended helicenes motivated us to investigate their semiconducting properties. Initially, TRMC measurements[12] were carried out in order to estimate their charge transport properties (Figure 9). The highest TRMC signal was observed for **DH3** ($\phi\Sigma\mu$ = 1.1×10^{-4} $cm^2\cdot V^{-1}\cdot s^{-1}$; ϕ: photo-generation efficiency of the charge carrier; $\Sigma\mu$: local mobility), followed by **DH1** (7.8×10^{-5} $cm^2\cdot V^{-1}\cdot s^{-1}$), **DH2** ($6.1\times10^{-5}$ $cm^2\cdot V^{-1}\cdot s^{-1}$), and **DH3-Cl$_4$** ($4.5\times10^{-5}$ $cm^2\cdot V^{-1}\cdot s^{-1}$). These results clearly demonstrate the charge transport ability of π-extended double helicenes, rendering these compounds promising prospects for organic semiconducting materials with unique molecular packing.

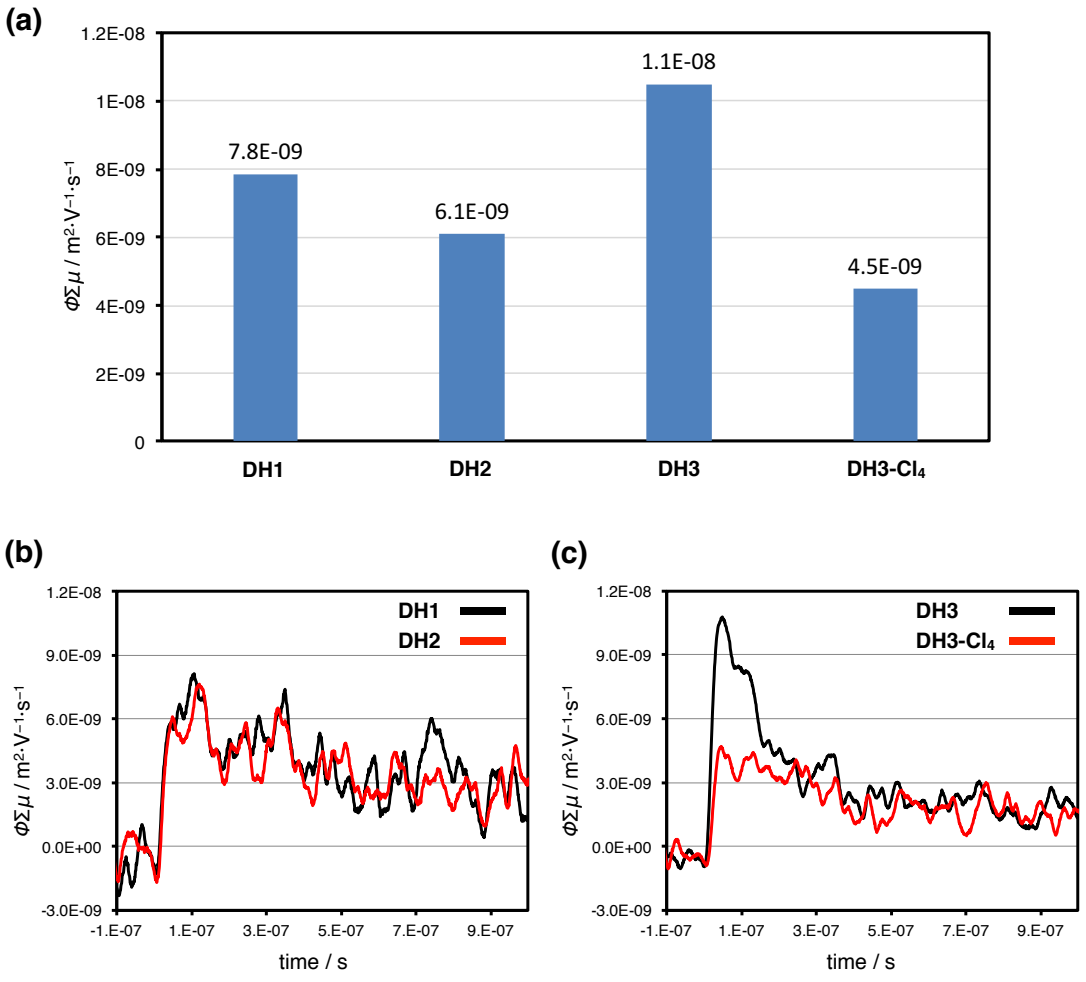

Figure 9. Transient conductivity observed for π-extended helicenes. Recrystallized samples were used in each case.

Considering its high TRMC signal, its solubility in organic solvents, and the absence of solvent molecules in its crystal structure, the transistor ability of **DH3** was also examined (Figure 10). For that purpose, a top-contact/bottom-gate transistor was fabricated on Si/SiO_2 substrates by a drop-coat method using toluene solutions of **DH3**, and subsequent gold electrode evaporation. The field-effect transistor of the defective crystalline domain of **DH3** functioned as a p-type semiconductor, exhibiting a hole mobility (μ_h) of 2.0×10^{-3} $cm^2\cdot V^{-1}\cdot s^{-1}$ in air. The highest mobility observed among several trials was 8.0×10^{-3} $cm^2\cdot V^{-1}\cdot s^{-1}$.

To shed more light on the hole-transporting ability, theoretical calculations at PW91/DZP level on ADF2014 program was conducted, and the transfer integrals for hole in the crystal of **DH3** were evaluated. As mentioned above, there exist two types of π–π stacking modes. The corresponding transfer integrals for hole were calculated to be 72.3 meV and 70.0 meV (Figure 8b). These values implied that the crystal structure of **DH3** provides an isotropic hole-transporting pathway spreading over the three-dimensional π–π stacking lattice.

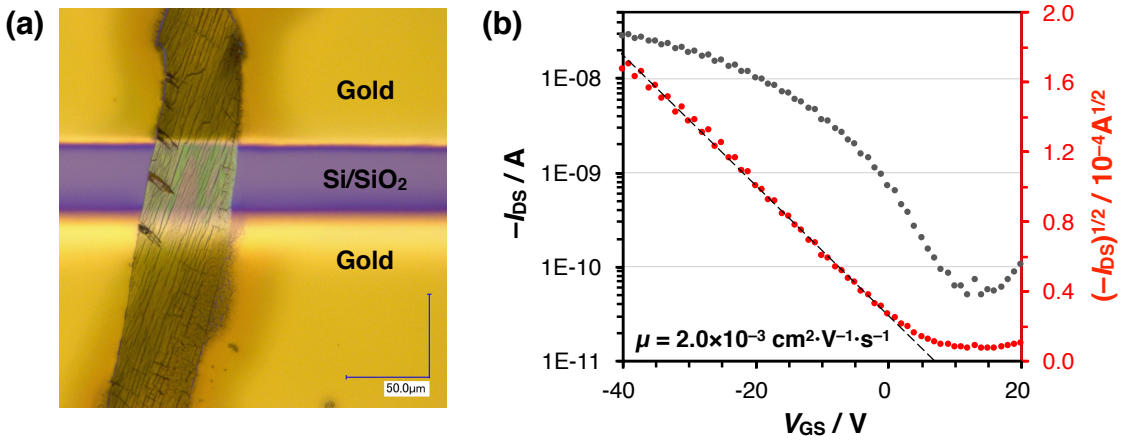

Figure 10. (a) Image of the OFET of **DH3** fabricated on a Si/SiO_2 substrate. (b) Transfer characteristics at $V_D = -50$ V.

Conclusion

In this chapter, the synthesis of π-extended dithia[6]helicenes with improved solubility and custom-tailored FMOs was disclosed. A comparison of carbo[6]helicene **DH2** and dithia[6]helicene **DH3** showed that an annulation with thiophene rings results in various perturbations on the double helical π-system, including the distribution of FMOs, the thermodynamic stability of diastereomers, the interconversion barriers, the photophysical properties, and the electrochemical behavior. Single-crystal X-ray diffraction analyses revealed that the planar–helix hybrid π-system of **DH3** displays an unprecedented three-dimensional π–π stacking lattice comprising two distinct slipped stackings. TRMC measurements confirmed charge transport properties for these π-extended helicenes, and indeed, an organic field-effect transistor using **DH3** on a Si/SiO_2 substrate functions as a p-type transistor with a hole mobility of 2.0×10^{-3} $cm^2\cdot V^{-1}\cdot s^{-1}$. The ADF calculations predicted that the two different stacking modes of **DH3** have same degree of hole transfer integrals, which implied that the crystal structure of **DH3** provides an isotropic hole-transporting pathway spreading over the three-dimensional π–π stacking lattice.

Experimental Section

General

Unless otherwise noted, all materials including dry solvents were obtained from commercial suppliers and used without further purification. 3,6-Dibromonaphthalene-2,7-diyl bis(trifluoromethanesulfonate) (**4**)[13] was prepared according to the procedure reported in the literature. Unless otherwise noted, all reactions were performed with dry solvents under an atmosphere of nitrogen in dried glassware with standard vacuum-line techniques. All work-up and purification procedures were carried out with reagent-grade solvents in air.

Analytical thin-layer chromatography (TLC) was performed using E. Merck silica gel 60 F_{254} precoated plates (0.25 mm). The developed chromatogram was analyzed by UV lamp (254 nm and 365 nm). High-resolution mass spectra (HRMS) were obtained from a JEOL JMS-S3000 SpiralTOF (MALDI-TOF MS). Cyclic voltammetry (CV) measurements were performed by BAS ALS-600D Electrochemical Analyzer. Melting points were measured on a MPA100 Optimelt automated melting point system. NMR spectra were recorded on a JEOL JNM-ECA-600 (^{1}H 600 MHz, ^{13}C 150 MHz) or a JEOL ECA 600II spectrometer with Ultra COOLTM probe (^{1}H 600 MHz, ^{13}C 150 MHz). Chemical shifts for ^{1}H NMR are expressed in parts per million (ppm) relative to $CHCl_3$ (δ 7.26 ppm) or C_2DHCl_4 (δ 6.00 ppm). Chemical shifts for ^{13}C NMR are expressed in ppm relative to $CDCl_3$ (δ 77.16 ppm) or $C_2D_2Cl_4$ (δ 73.78 ppm). Data are reported as follows: chemical shift, multiplicity (s = singlet, d = doublet, t = triplet, m = multiplet, br = broad signal), coupling constant (Hz), and integration.

Synthesis of 2

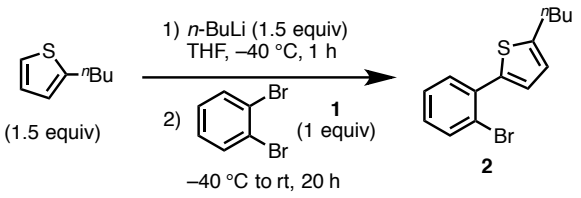

To a solution of 2-butylthiophene (8.42 g, 60.0 mmol, 1.5 equiv.) in THF (100 mL) was added a pentane solution of *n*-butyllithium (1.6 M, 37.5 mL, 60 mmol, 1.5 equiv) at –40 °C dropwise over 20 min, and the mixture was stirred for 1 h under nitrogen. 1,2-Dibromobenzene (**1**) (9.44 g, 40.0 mmol, 1 equiv) was added dropwise over 10 min, and then the reaction mixture was allowed to warm to room temperature. After stirring the mixture for 20 h, the reaction was quenched by the addition of saturated NH_4Cl aqueous solution. The organic layer was extracted with Et_2O, washed with brine, dried over Na_2SO_4, and then evaporated *in vacuo*. The crude material was purified by silica gel column chromatography (eluent: hexane) to afford **2**

(11.5 g, 97%) as a colorless oil.

^{1}H NMR (600 MHz, $CDCl_3$) δ 7.65 (dd, *J* = 8.0, 1.2 Hz, 1H), 7.46 (dd, *J* = 7.7, 1.6 Hz, 1H), 7.30 (ddd, *J* = 7.5, 7.5, 1.2 Hz, 1H), 7.14 (ddd, *J* = 7.9, 7.4, 1.7 Hz, 1H), 7.12 (d, *J* = 3.5 Hz, 1H), 6.77 (dt, *J* = 3.5, 0.9 Hz, 1H), 2.84 (t, *J* = 7.7 Hz, 2H), 1.71 (quintet, *J* = 7.6 Hz, 2H), 1.44 (sextet, *J* = 7.4 Hz, 2H), 0.96 (t, *J* = 7.4 Hz, 3H); ^{13}C NMR (150 MHz, $CDCl_3$) δ 147.1 (4º), 139.1 (4º), 135.8 (4º), 133.8 (CH), 131.9 (CH), 128.7 (CH), 127.6 (CH), 127.5 (CH), 124.1 (CH), 122.7 (CH), 33.9 (CH_2), 30.0 (CH_2), 22.4 (CH_2), 14.0 (CH_3); HRMS (FAB) *m/z* calcd for $C_{14}H_{15}BrS$ $[M+H]^+$: 294.0078, found: 294.0087.

Synthesis of 5

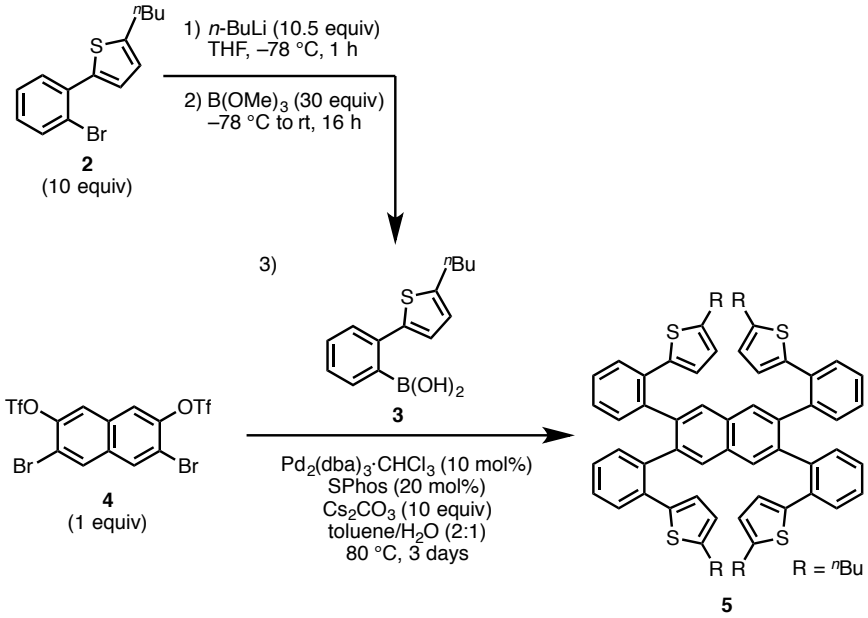

To a solution of **2** (5.90 g, 20.0 mmol, 10 equiv) in THF (100 mL) was added a pentane solution of *n*-butyllithium (1.6 M, 13.1 mL, 21.0 mmol, 10.5 equiv) at –78 °C dropwise over 10 min, and the mixture was stirred for 1 h under nitrogen. Trimethoxyborane (6.69 mL, 60.0 mmol, 30 equiv) was added, and then the reaction mixture was allowed to warm to room temperature. After stirring the mixture for 16 h, the reaction was quenched by the addition of saturated NH_4Cl aqueous solution. The organic layer was extracted with Et_2O, washed with brine, dried over Na_2SO_4, and then evaporated *in vacuo* to afford a crude mixture of (2-(5-butylthiophen-2-yl)phenyl)boronic acid (**3**) (5.23 g, quant) as a white slurry. Compound **3** was used in next step without further purification.

To a solution of 3,6-dibromonaphthalene-2,7-diyl bis(trifluoromethanesulfonate) (**4**) (1.16 g, 2.00 mmol, 1 equiv), **3**, $Pd_2(dba)_3{\cdot}CHCl_3$ (207 mg, 0.20 mmol, 10 mol%), and SPhos (164 mg, 0.40 mmol, 20 mol%) in toluene (10 mL) was added a solution of Cs_2CO_3 (6.52 g, 20.0

mmol, 10 equiv) in H_2O (5 mL), and the mixture was stirred at 80 °C for 3 days under nitrogen. After cooling the mixture to room temperature, the reaction mixture was quenched by the addition of 2N HCl aqueous solution. The organic layer was extracted with ethyl acetate, washed with brine, dried over Na_2SO_4, and then evaporated *in vacuo*. A $CHCl_3$ solution of the crude material was passed through a pad of silica gel and dried again. Recrystallization from $CHCl_3$/*n*-hexane bilayer system afforded **5** (1.42 g, 72%) as a pale yellow crystal.

^{1}H NMR (600 MHz, $C_2D_2Cl_4$, 130 °C) δ 7.81 (s, 4H), 7.34 (dd, *J* = 7.7, 0.8 Hz, 4H), 7.19 (td, *J* = 7.6, 1.3 Hz, 4H), 7.02 (td, *J* = 7.5, 1.1 Hz, 4H), 6.75 (d, *J* = 7.6 Hz, 4H), 6.53 (d, *J* = 3.8 Hz, 4H), 6.31 (d, *J* = 3.8 Hz, 4H), 2.80 (t, *J* = 7.6 Hz, 8H), 1.71 (quintet, *J* = 7.4 Hz, 8H), 1.49 (sextet, *J* = 7.4 Hz, 8H), 1.01 (t, *J* = 7.4 H, 12H); ^{13}C NMR (150 MHz, $C_2D_2Cl_4$, 130 °C) δ 145.5 (4º), 141.0 (4º), 139.7 (4º), 138.8 (4º), 133.7 (4º), 132.2 (4º), 131.2 (CH), 129.9 (CH), 128.3 (CH), 126.7 (CH), 126.0 (CH), 125.9 (CH), 123.5 (CH), 33.4 (CH_2), 29.4 (CH_2), 21.8 (CH_2), 13.3 (CH_3); HRMS (MALDI-TOF MS) *m/z* calcd for $C_{66}H_{64}S_4Na$ $[M+Na]^+$: 1007.3789, found: 1007.3797; mp: 186–187 ºC (recrystallized from dichloromethane/*n*-hexane).

Synthesis of DH3-Cl$_4$

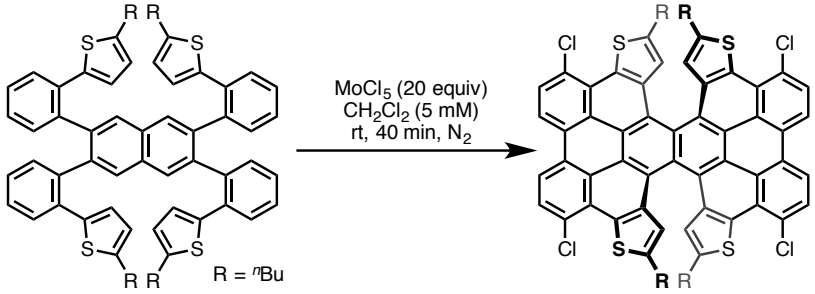

To a solution of **5** (493 mg, 0.500 mmol, 1 equiv) in dichloromethane (100 mL) was added $MoCl_5$ (2.73 g, 10.0 mmol, 20 equiv) at room temperature, and then the reaction mixture was stirred for 40 min under nitrogen. The reaction was quenched by the addition of MeOH/$CHCl_3$ (7:3, 100 mL) solution and the resultant solution was directly passed through a pad of silica-gel with $CHCl_3$ eluent. The filtrate was evaporated *in vacuo*. Recrystallization from nitrobenzene afforded **8** (143 mg, 26%) as a red crystal.

^{1}H NMR (600 MHz, $CDCl_3$) δ 8.92 (d, *J* = 8.6 Hz, 4H), 8.18 (d, *J* = 8.5 Hz, 4H), 6.99 (s, 4H), 2.57 (dt, ^2J = 14.9, ^3J = 7.3 Hz, 4H), 2.49 (dt, ^2J = 15.1, ^3J = 7.4 Hz, 4H), 1.39 (quintet, *J* = 7.5 Hz, 8H), 1.17–1.07 (m, 8H), 0.83 (t, *J* = 7.7 Hz, 12H); ^{13}C NMR (150 MHz, $CDCl_3$) δ 132.5 (4º), 130.3 (4º), 129.2 (CH), 129.1 (4º), 127.1 (4º), 125.7 (4º), 123.6 (CH), 123.0 (4º), 122.7 (4º), 121.8 (4º), 120.5 (CH), 33.7 (CH_2), 29.6 (CH_2), 21.9 (CH_2), 14.0 (CH_3); HRMS (MALDI TOF-MS) *m/z* calcd for $C_{66}H_{48}Cl_4S_4$ $[M]^+$: 1110.1363, found: 1110.1371; mp: >300 ºC (recrys-

tallized from nitrobenzene).

Synthesis of DH3

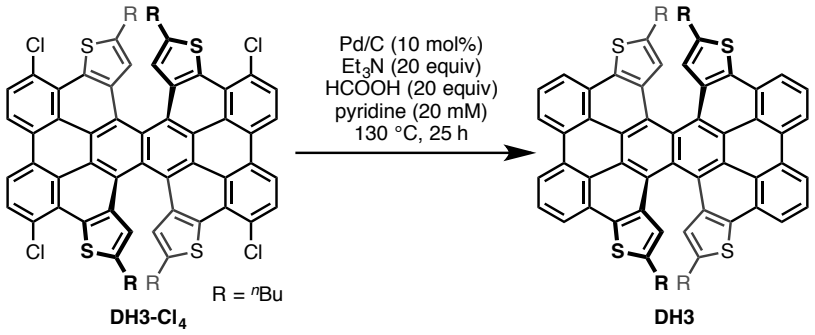

A mixture of **DH3-Cl$_4$** (22.2 mg, 0.0200 mmol, 1 equiv), 5% Pd/C containing 55% water (9.5 mg, 2.0 μmol, 10 mol%), triethylamine (40.5 mg, 0.400 mmol, 20 equiv), and formic acid (18.4 mg, 0.400 mmol, 20 equiv) in pyridine (1 mL) was stirred at 130 °C for 25 h in a 20-mL Schlenk tube sealed with J. Young® O-ring tap. After cooling to room temperature, the precipitate was dissolved in $CHCl_3$ and Pd/C residue was removed by filtration through Celite®. The filtrate was washed with water, dried with over Na_2SO_4, and then evaporated *in vacuo* to afford **3** (20.1 mg, quant) as a red solid.

^{1}H NMR (600 MHz, $CDCl_3$) δ 9.07 (dd, J = 7.9, 0.72 Hz, 4H), 8.45 (dd, J = 7.7, 0.72 Hz, 4H), 8.10 (t, J = 7.7 Hz, 4H), 6.97 (s, 4H), 2.61 (dt, ^2J = 15.4, ^3J = 7.4 Hz, 4H), 2.56 (dt, ^2J = 14.9, ^3J = 7.6 Hz, 4H), 1.46–1.40 (m, 8H), 1.22–1.13 (m, 8H), 0.83 (t, J = 7.4 Hz, 12H); ^{13}C NMR (150 MHz, $CDCl_3$) δ 144.9 (4º), 136.5 (4º), 135.6 (4º), 131.8 (4º), 129.2 (4º), 127.0 (CH), 125.2 (CH), 123.8 (4º), 122.9 (4º), 122.6 (CH), 122.1 (4º), 121.8 (4º), 120.4 (CH). 33.7 (CH_2), 30.2 (CH_2), 21.9 (CH_2), 14.1 (CH_3); HRMS (MALDI TOF-MS) *m/z* calcd for $C_{66}H_{52}S_4$ $[M]^+$: 972.2952, found: 972.2965; mp: >300 ºC (recrystallized from nitrobenzene).

Photophysical Study

UV–Vis absorption spectra were recorded on a Shimadzu UV-3510 spectrometer with a resolution of 0.5 nm. Emission spectra were measured with an FP-6600 Hitachi spectrometer with a resolution of 0.2 nm. CD spectra were measured with a JASCO FT/IR6100. Dilute solutions in degassed spectral grade chloroform in a 1 cm square quartz cell were used for measurements. Absolute fluorescence quantum yields were determined with a Hamamatsu C9920-02 calibrated integrating sphere system upon excitation at 400 nm for **DH3-Cl$_4$** and at 405 nm for **DH3**.

Time-Resolved Microwave Conductivity Measurement

Transient photoconductivity was measured by flash-photolysis time-resolved microwave conductivity (FP-TRMC). A resonant cavity was used to obtain a high degree of sensitivity in the measurement of conductivity. The resonant frequency was set at ~9.1 GHz and the microwave power was set at 3 mW, so that the electric field of the microwave was sufficiently small not to disturb the motion of charge carriers. The value of conductivity is converted to the product of the quantum yield ϕ and the sum of charge carrier mobilities $\Sigma\mu$, by $\phi\Sigma\mu = \Delta\sigma(eI_0F_{\text{light}})^{-1}$, where e, I_0, F_{light}, and $\Delta\sigma$ are the unit charge of a single electron, incident photon density of excitation laser (photons/m^2), a correction (or filling) factor (/m), and a transient photoconductivity, respectively. The charge of conductivity is equivalent with $\Delta P_r/(AP_r)$, where ΔP_r, P_r, and A are change of reflected microwave power, a power of reflected microwave, and a sensitivity factor [(S/m)$^{-1}$], respectively. Third harmonic generation (355 nm) from an Optical Parametric Oscillator (OPO) of a ND:YAG laser (Continuum Surelite II, 5–8 ns pulse duration) was used as an excitation source. The incident photon density was set at 4.6×10^{15} photons/cm^2. The sample was set at the highest electric field in a resonant cavity. FP-TRMC experiments were performed at room temperature.

Organic Field-Effect Transistor Fabrication

OFETs were fabricated in a top-contact/bottom-gate configuration on a heavily doped n^+-Si (100) wafer with 300-nm thermal silicon oxide (SiO_2) as the dielectric layer. The Si/SiO_2 substrate was cleaned by a sonication in acetone and 2-propanol, and dried before use. A crystalline domain of **3** was grown on the Si/SiO_2 substrate by drop-coat method using toluene solution (ca. 0.5 mg/mL) at room temperature. On top of the organic crystalline domain, gold films (30 nm) as drain and source electrodes were deposited through a shadow mask. The characteristics of the devices were measured at room temperature in air with a Keithly 4200. Field-effect hole mobility (μ_h) was calculated in the saturation regime (V_{DS} = –50 V) of the I_{DS} using the following equation, $I_{DS} = (WC_i/2L)\mu_h(V_{GS}-V_{th})^2$, where W and L are the drain-source channel width (W) and length (L), C_i is the capacitance of the SiO_2 insulator, and V_{GS} and V_{th} are the gate and threshold voltages, respectively.

X-ray Crystallography

Single crystals of **DH3** suitable for X-ray crystal structure analysis were obtained by re-crystallization of a racemic mixture from hot nitrobenzene. Details of the crystal data and a summary of the intensity data collection parameters for **DH3** are listed in Table 1. A suitable crystal was mounted with mineral oil on a glass fiber and transferred to the goniometer of a Rigaku PILATUS diffractometer. Graphite-monochromated Mo Kα radiation (λ = 0.71075 Å) was used. The structures were solved by direct methods with (SIR-97)[14] and refined by full-matrix least-squares techniques against F^2 (SHELXL-97).[15] The intensities were corrected for Lorentz and polarization effects. The non-hydrogen atoms were refined anisotropically. Hydrogen atoms were placed using AFIX instructions.

Table 1. Crystallographic data and structure refinement details for **DH3**.

	DH3
formula	$C_{66}H_{52}S_4$
fw	973.31
T (K)	123(2)
λ (Å)	0.71075
cryst syst	Monoclinic
space group	$C2/c$
a (Å)	16.046(3)
b (Å)	26.399(5)
c (Å)	11.908(2)
α	90°
β	110.469(3)°
γ	90°
V (Å^3)	4725.7(15)
Z	4
D_{calc} (g / cm^3)	1.368
μ (mm^{-1})	0.247
F(000)	2048
cryst size (mm)	0.20 × 0.05 × 0.01
θ range	3.087–25.00°
reflns collected	17282
indep reflns/R_{int}	4144/0.0344
params	354
GOF on F^2	1.114
R_1, wR_2 [$I>2\sigma(I)$]	0.0753, 0.1903
R_1, wR_2 (all data)	0.0927, 0.2061

Computational Study

The Gaussian 09 program[16] running on a SGI Altix4700 system was used for optimization (B3LYP/6-31G(d)).[17] All structures were optimized without any symmetry assumptions. Zero-point energy, enthalpy, and Gibbs free energy at 298.15 K and 1 atm were estimated from the gas-phase studies unless otherwise noted. Harmonic vibration frequency calculations at the same level were performed to verify all stationary points as local minima (with no imaginary frequency) or transition states (with one imaginary frequency). Visualization of the results was performed by use of GaussView 5.0 software.

Table 2. Uncorrected and thermal-corrected (298 K) energies of stationary points (Hartree).[a]

structure	*E*	*E* + *ZPE*	*H*	*G*
twisted-**DH2**	-2384.48556171	-2383.708006	-2383.662450	-2383.784239
twisted-**DH3**	-3667.55069824	-3666.906436	-3666.862250	-3666.979972
meso-**DH3**	-3667.53900632	-3666.895159	-3666.850933	-3666.968493
TS (**DH3**)	-3667.47120342	-3666.827778	-3666.784555	-3666.899034

a) *E*: electronic energy; *ZPE*: zero-point energy; *H* (= $E + ZPE + E_{vib} + E_{rot} + E_{trans} + RT$): sum of electronic and thermal enthalpies; *G* (= $H - TS$): sum of electronic and thermal free energies.

Reference

1. For selected examples on the control of molecular packing for functional materials, see: (a) Haedler, A. T.; Kreger, K.; Issac, A.; Wittmann, B.; Kivala, M.; Hammer, N.; Köhler, J.; Schmidt, H.-W.; Hildner, R. *Nature* **2015**, *523*, 196. (b) Hatakeyama, T.; Hashimoto, S.; Oba, T.; Nakamura, M. *J. Am. Chem. Soc.* **2012**, *134*, 19600. (c) Pola, S.; Kuo, C.-H.; Peng, W.-T.; Islam, M. M.; Chao, I.; Tao, Y.-T. *Chem. Mater.* **2012**, *24*, 2566. (d) Würthner, F.; Kaiser, T. E.; Saha-Möller, C. R. *Angew. Chem., Int. Ed.* **2011**, *50*, 3376. (e) Amaya, T.; Seki, S.; Moriuchi, T.; Nakamoto, K.; Nakata, T.; Sakane, H.; Saeki, A.; Tagawa, S.; Hirao, T. *J. Am. Chem. Soc.* **2009**, *131*, 408. (f) Kaiser, T. E.; Wang, H.; Stepanenko, V.; Würthner, F. *Angew. Chem., Int. Ed.* **2007**, *46*, 5541. (g) Bhosale, S.; Sisson, A. L.; Talukdar, P.; Fürstenberg, A.; Banerji, N.; Vauthey, E.; Bollot, G.; Mareda, J.; Röger, C.; Würthner, F.; Sakai, N.; Matile, S. *Science* **2006**, *313*, 84. (h) Tanaka, H.; Okano, Y.; Kobayashi, H.; Suzuki, W.; Kobayashi, A. *Science* **2001**, *291*, 285. (i) Verbiest, T.; Elshocht, S. V.; Kauranen, M.; Hellemans, L.; Snauwaert, J.; Nuckolls, C.; Katz, T. J.; Persoons, A. *Science* **1998**, *282*, 913.
2. Mei, J.; Diao, Y.; Appleton, A. L.; Fang, L.; Bao, Z. *J. Am. Chem. Soc.* **2013**, *135*, 6724.
3. (a) Zhang, L.; Cao, Y.; Colella, N. S.; Liang, Y.; Brédas, J.-L.; Houk, K. N., Briseno, A. L. *Acc. Chem. Res.* **2015**, *48*, 500. (b) Zhang, L.; Fonari, A.; Zhang, Y.; Zhao, G.; Coropceanu, V.; Hu, W.; Parkin, S.; Brédas, J.-L.; Briseno, A. L. *Chem. Eur. J.* **2013**, *19*, 17907. (c) Anthony, J. E.; Brooks, J. S.; Eaton, D. L.; Parkin, S. R. *J. Am. Chem. Soc.* **2001**, *123*, 9482.
4. (a) Gsänger, M.; Oh, J. H.; Könemann, M.; Höffken, H. W.; Krause, A.-M.; Bao, Z.; Würthner, F. *Angew. Chem., Int. Ed.* **2010**, *49*, 740. (b) Genereux, J. C.; Barton, J. K. *Chem. Rev.* **2010**, *110*, 1642. (c) Kobayashi, K.; Masu, H.; Shuto, A.; Yamaguchi, K. *Chem. Mater.* **2005**, *17*, 6666. (d) Werz, D. B.; Gleiter, R.; Rominger, F. *J. Am. Chem. Soc.* **2002**, *124*, 10638.
5. (a) David, W. I. F.; Ibberson, R. M.; Matthewman, J. C.; Prassides, K.; Dennis, T. J. S.; Hare, J. P.; Kroto, H. W.; Taylor, R.; Walton, D. R. M. *Nature* **1991**, *353*, 147. (b) Hirsch, A.; Brettreich, M. *Fullerenes: Chemistry and Reactions*, Wiley-VCH, Weiheim, **2005**. (c) *Fullerenes: Chemistry, Physics, and Technology* (Eds.: Kadish, K. M.; Ruoff, R. S.), Wiley, New York, **2000**. (d) *Fullerenes: Principles and Applications* (Eds.: Lang, F.; Nierengarten, J.-F.), RSC, Cambridge, **2007**.
6. Reviews on helicenes: (a) Gingras, M. *Chem. Soc. Rev.* **2013**, *42*, 968. (b) Gingras, M.; Félix, G.; Peresutti, R. *Chem. Soc. Rev.* **2013**, *42*, 1007. (c) Gingras, M. *Chem. Soc. Rev.* **2013**, *42*, 1051. (d) Shen, Y.; Chen, C.-F. *Chem. Rev.* **2012**, *112*, 1463.
7. For recent examples of multihelicenes, see: (a) Meng, D.; Fu, H.; Xiao, C.; Meng, X.; Winands, T.; Ma, W.; Wei, W.; Fan, B.; Huo, L.; Doltsinis, N. L.; Li, Y.; Sun, Y.; Wang, Z. *J. Am. Chem. Soc.* **2016**, *138*, 10184. (b) Katayama, T.; Nakatsuka, S.; Hirai, H.; Yasuda, N.; Kumar, J.; Kawai, T.; Hatakeyama, T. *J. Am. Chem. Soc.* **2016**, *138*, 5210. (c) Wang, X.-Y.; Narita, A.; Zhang, W.; Feng,

X.; Müllen, K. *J. Am. Chem. Soc.* **2016**, *138*, 9021. (d) Fujikawa, T.; Segawa, Y.; Itami, K. *J. Am. Chem. Soc.* **2016**, *138*, 3587. (e) Fujikawa, T.; Segawa, Y.; Itami, K. *J. Am. Chem. Soc.* **2015**, *137*, 7763. (f) Shan, L.; Liu, D.; Li, H.; Xu, X.; Shan, B.; Xu, J.-B.; Miao, Q. *Adv. Mater.* **2015**, *27*, 3418. (g) Gu, X.; Xu, X.; Li, H.; Liu, Z.; Miao, Q. *J. Am. Chem. Soc.* **2015**, *137*, 16203. (h) Kashihara, H.; Asada, T.; Kamikawa, K. *Chem. Eur. J.* **2015**, *21*, 6523. (i) Luo, J.; Xu, X.; Mao, R.; Miao, Q. *J. Am. Chem. Soc.* **2012**, *134*, 13796.

8. Takimiya, K.; Shinamura, S.; Osaka, I.; Miyazaki, E. *Adv. Mater.* **2011**, *23*, 4347.
9. For a review on the Scholl reaction, see: Grzybowski, M.; Skonieczny, K.; Butenschön, H.; Gryko, D. T. *Angew. Chem., Int. Ed.* **2013**, *52*, 9900.
10. Thamatam, R.; Skraba, S. L.; Johnson, R. P. *Chem. Commun* **2013**, *49*, 9122.
11. (a) Butterfield, A. M.; Gilomen, B.; Siegel, J. S. *Org. Process Res. Dev.* **2012**, *16*, 664. (b) Anwer, M. K.; Sherman, D. B.; Roney, J. G.; Spatola, A. F. *J. Org. Chem.* **1989**, *54*, 1284.
12. Saeki, A.; Koizumi, Y.; Aida, T.; Seki, S. *Acc. Chem. Res.* **2012**, *45*, 1193.
13. (a) Cooke, R. G.; Johnson, B. L.; Owen, W. R. *Aust. J. Chem.* **1960**, *13*, 256. (b) Shinamura, S.; Osaka, I.; Miyazaki, E.; Nakao, A.; Yamagishi, M.; Takeya, J.; Takimiya, K. *J. Am. Chem. Soc.* **2011**, *133*, 5024.
14. Altomare, A.; Burla, M. C.; Camalli, M.; Cascarano, G. L.; Giacovazzo, C.; Guagliardi, A.; Moliterni, A. G. G.; Polidori, G.; Spagna, R. *J. Appl. Crystallogr.* **1999**, *32*, 115.
15. Sheldrick, G. M. University of Göttingen: Göttingen, Germany, 1997.
16. Frisch, M. J.; Trucks, G. W.; Schlegel, H. B.; Scuseria, G. E.; Robb, M. A.; Cheeseman, J. R.; Scalmani, G.; Barone, V.; Mennucci, B.; Petersson, G. A.; Nakatsuji, H.; Caricato, M.; Li, X.; Hratchian, H. P.; Izmaylov, A. F.; Bloino, J.; Zheng, G.; Sonnenberg, J. L.; Hada, M.; Ehara, M.; Toyota, K.; Fukuda, R.; Hasegawa, J.; Ishida, M.; Nakajima, T.; Honda, Y.; Kitao, O.; Nakai, H.; Vreven, T.; Montgomery, Jr., J. A.; Peralta, J. E.; Ogliaro, F.; Bearpark, M.; Heyd, J. J.; Brothers, E.; Kudin, K. N.; Staroverov, V. N.; Keith, T.; Kobayashi, R.; Normand, J.; Raghavachari, K.; Rendell, A.; Burant, J. C.; Iyengar, S. S.; Tomasi, J.; Cossi, M.; Rega, N.; Millam, J. M.; Klene, M.; Knox, J. E.; Cross, J. B.; Bakken, V.; Adamo, C.; Jaramillo, J.; Gomperts, R.; Stratmann, R. E.; Yazyev, O.; Austin, A. J.; Cammi, R.; Pomelli, C.; Ochterski, J. W.; Martin, R. L.; Morokuma, K.; Zakrzewski, V. G.; Voth, G. A.; Salvador, P.; Dannenberg, J. J.; Dapprich, S.; Daniels, A. D.; Farkas, O.; Foresman, J. B.; Ortiz, J. V.; Cioslowski, J.; Fox, D. J. Gaussian 09, Revision D.01, Gaussian, Inc., Wallingford CT, 2013.
17. (a) Becke, A. D. *J. Chem. Phys.* **1993**, *98*, 5648. (b) Lee, C.; Yang, W.; Parr, R. G. *Phys. Rev. B* **1988**, *37*, 785.

Chapter 4

Laterally π-Extended Dithia[6]helicenes with Heptagons: Saddle–Helix Hybrid Molecules

ABSTRACT: A laterally π-extended dithia[6]helicene **SH**, representing an interesting saddle-helix hybrid with an unusual heptagon, has been synthesized by $MoCl_5$-mediated oxidative stitching of tetrakis(thienylphenyl)naphthalene precursor **1** involving reactive-site capping by chlorination, and subsequent Pd-catalyzed dechlorination of tetrachlorinated intermediate **SH-Cl$_4$**. Highly distorted, wide helical structures of dithia[6]helicenes (**SH** and **SH-Cl$_4$**) were clarified by single crystal X-ray diffraction analyses, where heterochiral slipped π-π stacking was displayed in one-dimensional fashion. Notably, theoretical studies on the thermodynamic behavior of **SH** predicted an extraordinary high isomerization barrier of 49.7 kcal·mol^{-1}, which enabled optical resolution and chiroptical measurements. Electronic structures of these huge helicenes were also examined by photophysical and electrochemical measurements.

Introduction

Helicenes are helical, *ortho*-fused polyaromatic compounds whose π-electron systems are characterized by nonplanarity, chiroptical properties, and unique dynamic behavior. In order to exploit the peculiar properties of helicenes in materials science, a variety of chemical modifications about the helix have been attempted despite the innate difficulty of constructing such highly crowded structures (see the General Introduction). In particular, the π-extension of the helical motif (Figure 1a, left) results in a significant perturbation of the optoelectronic properties and control over solid-state aggregation as well as molecular dynamics. In this context, the helical elongation approach has been historically studied in the synthesis of carbo- and hetera[*n*]helicenes (*n* is the number of fused rings). The lateral π-extension approach has also become frequent in recent years (Figure 1a, right). Compared with the simplicity of the former approach, the latter has a significant flexibility in molecular design. Synthetic work related to benzo- and pyrenohelicenes has dominated the field,[1,2] and recently, corannulene- and perylene-based helicenes have also appeared, in which the characters of fused polyaromatic moieties such as dynamic motion and redox ability were merged with helical properties.[3,4] In these laterally π-extended helicenes, however, the helix is partially fused with polyaromatic moieties. A fully-fused congener has never been reported except the graphitic helicene designed in the computational study by Mezey (Figure 1b).[5] As groundwork towards the preparation of these helical nano-architectures, wide laterally π-extended dithia[6]helicenes, the first fully-fused helicenes having heptagonal rings, were prepared and characterized in this chapter (Figure 2).

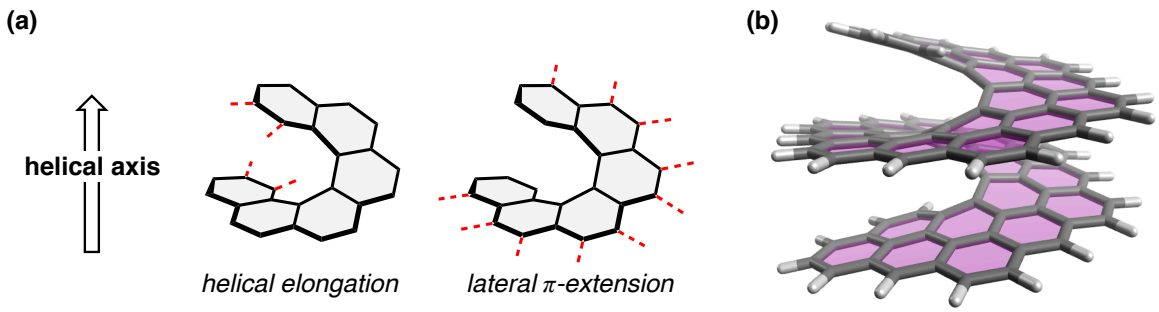

Figure 1. (a) Two π-extension approach in the chemistry of helicenes. (b) Graphitic helicene designed in the report by Mezey.

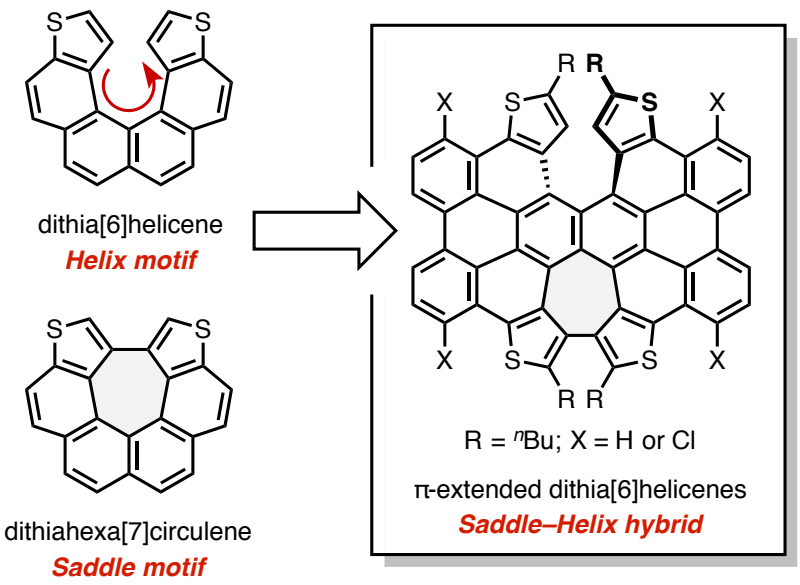

Figure 2. Structural motifs of π-extended dithia[6]helicenes.

Result and Discussion

Synthesis of π-Extended Single Dithia[6]helicenes with Heptagons (SH-Cl_4 and SH)

During the condition screening of the synthesis of π-extended double dithia[6]helicenes **DH3-Cl_4** described in Chapter 3, it was found that treatment of 20 equivalents of $MoCl_5$ with tetrakis(thienylphenyl)naphthalene precursor **1** under oxygen atmosphere afforded fourfold chlorinated π-extended single dithia[6]helicene **SH-Cl_4** in 36%. It is of note that the formation of seven-membered ring (dithiahexa[7]circulene framework) occurred under mild conditions.[6] When compared with the yield of the synthesis of **DH3-Cl_4** (26%), slight increase of the yield was observed in this time despite the one extra C–C bond formation. Therefore, it is likely that the oxidation process proceeded smoothly in the presence of molecular oxygen although the influence of oxygen is unclear. As with the conversion from **DH3-Cl_4** to **DH3**, dechlorination can be accomplished in one step after cyclization yielding **SH** in 94% yield.

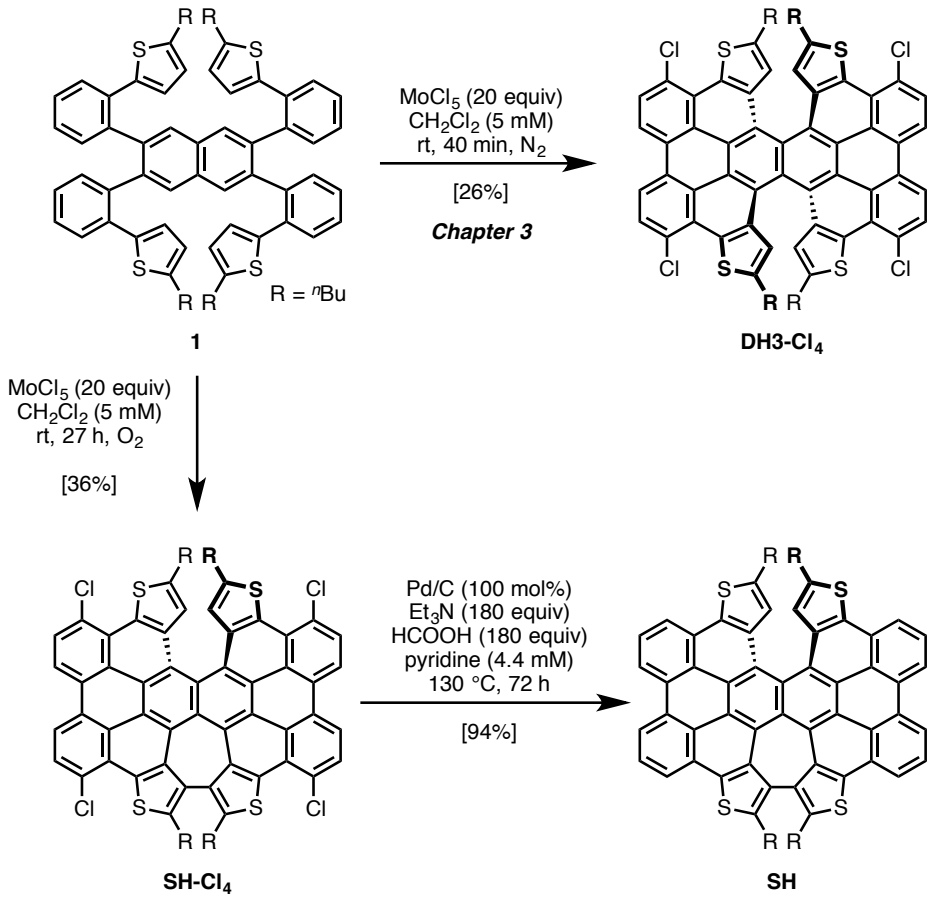

Scheme 1. Synthesis of **SH-Cl_4** and **SH**.

Structures

The assumed structures of dithia[6]helicenes **SH-Cl$_4$** and **SH** were derived by ^{1}H- and ^{13}C-NMR spectra and mass spectroscopy. For example, ^{1}H NMR spectrum of **SH-Cl$_4$** showed four doublet peals and one singlet peak in the aromatic region, which obviously indicated lower symmetry of the cyclization product than of initially intended double dithia[6]helicenes (**DH3** and **DH3-Cl$_4$**). A moderate shielding effect, one of the characteristics of helicene, also appeared as the upfield shift of the singlet peaks corresponding to the hydrogen atoms at the end of the inner helix (δ 6.39 and 6.35 ppm for **SH-Cl$_4$** and **SH**, respectively). To add firm support, single-crystal X-ray diffraction analyses were carried out using racemic crystals of **SH-Cl$_4$** and **SH**. The former were obtained from recrystallization of **SH-Cl$_4$** from chloroform as co-crystals with chloroform molecules, while the latter were obtained from recrystallization of **SH** from hot nitrobenzene. As depicted in Figure 3, refined X-ray structures corroborated the assumed structures, exhibiting global distortion of π-surfaces.

The π-skeletons of **SH-Cl$_4$** and **SH** consist of three structural components: a helical dithia[6]helicene motif, a saddle-shaped dithiahexa[7]circulene motif, and relatively planar bilateral motifs. Helical distortions of dithia[6]helicene motifs were evaluated by the distances between the two carbon atoms at the helical termini (C19–C32 = 3.462(7) Å for **SH-Cl$_4$**; C2–C2' = 3.308(5) Å for **SH**), and the splay angles (C20–C24–C26–C31 = 58.3(4)° for **SH-Cl$_4$**; C3–C24–C24'–C3' = 56.6(3)° for **SH**). Both values in the X-ray structures were reproduced in the optimized structures of **TetraMe-SH-Cl$_4$** and **TetraMe-SH**, methyl analogs of **SH-Cl$_4$** and **SH**, calculated at the B3LYP/6-31G(d) level of theory (3.45 Å and 60.6° for **TetraMe-SH-Cl$_4$**; 3.40 Å and 57.7° for **TetraMe-SH**). Meanwhile, a significant disparity in these values is recognized when compared with those in the optimized structure of 2,13-dimethyldithia[6]helicene **2** (3.07 Å and 46.4°), presumably attributed to the stretching force along the helical axis derived from the negatively curved heptagonal ring of the adjoining dithiahexa[7]circulene motif. Simultaneously, the heptagonal ring annulation compresses the helix in a direction vertical to the helical axis as probed by the reduced inner C–C–C bond angles. For example, the central bond angles inside the helices of **SH-Cl$_4$** and **SH** are markedly smaller than that of **2** by almost 5° (C24–C25–C26 = 119.9(4)° for **SH-Cl$_4$**; C24–C25–C24' = 120.7(3)° for **SH**; C(14b)–C(14c)–C(14d) = 125.75° for **2**). The sum of five inner bond angles also results in smaller values for **SH-Cl$_4$** (619.5°) and **SH** (624.5°) than for **2** (634.9°), which indicates an enlarged eclipse of the helical termini.

One of the curiosities was why one extra heptagonal ring formation did not occur after the generation of **SH-Cl$_4$** during the oxidative stitching reaction. This is easily attributed to the stretching of the helical motif along the helical axis. As reported by Wynberg, pristine

dithia[6]helicene is known to be convertible to dithiahexa[7]circulene at 140 °C in a melt of $AlCl_3$/NaCl.[6] The distance between the two carbon atoms at the helical termini was found to be 3.079 Å for the crystal structure of double helicene **DH3**, which is comparable to that for the optimized structure of dimethyldithia[6]helicene **2**. Hence, it is speculated that this proximity promoted the first heptagonal closure but the second one did not proceed due to the widened helical termini.

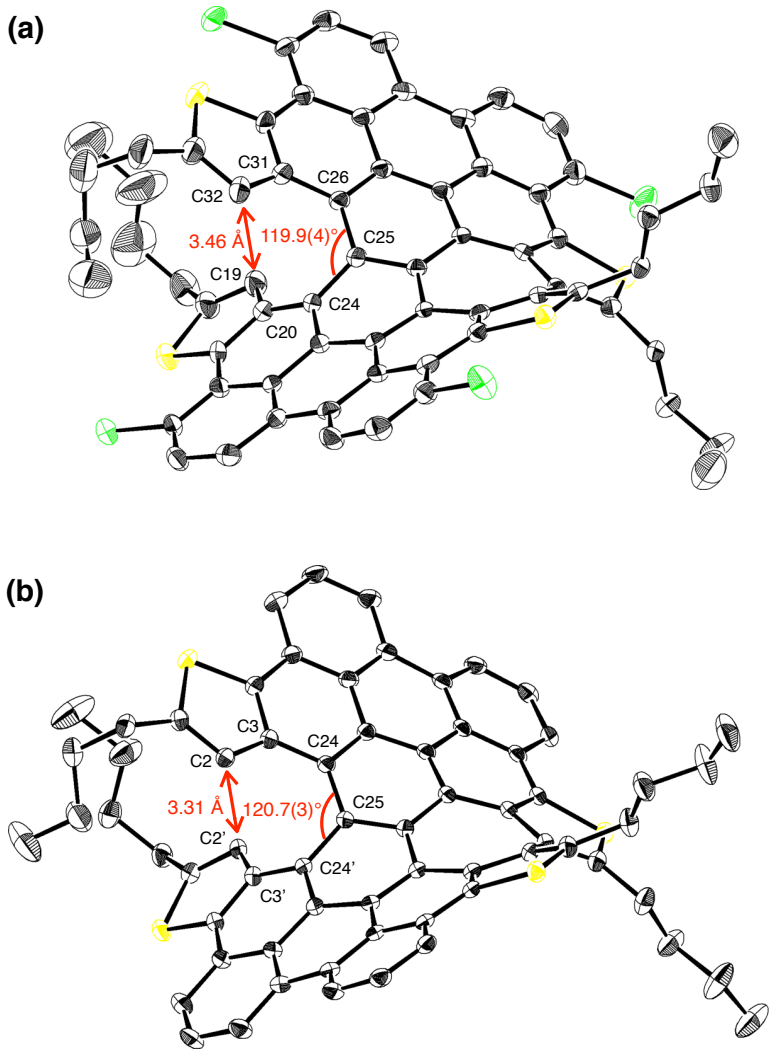

Figure 3. ORTEP drawings of (*P*)-isomers of (a) **SH-Cl$_4$** and (b) **SH** with thermal ellipsoids shown at 50% probability (the hydrogen atoms, the minor part of the disordered moieties, and solvent molecules are omitted for clarity).

As illustrated in Figure 4, the relatively planar bilateral motifs of both dithia[6]helicenes are key points of heterochiral slipped one-dimensional π-π stacking arrays. Whereas the inter-plane distance ($d_{\pi-\pi}$) of 3.48 Å indicates moderate π-π interactions through the one-dimensional column of **SH-Cl$_4$**, a broader $d_{\pi-\pi}$ of 3.69 Å in the crystal of **SH** indicates weak π-π interactions. Large cofacial overlap was realized in both cases, which is one of the important merits of lateral π-extension.[7]

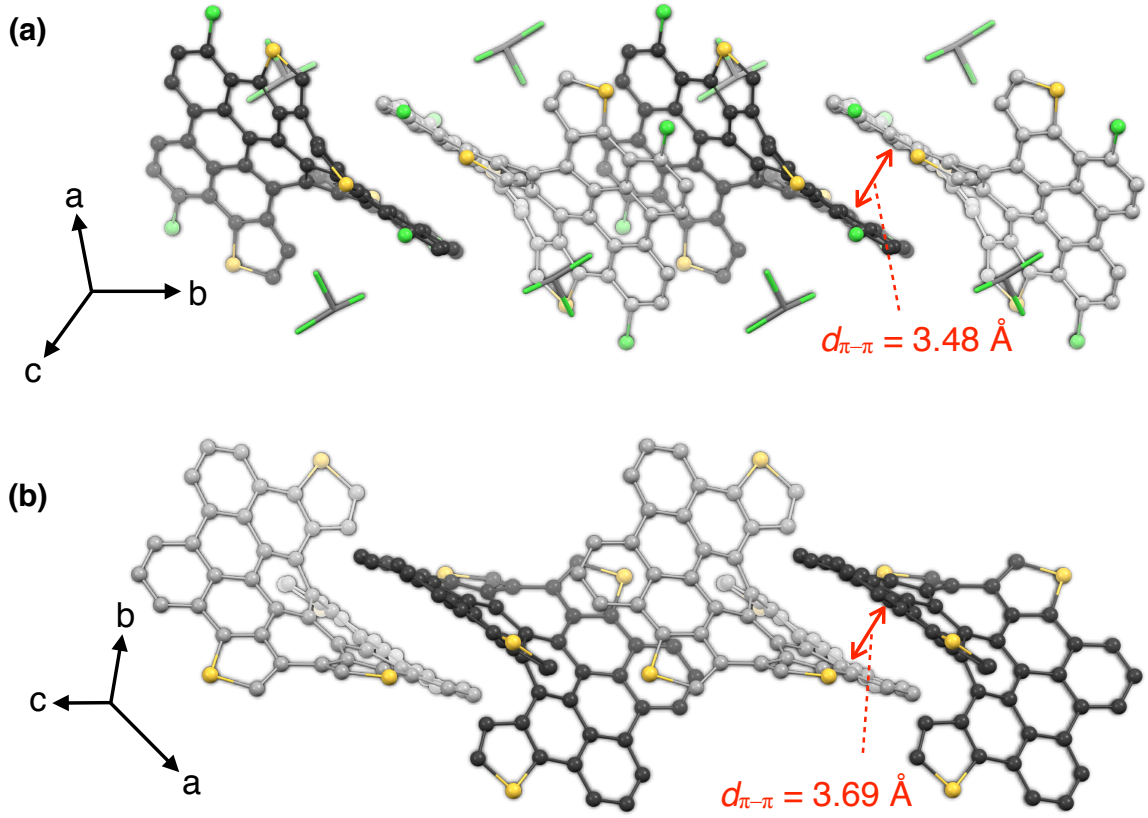

Figure 4. Packing structures of (a) **SH-Cl$_4$** and (b) **SH** (π-skeletons are depicted using a ball-and-stick model; the chloroform molecules in (a) are depicted using a capped stick model; carbon atoms of (*P*)-isomers and (*M*)-isomers are colored in black and gray, respectively; *n*-butyl groups are omitted for clarity).

Isomerization

Next, the enantiomeric interconversion pathway of **TetraMe-SH** was examined theoretically (B3LYP/6-31G(d)). In addition to the helicity of the dithia[6]helicene motif, steric repulsion between the two *n*-butyl groups in the bay-region of the dithiahexa[7]circulene motif manifests as another helicity. Accordingly, besides the most stable isomers ((*P*,*P*)- and (*M*,*M*)-**TetraMe-SH**, ΔG = 0.0 kcal·mol^{-1}) observed in the X-ray crystallography, meta-stable diastereomers ((*P*,*M*)- and (*M*,*P*)-**TetraMe-SH**, ΔG = 14.7 kcal·mol^{-1}) exist, where the two different helical motifs possess opposite helicity (helicity notation in the left top of Figure 5). In the enantiomerizations, two distinct transition states were found; one involves the inversion of the dithiahexa[7]circulene motif via a planarization of the heptagonal ring (TS1, ΔG = 29.1 kcal·mol^{-1}), and the other involves the inversion of the dithia[6]helicene motif via a face-to-face orientation of the terminal aromatic rings (TS2, ΔG = 49.7 kcal·mol^{-1}). The isomerization barrier estimated for **TetraMe-1** (49.7 kcal·mol^{-1}) is an extraordinarily high value compared with that for **3** (39.3 kcal·mol^{-1} at the same calculation level), which is probably due to the heptagonal ring distortion and the steric congestion of the alkyl groups at the bay-region during the transition. The barriers for enantiomerization of **TetraMe-1** are large even when compared with related barriers for double-layered carbo[*n*]helicene (41.7–43.5 kcal·mol^{-1} as experimental values with *n* = 7–9).[8]

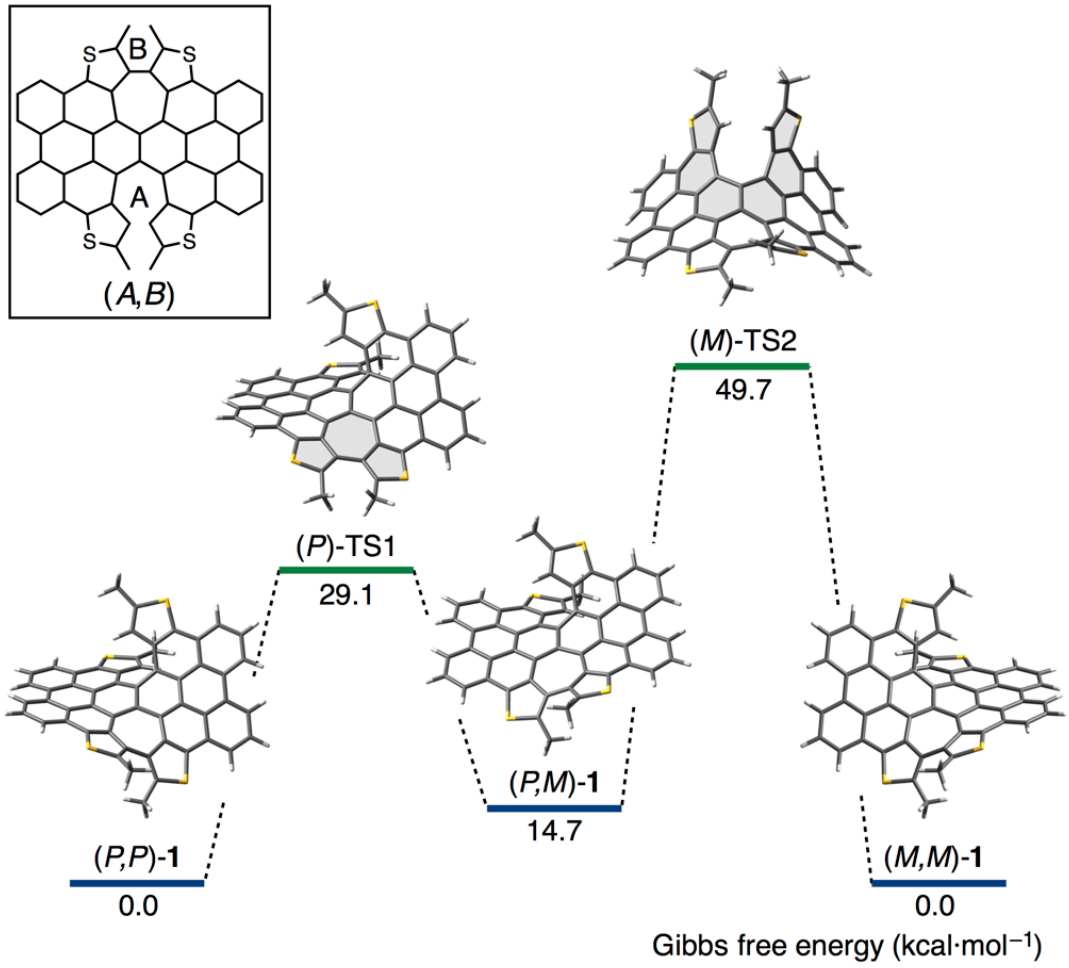

Figure 5. The enantiomeric interconversion pathways of **TetraMe-1** (enantiomeric structures of (*M*)-TS1, (*P*)-TS2, and (*M*,*P*)-**TetraMe-1**, and the pathways among them are omitted for clarity). Relative Gibbs free energies (ΔG) were calculated at the B3LYP/6-31G(d) level of theory. The *n*-butyl groups were replaced with methyl groups to simplify the calculations.

Optical Resolution and Electronic Properties

The high isomerization barrier of **SH** enabled its optical resolution by means of HPLC equipped with a COSMOSIL Cholester column (Figure 6). The specific rotation of the fast-moving enantiomer was determined to be $[\alpha]^{22}_{D}$ −1439 (c = 0.00018), and its CD spectrum exhibited negative Cotton effects at 501 nm ($\Delta\varepsilon$ = −82 $M^{-1}\cdot cm^{-1}$) and 471 nm ($\Delta\varepsilon$ = −44 $M^{-1}\cdot cm^{-1}$), and positive Cotton effects at 421 nm ($\Delta\varepsilon$ = +111 $M^{-1}\cdot cm^{-1}$), 398 nm ($\Delta\varepsilon$ = +75 $M^{-1}\cdot cm^{-1}$), and 326 nm ($\Delta\varepsilon$ = +54 $M^{-1}\cdot cm^{-1}$) (Figure 7). By comparing with the simulated CD spectrum, the fast-moving enantiomer was assigned as (−)-(*P*,*P*)-**SH**. The slow-moving isomer gave a mirror-image CD spectrum, which was assigned as (+)-(*M*,*M*)-**SH**.

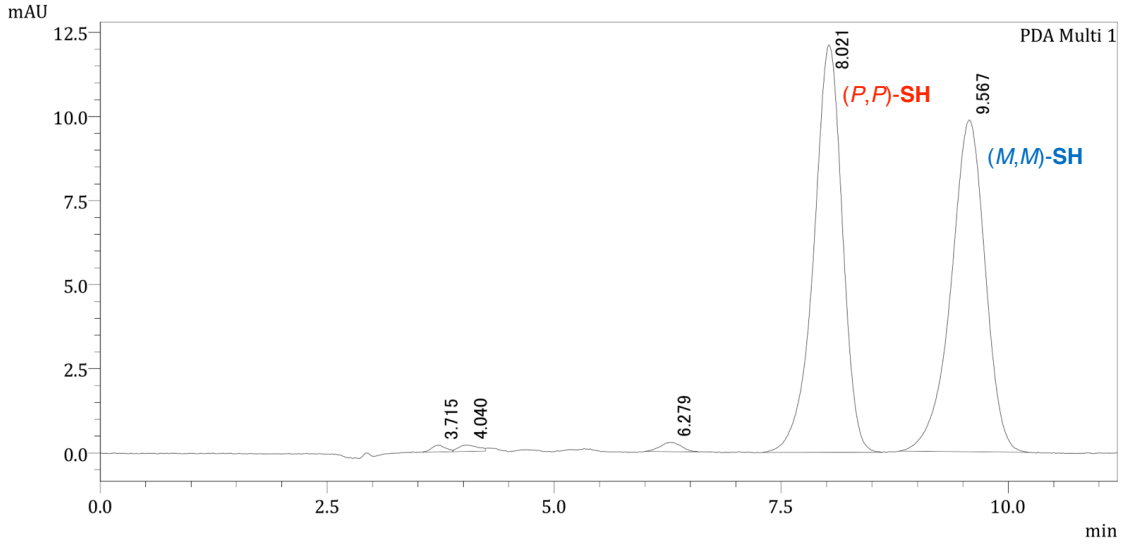

Figure 6. HPLC analysis of the racemic mixture of **SH**.

The UV–Vis absorption spectra of **SH-Cl$_4$** and **SH** exhibit two major absorption bands; *i.e.*, longer-wavelength absorption with clear vibronic structures and intense absorption around 400 nm (Figure 7b). Absorption maxima for **SH-Cl$_4$** are observed at 518 nm, 486 nm, 455 nm, and 404 nm. In comparison, these maxima are blue-shifted for **SH** appearing at 502 nm, 472 nm, 442 nm, and 394 nm. TD DFT calculations (B3LYP/6-31G(d)) attributed the longer-wavelength absorption bands to HOMO→LUMO transition (S_1, f_{calc} = 0.1889 for **TetraMe-SH-Cl$_4$** and 0.1690 for **TetraMe-SH**), and the intense absorption bands to almost equal contribution of HOMO–2→LUMO and HOMO→LUMO+2 transitions (S_6, f_{calc} = 0.7023 for **TetraMe-SH-Cl$_4$** and 0.7626 for **TetraMe-SH**). The fluorescence spectra also show a similar tendency in the spectral shift with that in absorption, giving maxima at 530 nm and 566 nm for **SH-Cl$_4$** (Φ_F = 0.37), and at 514 nm and 548 nm for **SH** (Φ_F = 0.23). The absorption and

fluorescence spectra of **SH-Cl$_4$** and **SH** were similar to the corresponding double helicene analogs **DH-Cl$_4$** and **DH** but slightly blue-shifted in both case.

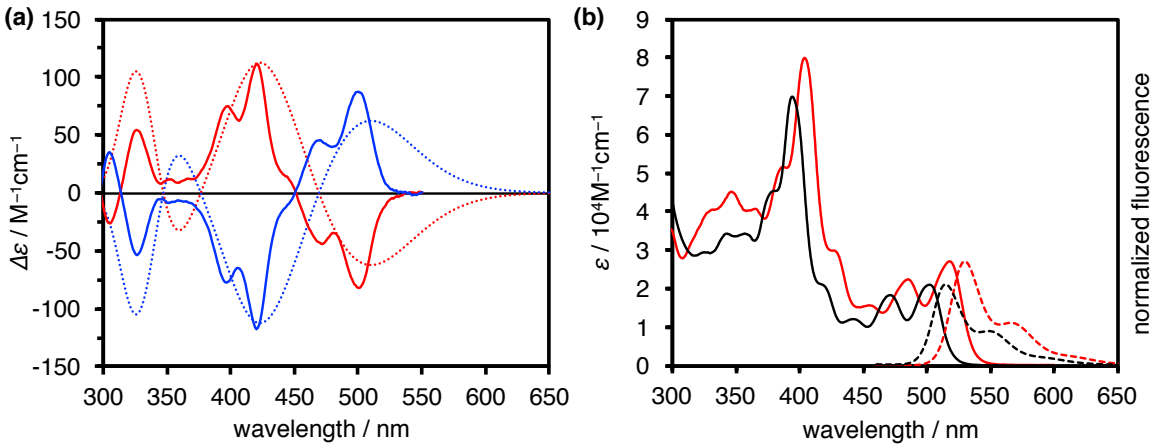

Figure 7. (a) Experimental CD spectra of the fast-moving enantiomer ((−)-**SH**, red solid line) and the slow-moving enantiomer ((+)-**SH**, blue solid line) in HPLC, and simulated CD spectra of (*P*,*P*)-**TetraMe-SH** (red dotted line) and (*M*,*M*)-**TetraMe-SH** (blue dotted line) calculated at the B3LYP/6-31G(d) level of theory. (b) UV–Vis absorption and fluorescence spectra of **SH-Cl$_4$** (red lines) and **SH** (black lines). Chloroform solutions were used for all photophysical measurements.

Frontier molecular orbitals were computationally estimated to be lower for **TetraMe-SH-Cl$_4$** than for **TetraMe-SH** due to the presence of electron-accepting chloride groups (E_{HOMO} = −5.07 eV and E_{LUMO} = −2.34 eV for **TetraMe-SH-Cl$_4$**; E_{HOMO} = −4.85 eV and E_{LUMO} = −2.05 eV for **TetraMe-SH**), which apparently perturb electronic states as observed in the photophysical properties. To elucidate the electrochemical behavior of these structures, cyclic voltammetry was performed in dichloromethane solutions containing 0.1 M of $TBAPF_6$ (vs FcH/FcH^+). The voltammograms exhibited two-step oxidation waves, whose first steps were reversible ($E_{1/2}$ = 0.50 V for **SH-Cl$_4$**, 0.43 V for **SH**) and second steps were irreversible (E_p = 0.84 V for **SH-Cl$_4$**, 0.83 V for **SH**) at scan rate of 0.1 $V \cdot s^{-1}$ (Figure 8). The slight anodic shift of the first oxidation potential (0.07 V) upon chlorination reflects the differences in the estimated HOMO energies.

Interestingly, unlike the oxidation behavior of double dithia[6]helicenes **DH3-Cl$_4$** and **DH3**, the heptagonal ring cyclization destabilized the oxidized species after the second step oxidation events in both **SH-Cl$_4$** and **SH**. There are two possible reasons. One is that the negatively de-

formed π-system increases the reactivity of oxidized species. The other is that extra C–C bond formation efficiently connects the two relatively planar bilateral motifs, wherein the HOMOs of single helicenes distributes mainly (Figure 9), and two or more positive charges repel each other, destabilizing the oxidized species. Although the correct answer is unknown, the existence of saddle-shaped structural motifs derived from the heptagonal rings definitely destabilized the whole π-systems in any case.

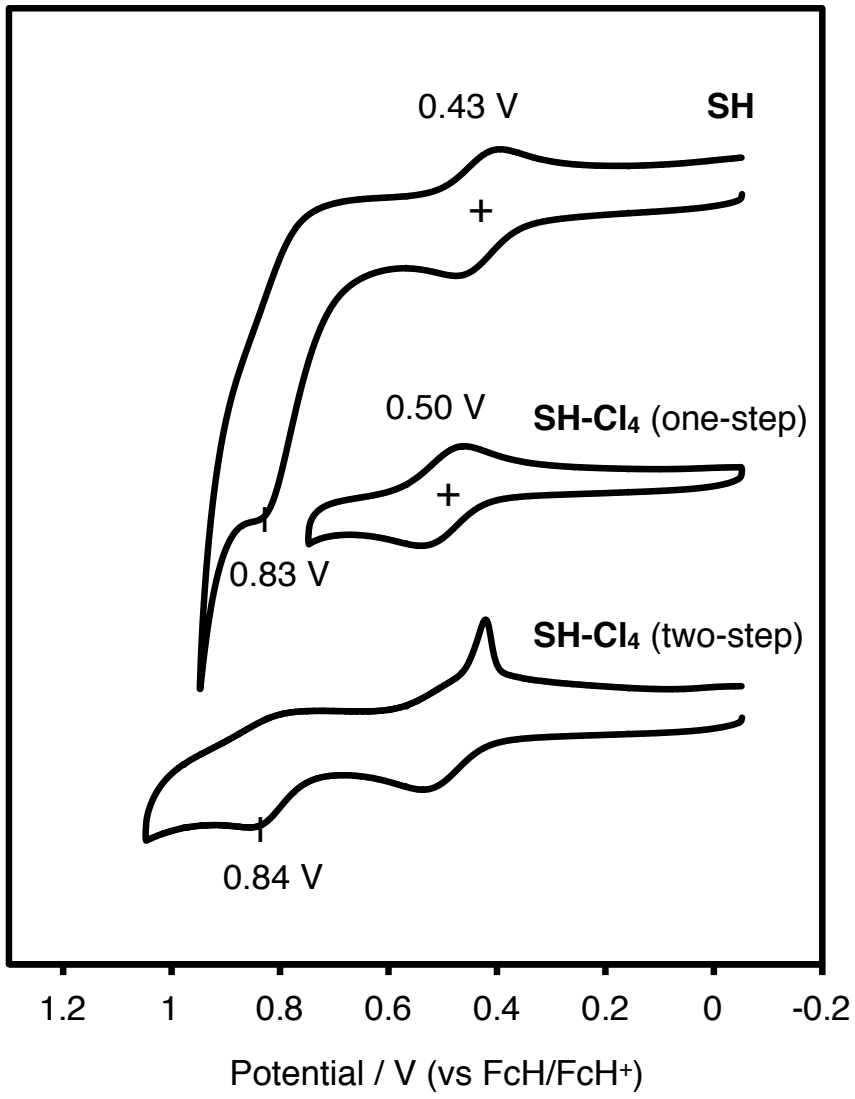

Figure 8. Cyclic voltammograms of **SH-Cl$_4$** and **SH** in dichloromethane containing 0.1 M of $TBAPF_6$ at scan rate of 0.1 $V \cdot s^{-1}$. FcH = ferrocene.

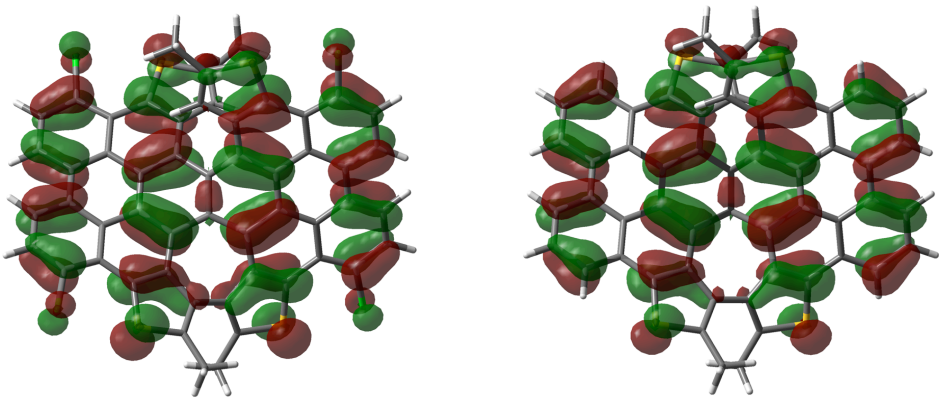

HOMO of **TetraMe-SH-Cl$_4$** HOMO of **TetraMe-SH**

Figure 9. Spatial distributions of HOMO and LUMO of methyl analog of **TetraMe-SH-Cl$_4$** and **TetraMe-SH**.

Conclusion

Laterally π-extended dithia[6]helicenes, representing an interesting saddle-helix hybrid with an unusual heptagon, have been synthesized, isolated, purified, and fully characterized. A chlorinated dithia[6]helicene **SH-Cl$_4$** was obtained by treating tetrakis(thienylphenyl)naphthalene precursor **1** with a large excess of $MoCl_5$ under oxygen atmosphere, and subsequent Pd-catalyzed reduction afforded fully dechlorinated dithia[6]helicene **SH**. Highly distorted, wide helical structures of dithia[6]helicenes (**SH** and **SH-Cl$_4$**) were unambiguously determined by single crystal X-ray diffraction analyses. One-dimensionally stacked molecular arrays were presented utilizing the large π-surfaces of relatively planar bilateral motifs. An extraordinarily high isomerization barrier (49.7 kcal·mol^{-1}) was predicted theoretically for **SH**, suggesting its excellent chiral stability. Indeed, optical resolution of **SH** was achieved by the chiral HPLC, which enabled chiroptical measurements. Electronic states of **SH-Cl$_4$** and **SH** were also compared in photophysical, electrochemical, and theoretical studies, and the effects of chloride atom substitution and heptagonal ring closure were examined. Although fully-fused wide helicenes have attracted researchers' interests because of their physicochemical properties, a lack of synthetic methodology has hampered development in this area. A rapid synthetic approach reported herein will not only accelerate the chemistry of laterally π-extended helicenes, but also stimulate molecular design for unprecedented helical nano-architectures.

Experimental Section

General

Unless otherwise noted, all materials including dry solvents were obtained from commercial suppliers and used without further purification. Tetrakis(thienylphenyl)naphthalene precursor (**1**) was prepared according to the procedure described in Chapter 3. Unless otherwise noted, all reactions were performed with dry solvents under an atmosphere of nitrogen in dried glassware with standard vacuum-line techniques. All work-up and purification procedures were carried out with reagent-grade solvents in air.

Analytical thin-layer chromatography (TLC) was performed using E. Merck silica gel 60 F_{254} precoated plates (0.25 mm). The developed chromatogram was analyzed by UV lamp (254 nm and 365 nm). High-resolution mass spectra (HRMS) were obtained from a JEOL JMS-S3000 SpiralTOF (MALDI-TOF MS). Cyclic voltammetry (CV) measurements were performed by BAS ALS-600D Electrochemical Analyzer. Melting points were measured on a MPA100 Optimelt automated melting point system. Nuclear magnetic resonance (NMR) spectra were recorded on a JEOL JNM-ECA-600 (^{1}H 600 MHz, ^{13}C 150 MHz) or a JEOL ECA 600II spectrometer with Ultra COOLTM probe (^{1}H 600 MHz, ^{13}C 150 MHz). Chemical shifts for ^{1}H NMR are expressed in parts per million (ppm) relative to $CHCl_3$ (δ 7.26 ppm) or C_2DHCl_4 (δ 6.00 ppm). Chemical shifts for ^{13}C NMR are expressed in ppm relative to $CDCl_3$ (δ 77.16 ppm) or $C_2D_2Cl_4$ (δ 73.78 ppm). Data are reported as follows: chemical shift, multiplicity (s = singlet, d = doublet, t = triplet, m = multiplet, br = broad signal), coupling constant (Hz), and integration.

Synthesis of SH-Cl_4

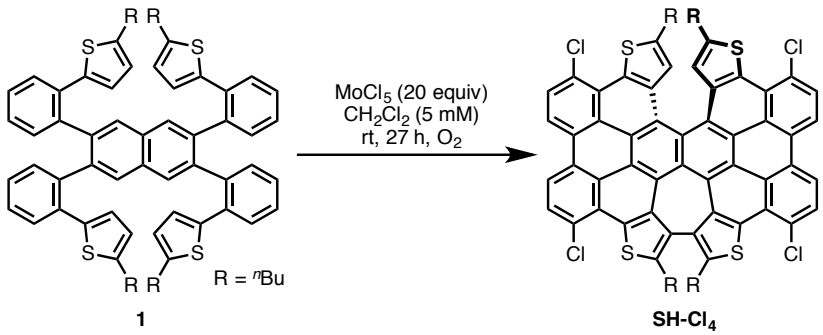

Dichloromethane was purged by oxygen gas and dried by molecular sieves 3A overnight before use. To a solution of **1** (49.3 mg, 0.0500 mmol, 1 equiv) in dichloromethane (10 mL) was added $MoCl_5$ (273 mg, 1.00 mmol, 20 equiv) at room temperature, and then the reaction mixture was stirred for 27 h under nitrogen atmosphere. The reaction was quenched by the ad-

dition of MeOH/$CHCl_3$ (1:1, 10 mL) solution and the resultant solution was directly passed through a pad of silica-gel with $CHCl_3$ eluent. The filtrate was evaporated *in vacuo*. The residue was dissolved in $CHCl_3$ and passed through a pad of silica-gel again with *n*-hexane/$CHCl_3$ (1:1) eluent. The filtrate was evaporated *in vacuo* to afford **SH-Cl$_4$** (20.1 mg, 36%) as a red solid.

^{1}H NMR (600 MHz, $CDCl_3$) δ 8.70 (d, J = 8.6 Hz, 2H), 8.68 (d, J = 8.5 Hz, 2H), 8.10 (d, J = 8.5 Hz, 2H), 8.06 (d, J = 8.5 Hz, 2H), 6.39 (s, 2H), 3.17–3.12 (m, 2H), 2.94–2.88 (m, 2H), 2.48 (dt, ^2J = 15.0, ^3J = 6.6 Hz, 2H), 2.35 (dt, ^2J = 15.1, ^3J = 7.0 Hz, 2H), 1.88–1.80 (m, 2H), 1.71–1.63 (m, 2H), 1.34–1.24 (m, 8H), 1.00–0.88 (m, 4H), 0.80 (t, J = 7.4 Hz, 6H), 0.74 (t, J = 7.4 Hz, 6H); ^{13}C NMR (150 MHz, $CDCl_3$) δ 146.9 (4º), 143.7 (4º), 138.1 (4º), 138.0 (4º), 132.5 (4º), 131.7 (4º), 130.1 (4º), 129.8 (4º), 129.4 (CH), 129.3 (CH), 129.1 (4º), 129.0 (4º), 128.0 (4º), 126.7 (4º), 126.6 (4º), 126.5 (4º), 125.3 (4º), 124.8 (4º), 124.3 (4º), 124.0 (4º), 123.4 (4º), 122.4 (CH), 121.0 (CH), 120.5 (CH), 119.7 (4º), 119.2 (4º), 34.6 (CH_2), 33.4 (CH_2), 30.4 (CH_2), 29.4 (CH_2), 22.7 (CH_2), 21.5 (CH_2), 13.9 (CH_3), 13.9 (CH_3); HRMS (MALDI TOF-MS) *m/z* calcd for $C_{66}H_{46}Cl_4S_4$ $[M]^+$: 1108.1207, found: 1108.1209; mp: >300 ºC (recrystallized from chloroform).

Synthesis of SH

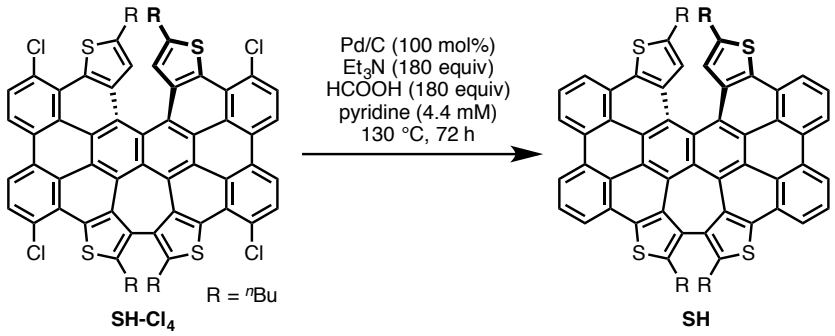

A mixture of **SH-Cl$_4$** (4.9 mg, 4.4 μmol), 5% Pd/C containing 55% water (18.9 mg, 4.0 μmol, 100 mol%), triethylamine (112 μL, 0.800 mmol), and formic acid (30 μL, 0.80 mmol) in pyridine (1 mL) was stirred at 130 °C for 72 h in a 20-mL Schlenk tube sealed with J. Young® O-ring tap. After cooling to room temperature, the precipitate was dissolved in $CHCl_3$ (150 mL) and passed through a pad of silica-gel with $CHCl_3$ eluent. The filtrate was evaporated *in vacuo* to afford **SH** (4.0 mg, 94%) as a yellow solid.

^{1}H NMR (600 MHz, $C_2D_2Cl_4$) δ 8.95 (t, J = 8.3 Hz, 4H), 8.40 (d, J = 7.6 Hz, 2H), 8.37 (d, J = 7.7 Hz, 2H), 6.35 (s, 2H), 3.18–3.13 (m, 2H), 2.98–2.92 (m, 2H), 2.54 (dt, ^2J = 14.8, ^3J = 7.1 Hz, 2H), 2.45 (dt, ^2J = 15.1, ^3J = 7.2 Hz, 2H), 1.89–1.81 (m, 2H), 1.72–1.66 (m, 2H), 1.34 (septet, J = 7.4 Hz, 8H), 1.13–1.03 (m, 4H), 0.84–0.79 (m, 12H); ^{13}C NMR (150 MHz,

$C_2D_2Cl_4$) δ 144.7 (4º), 140.7 (4º), 136.3 (4º), 135.5 (4º), 135.2 (4º), 134.1 (4º), 131.0 (4º), 130.9 (4º), 130.5 (4º), 129.0 (4º), 128.5 (4º), 128.2 (4º), 127.3 (CH), 127.2 (4º), 127.1 (CH), 124.2 (4º), 124.0 (4º), 123.6 (CH), 123.5 (4º), 122.5 (CH), 122.3 (4º), 122.2 (4º), 121.4 (CH), 120.5 (CH), 120.3 (CH), 120.0 (4º), 34.5 (CH_2), 33.3 (CH_2), 30.8 (CH_2), 29.7 (CH_2), 22.4 (CH_2), 21.3 (CH_2), 13.9 (CH_3), 13.8 (CH_3); HRMS (MALDI TOF-MS) *m/z* calcd for $C_{66}H_{50}S_4$ $[M]^+$: 970.2795, found: 970.2779; mp: >300 ºC (recrystallized from nitrobenzene).

X-ray Crystallography

Single crystals of **SH** suitable for X-ray crystal structure analysis were obtained by recrystallization of a racemic mixture from hot nitrobenzene. Single crystals of **SH-Cl$_4$** suitable for X-ray crystal structure analysis were also obtained by recrystallization of a racemic mixture from $CHCl_3$. Details of the crystal data and a summary of the intensity data collection parameters for **SH** and **SH-Cl$_4$** are listed in Table 1. A suitable crystal was mounted with mineral oil on a glass fiber and transferred to the goniometer of a Rigaku PILATUS diffractometer. Graphite-monochromated Mo Kα radiation (λ = 0.71075 Å) was used. The structures were solved by direct methods with (SIR-97)[9] and refined by full-matrix least-squares techniques against F^2 (SHELXL-97).[10] The intensities were corrected for Lorentz and polarization effects. The non-hydrogen atoms were refined anisotropically. Hydrogen atoms were placed using AFIX instructions.

Table 1. Crystallographic data and structure refinement details for **SH-Cl$_4$** and **SH**.

	SH-Cl$_4$	**SH**
formula	$C_{67}H_{47}Cl_7S_4$	$C_{66}H_{50}S_4$
fw	1228.43	971.30
T (K)	123(2)	123(2)
λ (Å)	0.71075	0.71075
cryst syst	Triclinic	Monoclinic
space group	*P*-1	*C*2/*c*
a (Å)	10.053(7)	20.5308(10)
b (Å)	17.077(14)	18.073(7)
c (Å)	18.207(14)	15.785(7)
α	113.715(13)°	90°
β	98.367(3)°	127.463(8)°
γ	99.656(13)°	90°
V (Å^3)	2742(4)	4649(3)
Z	2	4
D_{calc} (g / cm^3)	1.488	1.388
μ (mm^{-1})	0.560	0.251
F(000)	1264	2040
cryst size (mm)	0.10 × 0.02 × 0.02	0.25 × 0.01 × 0.01
θ range	3.277–24.998°	3.005–25.00°
reflns collected	33657	20962
indep reflns/R_{int}	9567/0.0540	4098/0.0768
params	743	319
GOF on F^2	1.025	0.954
R_1, wR_2 [I>2σ(I)]	0.0635, 0.1759	0.0458, 0.1191
R_1, wR_2 (all data)	0.0997, 0.1922	0.0613, 0.1263

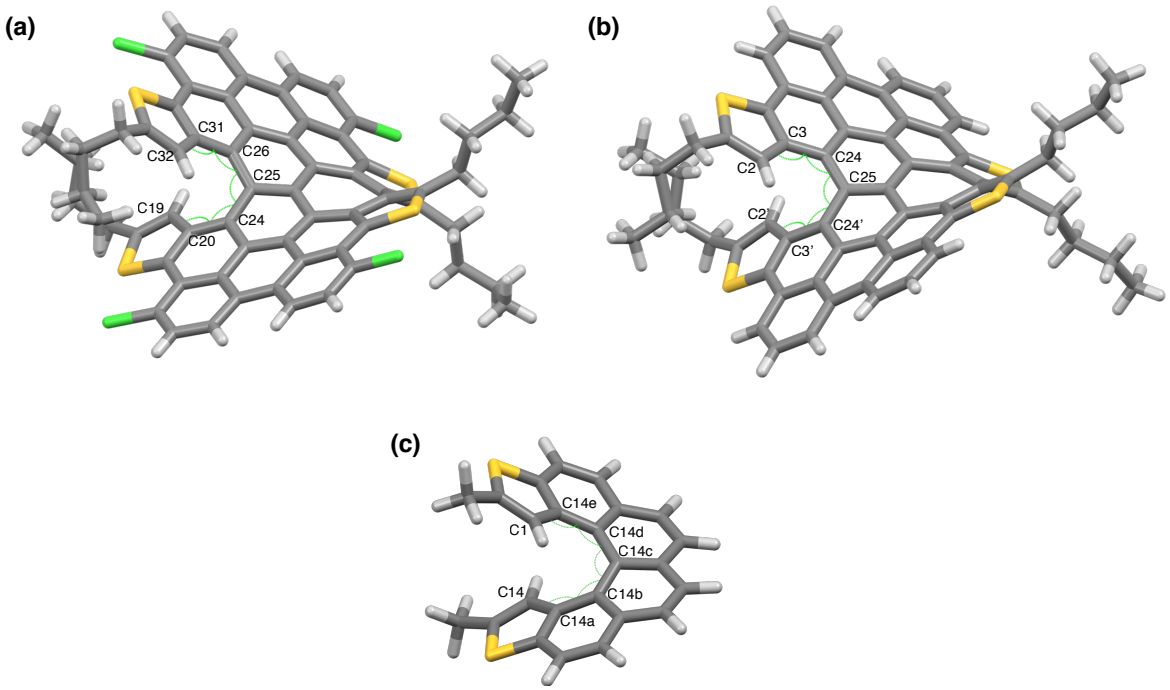

bond angle	**SH-Cl$_4$**
C32–C31–C26	128.2(4)°
C31–C26–C25	122.1(4)°
C26–C25–C24	119.9(4)°
C25–C24–C20	121.3(4)°
C24–C20–C19	128.0(4)°
sum of bond angles	619.5°

bond angle	**SH**
C2–C3–C24	129.53(19)°
C3–C24–C25	122.39(19)°
C24–C25–C24’	120.7(3)°
C25–C24’–C3’	122.39(19)°
C24’–C3’–C2’	129.53(19)°
sum of bond angles	624.5°

bond angle	**2** (optimized)
C1–C14e–C14d	129.70°
C14e–C14d–C14c	124.85°
C14d–C14c–C14b	125.75°
C14c–C14b–C14a	124.85°
C14b–C14a–C14	129.70°
sum of bond angles	624.5°

Figure 10. X-ray structures of (a) **SH-Cl$_4$** and (b) **SH**, and (c) the optimized structure of **2** with the inner C–C–C bond angles of their helices.

Photophysical Study

UV–Vis absorption spectra were recorded on a Shimadzu UV-3510 spectrometer with a resolution of 0.5 nm. Emission spectra were measured with an FP-6600 Hitachi spectrometer with a resolution of 0.2 nm. CD spectra were measured with a JASCO FT/IR6100. Dilute solutions in degassed spectral grade chloroform in a 1 cm square quartz cell were used for measurements. Absolute fluorescence quantum yields were determined with a Hamamatsu C9920-02 calibrated integrating sphere system upon excitation at 390 nm for **SH** and at 400 nm for **SH-Cl$_4$**.

Computational Study

The Gaussian 09 program[11] running on a SGI Altix4700 system was used for optimization (B3LYP/6-31G(d)).[12] All structures were optimized without any symmetry assumptions. Zero-point energy, enthalpy, and Gibbs free energy at 298.15 K and 1 atm were estimated from the gas-phase studies unless otherwise noted. Harmonic vibration frequency calculations at the same level were performed to verify all stationary points as local minima (with no imaginary frequency) or transition states (with one imaginary frequency). IRC calculations[13] were also performed to check transition states. Visualization of the results was performed by use of GaussView 5.0 software.

Table 2. Uncorrected and thermal-corrected (298 K) energies of stationary points (Hartree).[a]

structure	*E*	*E* + *ZPE*	*H*	*G*
(*P*,*P*)-**TetraMe-SH-Cl$_4$**	-5504.70342030	-5504.119403	-5504.071578	-5504.197561
(*P*,*P*)-**TetraMe-SH**	-3666.34989535	-3665.726369	-3665.683855	-3665.796476
(*P*,*M*)-**TetraMe-SH**	-3666.32618076	-3665.702628	-3665.660300	-3665.772976
(*P*)-TS1	-3666.30397405	-3665.680201	-3665.638612	-3665.750119
(*M*)-TS2	-3666.27275077	-3665.649671	-3665.608308	-3665.717242
2	-1641.96934408	-1641.701052	-1641.683407	-1641.744832

a) *E*: electronic energy; *ZPE*: zero-point energy; *H* (= $E + ZPE + E_{vib} + E_{rot} + E_{trans} + RT$): sum of electronic and thermal enthalpies; *G* (= $H - TS$): sum of electronic and thermal free energies.

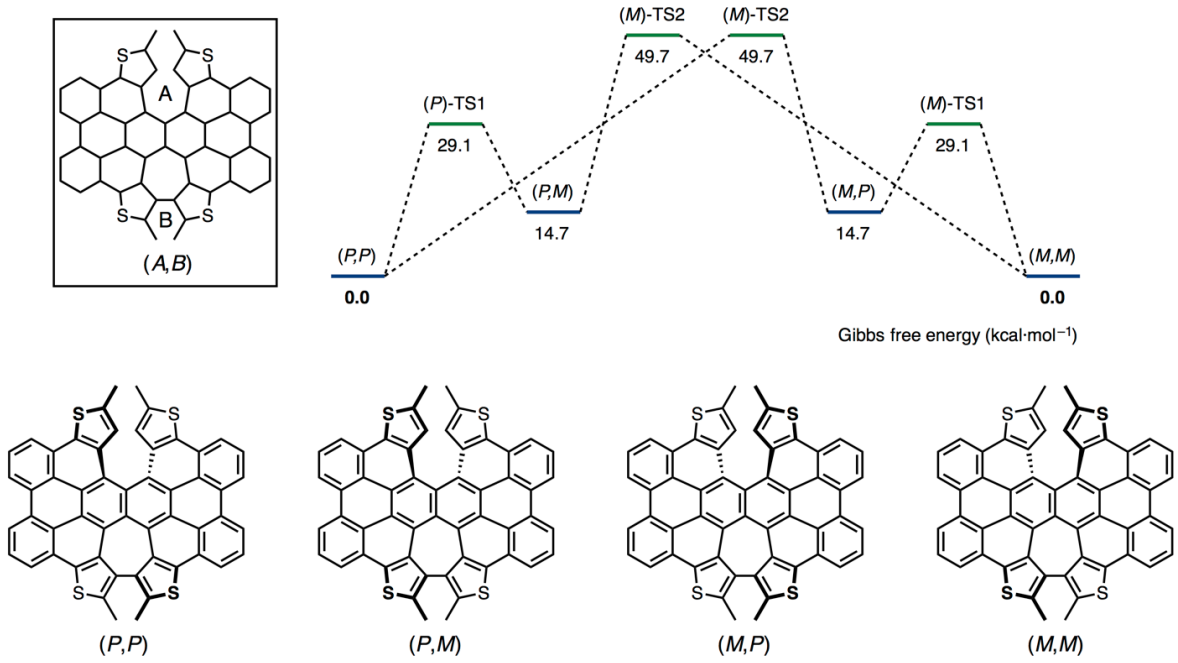

Figure 11. Overall view of the interconversion pathways of **TetraMe-SH** (B3LYP/6-31G(d)). The *n*-butyl groups were replaced with methyl groups to simplify the calculations.

Table 3. TD DFT vertical one-electron excitations (9 states) calculated for the optimized structure of **TetraMe-SH-Cl$_4$**.

Excited State	1:		
2.3684 eV	523.49 nm	f=0.1889	
	HOMO -> LUMO		0.69398
Excited State	2:		
2.5995 eV	476.95 nm	f=0.0035	
	HOMO–2 -> LUMO		-0.38897
	HOMO–1 -> LUMO		-0.21504
	HOMO -> LUMO+1		0.46103
	HOMO -> LUMO+2		-0.28307
Excited State	3:		
2.6849 eV	461.79 nm	f=0.0279	
	HOMO–2 -> LUMO		-0.19640
	HOMO–1 -> LUMO		0.61519
	HOMO -> LUMO+2		-0.26726
Excited State	4:		
2.8587 eV	433.71 nm	f=0.0006	
	HOMO–3 -> LUMO		0.68222
	HOMO–1 -> LUMO+2		0.10459
	HOMO -> LUMO+3		-0.10873
Excited State	5:		
2.8595 eV	433.58 nm	f=0.1396	
	HOMO–2 -> LUMO		0.16941
	HOMO–1 -> LUMO		0.25548
	HOMO -> LUMO+1		0.49769
	HOMO -> LUMO+2		0.38038
Excited State	6:		
3.0430 eV	407.44 nm	f=0.7023	
	HOMO–2 -> LUMO		0.51434
	HOMO -> LUMO+1		0.15848
	HOMO -> LUMO+2		-0.42411
Excited State	7:		
3.0494 eV	406.59 nm	f=0.0157	
	HOMO–4 -> LUMO		-0.30009
	HOMO–2 -> LUMO+1		-0.16900
	HOMO–2 -> LUMO+2		-0.14643
	HOMO–1 -> LUMO+1		0.50233
	HOMO–1 -> LUMO+2		-0.28915
Excited State	8:		
3.1767 eV	390.30 nm	f=0.0039	
	HOMO–4 -> LUMO		0.52927
	HOMO–1 -> LUMO+1		0.27231
	HOMO -> LUMO+3		0.32506
Excited State	9:		
3.2013 eV	387.30 nm	f=0.0007	
	HOMO–4 -> LUMO		-0.14720
	HOMO–2 -> LUMO+1		0.39821
	HOMO–1 -> LUMO+1		0.31256
	HOMO–1 -> LUMO+2		0.44002
	HOMO -> LUMO+3		0.10908

Table 4. TD DFT vertical one-electron excitations (9 states) calculated for the optimized structure of **TetraMe-SH-1**.

Excited State 1:	
2.4499 eV 506.08 nm f=0.1690	
HOMO–2 ->LUMO+2	-0.1116
HOMO ->LUMO	0.69294
Excited State 2:	
2.6671 eV 464.87 nm f=0.0037	
HOMO–2 ->LUMO	0.46305
HOMO–1 ->LUMO	-0.21294
HOMO ->LUMO+1	-0.29056
HOMO ->LUMO+2	0.38232
Excited State 3:	
2.7721 eV 447.26 nm f=0.0112	
HOMO–2 ->LUMO	0.22872
HOMO–1 ->LUMO	0.58310
HOMO ->LUMO+1	0.22443
HOMO ->LUMO+2	0.21652
Excited State 4:	
2.9299 eV 423.18 nm f=0.0000	
HOMO–3 ->LUMO	0.68508
HOMO ->LUMO+3	0.10704
Excited State 5:	
2.9359 eV 422.30 nm f=0.0989	
HOMO–1 ->LUMO	-0.32080
HOMO ->LUMO+1	0.58866
HOMO ->LUMO+2	0.17770
Excited State 6:	
3.1336 eV 395.67 nm f=0.7626	
HOMO–2 ->LUMO	-0.46016
HOMO ->LUMO+2	0.50137
Excited State 7:	
3.1537 eV 393.14 nm f=0.0053	
HOMO–4 ->LUMO	0.38607
HOMO–2 ->LUMO+1	0.29735
HOMO–1 ->LUMO+1	0.27058
HOMO–1 ->LUMO+2	-0.38594
Excited State 8:¥	
3.2535 eV 381.08 nm f=0.0015	
HOMO–4 ->LUMO	0.47997
HOMO–2 ->LUMO+1	-0.31804
HOMO–1 ->LUMO+1	-0.10162
HOMO–1 ->LUMO+2	0.21434
HOMO ->LUMO+3	0.29743
Excited State 9:	
3.2649 eV 379.75 nm f=0.0000	
HOMO–2 ->LUMO+1	-0.26823
HOMO–2 ->LUMO+2	0.18880
HOMO–1 ->LUMO+1	0.55067
HOMO–1 ->LUMO+2	0.16478
HOMO ->LUMO+3	-0.22222

Reference

1. Benzohelicenes: (a) Klívar, J.; Jančařík, A.; Šaman, D.; Pohl, R.; Fiedler, P.; Bednárová, L.; Starý, I. G.; Stará, I. *Chem. Eur. J.* **2016**, *22*, 14401. (b) Šámal, M.; Chercheja, S.; Rybáček, J.; Chocholoušová, J. V.; Vacek, J.; Bednárová, L.; Šaman, D.; Stará, I. G.; Starý, I. *J. Am. Chem. Soc.* **2015**, *137*, 8469. (c) Bock, H.; Subervie, D.; Mathey, P.; Pradhan, A.; Sarkar, P.; Dechambenoit, P.; Hillard, E. A.; Durola, F. *Org. Lett.* **2014**, *16*, 1546. (d) Chercheja, S.; Klívar, J.; Jančařík, A.; Rybáček, J.; Salzl, S.; Tarábek, J.; Pospíšil, L.; Chocholoušová, J. V.; Vacek, J.; Pohl, R.; Císařová, I.; Starý, I.; Stará, I. G. *Chem. Eur. J.* **2014**, *20*, 8477. (e) Jančařík, A.; Rybáček, J.; Cocq, K.; Chocholoušová, J. V.; Vacek, J.; Pohl, R.; Bednárová, L.; Fiedler, P.; Císařová, I.; Stará, I. G.; Starý, I. *Angew. Chem., Int. Ed.* **2013**, *52*, 9970. (f) Seibel, J.; Allemann, O.; Siegel, J. S.; Ernst, K.-H. *J. Am. Chem. Soc.* **2013**, *135*, 7434. (g) Hatakeyama, T.; Hashimoto, S.; Oba, T.; Nakamura, M. *J. Am. Chem. Soc.* **2012**, *134*, 19600. (h) Sawada, Y.; Furumi, S.; Takai, A.; Takeuchi, M.; Noguchi, K.; Tanaka, K. *J. Am. Chem. Soc.* **2012**, *134*, 4080. (i) Laarhoven, W. H.; Nivard, R. J. F. *Tetrahedron* **1976**, *32*, 2445. (j) Laarhoven, W. H.; Cuppen, Th. J. H. M.; Nivard, R. J. F. *Tetrahedron* **1970**, *26*, 4865.
2. Pyrenohelicenes: (a) Buchta, M.; Rybáček, J.; Jančařík, A.; Kudale, A. A.; Buděšínský, M.; Chocholoušová, J. V.; Vacek, J.; Bednárová, L.; Císařová, I.; Bodwell, G. J.; Starý, I.; Stará, I. G. *Chem. Eur. J.* **2015**, *21*, 8910. (b) Bédard, A.-C.; Vlassova, A.; Hernandez-Perez, A. C.; Bessette, A.; Hanan, G. S.; Heuft, M. A.; Collins, S. K. *Chem. Eur. J.* **2013**, *19*, 16295. (c) Hu, J.-Y.; Paudel, A.; Seto, N.; Feng, X.; Era, M.; Matsumoto, T.; Tanaka, J.; Elsegood, M. R. J.; Redshaw, C.; Yamato, T. *Org. Biomol. Chem.* **2013**, *11*, 2186. (d) Hu, J.-Y.; Feng, X.; Paudel, A.; Tomiyasu, H.; Rayhan, U.; Thuéry, P.; Elsegood, M. R. J.; Redshaw, C.; Yamato, T. *Eur. J. Org. Chem.* **2013**, 5829. (e) ref 1c. (f) Hayward, R. J.; Hopkinson, A. C.; Leznoff, C. C. *Tetrahedron* **1972**, *28*, 439. (g) Vingiello, F. A.; Henson, P. D. *J. Org. Chem.* **1965**, *30*, 2842.
3. (a) Fujikawa, T.; Preda, D. V.; Segawa, Y.; Itami, K.; Scott, L. T. *Org. Lett.* **2016**, *18*, 3992. (b) Rajeshkumar, V.; Stuparu, M. C. *Chem. Commun.* **2016**, *52*, 9957.
4. Schuster, N. J.; Paley, D. W.; Jockusch, S.; Ng, F.; Steigerwald, M. L.; Nuckolls, C. *Angew. Chem., Int. Ed.* **2016**, *55*, 13519.
5. Wang, L.; Warburton, P. L.; Szekeres, Z.; Surjan, P.; Mezey, P. G. *J. Chem. Inf. Model.* **2005**, *45*, 850.
6. Dopper, J. H.; Oudman, D.; Wynberg, H. *J. Org. Chem.* **1975**, *40*, 3398.
7. Shan, L.; Liu, D.; Li, H.; Xu, X.; Shan, B.; Xu, J.-B.; Miao, Q. *Adv. Mater.* **2015**, *27*, 3418.

8. Martin, R. H.; Marchant, M. J. *Tetrahedron* **1974**, *30*, 347.
9. Altomare, A.; Burla, M. C.; Camalli, M.; Cascarano, G. L.; Giacovazzo, C.; Guagliardi, A.; Moliterni, A. G. G.; Polidori, G.; Spagna, R. *J. Appl. Crystallogr.* **1999**, *32*, 115.
10. Sheldrick, G. M. University of Göttingen: Göttingen, Germany, 1997.
11. Frisch, M. J.; Trucks, G. W.; Schlegel, H. B.; Scuseria, G. E.; Robb, M. A.; Cheeseman, J. R.; Scalmani, G.; Barone, V.; Mennucci, B.; Petersson, G. A.; Nakatsuji, H.; Caricato, M.; Li, X.; Hratchian, H. P.; Izmaylov, A. F.; Bloino, J.; Zheng, G.; Sonnenberg, J. L.; Hada, M.; Ehara, M.; Toyota, K.; Fukuda, R.; Hasegawa, J.; Ishida, M.; Nakajima, T.; Honda, Y.; Kitao, O.; Nakai, H.; Vreven, T.; Montgomery, Jr., J. A.; Peralta, J. E.; Ogliaro, F.; Bearpark, M.; Heyd, J. J.; Brothers, E.; Kudin, K. N.; Staroverov, V. N.; Keith, T.; Kobayashi, R.; Normand, J.; Raghavachari, K.; Rendell, A.; Burant, J. C.; Iyengar, S. S.; Tomasi, J.; Cossi, M.; Rega, N.; Millam, J. M.; Klene, M.; Knox, J. E.; Cross, J. B.; Bakken, V.; Adamo, C.; Jaramillo, J.; Gomperts, R.; Stratmann, R. E.; Yazyev, O.; Austin, A. J.; Cammi, R.; Pomelli, C.; Ochterski, J. W.; Martin, R. L.; Morokuma, K.; Zakrzewski, V. G.; Voth, G. A.; Salvador, P.; Dannenberg, J. J.; Dapprich, S.; Daniels, A. D.; Farkas, O.; Foresman, J. B.; Ortiz, J. V.; Cioslowski, J.; Fox, D. J. Gaussian 09, Revision D.01, Gaussian, Inc., Wallingford CT, 2013.
12. (a) Becke, A. D. *J. Chem. Phys.* **1993**, *98*, 5648. (b) Lee, C.; Yang, W.; Parr, R. G. *Phys. Rev. B* **1988**, *37*, 785.
13. (a) Gonzalez, C.; Schlegel, H. B. *J. Chem. Phys.* **1989**, *90*, 2154. (b) Gonzalez, C.; Schlegel, H. B. *J. Phys. Chem.* **1990**, *94*, 5523.

Chapter 5

Synthesis and Structural Features of Quadruple Helicenes: Interplay of Fourfold Helix Accumulation

ABSTRACT: Quadruple helicenes, bearing dithia[6]helicene and [5]helicene substructures, were prepared by a well-controlled oxidative stitching reaction. The fourfold helicity provides nine stereoisomers including four pairs of enantiomers and one *meso*-isomer. Among them, differently distorted structures of a *propeller*-shaped isomer (**QH-A**) and a *saddle*-shaped isomer (**QH-B**) were unambiguously determined by X-ray crystallography. Especially in the latter isomer, a proper accumulation of repulsions on the helical substructures twisted the naphthalene core to the limit (69.5°), the highest degree of twisting deformation per benzene unit (35.3° at the most). Photophysical and electrochemical studies showed a broadened HOMO–LUMO gap and a lower lying HOMO of **QH-B** compared to those of **QH-A**. These results together with the DFT calculation have clearly demonstrated the electronic state dependency on the molecular geometry. Additionally, kinetic studies of the isomerization between these isomers using ^{1}H NMR, CD spectroscopy, and DFT calculations shed light on the interconversion pathways among the stereoisomers. The height of barriers in the inversion of a certain helical substructure may be affected by the neighboring helical substructures.

Introduction

The creation of nonplanar π-systems and the development of new synthetic methods have attracted much interest to understand the limits and possibilities of π-systems.[1] In this regard, twisted aromatics, one of the nonplanar π-systems exhibiting chiroptical properties and dynamic behavior, have been intensively studied over the past two decades.[2] In the field of twisted aromatics, profound twisting deformation has been achieved exclusively by introducing steric hindrance stemming from atom crowdedness and evaluated by the end-to-end twist angle of the core π-system. Pascal's twisted pentacene is the most illustrious example, with a total twist angle of 144° (Figure 1, top).[2c] Besides such twisted acenes, Shinokubo and coworkers also reported the synthesis of a twisted porphyrin tetramer with the total twist angle of ca. 300° (Figure 1, bottom).[3] Like these examples, "total" twisting occurs as long as the core π-system is elongated.

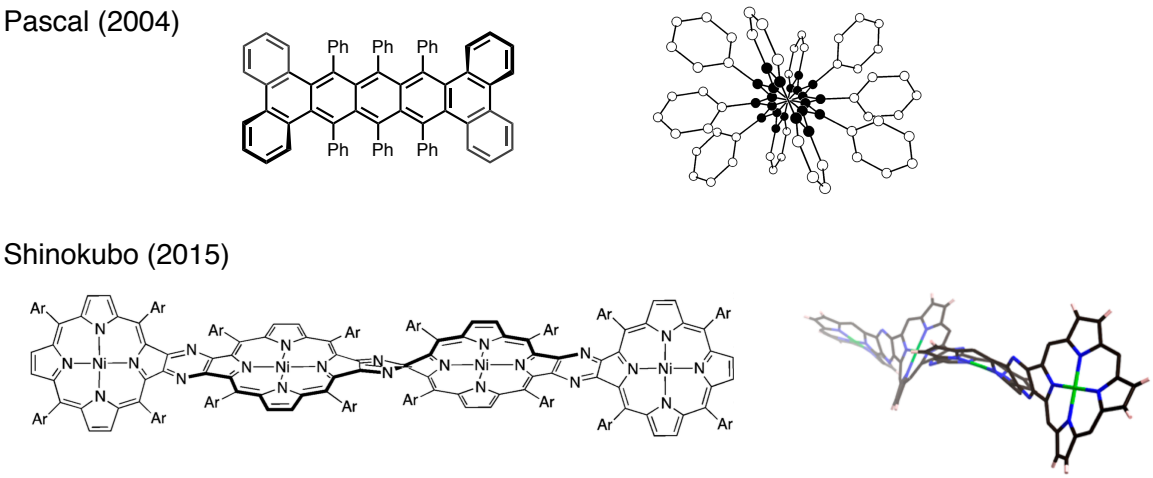

Figure 1. Representative twisted aromatics with large total twist angles.

Another viewpoint of twisting deformation is twist angle per a ring of specific number. As well-documented in all the studies on twisted acenes, aromatic annulation provides a strong repulsive effect on the core π-system compared to bulky substituents. Thus, a twisted pentacene records the largest twist angle of 30° per a single benzene unit as the outcome of fourfold benzannulation in addition to six-fold phenylation (Figure 2, left). Kamikawa recently reported a double [5]helicene, exhibiting the same degree of twisting due to the steric hindrance of fourfold annulation of naphthalene rings on its central naphthalene core (Figure 2, right).[4]

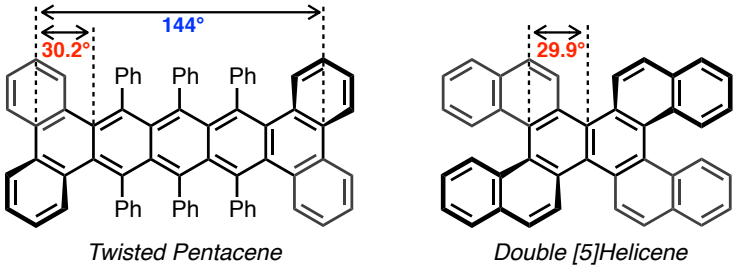

Figure 2. Twisted aromatics exhibiting the largest degree of twisting per a single benzene unit.

This chapter presents the unprecedented twisted nature of quadruple helicenes as a new milestone of twisted π-systems. The arrangement of dithia[6]helicene[5] and [5]helicene substructures around a naphthalene core generates fourfold helical π-systems (Figure 3). Because of the proper accumulation of repulsions on helical substructures, the most severely twisted benzene rings of up to 35° as well as a naphthalene core near 70° were achieved as a *saddle*-shaped isomer. A comparison with *propeller*-shaped isomer also showed the dependence of electronic structure on the molecular geometry of π-systems.

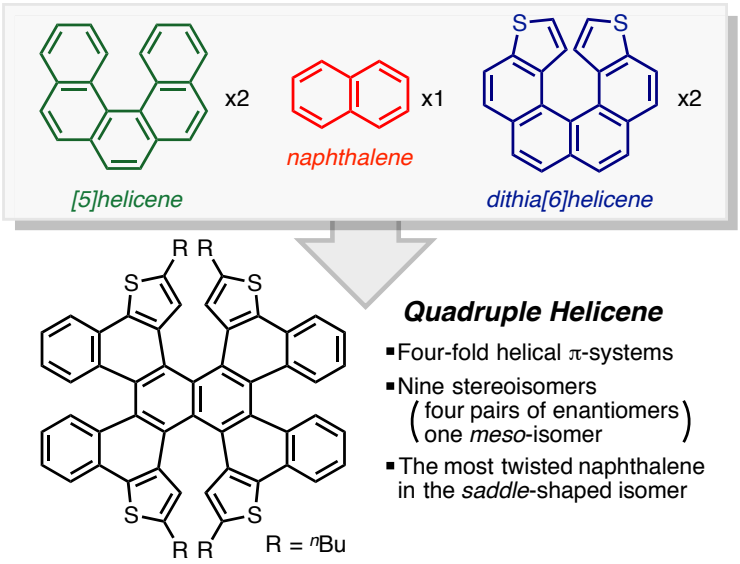

Figure 3. Chemical structure of quadruple helicene.

Result and Discussion

Synthesis, Isomerization, and Racemization

The quadruple helicenes (**QHs**) were unexpectedly obtained during the synthesis of the π-extended double dithia[6]helicene (**DH3**) and single dithia[6]helicene (**SH**), which is described in Chapter 3 and 4. Therein, the fourfold chlorinated products of **DH3** and **SH** were synthesized by the Scholl reaction of the naphthalene derivative **1** using a little bit excess amount of $MoCl_5$ in a diluted dichloromethane solution under inert and aerobic atmosphere, respectively (Scheme 1). It was also found that, as an unexpected result, an incompletely cyclized product **QH-A** can be generated in 57% yield instead of **DH3-Cl$_4$** and **SH-Cl$_4$** when smaller amount of $MoCl_5$ was added in the presence of molecular sieves.

Scheme 1. Synthesis of **DH3-Cl$_4$**, **SH-Cl$_4$**, and quadruple helicenes (**QHs**). One of two enantiomers are shown in each case.

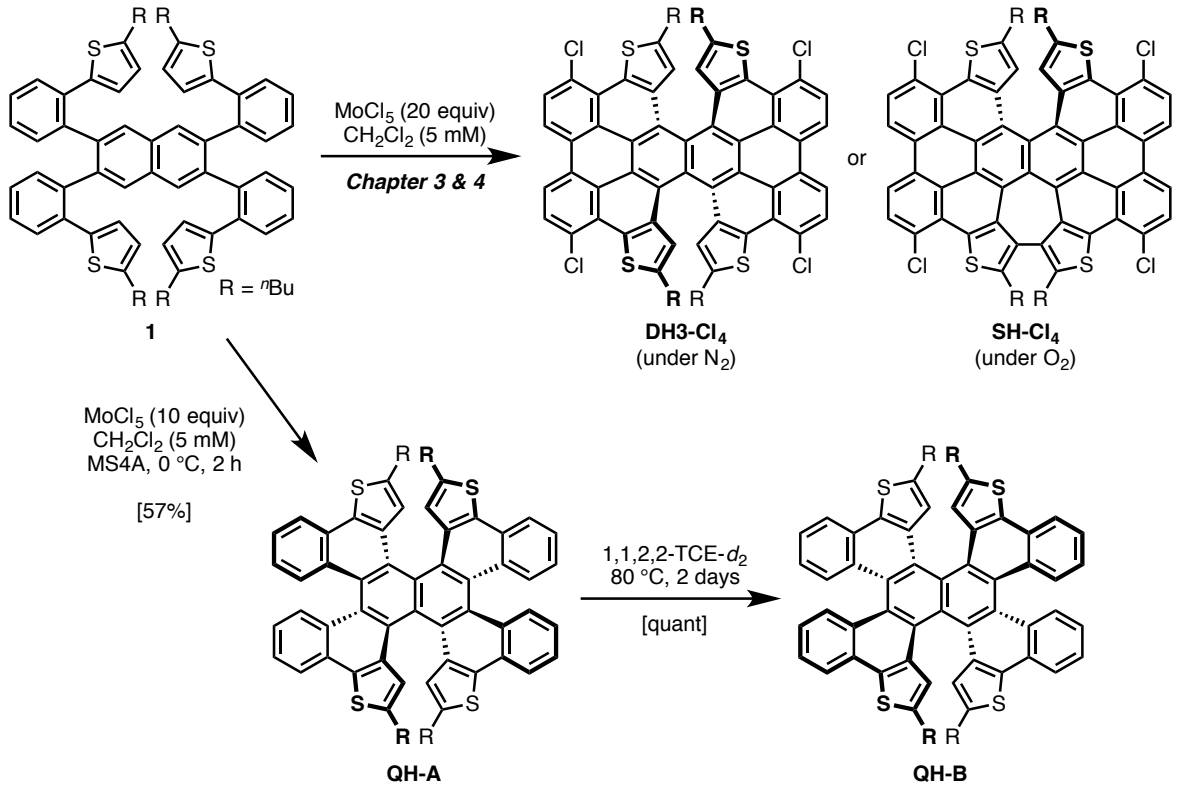

In general, two distinctive reaction mechanisms have been proposed in the Scholl reaction.[6] One is the radical cation mechanism, in which single electron transfer occurs at the beginning to generate radical cation species and cyclization follows. The other is the arenium cation mechanism, in which an electrophilic attack of the Brønsted or Lewis acid occurred first to

generate arenium cation species, and cyclization and oxidation follows. Especially in the Scholl reaction using $MoCl_5$, molecular sieves is known to scavenge the hydrochloric acid generated *in situ*, thus maintaining the oxidizing power of $MoCl_5$ by preventing the acid-coordination to the metal center.[7] In this time, however, the cyclization stopped at the intermediate (**QH**) before completion to **DH3**, **SH**, or their chlorinated products, inferring some kind of lost of oxidizing power. Therefore, it can be concluded that further cyclization after the generation of **QH** proceeds through the arenium cation mechanism in which the hydrochloric acid generated *in situ* promotes the cyclization.

Going back to the synthesis of **QHs**, a quantitative thermal conversion of **QH-A** to another isomer **QH-B** was also accomplished by reacting for 2 days at 80 °C in 1,1,2,2-tetrachloroethane-d_2. This result indicates that **QH-A** is a kinetic product in the Scholl reaction, and can be converted into a more stable isomer **QH-B**, and the barrier to the isomerization is sufficiently high to handle **QH-A** at room temperature without isomerization.

Thus-obtained **QHs** have two substructures, dithia[6]helicene and [5]helicene, in a fully conjugated manner. The ^{1}H NMR analysis showed a simple spectrum with one singlet, two doublets, and two triplets for each isomer. Notably, the singlet peaks corresponding to the hydrogen atoms at the end of the inner helix of dithia[6]helicene substructures in **QH-A** (δ 6.14 ppm) showed a large downfield shift after the conversion to **QH-B** (δ 7.29 ppm), indicating a significant deshielding upon structural change (Figure 4).

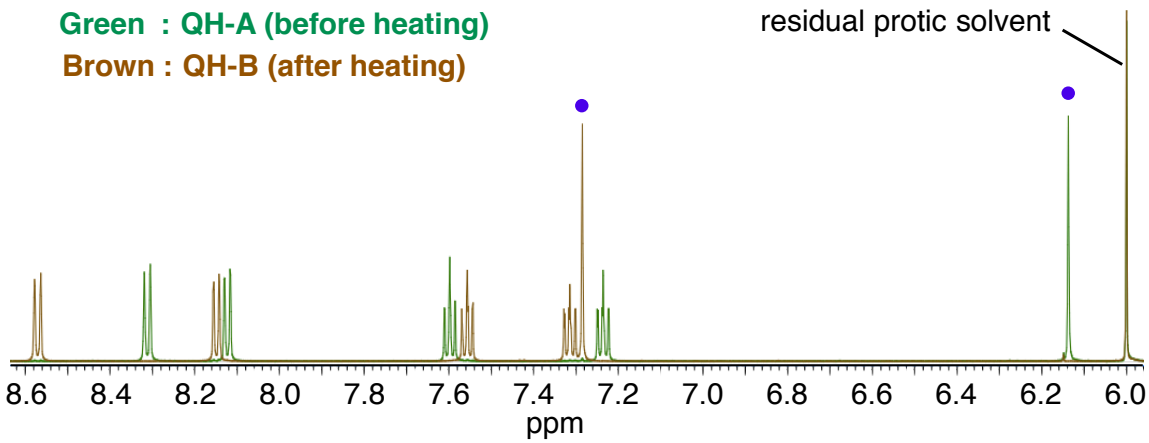

Figure 4. ^{1}H NMR spectra of **QHs** in 1,1,2,2-tetrachloroethane-d_2. The spectra of **QH-A** (before heating) and **QH-B** (after heating) are colored in green and brown, respectively. Singlet peaks of the hydrogens at the end of inner helix of dithia[6]helicene substructures are marked by purple circles.

Considering the fourfold helicity of **QH**, nine stereoisomers including four pairs of enantiomers and one *meso*-isomer can be depicted (five diastereomers in total, Figure 5). Therefore, the X-ray crystallography of both the products was performed to determine their stereochemistry. **QH-A** was characterized as a racemate of (*P*,*P*)-(*P*,*P*)-**QH** and (*M*,*M*)-(*M*,*M*)-**QH** (the helicity notation is shown in the right bottom of Figure 5); all the helical substructures possess identical helicity forming a *propeller*-shaped molecular geometry (*vide infra*). **QH-B** was also characterized as a racemate of (*P*,*P*)-(*M*,*M*)-**QH** and (*M*,*M*)-(*P*,*P*)-**QH**; the two different helical substructures possess opposite helicity forming a *saddle*-shaped molecular geometry. Both the structures determined here have a higher symmetry of D_2 than those of C_2 for **QH-C** and **QH-D** or C_i for **QH-E**. This is also consistent with their simple ^{1}H NMR spectra.

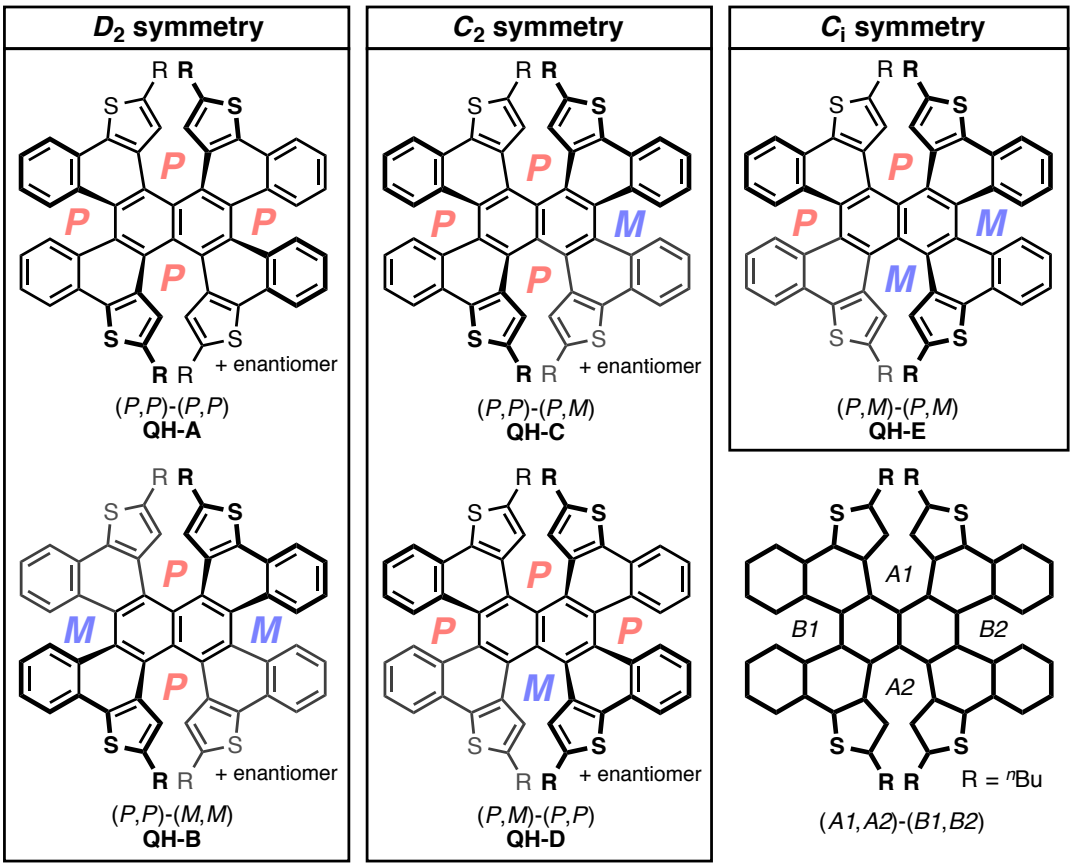

Figure 5. Stereoisomers of **QHs**.

The presence of chiral π-systems resulting from the combination of helicity in **QHs** motivated us to separate their enantiomers (Figure 6). First, optical resolution of **QH-A** was carried out using means of HPLC equipped with a COSMOSIL Cholester column. The specific optical

rotation $[\alpha]^{20}_{D}$ of the faster eluting peak (>99% *ee*, Figure 6b; (+)-**QH-A**) was measured to be +496 (*c* 0.10, CH_2Cl_2). In contrast, because the complete chiral separation of **QH-B** by HPLC failed, the thermal conversion of enantiopure **QH-A** to the corresponding enantiopure **QH-B** without racemization was tried (Scheme 2). By heating a toluene solution of (+)-**QH-A** at 80 °C for 2 days, an enantiopure product (+)-**QH-B** with a specific rotation $[\alpha]^{20}_{D}$ of +426 (*c* 0.0496, CH_2Cl_2) was successfully obtained (Figure 6d). These $[\alpha]^{20}_{D}$ values were rather small compared to those of single helicenes, which are generally above 1000 as the absolute value.[8] The progress in the racemization of **QH-B** was also confirmed by heating a 1,2,4-trichlorobenzene solution of (+)-**QH-B** at an elevated temperature of above 185 °C (Figure 6e).

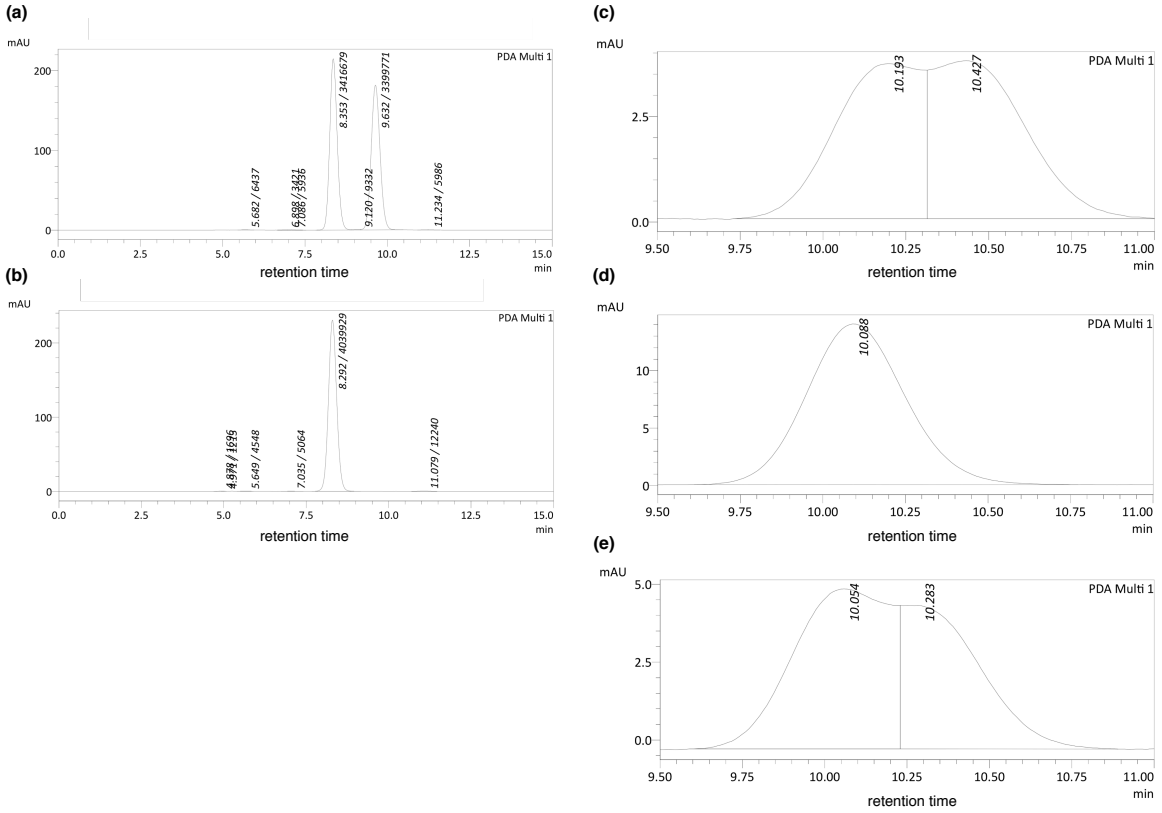

Figure 6. HPLC analysis of (a) the racemic mixture of **QH-A**, (b) the separated (+)-**QH-A**, (c) the racemic mixture of **QH-B**, (d) (+)-**QH-B** obtained by the thermal conversion of (+)-**QH-A**, and (e) the thermal racemization progress of (+)-**QH-B** after heating over 185 °C in 1,2,4-trichlorobenzene for 22 h.

Scheme 2. Optically preserved thermal isomerization from (+)-**QH-A** to (+)-**QH-B** in toluene solution and racemization of (+)-**QH-B** in 1,2,4-trichlorobenzene solution.

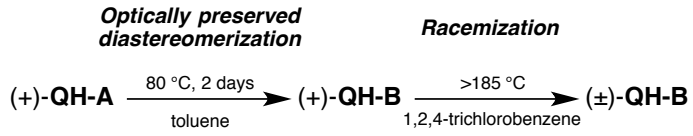

Structures

Single-crystal X-ray structure analyses were performed using the racemic single crystals of **QH-A** recrystallized from *n*-pentane solution and **QH-B** recrystallized from a solution of chloroform and 2-propanol. The crystal of **QH-A** contained two crystallographically independent molecules (**QH-A-1** colored in red and **QH-A-2** colored in green in Figures 7a,b).

The most notable structural difference between two isomers is the end-to-end twist of central naphthalene cores. For **QH-A**, the twist angle ranges from 6.5° (**QH-A-2**) to 13.9° (**QH-A-1**). Conversely, **QH-B** showed a profound twist angle reaching 69.5° (Figure 7c). This twisting deformation of a naphthalene core is the highest among various nonplanar π-systems when converted to those of a single benzene unit (35.3° and 34.2°).[2,4] Clearly, the origin of this exceptional distortion can be attributed to a proper accumulation of repulsions on helical substructures. As shown by the studies on twisted acenes developed by the group of Pascal,[9] the rigidness caused by annulation provides a large repulsive effect, forcing the core π-system to form highly twisted geometries. In the case of **QH-B**, all the repulsions on helical substructures cause the same directional distortion to the central naphthalene, resulting in such an extremely twisted structure.

A large distortion of **QH-B** was also reflected in the splay angles of helical substructures, herein defined as the selected dihedral angles of four inner carbon atoms (Figure 7d). Although the splay angles of 23.7° in [5]helicene substructures and 51.4° in dithia[6]helicene substructures on average for **QH-A-1**, and 29.5° and 46.0° on average for **QH-A-2** are comparable to those in pristine [5]helicene (27.9° in the X-ray structure)[10] and dithia[6]helicene (46.4° in the optimized structure), respectively, **QH-B** showed larger splay angles of 43.7° and 62.6°. This structural difference in helical distortion may be maintained in the solution phase because of the significant disparity of the chemical shift of inner singlet hydrogen atoms between the two isomers (Figure 4) indicating more compressed dithia[6]helicene substructures of **QH-A**. The inner hydrogen atoms in **QH-A** are properly located over the polycyclic aromatic system and therefore have a great shielding effect. To support this assumption, the NMR calculations were performed on the optimized structures and imperfect structures by removing two biaryl units

and replacing the inner hydrogen atoms with dummy atoms. The difference in the estimated shielding constants ($\Delta\delta$ = 1.39) of dummy atoms is in good agreement with the difference in the estimated chemical shifts of inner hydrogen atoms ($\Delta\delta$ = 1.13); thus, the possibility of the ring current deterioration of annulated thiophene rings was excluded (Figure 8).

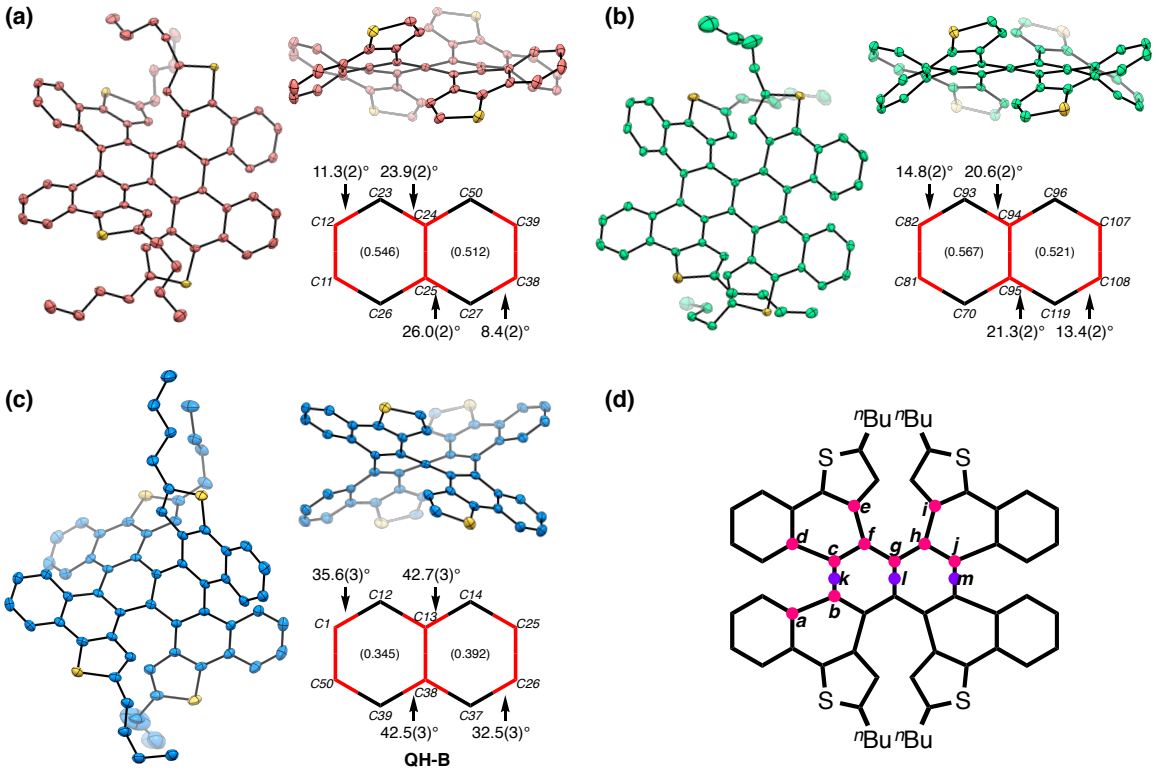

Figure 7. X-ray structures and their naphthalene cores with HOMA values (in parentheses) and dihedral angles (colored in red) of (a) **QH-A-1** ((*P*,*P*)-(*P*,*P*), red), (b) **QH-A-2** ((*P*,*P*)-(*P*,*P*), green)), and (c) **QH-B** ((*P*,*P*)-(*M*,*M*), blue). ORTEP drawings are shown with 50% probability; the hydrogen atoms and the minor part of the disordered moieties are omitted for clarity. The *n*-butyl groups are also omitted for clarity in side views. (d) Selected carbon atoms and centroids for the estimation of end-to-end twist angles (C(c)–C(k)–C(m)–C(j)), twist angles per benzene unit (C(c)–C(k)–C(l)–C(g) and C(g)–C(l)–C(m)–C(j)), and splay angels of helical substructures (C(a)–C(b)–C(c)–C(d) for [5]helicene substructures and C(e)–C(f)–C(h)–C(i) for dithia[6]helicene substructures).

Another characteristic difference between two isomers is the dihedral angles of four selected carbon atoms in their central naphthalene skeletons. The naphthalene cores of **QH-A** showed relatively small dihedral angles at the edge of naphthalene cores (8.4(2)° and 11.3(2)°

for **QH-A-1**, and 13.4(2)° and 14.8(2)° for **QH-A-2**) and at the center (23.9(2)° and 26.0(2)° for **QH-A-1**, and 20.6(2)° and 21.3(2)° for **QH-A-2**), compared to those of **QH-B** (32.5(3)° and 35.6(3)° at the edge, and 42.5(3)° and 42.7(3)° at the center). In contrast to these substantial differences in the dihedral angles, a negligible difference was observed in the bond lengths of naphthalene rings between two isomers (Figure 9). Hence, only a slightly enhanced bond alternation upon the conversion from **QH-A** to **QH-B** was estimated from the value of the harmonic oscillator model of aromaticity (HOMA)[11] of two independent rings (ave. HOMA = 0.369 for **QH-A** and ave. HOMA = 0.537 for **QH-B**).

(a)

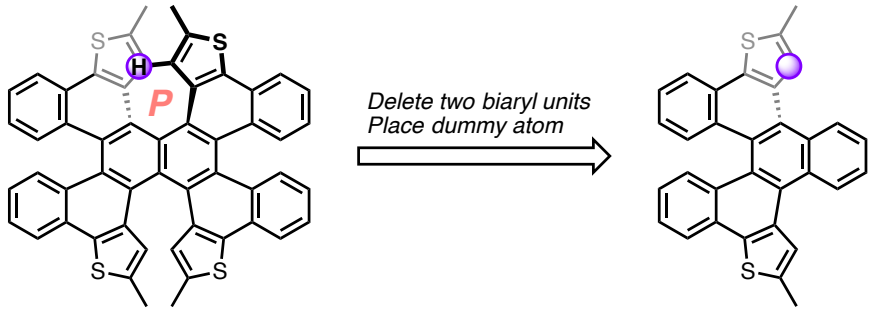

	QH-A	**QH-B**	$\Delta(\delta H_B - \delta H_A)$	**QH-A** (partial)	**QH-B** (partial)	$\Delta(\delta Bq_B - \delta Bq_A)$
Chemical shifts (ppm)	6.36	7.49	1.13	-	-	-
Shielding constants (ppm)	-	-	-	–1.57	–0.18	1.39

(b)

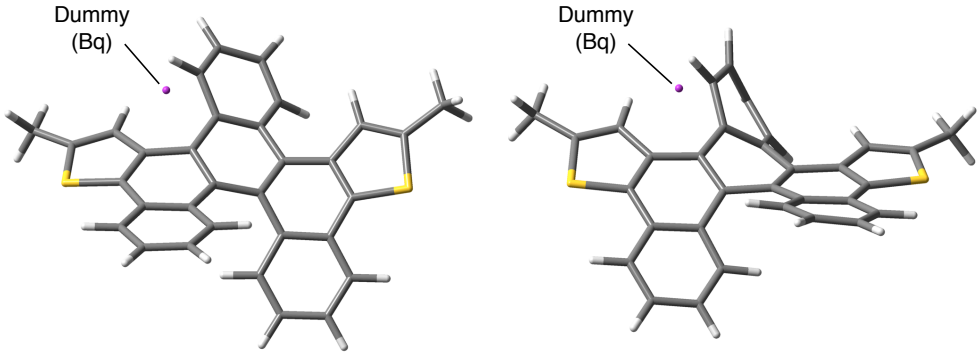

Figure 8. (a) Virtual scheme for the preparation of imperfect structures of **QH-A** and **QH-B** removing two biaryl units. Dummy atoms were placed instead of hydrogen atoms at the end of inner helix of dithia[6]helicene substructures. Results of NMR chemical shifts calculations were also summarized. (b) Structures of imperfect form of **QH-A** and **QH-B** with dummy atoms (Bq).

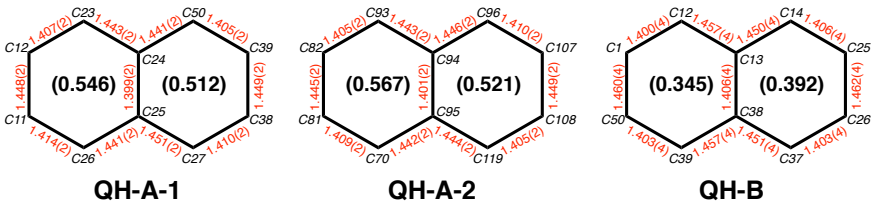

Figure 9. Bond lengths and values of HOMA of naphthalene cores in X-ray structures.

Electronic Structures of QH-A and QH-B

The UV–Vis absorption and fluorescence spectra of **QH-A** and **QH-B** clearly showed the difference in the molecular geometries, affecting electronic structures (Figure 10). The *propeller*-shaped geometry (**QH-A**) resulted in a weak shoulder-like absorption band at ~520 nm in addition to a weak absorption maximum at 459 nm and an intense absorption maximum at 405 nm ($\varepsilon = 5.9 \times 10^4$). In comparison, the *saddle*-shaped geometry (**QH-B**) afforded a similar but blue-shifted spectrum with a weak shoulder-like absorption band at ~495 nm in addition to a weak broad absorption band in the region 400–480 nm and an intense absorption at 381 nm ($\varepsilon = 7.7 \times 10^4$). A blue-shift was observed in the fluorescence spectra in the same manner, producing fluorescence maxima at 536 nm and 570 nm ($\Phi_F = 0.017$) for **QH-A**, and at 514 nm for **QH-B** ($\Phi_F = 0.11$).

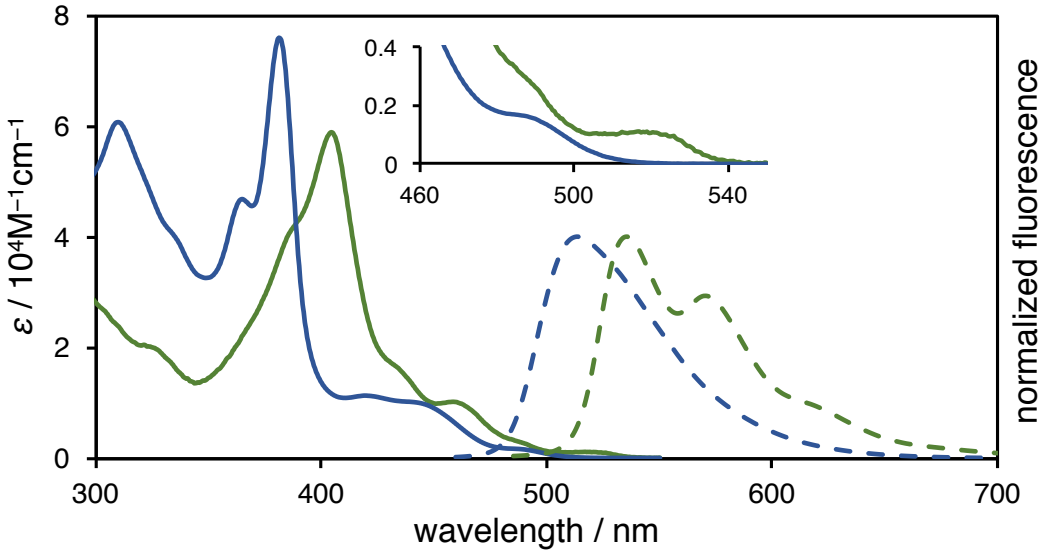

Figure 10. UV–Vis absorption spectra (solid lines) and fluorescence spectra (broken lines) of **QH-A** (green) and **QH-B** (blue) in dichloromethane.

TD DFT calculations (B3LYP/6-31G(d)) confirmed the spectral change between **QH-A** and **QH-B**. Both the absorptions of shoulder bands at ~500 nm (S_1) and intense absorptions around 400 nm (S_4) were assigned to the HOMO−1→LUMO/HOMO→LUMO+1 transitions, and the weak absorptions at ~450 nm (S_2) were assigned to the HOMO→LUMO/HOMO−1→LUMO+1 transitions (Figure 11). Notably, computations showed that the energy levels of HOMO−1/HOMO and LUMO/LUMO+1 were reversed upon the change in geometry, affording different frontier orbitals in each isomer. These inversions of frontier orbitals can be attributed to the difference in connectivity of π-conjugation along the shorter axis of the naphthalene core. The larger dihedral angle at the edge of central naphthalene in **QH-B** (Figure 7) probably disrupts the π-conjugation along the path from one thiophene ring to the other (i.e. along the *p*-dithiophenylbenzene skeleton), and lowers the energies of orbitals involving this conjugation such as the HOMO and LUMO of **QH-A**.

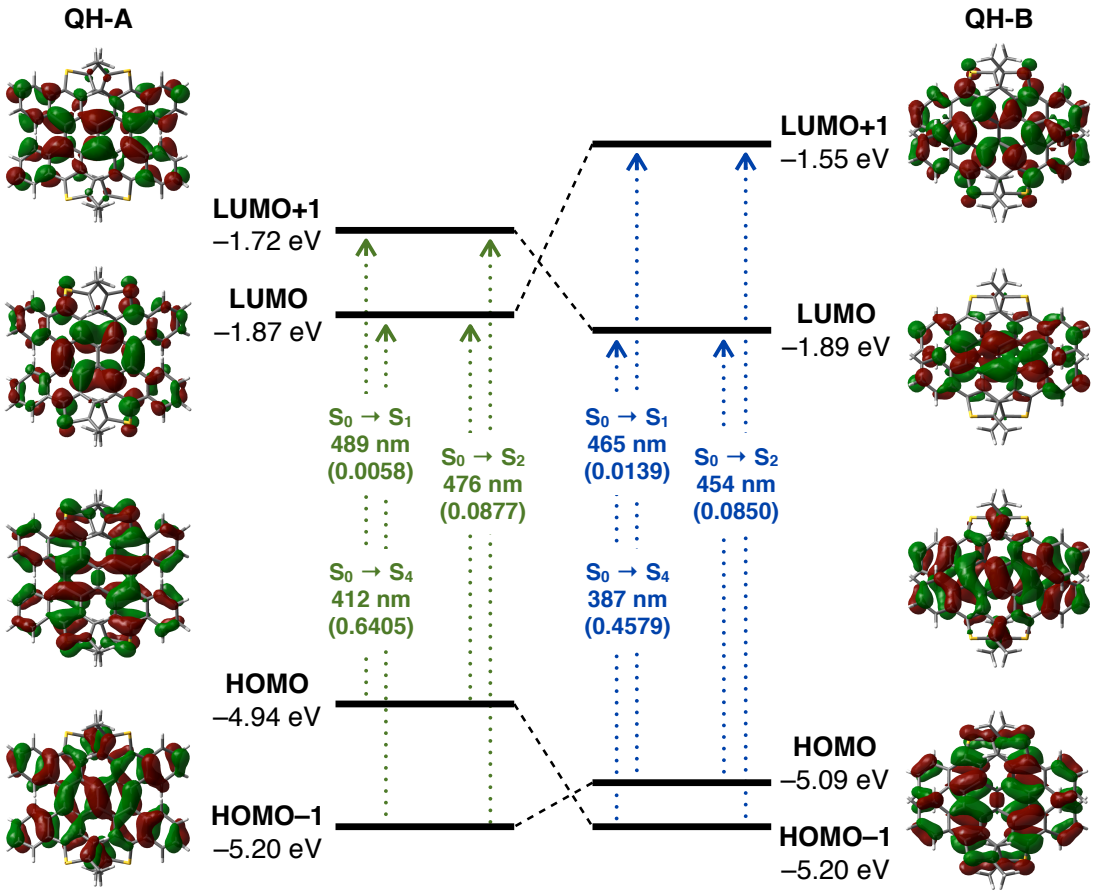

Figure 11. Energy diagrams of **QH-A** and **QH-B** calculated at the B3LYP/6-31G(d) level of theory. Excitation energies were computed by TD DFT calculations at the same levels. Values in parentheses represents oscillator strengths (*f*).

The energy level difference of HOMOs of **QH-A** (−4.94 eV) and **QH-B** (−5.09 eV) estimated from DFT calculations was confirmed electrochemically (Figure 12). The cyclic voltammetry of **QH-A** showed reversible two-step oxidation wave with the half-wave potential $E_{1/2}$ of 0.48 V and 0.87 V (vs FcH/FcH^+), and that of **QH-B** showed reversible oxidation wave with the half-wave potential $E_{1/2}$ of 0.64 V (vs FcH/FcH^+). The second oxidation wave of **QH-B** was not observed reversibly, which may be due to the instability of the oxidized product. A difference of 0.16 V in the first oxidation potentials of the two isomers is consistent with the calculated results.

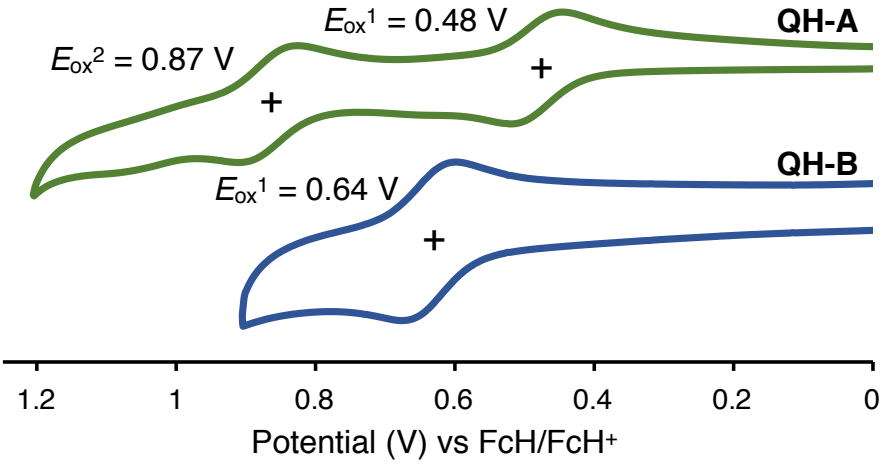

Figure 12. Cyclic voltammograms of **QH-A** (green) and **QH-B** (blue) in dichloromethane containing 100 mM of $TBAPF_6$ at scan rate of 0.1 V s^{-1}. FcH = ferrocene.

The CD spectra of (+)-**QH-A** exhibited negative Cotton effects in the region 370–530 nm in response to the extinction coefficient of absorption spectra, and an intense signal with a positive Cotton effect at ~330 nm (Figure 13). In contrast, the CD spectra of (+)-**QH-B** in the longer wavelength region showed almost opposite Cotton effects to those of (+)-**QH-A** except the negative signal at ~445 nm. The signal corresponding to the intense signal at ~330 nm in the spectra of (+)-**QH-A** became so weakened and unclear in the case of (+)-**QH-B**. Because of the good agreement of the experimental CD spectra with the simulated spectra obtained from the TD DFT calculations (Figures 14a,b), (+)-**QH-A** was assigned as (*P*,*P*)-(*P*,*P*)-**QH**, and (+)-**QH-B** was assigned as (*P*,*P*)-(*M*,*M*)-**QH**. Inevitably, (−)-**QH-A**, which eluted slower and showed mirror-image CD spectra of (+)-**QH-A**, was assigned as (*M*,*M*)-(*M*,*M*)-**QH** (Figure 14c).

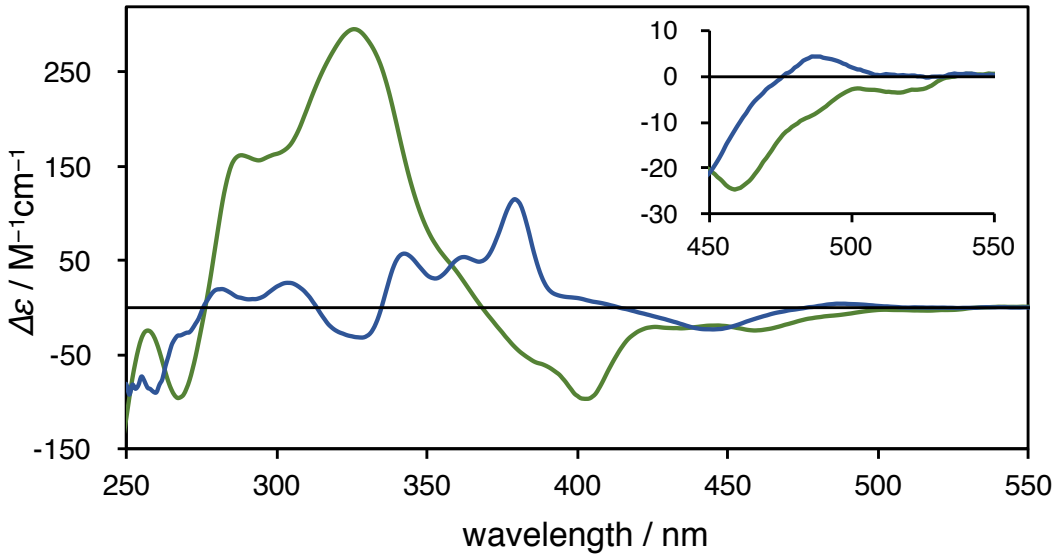

Figure 13. Experimental CD spectra of (+)-**QH-A** (green; assigned to (*P*,*P*)-(*P*,*P*)-**QH**) and (+)-**QH-B** (blue; assigned to (*P*,*P*)-(*M*,*M*)-**QH**).

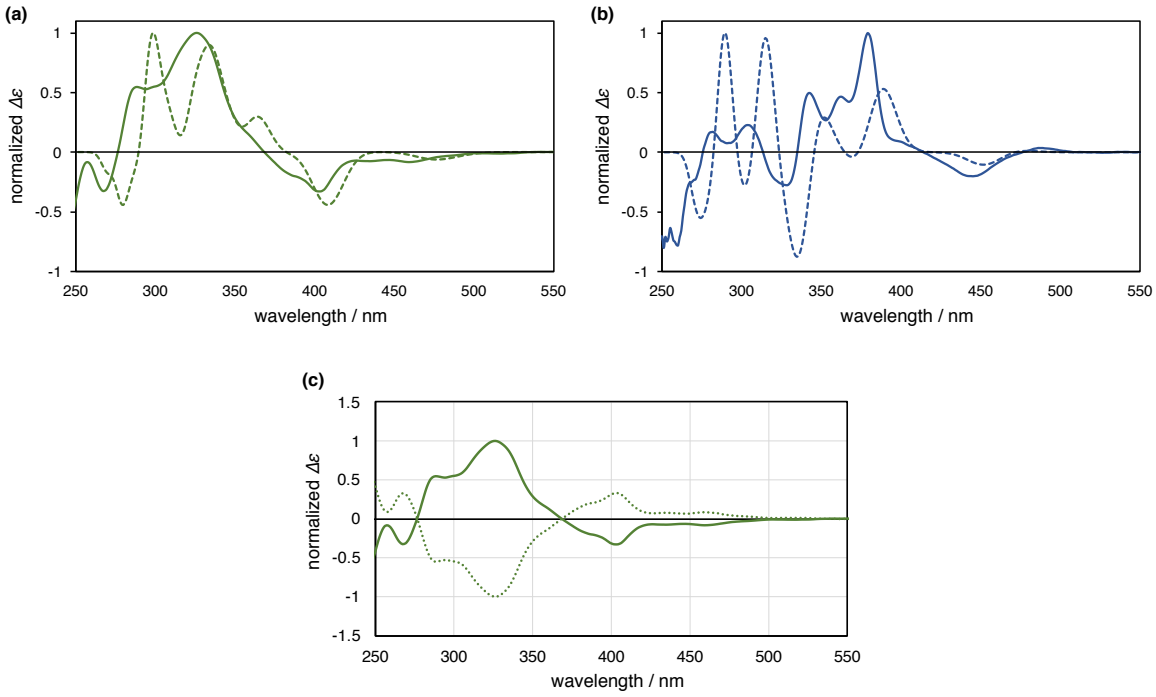

Figure 14. Superpositions of experimental (solid lines) and simulated (broken lines) CD spectra of (a) (+)-**QH-A** and (b) (+)-**QH-B**. Calculated at the B3LYP/6-31G(d) level. (c) CD spectra of (+)-**QH-A** (solid line) and (−)-**QH-A** (dot line).

Several multihelical π-systems have plural electronic structures due to the presence of diastereomers. Only a few literature, however, mentioned the dependence of electronic structure on the molecular geometry based on the experimental results.[12,13] In this case, a variety of the geometry dependence was discovered such as HOMO–LUMO energy gaps, HOMO energy levels, frontier orbitals, fluorescence quantum yields, and chiroptical properties between **QH-A** and **QH-B** from the photophysical and electrochemical analyses in addition to DFT studies.

Kinetics of the Interconversion Pathway among QHs

In association with any transitions between the five diastereomers, one of the four helical substructures of **QHs** inverts. Based on this inversion law, the interconversion pathway was investigated theoretically (B3LYP/6-31G(d)). The *n*-butyl groups of **QHs** were replaced with methyl groups to simplify the calculations. As a consequence, six transition states with face-to-face oriented terminal aromatic rings of helical substructures were found (Figure 15).[14] This indicates that **QH-A** isomerizes to the most thermodynamically stable **QH-B** (stable by 8.1 kcal·mol^{-1}) after the temporal isomerization to **QH-C** (Figure 16). Along this conversion, only the inversions of [5]helicene substructures occur; the calculated activation free energy from **QH-A** to $\mathbf{TS_{A–C}}$ ($\Delta G^{\ddagger}$ = 29.0 kcal·mol^{-1}) is higher than that from **QH-C** to $\mathbf{TS_{B–C}}$ ($\Delta G^{\ddagger}$ = 25.5 kcal·mol^{-1}). Thus, it can be inferred that the former step is the rate-determining step (RDS).

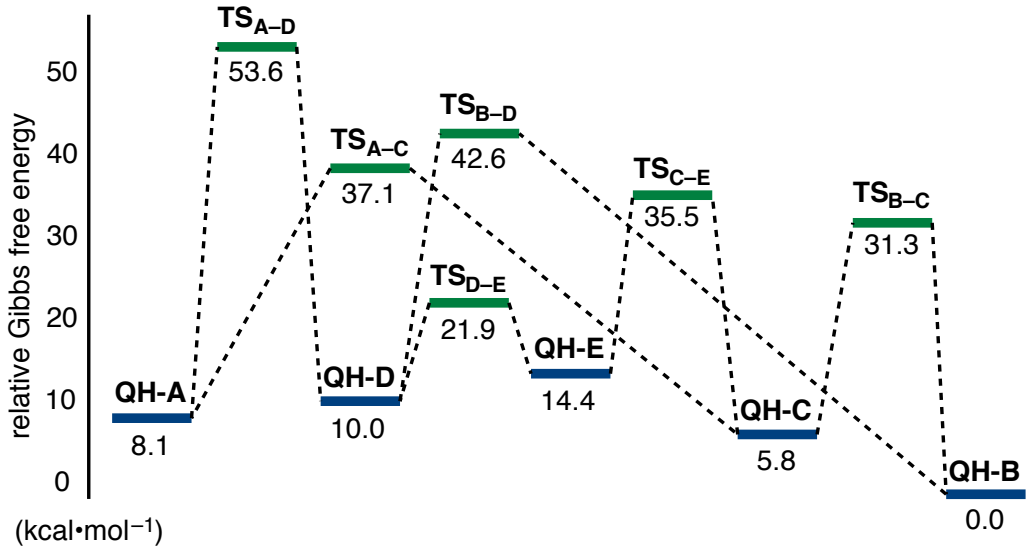

Figure 15. Interconversion pathway among five diastereomers calculated at the B3LYP/6-31G(d) level.

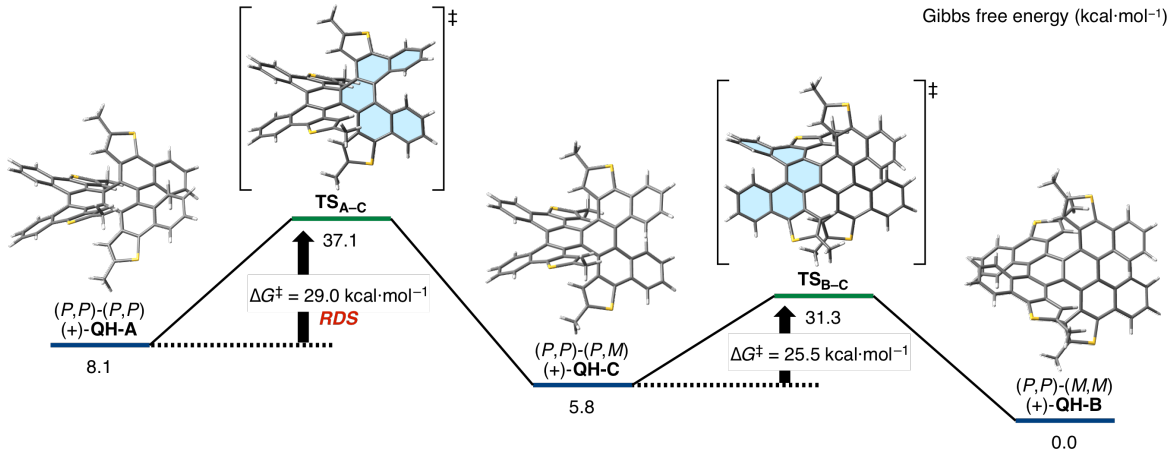

Figure 16. Structures of intermediates and transition states during the most plausible diastereomerization from (*P*,*P*)-(*P*,*P*)-**QH** ((+)-**QH-A**) to (*P*,*P*)-(*M*,*M*)-**QH** ((+)-**QH-B**). Helical substructures that invert in transition states are highlighted in blue.

The kinetics of the isomerization from **QH-A** to **QH-B** were studied experimentally by monitoring the decreasing integration of **QH-A** in the ^{1}H NMR spectra in 1,1,2,2-tetrachloroethane-d_2. As simulated theoretically, the ignorable emergence of the integration of tentatively assigned **QH-C** supported the predicted location of the RDS (Figure 17). Because of the substantial disparity in thermodynamic stabilities, the reverse conversion could be neglected. The first-order rate constants k_c (s^{-1}) of the forward conversion at various temperatures were estimated using the following equation:

$$\ln([\textbf{QH-A}]_t/[\textbf{QH-A}]_0) = -k_c t \qquad (1)$$

where $[\textbf{QH-A}]_0$ is the initial ratio of the integration of **QH-A** to the sum of the integration of **QH-A** and **QH-B**, and $[\textbf{QH-A}]_t$ is the ratio of the integration of **QH-A** at a certain time t during the conversion (Figure 18a). Using these data, an Eyring plot was constructed using the following equation:

$$\ln(k/T) = -\Delta H^{\ddagger}/RT + [\ln(k_B/h) + \Delta S^{\ddagger}/R] \qquad (2)$$

where R is the gas constant, T is the measured temperature, $\Delta H^{\ddagger}$ is the activation enthalpy, k_B is the Boltzmann constant, h is the Planck constant, and $\Delta S^{\ddagger}$ is the activation entropy. This plot provided the activation parameters: $\Delta H^{\ddagger}$ = 28.6 kcal·mol^{-1}, $\Delta S^{\ddagger}$ = 2.6 cal·mol^{-1}·K^{-1}, and $\Delta G^{\ddagger}$ = 27.8 kcal·mol^{-1} at 298 K (Figure 18c). A higher barrier to this conversion than that of the inversion of [5]helicene ($\Delta G^{\ddagger}$ = 24.1 kcal·mol^{-1})[15] may reflect the presence of additional repulsion from the neighboring dithia[6]helicene substructure at the transition state.

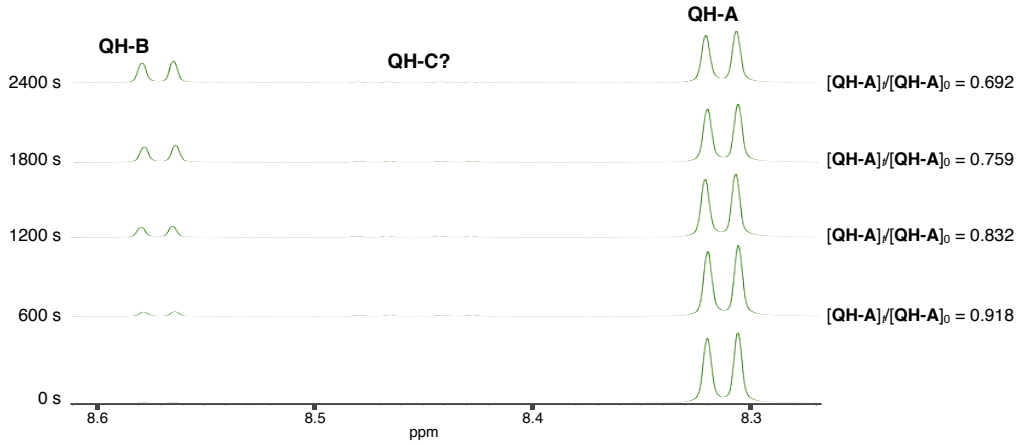

Figure 17. Conversion progress from **QH-A** to **QH-B** at 88.4 °C monitored by ^{1}H NMR.

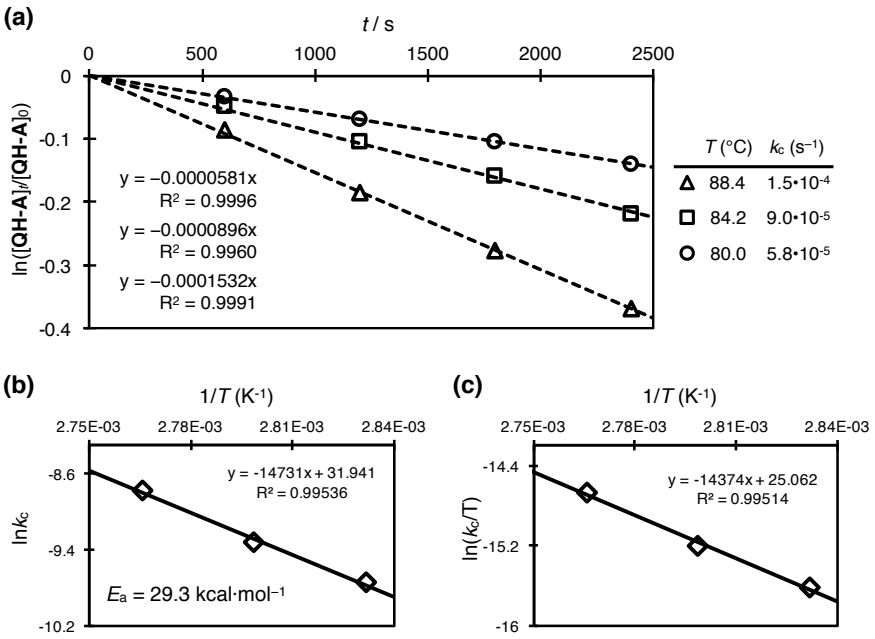

Figure 18. (a) Plots of the decreasing integration of **QH-A** in the ^{1}H NMR spectra in 1,1,2,2-tetrachloroethane-d_2 upon heating at 80.0, 84.2, and 88.4 °C. (b) Arrhenius plot and (c) Eyring plot of the thermal conversion from **QH-A** to **QH-B**.

The interconversion pathway of **QHs** (Figure 15) indicates that any one of the barriers obtained with the inversion of dithia[6]helicene substructures can be estimated by monitoring the racemization progress of the enantiopure **QH-B**, necessarily including the inversions of both the helicene substructures. The most plausible racemization process is the path: *ent*-**QH-B** → *ent*-**QH-C** → **QH-E** (*meso*) → *rac*-**QH-C** → *rac*-**QH-B**, where the RDS is the step from

ent-**QH-B** to $\mathbf{TS_{C–E}}$ ($\Delta G^{‡}$ = 35.5 kcal·mol^{-1}) (Figure 19).[14] This process differs from the usual racemization of single helicenes[15] because **QH-B** loses its initial chiral information upon conversion to the achiral intermediate **QH-E**, whereas the initial chirality information is maintained as the opposite helicity in the case of single helicenes. This indicates that the rate constant of racemization (k_r) is equal to that of the isomerization (k_i) from **QH-B** to **QH-E**.

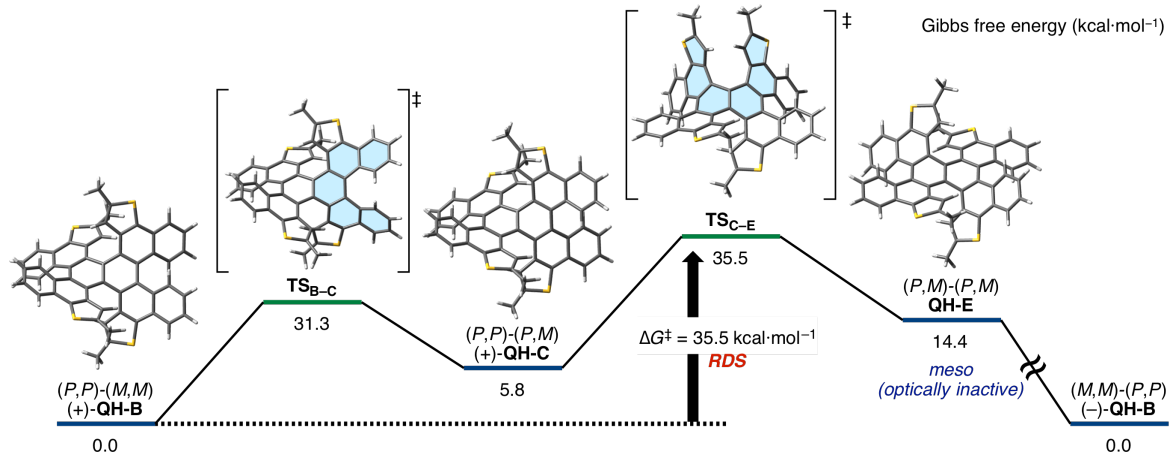

Figure 19. Structures of intermediates and transition states during the most plausible enantiomerization from (*P*,*P*)-(*M*,*M*)-**QH** ((+)-**QH-B**) to (*M*,*M*)-(*P*,*P*)-**QH** ((−)-**QH-B**) (the energy diagram of the process from **QH-E** to (−)-**QH-B** is equal to that of the process from **QH-E** to (+)-**QH-B**; therefore, it was omitted here). Helical substructures that invert in transition states are highlighted in blue.

Because **QH-B** was the most thermodynamically stable isomer and the ratio of other metastable isomers were vanishingly small during the thermal interconversion, kinetics of the racemization of enantioenriched **QH-B** were studied experimentally by monitoring the decreasing ellipticity in the CD spectra in 1,2,4-trichlorobenzene (Figure 20). The first-order rate constants k_r (s^{-1}) at various temperatures were estimated using the following equation:

$$\ln([CD]_t/[CD]_0) = -k_r t \qquad (3)$$

where $[CD]_0$ is the initial ellipticity of enantioenriched **QH-B**, and $[CD]_t$ is the ellipticity at a certain time t during the racemization (Figure 21a). Using these data, the Eyring plot was constructed using equation (2). This plot provided the activation parameters: $\Delta H^{‡}$ = 37.8 kcal·mol^{-1}, $\Delta S^{‡}$ = 2.6 cal·mol^{-1}·K^{-1}, and $\Delta G^{‡}$ = 37.1 kcal·mol^{-1} at 298 K (Figure 21c). The barrier to this racemization was comparable to that of [6]helicene ($\Delta G^{‡}_{300\ K}$ = 36.2 kcal·mol^{-1}).[16] Unlike the case of the conversion from **QH-A** to **QH-B**, none of the additional

repulsion from the neighboring [5]helicene substructures exists at the transition state, and therefore a slightly lower barrier compared to the calculated barrier of the corresponding single dithia[6]helicene ($\Delta G^{\ddagger}$ = 39.3 kcal·mol^{-1}) was obtained.

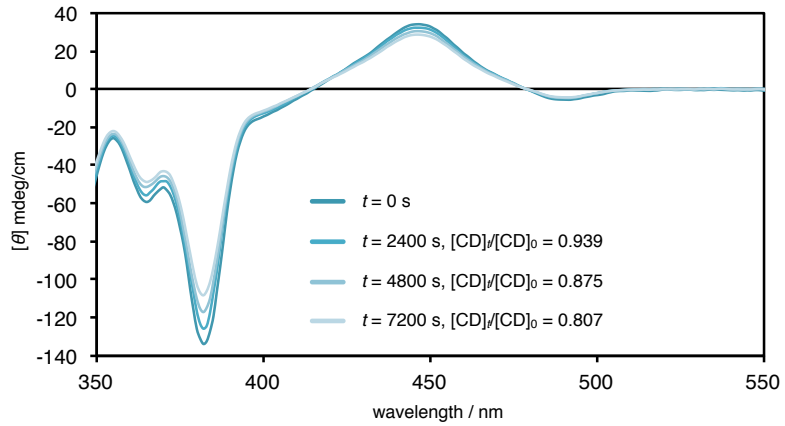

Figure 20. Racemization progress of (−)-**QH-B** ((*M*,*M*)-(*P*,*P*)-**QH**) in 1,2,4-trichlorobenzene at 183.8 °C monitored by CD spectra.

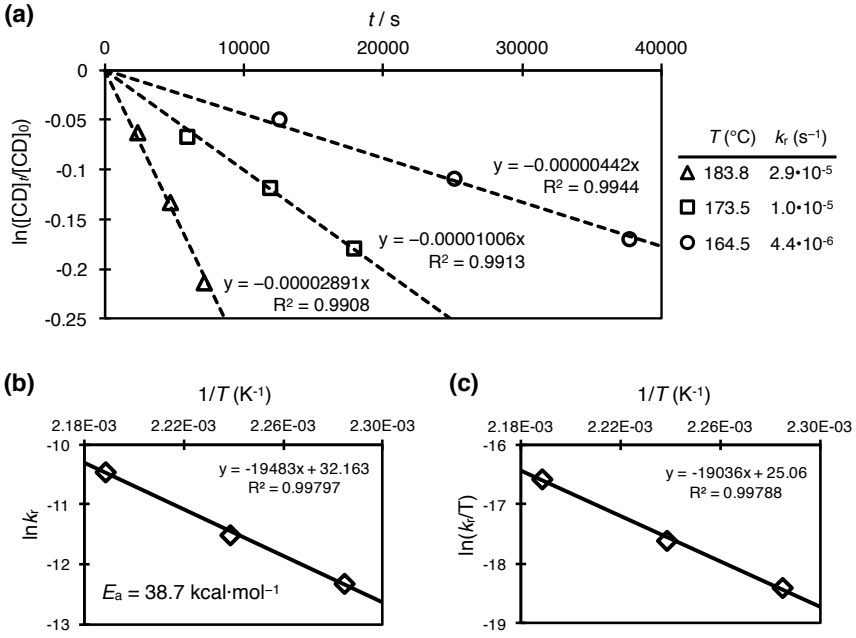

Figure 21. (a) Plots of the decreasing ellipticity at 382 nm in the CD spectra of enantio-enriched (−)-**QH-B** in 1,2,4-trichlorobenzene upon heating at 164.5, 173.5, and 183.8 °C. (b) Arrhenius plot and (c) Eyring plot of the thermal racemization of (−)-**QH-B**.

Conclusion

In this chapter, the synthesis and structural features of quadruple helicenes were described. The presence of fourfold helicity resulted in nine stereoisomers including four pairs of enantiomers and one *meso*-isomer. Interestingly, the significant distortion of *saddle*-shaped isomer (**QH-B**), derived from the proper accumulation of repulsions on helical substructures, had the highest degree of twisting deformation per benzene unit (35.3° at the most). The photophysical and electrochemical studies showed the clear difference of electronic properties between **QH-A** (*propeller*-shaped isomer) and **QH-B**, providing information for the better understanding of the dependence of electronic structure on the molecular geometry. The experimental and theoretical kinetic studies also unraveled the complicated interconversion pathway among the stereoisomers. The higher multihelicity the molecule has, the larger number of isolable configurations are generated. Quadruple helicenes described in this chapter are the highest multiplex helicene providing such configurational complexity among multihelicenes reported so far.

Experimental Section

General

Unless otherwise noted, all materials including dry solvents were obtained from commercial suppliers and used without further purification. Compound **1** was prepared according to the procedures described in Chapter 3. Unless otherwise noted, all reactions were performed with dry solvents under an atmosphere of nitrogen in dried glassware with standard vacuum-line techniques. All work-up and purification procedures were carried out with reagent-grade solvents in air.

Analytical thin-layer chromatography (TLC) was performed using E. Merck silica gel 60 F_{254} precoated plates (0.25 mm). The developed chromatogram was analyzed by UV lamp (254 nm and 365 nm). High-resolution mass spectra (HRMS) were obtained from a JEOL JMS-S3000 SpiralTOF (MALDI-TOF MS). Melting points were measured on a MPA100 Optimelt automated melting point system. Chiral HPLC analysis was conducted on a Shimadzu Prominence 2000 instrument equipped with COSMOSIL Cholester column (10 mm x 250 mm). Cyclic voltammetry (CV) measurements were performed by BAS ALS-600D Electrochemical Analyzer. NMR spectra were recorded on a JEOL JNM-ECA-600 (^{1}H 600 MHz, ^{13}C 150 MHz) spectrometer or a JEOL ECA 600II spectrometer with Ultra COOL^{TM} probe (^{1}H 600 MHz, ^{13}C 150 MHz). Chemical shifts for ^{1}H NMR are expressed in parts per million (ppm) relative to $CHCl_3$ (δ 7.26 ppm) or C_2DHCl_4 (δ 6.00 ppm). Chemical shifts for ^{13}C NMR are expressed in ppm relative to $CDCl_3$ (δ 77.16 ppm). Data are reported as follows: chemical shift, multiplicity (s = singlet, d = doublet, t = triplet, m = multiplet, br = broad signal), coupling constant (Hz), and integration.

Synthesis of QH-A

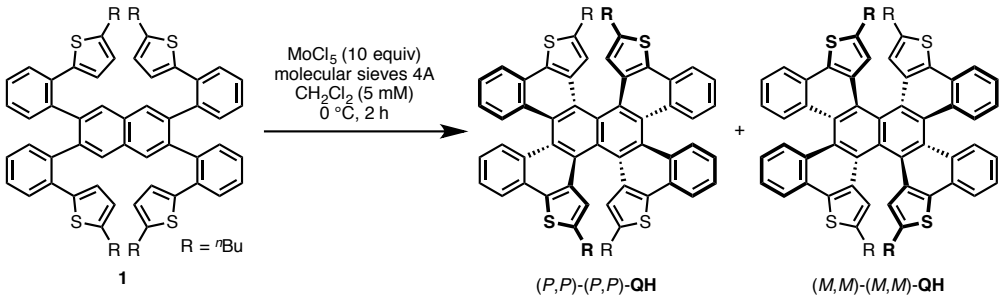

Molecular sieves 4 Å (1.00 g) placed in the 100 mL Schlenk flask was dried *in vacuo* with heating by heat gun. After cooling, nitrogen was backfilled to the flask, and **1** (246 mg, 0.250 mmol, 1 equiv) and dry CH_2Cl_2 (50 mL) was added. Fresh $MoCl_5$ (683 mg, 2.50 mmol, 10 equiv) was added to the flask under gentle nitrogen flow at 0 °C and the reaction mixture was

stirred for 2 h. The reaction was quenched by the addition of MeOH/$CHCl_3$ (1:1, 40 mL) solution and the resultant solution was directly passed through a pad of silica-gel with $CHCl_3$ eluent. The filtrate was washed with $NaHCO_3$ aqueous solution, dried over Na_2SO_4, and then evaporated *in vacuo*. The crude material was purified by silica-gel column chromatography (eluent: hexane/CH_2Cl_2 = 100:0 to 90:10) to afford **QH-A** (140 mg, 57%) as an orange solid.
^{1}H NMR (600 MHz, $CDCl_3$) δ 8.32 (d, J = 8.3 Hz, 4H), 8.10 (dd, J = 8.0, 0.9 Hz, 4H), 7.57 (ddd, J = 8.0, 6.9, 0.9 Hz, 4H), 7.21 (ddd, J = 8.3, 6.9, 1.3 Hz, 4H), 6.13 (s, 4H), 2.51 (dt, ^2J = 15.1, ^3J = 7.4 Hz, 4H), 2.44 (dt, ^3J = 15.2, ^3J = 7.4 Hz, 4H), 1.38–1.27 (m, 8H), 1.14 (sextet, J = 7.4 Hz, 8H), 0.83 (t, J = 7.4 Hz, 12H); ^{13}C NMR (150 MHz, $CDCl_3$) δ 143.5 (4º), 137.3 (4º), 133.5 (4º), 131.7 (CH), 129.2 (4º), 128.1 (4º), 126.9 (CH), 126.6 (4º), 125.9 (4º), 125.7 (4º), 124.6 (CH), 123.5 (CH), 123.4 (CH), 33.6 (CH_2), 29.9 (CH_2), 22.0 (CH_2), 14.1 (CH_3); HRMS (MALDI-TOF MS) *m/z* calcd for $C_{66}H_{56}S_4$ $[M]^+$: 976.3265, found: 976.3264; mp: >300 ºC.

Synthesis of QH-B

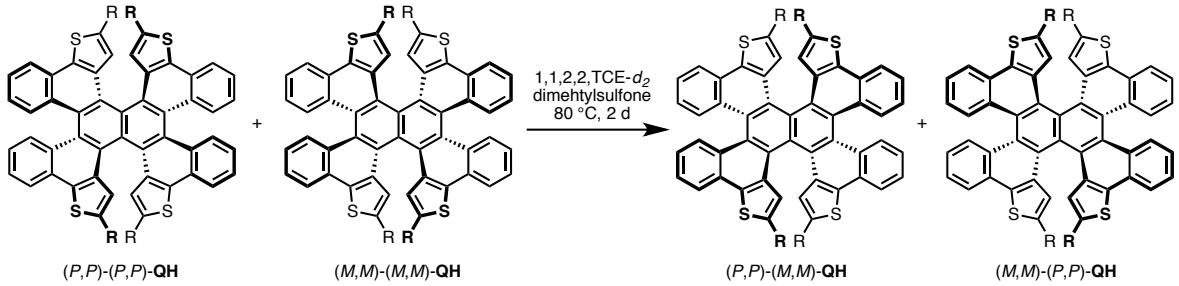

A solution of **QH-A** (*ca*. 3.2 mg, 0.0033 mmol) in 1,1,2,2-tetrachloroehtane-d_2 (0.4 mL) and dimethylsulfone (*ca*. 0.28 mg) in NMR tube was warmed to 80 °C for 2 days and then analyzed by ^{1}H NMR at room temperature. Using dimethylsulfone as an internal standard, NMR yield of **QH-B** was determined to be 100%.
^{1}H NMR (600 MHz, $CDCl_3$) δ 8.55 (d, J = 8.6 Hz, 4H), 8.13 (dd, J = 8.0, 0.8 Hz, 4H), 7.52 (ddd, J = 8.1, 6.9, 1.1 Hz, 4H), 7.29 (ddd, J = 8.6, 6.8, 1.3 Hz, 4H), 7.28 (s, 4H), 2.67 (t, J = 7.4 Hz, 8H), 1.52–1.47 (m, 8H), 1.29–1.18 (m, 8H), 0.84 (t, J = 7.3 Hz, 12H); ^{13}C NMR (150 MHz, $CDCl_3$) δ 144.8 (4º), 137.5 (4º), 133.7 (4º), 132.7 (4º), 131.5 (CH), 129.1 (4º), 128.6 (4º), 126.7 (CH), 125.7 (4º), 124.9 (CH), 124.8 (4º), 124.2 (CH), 124.1 (CH), 33.7 (CH_2), 30.4 (CH_2), 22.0 (CH_2), 14.0 (CH_3); HRMS (MALDI-TOF MS) *m/z* calcd for $C_{66}H_{56}S_4$ $[M]^+$: 976.3265, found: 976.3266; mp: >300 ºC.

Enantiomer Separation by HPLC

HPLC analysis was conducted on a Shimadzu Prominence 2000 instrument equipped with COSMOSIL Cholester column (10 mm x 250 mm). Eluted products were analyzed at 400 nm. Flow rate was 3.0 mL/min and temperature was 30 ˚C. Eluted by chloroform/2-propanol (3:7).

Optical purity of (+)-**QH-B** obtained from the thermal conversion of (+)-**QH-A**

The optical purity of (+)-**QH-B** most plausibly drops when **QH-C** is converted into **QH-E**. From the DFT calculations, the $\Delta G^{\ddagger}$ values from **QH-C** to $\mathbf{TS_{B-C}}$ and $\mathbf{TS_{C-E}}$ were 25.5 kcal·mol^{-1} and 29.7 kcal·mol^{-1}, respectively (Figure 15). This difference in the activation free energies by 4.2 kcal·mol^{-1} would result in a 1200-fold larger rate constant of the former process than latter process at 298 K (estimated using the equation $k = (k_B T/h)\exp(-\Delta G^{\ddagger}/RT)$).

X-ray Crystallography and Structural Analysis

Recrystallization of racemic mixture of **QH-A** by evaporating *n*-pentane solution yielded yellow crystals suitable for X-ray crystal structure analysis, and recrystallization of racemic mixture of **QH-B** from chloroform/2-propanol in vapor diffusion method yielded yellow crystals suitable for X-ray crystal structure analysis. Details of the crystal data and a summary of the intensity data collection parameters are listed in Table 1. A suitable crystal was mounted with mineral oil on a glass fiber and transferred to the goniometer of a Rigaku PILATUS diffractometer. Graphite-monochromated Mo Kα radiation (λ = 0.71075 Å) was used. The structures were solved by direct methods with (SIR-97)[17] and refined by full-matrix least-squares techniques against F^2 (SHELXL-97).[18] The intensities were corrected for Lorentz and polarization effects. The non-hydrogen atoms were refined anisotropically. Hydrogen atoms were placed using AFIX instructions.

Table 1. Crystallographic data and structure refinement details for **QH-A** and **QH-B**.

	QH-A	**QH-B**
formula	$C_{132}H_{112}S_8$	$C_{66}H_{56}S_4$
fw	1954.70	977.35
T (K)	123(2)	123(2)
λ (Å)	0.71075	0.71075
cryst syst	Triclinic	Monoclinic
space group	P-1	$P2_1/n$
a (Å)	16.2172(4)	17.2313(19)
b (Å)	17.2657(8)	12.0935(11)
c (Å)	21.5757(10)	25.119(3)
α	85.709(4)°	90°
β	68.480(3)°	106.951(2)°
γ	64.959(3)°	90°
V (Å^3)	5068.6(4)	5007.1(9)
Z	2	4
D_{calc} (g / cm^3)	1.281	1.297
μ (mm^{-1})	0.231	0.233
F(000)	2064	2064
cryst size (mm)	0.15 × 0.15 × 0.10	0.20 × 0.05 × 0.05
θ range	3.02–25.00°	3.05–25.00°
reflns collected	144604	67832
indep reflns/R_{int}	17822/0.0285	8788/0.0438
params	1314	680
GOF on F^2	1.036	1.058
R_1, wR_2 [I>2σ(I)]	0.0358, 0.0903	0.0472, 0.1124
R_1, wR_2 (all data)	0.0414, 0.0954	0.0676, 0.1275

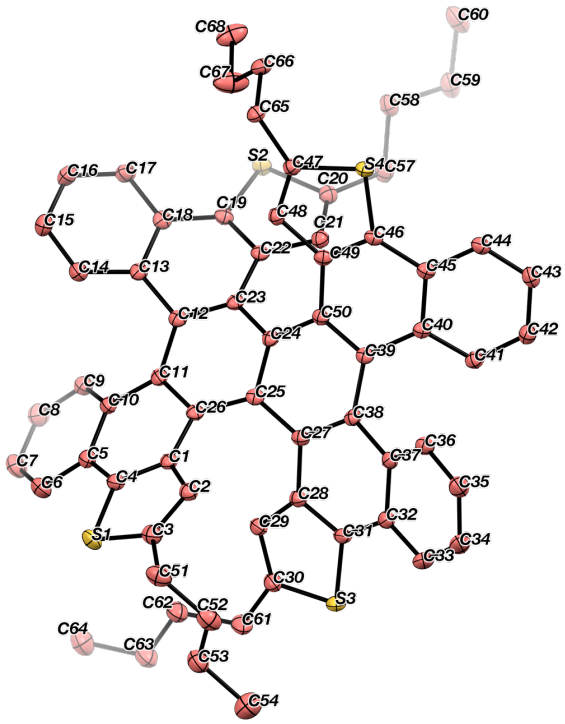

Splay angles of dithia[6]helicene substructures

C1–C26–C27–C28 = 49.71(14)°
C22–C23–C50–C49 = 53.18(14)°

Splay angles of [5]helicene substructures

C10–C11–C12–C13 = 27.2(3)°
C37–C38–C39–C40 = 20.2(3)°

Twist angles of each blades against naphthalene core

C1–C26–C11–C10 = 28.9(2)°
C13–C12–C23–C22 = 29.5(2)°
C28–C27–C38–C37 = 27.0(2)°
C40–C39–C50–C49 = 28.9(2)°

Splay angles of dithia[6]helicene substructures

C71–C70–C119–C118 = 45.33(14)°
C92–C93–C96–C97 = 46.62(14)°

Splay angles of [5]helicene substructures

C80–C81–C82–C83 = 29.7(3)°
C106–C107–C108–C109 = 29.3(3)°

Twist angles of each blades against naphthalene core

C71–C70–C81–C80 = 28.3(2)°
C83–C82–C93–C92 = 32.4(2)°
C97–C96–C107–C106 = 28.9(2)°
C109–C108–C119–C118 = 32.0(2)°

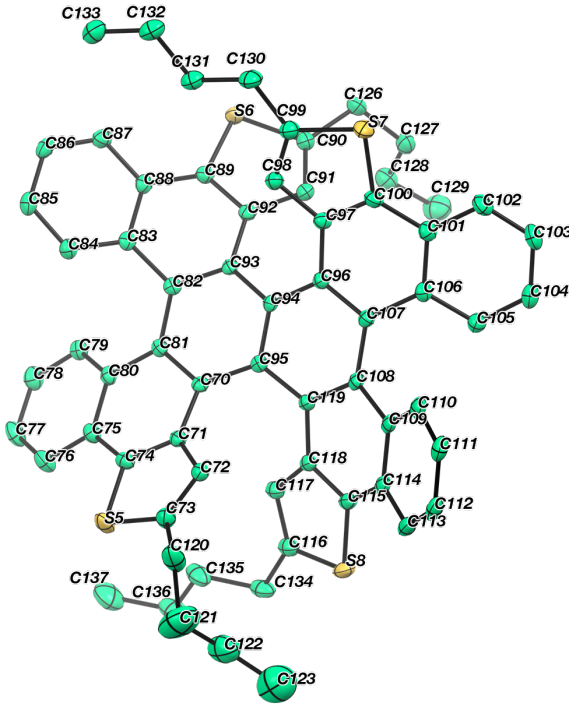

Figure 22. ORTEP drawing of **QH-A-1** ((*P*,*P*)-(*P*,*P*), top) and **QH-A-2** ((*P*,*P*)-(*P*,*P*), bottom) with 50% probability. All hydrogen atoms and the minor part of the disordered moieties are omitted for clarity. Selected dihedral angles are also listed.

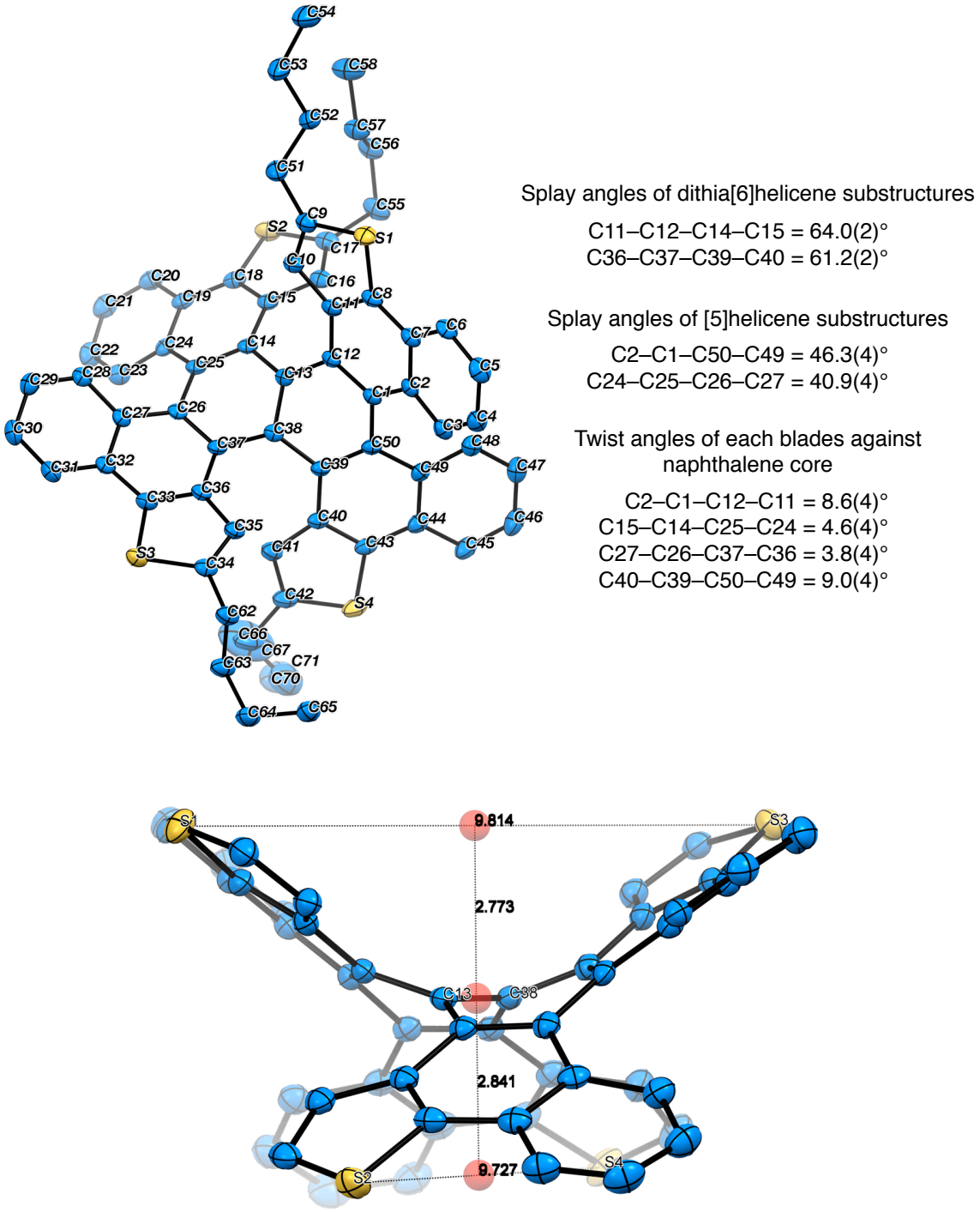

Figure 23. ORTEP drawing of **QH-B** with 50% probability. All hydrogen atoms and the minor part of the disordered moieties are omitted for clarity. Selected dihedral angles are also listed. Depth of double concave structures was estimated by using the distance from the centroids of sulfur atoms at the diagonal positions to the centroid of the bond C13–C38 in the naphthalene core (centroids are colored in red).

Table 2. Comparison of dihedral angles of the X-ray structures and the optimized structures of **QH-A** and **QH-B**.

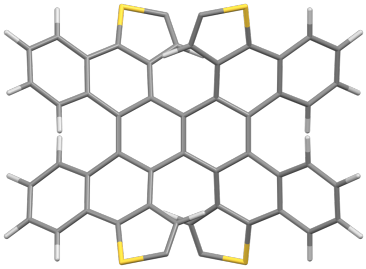

QH-A

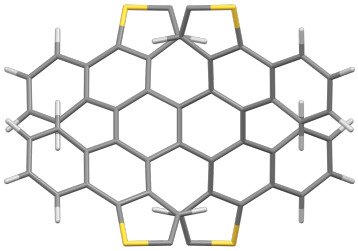

QH-B

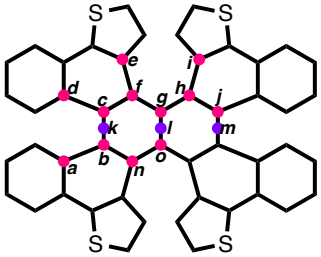

	QH-A			**QH-B**	
	X-ray (**QH-A-1**)	X-ray (**QH-A-2**)	optimized[a]	X-ray	optimized[a]
twist angles					
C(c)–C(k)–C(m)–C(j)	13.9°	6.5°	8.9°	69.5°	70.2°
C(c)–C(k)–C(l)–C(g)	8.1°/5.8°	3.7°/2.8°	4.4°	35.3°/34.2°	35.1°
splay angles					
C(a)–C(b)–C(c)–C(d)	27.2°/20.2°	29.7°/29.3°	26.1°	46.3°/40.9°	42.3°
C(e)–C(f)–C(h)–C(i)	49.7°/53.2°	45.3°/46.6°	49.5°	64.0°/61.2°	61.9°
dihedral angles of naphthalene core					
C(f)–C(c)–C(b)–C(n)	11.3°/8.4°	14.8°/13.4°	13.8°	35.6°/32.5°	33.6°
C(f)–C(g)–C(l)–C(o)	23.9°/26.0°	20.6°/21.3°	23.3°	42.7°/42.5°	43.6°

[a] B3LYP/6-31G(d)

Photophysical Study

UV–Vis absorption spectra were recorded on a Shimadzu UV-3510 spectrometer with a resolution of 0.5 nm. Emission spectra were measured with an FP-6600 Hitachi spectrometer with a resolution of 0.2 nm upon excitation at 381 nm for **QH-A** and 405 nm for **QH-B**. CD spectra were measured with a JASCO FT/IR6100. Dilute solutions in degassed spectral grade dichloromethane in a 1 cm square quartz cell were used for measurements. Absolute fluorescence quantum yields were determined with a Hamamatsu C9920-02 calibrated integrating sphere system upon excitation at 400 nm for **QH-A** or at 420 nm for **QH-B**.

Computational Study

The Gaussian 09 program[19] running on a SGI Altix4700 system was used for optimization (B3LYP/6-31G(d)).[20] All structures were optimized without any symmetry assumptions. Zero-point energy, enthalpy, and Gibbs free energy at 298.15 K and 1 atm were estimated from the gas-phase studies unless otherwise noted. Harmonic vibration frequency calculations at the same level were performed to verify all stationary points as local minima (with no imaginary frequency) or transition states (with one imaginary frequency). All NMR study was performed at B3LYP/6-311+G(2d,p) level. Tetramethylsilane ($SiMe_4$) was used as reference (δ 0.00 ppm) for the estimation of ^{1}H NMR chemical shifts. Visualization of the results was performed by use of GaussView 5.0 software.

Table 3. Uncorrected and thermal-corrected (298 K) energies of stationary points (Hartree).[a]

structure	*E*	*E* + *ZPE*	*H*	*G*
QH-A	-3669.85187963	-3669.165165	-3669.118799	-3669.241538
QH-B	-3669.86422209	-3669.177467	-3669.131027	-3669.254435
QH-C	-3669.85486381	-3669.168189	-3669.121772	-3669.245131
QH-D	-3669.84831139	-3669.161862	-3669.115471	-3669.238444
QH-E	-3669.84143375	-3669.154818	-3669.108493	-3669.231471
$TS_{A–C}$	-3669.80498465	-3669.119266	-3669.073412	-3669.195353
$TS_{A–D}$	-3669.77916720	-3669.093652	-3669.047956	-3669.169088
$TS_{B–C}$	-3669.81404938	-3669.128210	-3669.082306	-3669.204508
$TS_{B–D}$	-3669.79518508	-3669.109794	-3669.063862	-3669.186529
$TS_{C–E}$	-3669.80849210	-3669.122642	-3669.076938	-3669.197818
$TS_{D–E}$	-3669.82961756	-3669.143677	-3669.097875	-3669.219463
dithia[6]helicene	-1720.60918362	-1720.285264	-1720.263932	-1720.333347
$TS_{dithia[6]helicene}$	-1720.54702510	-1720.223952	-1720.203311	-1720.270761

a) *E*: electronic energy; *ZPE*: zero-point energy; *H* (= $E + ZPE + E_{vib} + E_{rot} + E_{trans} + RT$): sum of electronic and thermal enthalpies; *G* (= $H - TS$): sum of electronic and thermal free energies.

Table 4. TD DFT vertical one-electron excitations (6 states) calculated for optimized structure of **QH-A**.

excited state	energy	wavelength	oscillator strength (*f*)	description	
1	2.5340 eV	489.29 nm	0.0058	HOMO-1 -> LUMO	0.44527
				HOMO -> LUMO+1	0.54151
2	2.6066 eV	475.65 nm	0.0877	HOMO-1 -> LUMO+1	-0.22863
				HOMO -> LUMO	0.66579
3	2.9654 eV	418.11 nm	0.0090	HOMO-2 -> LUMO	0.69577
4	3.0091 eV	412.02 nm	0.6413	HOMO-1 -> LUMO	0.53704
				HOMO -> LUMO+1	-0.43847
5	3.0382 eV	408.08 nm	0.0000	HOMO-3 -> LUMO	-0.12231
				HOMO-2 -> LUMO+1	0.66331
				HOMO-1 -> LUMO+2	-0.16013
6	3.0692 eV	403.96 nm	0.4126	HOMO-1 -> LUMO+1	0.65638
				HOMO -> LUMO+1	0.22301

Table 5. TD DFT vertical one-electron excitations (6 states) calculated for optimized structure of **QH-B**.

excited state	energy	wavelength	oscillator strength (*f*)	description	
1	2.6681 eV	464.69 nm	0.0139	HOMO-1 -> LUMO	0.61548
				HOMO -> LUMO+1	-0.33392
2	2.7294 eV	454.26 nm	0.0851	HOMO-1 -> LUMO+1	0.16329
				HOMO -> LUMO	0.68437
3	2.9751 eV	416.74 nm	0.0000	HOMO-2 -> LUMO	0.68220
				HOMO -> LUMO+2	0.15646
4	3.1999 eV	387.46 nm	0.4581	HOMO-5 -> LUMO	-0.14806
				HOMO-1 -> LUMO	0.32792
				HOMO -> LUMO+1	0.59218
5	3.2164 eV	385.47 nm	0.1935	HOMO-1 -> LUMO+1	0.67076
				HOMO -> LUMO	-0.15814
				HOMO -> LUMO+4	0.11857
6	3.2763	378.43 nm	0.0014	HOMO-3 -> LUMO	0.67702
				HOMO -> LUMO+3	-0.15430

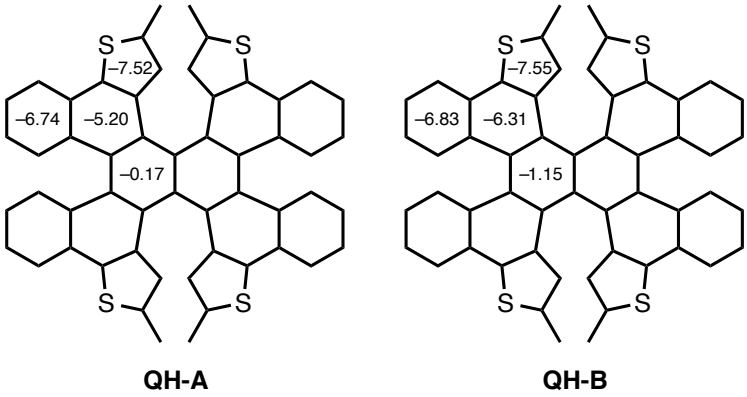

Figure 24. NICS(0) of each ring in **QH-A** and **QH-B**.

Kinetic Study

Thermal conversion from **QH-A** to **QH-B**

Kinetics of the conversion from **QH-A** to **QH-B** was studied by monitoring the decreasing integration of **QH-A** in the ^{1}H NMR spectra in 1,1,2,2-tetrachloroethane-d_2 at 80.0, 84.2, and 88.4 °C. All reaction was conducted in NMR tube upon the heating by oil bath under nitrogen. Reactions were stopped at each time for the ^{1}H NMR measurement by cooling the NMR tube in ice bath.

Thermal racemization of **QH-B**

Kinetics of the racemization of **QH-B** was studied by monitoring the decreasing ellipticity ([θ]) of (−)-**QH-B** ((*M*,*M*)-(*P*,*P*)-**QH**) in the CD spectra in 1,2,4-trichlorobenzene at 164.5, 173.5, and 183.8 °C. All reactions were conducted in test tube upon the heating by oil bath under nitrogen. Reactions were stopped at each time for the CD measurement by cooling the test tube in ice bath.

Additional Theoretical Kinetic Study

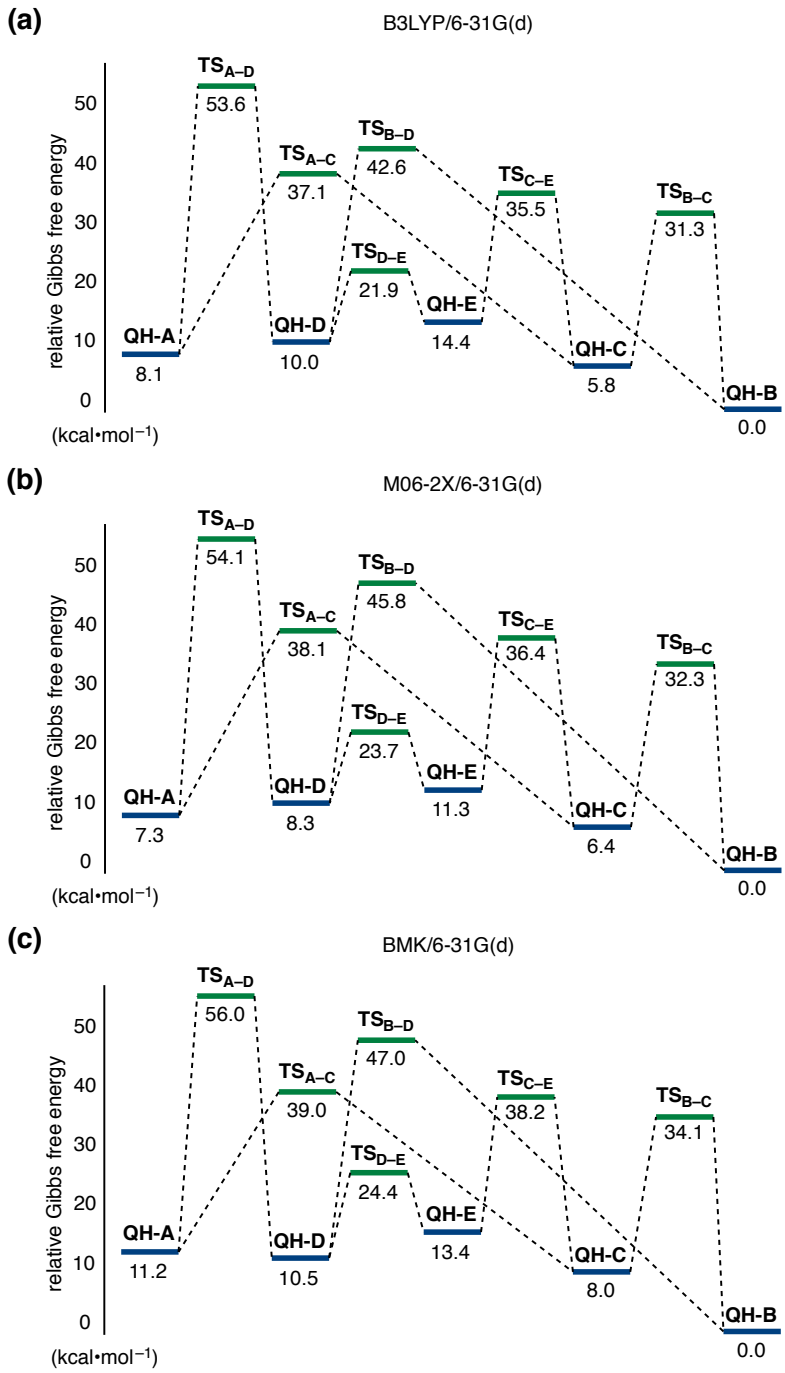

Figure 25. Theoretical study on the interconversion pathway of **QHs** at the (a) B3LYP/6-31G(d), (b) M06-2X/6-31G(d), and (c) BMK/6-31G(d) levels.

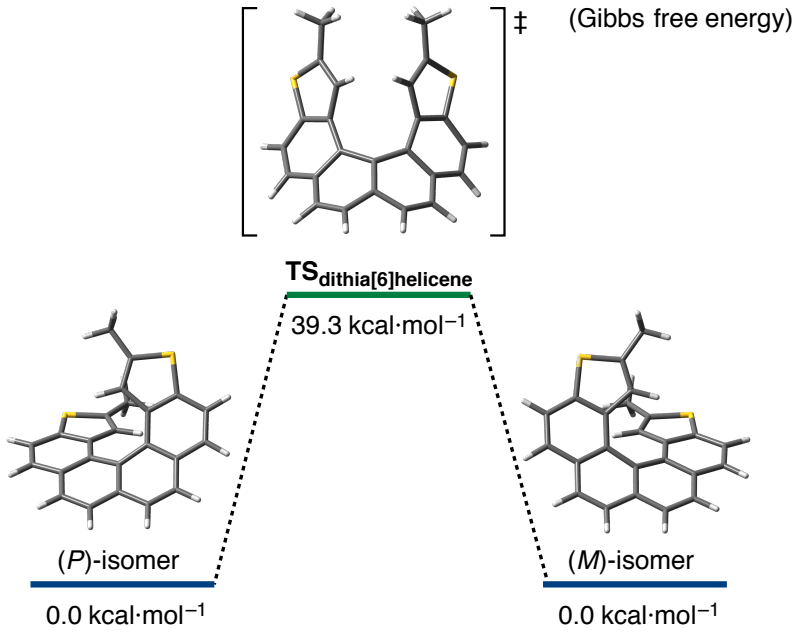

Figure 26. Racemization process of dithia[6]helicene.

Reference

1. Reviews on nonplanar π-systems: (a) Rieger, R.; Müllen, K. *J. Phys. Org. Chem.* **2010**, *23*, 315. (b) Dodziuk, H. *Strained Hydrocarbons: Beyond the van't Hoff and Le Bel Hypothesis*; Wiley-VCH: Weinheim, 2009. (c) Harvey, R. G. *Polycyclic Aromatic Hydrocarbons*; Wiley-VCH: New York, 1997. (d) Pascal, R. A., Jr. *Chem. Rev.* **2006**, *106*, 4809. (e) Tsefrikas, V. M.; Scott, L. T. *Chem. Rev.* **2006***, 106,* 4868. (f) Wu, Y.-T.; Siegel, J. S. *Chem. Rev.* **2006**, *106*, 4843.
2. Twisted π-systems: (a) Wang, K. K. *Top. Curr. Chem.* **2014**, *349*, 31. (b) ref 1d. (c) Lu, J.; Ho, D. M.; Vogelaar, N. J.; Kraml, C. M.; Pascal, R. A., Jr. *J. Am. Chem. Soc.* **2004**, *126*, 11168. (d) Schuster, I. I.; Craciun, L.; Ho, D. M.; Pascal, R. A., Jr. *Tetrahedron* **2002**, *58*, 8875. (e) Qiao, X.; Ho, D. M.; Pascal, R. A., Jr. *Angew. Chem., Int. Ed.* **1997**, *36*, 1531. (f) Qiao, X.; Padula, M. A.; Ho, D. M.; Vogelaar, N. J.; Schutt, C. E.; Pascal, R. A., Jr. *J. Am. Chem. Soc.* **1996**, *118*, 741. (g) Smyth, N.; Engen, D. V.; Pascal, R. A., Jr. *J. Org. Chem.* **1990**, *55*, 1937. (h) Pascal, R. A., Jr.; McMillan, W. D.; Engen, D. V.; Eason, R. G. *J. Am. Chem. Soc.* **1987**, *109*, 4660.
3. Ito, S.; Hiroto, S.; Lee, S.; Son, M.; Hisaki, I.; Yoshida, T.; Kim, D.; Kobayashi, N.; Shinokubo, H. *J. Am. Chem. Soc.* **2015**, *137*, 142.
4. Kashihara, H.; Asada, T.; Kamikawa, K. *Chem. Eur. J.* **2015**, *21*, 6523.
5. Thiahelicenes: (a) Waghray, D.; de Vet, C.; Karypidou, K.; Dehaen, W. *J. Org. Chem.* **2013**, *78*, 11147. (b) Pieters, G.; Gaucher, A.; Marque, S.; Maurel, F.; Lesot, P.; Prim, D. *J. Org. Chem.* **2010**, *75*, 2096. (c) Dopper, J. H.; Oudman, D.; Wynberg, H. *J. Am. Chem. Soc.* **1973**, *95*, 3692.
6. Review of Scholl reaction: Grzybowski, M.; Skonieczny, K.; Butenschön, H.; Gryko, D. T. *Angew. Chem., Int. Ed.* **2013**, *52*, 9900.
7. Kramer, B.; Fröhlich, R.; Waldvogel, S. R. *Eur. J. Org. Chem.* **2003**, 3549.
8. Nakai, Y.; Mori, T.; Inoue, Y. *J. Phys. Chem. A* **2012**, *116*, 7372.
9. Twist angles per benzene unit of twisted acenes are 19–25° for decaphenylanthracene, 22–29° for octaphenyldibenzotetracene, and 27–30° for hexaphenyltetrabenzopentacene (ref 5c,e,f).
10. Kuroda, R. *J. Chem. Soc., Perkin Trans. II* **1982**, 789.
11. (a) Krygowski, T. M.; Cyrański, M. K. *Chem. Rev.* **2001**, *101*, 1385. (b) Krygowski, T. M. *J. Chem. Inf. Model.* **1993**, *33*, 70. (c) Kruszewski, J.; Krygowski, T. M. *Tetrahedron Lett.* **1972**, *13*, 3839.
12. Fujikawa, T.; Segawa, Y.; Itami, K. *J. Am. Chem. Soc.* **2015**, *137*, 7763. See the chapter 2.
13. (a) Liu, X.; Yu, P.; Xu, L.; Yang, J.; Shi, J.; Wang, Z.; Cheng, Y.; Wang, H. *J. Org. Chem.* **2013**, *78*, 6316. (b) Luo, J.; Xu, X.; Mao, R.; Miao, Q. *J. Am. Chem. Soc.* **2012**, *134*, 13796. (c) Eversloh, C. L.; Liu, Z.; Müller, B.; Stangl, M.; Li, C.; Müllen, K. *Org. Lett.* **2011**, *13*, 5528. (d) Peña, D.; Cobas, A.; Pérez, D.; Guitián, E.; Castedo, L. *Org. Lett.* **2000**, *2*, 1629.

14. (a) Grimme, S.; Peyerimhoff, S. D. *Chem. Phys.* **1996**, *204*, 411. (b) Janke, R. H.; Haufe, G.; Würthwein, E.-U.; Borkent, J. H. *J. Am. Chem. Soc.* **1996**, *118*, 6031.
15. Goedicke, C.; Stegemeyer, H. *Tetrahedron. Lett.* **1970**, 937.
16. Martin, R. H.; Marchant, M. J. *Tetrahedron* **1974**, *30*, 347.
17. Altomare, A.; Burla, M. C.; Camalli, M.; Cascarano, G. L.; Giacovazzo, C.; Guagliardi, A.; Moliterni, A. G. G.; Polidori, G.; Spagna, R. *J. Appl. Crystallogr.* **1999**, *32*, 115.
18. Sheldrick, G. M. University of Göttingen: Göttingen, Germany, 1997.
19. Frisch, M. J.; Trucks, G. W.; Schlegel, H. B.; Scuseria, G. E.; Robb, M. A.; Cheeseman, J. R.; Scalmani, G.; Barone, V.; Mennucci, B.; Petersson, G. A.; Nakatsuji, H.; Caricato, M.; Li, X.; Hratchian, H. P.; Izmaylov, A. F.; Bloino, J.; Zheng, G.; Sonnenberg, J. L.; Hada, M.; Ehara, M.; Toyota, K.; Fukuda, R.; Hasegawa, J.; Ishida, M.; Nakajima, T.; Honda, Y.; Kitao, O.; Nakai, H.; Vreven, T.; Montgomery, Jr., J. A.; Peralta, J. E.; Ogliaro, F.; Bearpark, M.; Heyd, J. J.; Brothers, E.; Kudin, K. N.; Staroverov, V. N.; Keith, T.; Kobayashi, R.; Normand, J.; Raghavachari, K.; Rendell, A.; Burant, J. C.; Iyengar, S. S.; Tomasi, J.; Cossi, M.; Rega, N.; Millam, J. M.; Klene, M.; Knox, J. E.; Cross, J. B.; Bakken, V.; Adamo, C.; Jaramillo, J.; Gomperts, R.; Stratmann, R. E.; Yazyev, O.; Austin, A. J.; Cammi, R.; Pomelli, C.; Ochterski, J. W.; Martin, R. L.; Morokuma, K.; Zakrzewski, V. G.; Voth, G. A.; Salvador, P.; Dannenberg, J. J.; Dapprich, S.; Daniels, A. D.; Farkas, O.; Foresman, J. B.; Ortiz, J. V.; Cioslowski, J.; Fox, D. J. Gaussian 09, Revision D.01, Gaussian, Inc., Wallingford CT, 2013.
20. (a) Becke, A. D. *J. Chem. Phys.* **1993**, *98*, 5648. (b) Lee, C.; Yang, W.; Parr, R. G. *Phys. Rev. B* **1988**, *37*, 785.

Conclusion of This Thesis

In the PhD research, the author has been devoted to the design and creation of novel forms of nonplanar aromatics by blending helical motifs with other structural motifs. In Chapter 1, corannulene–[6]helicenes (bowl–helix hybrids) were synthesized as synthetic intermediates of circosesquifulvalene, the smallest of warped carbon flakes. Indeed, heptagonal ring closing of the [6]helicene moiety successfully proceeded in the well-tailored corannulene–thia[6]helicene. Chapter 2 described the synthesis of π-extended double carbo[6]helicenes (planar–helix hybrids), in which two relatively planar π-blades were concatenated, giving globally distorted nonplanar π-systems due to the steric repulsion of the two helices. Notably, *twisted*-isomers of double helicenes exhibited unconventional contorted two- and three-dimensional lamellar packing structures. Chapter 3 was the continuation of double helicene chemistry in Chapter 2, wherein π-extended double dithia[6]helicene was designed and synthesized. In crystalline state, this well-tailored planar–helix hybrid not only displayed an unconventional three-dimensional π–π stacking but also was predicted to have an isotropic electronic coupling for hole transfer. As described in Chapter 4, one extra C–C bond formation occurred during the oxidative stitching in the synthesis of π-extended double dithia[6]helicenes, unexpectedly to eventually yield wide laterally π-extended single dithia[6]helicenes (saddle–helix hybrids). Therein, the photophysical and electrochemical measurements uncovered the effects of heptagonal ring closing and chloride atom substitution. In Chapter 5, quadruple helicenes bearing dithia[6]helicene and [5]helicene moieties were synthesized. The crystal structure of the *saddle*-shaped isomer demonstrated that the helix accumulation was an effective strategy to construct the extremely twisted naphthalene core, breaking the limit of distorted aromatics. The molecular geometry dependence of electronic and thermodynamic properties was intensively examined by photophysical, electrochemical, kinetic, and theoretical studies.

Creation of novel forms of nonplanar aromatics is the real pleasure of aromatic chemistry because a diversity of electronic properties, molecular dynamics, and special usages are gifted depending on the three-dimensional shape of each π-system, giving a new field of materials science. In this PhD thesis, the essence of nonplanar aromatic chemistry was firstly grasped and the synthetic guideline was established. Then, the synthesis of helicene-based nonplanar aromatics with prominent structures was described with thorough examination of their properties. The author believes that the molecules unearthed here will not only lay the groundwork in the growing realm of nonplanar π-systems but also lead to the development of new functional materials.

List of Publications

副論文

1. Synthesis, Structures, and Properties of π-Extended Double Helicene: A Combination of Planar and Nonplanar π-Systems
   Takao Fujikawa, Yasutomo Segawa, Kenichiro Itami
   J. Am. Chem. Soc. **2015**, *137*, 7763–7768.

2. Synthesis and Structural Features of Quadruple Helicenes: Highly Distorted π Systems Enabled by Accumulation of Helical Repulsions
   Takao Fujikawa, Yasutomo Segawa, Kenichiro Itami
   J. Am. Chem. Soc. **2016**, *138*, 3587–3595.

3. Corannulene–Helicene Hybrids: Chiral π-Systems Comprising Both Bowl and Helical Motifs
   Takao Fujikawa, Dorin V. Preda, Yasutomo Segawa, Kenichiro Itami, Lawrence T. Scott
   Org. Lett. **2016**, *18*, 3992–3995.

4. Laterally π-Extended Dithia[6]helicenes with Heptagons
   Takao Fujikawa, Yasutomo Segawa, Kenichiro Itami
   Submitted.

5. Synthesis of π-Extended Double Dithia[6]helicene Exhibiting Three-Dimensional Stacking Lattice (Tentative)
   Takao Fujikawa, Nobuhiko Mitoma, Atsushi Wakamiya, Akinori Saeki, Yasutomo Segawa, Kenichiro Itami
   To be submitted.

参考論文

1. Thiophene-Fused π-Systems from Diarylacetylenes and Elemental Sulfur
   Lingkui Meng, Takao Fujikawa, Motonobu Kuwayama, Yasutomo Segawa, Kenichiro Itami
   J. Am. Chem. Soc. **2016**, *138*, 10351–10355.

2. Impact of Morphology, Side-Chains and Crystallinity on Charge-Transport Properties of π-Extended Double Helicenes
   Ilhan Yavuz, Janice B. Lin, Takao Fujikawa, Yasutomo Segawa, Kenichiro Itami, Kendall N. Houk
   Submitted.